

AD-A162 627

CORROSION FATIGUE OF Al-Zn-Mg AND AND Al-Mg-Li ALLOYS

1/3

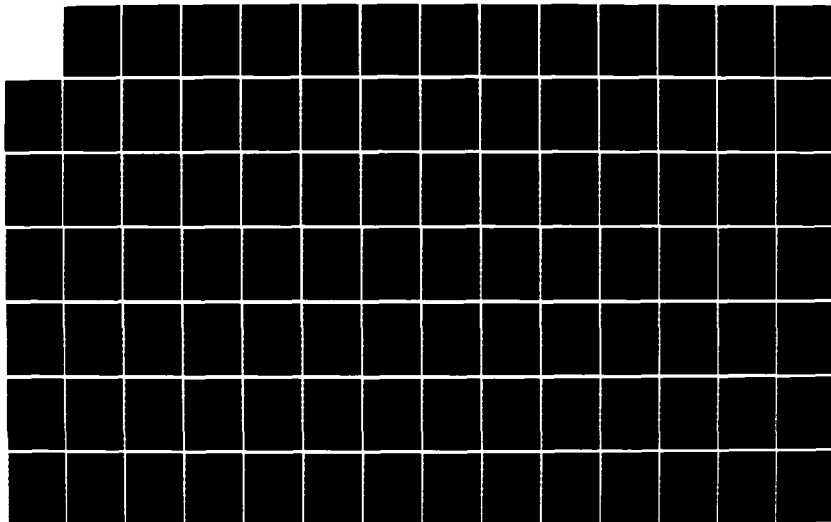
(U) RENSSELAER POLYTECHNIC INST TROY NY DEPT OF
MATERIALS ENGINEERING R E RICKER ET AL. JAN 86

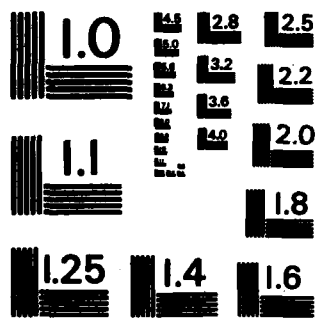
UNCLASSIFIED

N00014-67-A-0117-0012

F/G 11/6

NL





MICROCOPY RESOLUTION TEST CHART
NATIONAL BUREAU OF STANDARDS-1963-A

12

AD-A162 627

FINAL TECHNICAL REPORT

JANUARY 1986

OFFICE OF NAVAL RESEARCH

CONTRACT NO. N00014-67-A-0117-0012

CORROSION FATIGUE OF Al-Zn-Mg AND AN Al-Mg-Li ALLOYS

R.E. Ricker
University of Notre Dame
Department of Metallurgical & Material Science
Notre Dame, Indiana 46556

and

D.J. Duquette
Rensselaer Polytechnic Institute
Materials Engineering Department
Troy, New York 12180-3590

DTIC
ELECTE
DEC 26 1985
E

*REPRODUCTION IN WHOLE OR IN PART FOR ANY PURPOSE OF THE U.S. GOVERNMENT IS
PERMITTED. DISTRIBUTION OF THIS DOCUMENT IS UNLIMITED.

DTIC FILE COPY

0-10-0-108

Unclassified

SECURITY CLASSIFICATION OF THIS PAGE

AD-A162627

REPORT DOCUMENTATION PAGE

1a. REPORT SECURITY CLASSIFICATION Unclassified		1b. RESTRICTIVE MARKINGS	
2a. SECURITY CLASSIFICATION AUTHORITY		3. DISTRIBUTION/AVAILABILITY OF REPORT Reproduction in whole or in part for any purpose of the U.S. Government is permitted. Distribution of this document is unlimited.	
2b. DECLASSIFICATION/DOWNGRADING SCHEDULE		5. MONITORING ORGANIZATION REPORT NUMBER(S)	
4. PERFORMING ORGANIZATION REPORT NUMBER(S) N00014-67-A-0117-0012		7a. NAME OF MONITORING ORGANIZATION	
6a. NAME OF PERFORMING ORGANIZATION Rensselaer Polytechnic Inst.	6b. OFFICE SYMBOL (If applicable)	7b. ADDRESS (City, State and ZIP Code)	
6c. ADDRESS (City, State and ZIP Code) Materials Engineering Department Troy, New York 12180-3590		9. PROCUREMENT INSTRUMENT IDENTIFICATION NUMBER	
8a. NAME OF FUNDING/SPONSORING ORGANIZATION Office of Naval Research	8b. OFFICE SYMBOL (If applicable)	10. SOURCE OF FUNDING NOS.	
8c. ADDRESS (City, State and ZIP Code)		PROGRAM ELEMENT NO.	PROJECT NO.
		TASK NO.	WORK UNIT NO.
11. TITLE (Include Security Classification) Corrosion Fatigue of Al-Zn-Mg and An Al-Mg-Li Alloys			
12. PERSONAL AUTHOR(S) Ricker, R.E. and Duquette, D.J.			
13a. TYPE OF REPORT Final Technical Report	13b. TIME COVERED FROM _____ TO _____	14. DATE OF REPORT (Yr., Mo., Day)	15. PAGE COUNT
16. SUPPLEMENTARY NOTATION			
17. COSATI CODES		18. SUBJECT TERMS (Continue on reverse if necessary and identify by block number)	
FIELD	GROUP	SUB. GR.	
19. ABSTRACT (Continue on reverse if necessary and identify by block number)			
<p>Corrosion fatigue and related electrochemical experiments have been conducted on a high purity Al-Zn-Mg ternary alloy and a high purity Al-Mg-Li ternary alloy. The electrochemical experiments were performed in solutions of various concentrations of sodium chloride and sodium sulfate as functions of pH, temperature and degree of aeration. Thin sheets of the alloys were examined in strain controlled fatigue with controlled environmental conditions. Samples were heat treated to obtain the maximum tensile strength, electropolished, and stored in vacuum to remove absorbed hydrogen. Fatigue tests were performed in dry nitrogen gas as a reference environment, and compared with tests in humid nitrogen, distilled water, 0.5 molar sodium sulfate and 0.5 molar sodium chloride.</p> <p>The corrosion test results indicate that the corrosion potentials of the Al-Mg-Li alloy are considerably more active than those of the Al-Zn-Mg alloy and that the pitting potentials are slightly more active. Therefore, while the lithium alloy pits more readily at the same potential in a given environment, the overpotential or energy required</p>			
20. DISTRIBUTION/AVAILABILITY OF ABSTRACT UNCLASSIFIED/UNLIMITED <input checked="" type="checkbox"/> SAME AS RPT. <input type="checkbox"/> DTIC USERS <input type="checkbox"/>		21. ABSTRACT SECURITY CLASSIFICATION Unclassified	
22a. NAME OF RESPONSIBLE INDIVIDUAL D.J. Duquette		22b. TELEPHONE NUMBER (Include Area Code) (518) 266-6459	22c. OFFICE SYMBOL

Cont'd
Unclassified

SECURITY CLASSIFICATION OF THIS PAGE

to induce pitting in the lithium containing alloy is greater than that required for Al-Zn-Mg alloys.

The fatigue resistance of the Al-Mg-Li alloy in dry nitrogen is virtually identical to that of the Al-Zn-Mg alloy. However, in aggressive environments, the fatigue lives and fatigue limits were decreased in the Al-Zn-Mg alloy while only the fatigue lives were affected for the Al-Mg-Li alloy. Pre-exposure of the Al-Zn-Mg alloy to humid air followed by testing in dry nitrogen resulted in the same fatigue lives as testing in humid nitrogen. The Al-Mg-Li alloy was unaffected by pre-exposure to humid air. The pre exposure embrittlement of the Al-Zn-Mg alloy could be reversed by storage in vacuum.

These results are consistent with the hypothesis that corrosion fatigue of these alloys in environments containing water to water vapor results from hydrogen assisted fracture. The differences in the behavior of the alloys is attributed to either reduced hydrogen absorption or to reduced susceptibility to hydrogen assisted fracture.

Accession For	
NTIS GRA&I	<input checked="" type="checkbox"/>
DTIC TAB	<input type="checkbox"/>
Unannounced	<input type="checkbox"/>
Justification	
By _____	
Distribution/	
Availability Codes	
Dist	Avail and/or Special
A-1	



SECURITY CLASSIFICATION OF THIS PAGE

CONTENTS

LIST OF TABLES	IV
LIST OF FIGURES	V
ACKNOWLEDGEMENT	XVI
ABSTRACT	XVII
I. INTRODUCTION	1
II. HISTORICAL REVIEW	4
A. The Role of Environment on Crack Growth	4
B. Metallurgy of Aluminum Alloys	41
C. Corrosion of Aluminum Alloys	46
D. Stress Corrosion Cracking of Aluminum Alloys ...	49
E. Pre-exposure Embrittlement	54
F. Fatigue of Aluminum Alloys	60
G. Environmental Assisted Crack Propagation	70
H. Corrosion Fatigue Performance	75
III. EXPERIMENTAL	83
A. Objective and Hypothesis	83
B. Materials	84
C. Examination Techniques	93
D. Evaluation of Corrosion Behavior	94
E. Mechanical Testing	99
IV. RESULTS	113
A. Material Evaluation Examinations	113
B. Corrosion Behavior	119
C. Corrosion Fatigue	140
D. Fractography	161
V. DISCUSSION	192
A. Material Evaluation Examinations	192
B. Corrosion Evaluation Tests	195
C. Fatigue Tests	200
VI. CONCLUSIONS	222
VII. SUGGESTIONS FOR FUTURE WORK	225

REFERENCES	228
APPENDIX I. The Derivation of Strain, Load and Displacement Relationships	247
APPENDIX II. Absorption or Desorption From a Plane Sheet	252
APPENDIX III. Linear Regression Analysis of Low Amplitude Strain Controlled Fatigue Data	255

LIST OF TABLES

Table I	The orientation relationships observed between the MgZn precipitates and the aluminum lattice.	43
Table II	Relative predominance of the various precipitate-matrix orientation types of table I in an Al-5.8% Zn-1.1% Mg alloy after solution treatment at 485°C and aging between 130°C and 150°C to peak hardness.	44
Table III	Chemical composition of alloys.	85
Table IV	Properties of the Al-Mg-Li ternary alloy and of aluminum alloy 7075-T6.	88
Table V	Diffusion and thermodynamic information for hydrogen in aluminum and aluminum alloys.	105
Table VI	Effect of Aeration and pH on the electrochemical behavior of aluminum alloy 7050 and the Al-Mg-Li ternary alloy.	125
Table VII	Weight loss measurements for the Al-Mg-Li alloy and the Al-Zn-Mg alloy in sodium sulfate and sodium chloride.	137
Table VIII	Linear regression analysis of the strain control fatigue results.	160

LIST OF FIGURES

Figure 1	Schematic diagram of various sequential processes which may be required for crack propagation.	7
Figure 2	Schematic of crack growth rate and time to failure curves for static loading.	12
Figure 3	Influence of gaseous hydrogen on the static loading crack growth rate of three steels.	14
Figure 4	Arrhenius plot of the temperature dependence of the static loading steady state crack growth rate for AISI 4130 steel in gaseous hydrogen.	15
Figure 5	The effect of hydrogen gas pressure on the static loading steady state crack growth rate of AISI 4130 steel.	17
Figure 6	Arrhenius plot of the temperature dependence of the static loading crack growth rate in a dissociated hydrogen gas environment.	19
Figure 7	Crack growth rate under static loading at constant stress intensity vs. the electrochemical potential in solutions of pH=2.4, 9.3 and 11.7.	21
Figure 8	Arrhenius plot of the temperature dependence of the static loading crack growth rate of HY-180M steel in 3.5% sodium chloride at two electrochemical potentials.	24
Figure 9	Three basic types of corrosion fatigue crack growth behavior.	26
Figure 10	Fatigue crack growth rates of two aluminum alloys in various environments and vacuum at a loading frequency of 100 Hz.	28
Figure 11	Influence of water vapor on fatigue crack growth rate in 2219-T851 aluminum alloy. .	29

Figure 12	Comparison of the observed fatigue crack growth response for 2219-T851 aluminum alloy in water vapor and a transport-limited rate model.	31
Figure 13	Effect of oxygen pressure on fatigue crack growth rate of type 316 stainless steel at 500°C.	32
Figure 14	Fatigue life of nickel superalloy single crystals (low carbon MAR-M200) in air and vacuum at 20°C, 760°C and 925°C.	34
Figure 15	Fatigue crack growth in a cobalt base directionally solidified eutectic in air and vacuum at 25°C and 750°C.	35
Figure 16	Effect of loading variables on the corrosion fatigue crack growth of a 12Ni-5Cr-3Mo steel in 3.0% sodium chloride solution.	37
Figure 17	Effect of loading frequency on the fatigue crack growth rate of a 6Al-6V-2Sn titanium alloy in 0.6 N sodium chloride solution.	38
Figure 18	Effect of water additions on the fatigue crack growth rate of a titanium alloy in a 0.6 N lithium chloride methanol solution.	40
Figure 19	Electrochemical equilibrium or Pourbaix diagram for aluminum and the alloying elements used for this investigation.	48
Figure 20	The effect of humidity and stress intensity on the stress corrosion crack velocity of alloy 7075-T651.	51
Figure 21	The effect of loading mode on the stress corrosion cracking of Ti-8% Al-1% Mo-1% V, Alpha brass, and 7075-T6.	52
Figure 22	The effect of strain rate on the ductility of alloy 7049 in different environments.	55
Figure 23	The effect of strain rate on the	

	ductility of alloy 7049 in different environments after a three day pre-exposure to seawater.	56
Figure 24	Schematic illustration of the aluminum-water vapor reactions on the surface of aluminum alloys.	59
Figure 25	A schematic illustration of the various modes of fatigue fracture observed in age hardened aluminum alloys.	61
Figure 26	Diagrammatic summary of the important slip-band intrusion and extrusion features commonly observed.	63
Figure 27	Schematic diagram of a stage 1 crack and associated dipole array.	66
Figure 28	Schematic diagram illustrating micro-cracking ahead of the crack tip and the growth of dimples as the crack progresses.	68
Figure 29	Schematic of intrusions at a crack tip showing regions of ductile tearing.	69
Figure 30	Schematic of the mechanism of striation formation and the plane of propagation showing how propagation can occur on different crystallographic planes.	71
Figure 31	Schematic of proposed difference between "brittle" and "ductile" striation formation.	74
Figure 32	Effect of oxide surface layer thickness on the cycles to crack initiation and cycles to failure.	76
Figure 33	Effect of electrochemical potential on the cycles to failure the hydrogen permeation flux and the polarization current density of alloy 7075.	77
Figure 34	The effect of loading mode on the fatigue lives of alloy 7075 in air and aerated 0.5 N sodium chloride.	79

Figure 35	The effect of mean stress on the fatigue lives of alloy 7075 in aerated 0.5 N sodium chloride at different cyclic stress ranges.	80
Figure 36	Comparison of the fatigue lives of peak aged and overaged samples of alloy 7075 in air and in aerated 0.5 N sodium chloride.	82
Figure 37	Hardness versus the aging time for the Al-Zn-Mg ternary alloy in silicone oil at 120°C.	87
Figure 38	Cracks at the powder particle interfaces for the Al-Mg-Li alloy after cold rolling to 4% reduction in thickness.	89
Figure 39	Isothermal sections of the Al-Mg-Li ternary phase diagram at 450°C and 500°C. .	91
Figure 40	Hardness response as a function of aging time for the Al-Mg-Li alloy in silicone oil at various temperatures.	92
Figure 41	Schematic diagram of the electrochemical polarization cell.	96
Figure 42	Fatigue sample design and bending fatigue grips.	100
Figure 43	Diagram of the various equipment used to conduct the fatigue tests.	102
Figure 44	The correspondence of the diffusion equation derived in Appendix II for an estimated diffusion coefficient of 5.6×10^{-18} cm ² /sec with the hydrogen content versus exposure to humid air measurements of Ciaraldi (80) for a high purity Al-Zn-Mg ternary alloy.	107
Figure 45	The environmental regulation and maintenance system used for fatigue tests in dry nitrogen gas.	108
Figure 46	The environmental regulation and maintenance system for fatigue tests in 87% relative humidity nitrogen gas.	109

Figure 47	Test cell and electrochemical instruments used for conducting tests in 0.5 <u>M</u> sodium sulfate and sodium chloride.	112
Figure 48	Metallographic sections in the short transverse, long transverse and the rolling direction of a fatigue sample of the Al-Zn-Mg ternary alloy.	114
Figure 49	Metallographic sections in the short transverse, long transverse and the rolling direction of a fatigue sample of the Al-Mg-Li ternary alloy.	115
Figure 50	Phase contrast micrographs of the electropolished surfaces of an Al-Zn-Mg alloy sample (A) and an Al-Mg-Li alloy sample (B) after bending to a surface strain of approximately 1.5%.	116
Figure 51	Phase contrast image of the deformation at at a fatigue crack tip in an Al-Zn-Mg alloy sample.	118
Figure 52	Auger electron spectroscopy of the surfaces of an Al-Zn-Mg alloy and an Al-Mg-Li alloy sample after exposure to humid air.	120
Figure 53	Effect of potentiodynamic scan rate on the polarization behavior of the Al-Mg-Li alloy in deaerated 0.5 <u>M</u> sodium chloride at 23°C.	121
Figure 54	Effect of solution aeration on the polarization behavior of the Al-Mg-Li alloy in 0.5 <u>M</u> sodium chloride at 23°C and 1 mV/sec scan rate.	123
Figure 55	Effect of pH on the polarization behavior of the alloys in deaerated 0.5 <u>M</u> sodium chloride at 23°C and 1 mV/sec scan rate. .	126
Figure 56	Effect of temperature on the polarization behavior of the alloys in deaerated 0.5 <u>M</u> sodium chloride at 1 mV/sec scan rate. ...	129
Figure 57	Temperature versus the corrosion and pitting potentials for the alloys in	

	deaerated 0.5 M sodium chloride.	131
Figure 58	Effect of chloride ion concentration on the polarization behavior of the alloys in deaerated sodium chloride at 23°C and 1 mV/sec scan rate.	133
Figure 59	Chloride ion activity versus the pitting and corrosion potentials of the Al-Mg-Li alloy in aerated and deaerated sodium chloride solutions at 23°C.	135
Figure 60	The dissolution rate determined from weight loss measurements for the Al-Zn-Mg ternary alloy in 0.5 M sodium sulfate and 0.5 M sodium chloride at constant electrochemical potentials.	138
Figure 61	The dissolution rate determined from weight loss measurements for the Al-Mg-Li ternary alloy in 0.5 M sodium sulfate and 0.5 M sodium chloride at constant electrochemical potentials.	139
Figure 62	Cyclic strain range versus the cycles to failure for the Al-Zn-Mg alloy and the Al-Mg-Li alloy in dry nitrogen after vacuum pre-exposure.	141
Figure 63	Cyclic strain range versus the cycles to failure for the Al-Zn-Mg alloy in humid and dry nitrogen.	143
Figure 64	Cyclic strain range versus the cycles to failure for the Al-Mg-Li alloy in humid and dry nitrogen.	144
Figure 65	The effect of different pre-exposure and test environments on the fatigue lives of Al-Zn-Mg alloy samples as compared with testing in dry nitrogen after a vacuum pre-exposure (solid line) and with testing in humid nitrogen after a humid air pre-exposure (dashed line).	145
Figure 66	The effect of different pre-exposure and test environments on the fatigue lives of Al-Mg-Li alloy samples as compared with testing in dry nitrogen after a vacuum	

	pre-exposure (solid line) and with testing in humid nitrogen after a humid air pre-exposure (dashed line).	147
Figure 67	The effect of varying vacuum pre-exposure times on the percent of recovered fatigue life of samples of the Al-Zn-Mg ternary alloy.	149
Figure 68	Cyclic strain range versus the cycles to failure for samples of the Al-Zn-Mg alloy in pure water, 0.5 M sodium sulfate and 0.5 M sodium chloride.	150
Figure 69	Cyclic strain range versus the cycles to failure for samples of the Al-Mg-Li alloy in pure water, 0.5 M sodium sulfate and 0.5 M sodium chloride.	152
Figure 70	Fatigue life at a cyclic strain range of 0.0045 m/m (0.45%) versus the potentiostatically held constant electrochemical potential for samples of the Al-Zn-Mg alloy in 0.5 M sodium sulfate and sodium chloride.	153
Figure 71	Fatigue life at a constant strain range of 0.0045 m/m (0.45%) versus the potentiostatically held constant electrochemical potential for samples of the Al-Mg-Li alloy in 0.5 M sodium sulfate and 0.5 M sodium chloride.	155
Figure 72	Linear regression analysis of the logarithm of the cyclic strain range versus the logarithm of the cycles to failure for the Al-Zn-Mg alloy in dry nitrogen, humid air, pure water, 0.5 M sodium sulfate and 0.5 M sodium chloride. .	157
Figure 73	Linear regression analysis of the logarithm of the cyclic strain range versus the logarithm of the cycles to failure for the Al-Mg-Li alloy in dry nitrogen, humid air, pure water, 0.5 M sodium sulfate and 0.5 M sodium chloride. .	158
Figure 74	The fracture surface of a sample of the Al-Zn-Mg alloy tested in dry nitrogen. ...	163

Figure 75	The transgranular cleavage-like fracture morphology of a sample of the Al-Zn-Mg alloy tested in dry nitrogen.	163
Figure 76	Comparison of the transgranular cleavage-like fracture in two grains of a sample of the Al-Zn-Mg alloy tested in dry nitrogen.	164
Figure 77	A region of transgranular cleavage-like fracture of a sample of the Al-Zn-Mg alloy tested in dry nitrogen.	164
Figure 78	A region of transgranular cleavage-like fracture of a sample of the Al-Zn-Mg alloy tested in dry nitrogen.	165
Figure 79	The intergranular fracture surface of a sample of the Al-Zn-Mg alloy tested in dry nitrogen.	167
Figure 80	The intergranular fracture surface of a sample of the Al-Zn-Mg alloy tested in dry nitrogen.	168
Figure 81	Stage 1 crack propagation of a sample of the Al-Zn-Mg alloy tested in dry nitrogen.	168
Figure 82	The morphology of three regions of stage 1 crack propagation of a sample of the Al-Zn-Mg alloy tested in dry nitrogen. ...	169
Figure 83	A crack initiation site for the fatigue fracture of a sample of the Al-Zn-Mg alloy tested in dry nitrogen.	170
Figure 84	An intergranular region at the initiation site of the fatigue fracture of a sample of the Al-Zn-Mg alloy tested in dry nitrogen.	170
Figure 85	The fracture surface of a sample of the Al-Zn-Mg alloy tested in humid nitrogen. .	171
Figure 86	The fracture surface of a sample of the Al-Zn-Mg alloy tested in humid nitrogen. .	171
Figure 87	The transgranular cleavage-like fracture	

	surface of a sample of the Al-Zn-Mg alloy tested in humid nitrogen.	173
Figure 88	A region of transgranular on the fracture surface of a sample of the Al-Zn-Mg alloy tested in humid nitrogen.	173
Figure 89	A region of intergranular fracture on the fracture surface of a sample of the Al-Zn-Mg alloy tested in humid nitrogen.	174
Figure 90	The fracture surface of a sample of the Al-Zn-Mg alloy tested in humid nitrogen. .	174
Figure 91	The intergranular fracture and secondary intergranular cracks on the fracture surface of a sample of the Al-Zn-Mg alloy tested in pure water.	175
Figure 92	A region of transgranular cleavage-like fracture of an Al-Zn-Mg alloy tested in pure water.	175
Figure 93	Mixed intergranular and transgranular fracture of a sample of the Al-Zn-Mg alloy tested in sodium sulfate.	177
Figure 94	A region of transgranular cleavage-like fracture of a sample of the Al-Zn-Mg alloy tested in 0.5 M sodium sulfate.	177
Figure 95	Regions of transgranular and intergranular fracture of a sample of the Al-Zn-Mg alloy tested in 0.5 M sodium sulfate.	178
Figure 96	The fragmented surface layer found on the intergranular fracture surface of an Al-Zn-Mg alloy sample tested in 0.5 M sodium sulfate.	178
Figure 97	The fracture surface of a sample of the Al-Zn-Mg alloy tested in 0.5 M sodium chloride at a constant potential of -0.8 V _{sc}	179
Figure 98	The external surface of a sample of the Al-Zn-Mg alloy tested in 0.5 M sodium chloride. at a constant potential of -0.8	

	Vsce.	179
Figure 99	The fracture surface of a sample of the Al-Zn-Mg alloy tested in 0.5 M sodium chloride. at a constant potential of -1.0 Vsce.	181
Figure 100	The fracture surface of a sample of the Al-Zn-Mg alloy tested in 0.5 M sodium chloride at a constant potential of -1.6 Vsce.	181
Figure 101	The fracture surface of a sample of the Al-Mg-Li alloy tested in dry nitrogen. ...	182
Figure 102	The crack initiation and stage 1 crack propagation regions of the fracture surface of an Al-Mg-Li alloy sample tested in dry nitrogen.	182
Figure 103	The crack initiation and stage 1 crack propagation regions of the fracture surface of an Al-Mg-Li alloy sample tested in dry nitrogen.	183
Figure 104	The fracture surface of a sample of the Al-Mg-Li alloy tested in humid nitrogen. .	183
Figure 105	The fracture surface of a sample of the Al-Mg-Li alloy tested in pure water.	185
Figure 106	The fracture surface of a sample of the Al-Mg-Li alloy tested in pure water.	185
Figure 107	Secondary transgranular cracks in the fracture surface of an Al-Mg-Li alloy sample tested in pure water.	186
Figure 108	Secondary cracks in the fracture surface of a sample of the Al-Mg-Li alloy tested in pure water.	186
Figure 109	The fracture surface of a sample of the Al-Mg-Li alloy tested in 0.5 M sodium sulfate.	187
Figure 110	Deposits on the fracture surface of a sample of the Al-Mg-Li alloy tested in 0.5 M sodium sulfate.	187

Figure 111	Deposits on the external surface of an Al-Mg-Li alloy sample tested in 0.5 M sodium sulfate.	188
Figure 112	The fracture surface of a sample of the Al-Mg-Li alloy tested in 0.5 M sodium sulfate at a constant potential of -1.2 V _{sce}	188
Figure 113	The fracture surface of a sample of the Al-Mg-Li alloy tested in 0.5 M sodium sulfate at a constant potential of -1.6 V _{sce}	189
Figure 114	The fracture surface of a sample of the Al-Mg-Li alloy tested in 0.5 M sodium chloride at a constant potential of -1.2 V _{sce}	189
Figure 115	The fracture surface of a sample of the Al-Mg-Li alloy tested in 0.5 M sodium chloride at a constant potential of -1.2 V _{sce}	191
Figure 116	The fracture surface of a sample of the Al-Mg-Li alloy tested in 0.5 M sodium chloride at a constant potential of -1.6 V _{sce}	191

ACKNOWLEDGEMENT

The author would like to express his gratitude to the students, faculty and staff of Rensselaer Polytechnic Institute who contributed to this investigation through their efforts or their insight. Those deserving recognition are too numerous to list, however, the contributions of M. Feeney, T. Slavin and R. Hahn are too great to go without acknowledgement. Also, I am indebted to Dr. Ford, Dr. Hudson, Dr. Aikens, Dr. Stolloff and Dr. Duquette for their assistance as well as acting as the examining committee. Professor Duquette also served as thesis advisor and without his support and understanding this work would not have been undertaken nor reached conclusion. Finally, I would like to thank Winifred, Carrie and Jacob Ricker for their tolerance, assistance and sacrifice.

ABSTRACT

Corrosion fatigue and related electrochemical experiments have been conducted on a high purity Al-Zn-Mg ternary alloy and a high purity Al-Mg-Li ternary alloy. The electrochemical experiments were performed in solutions of various concentrations of sodium chloride and sodium sulfate as functions of pH, temperature and degree of aeration. Thin sheets of the alloys were examined in strain controlled fatigue with controlled environmental conditions. Samples were heat treated to obtain the maximum tensile strength, electropolished, and stored in vacuum to remove absorbed hydrogen. Fatigue tests were performed in dry nitrogen gas as a reference environment, and compared with tests in humid nitrogen, distilled water, 0.5 molar sodium sulfate and 0.5 molar sodium chloride.

The corrosion test results indicate that the corrosion potentials of the Al-Mg-Li alloy are considerably more active than those of the Al-Zn-Mg alloy and that the pitting potentials are slightly more active. Therefore, while the lithium alloy pits more readily at the same potential in a given environment, the overpotential or energy required to induce pitting in the lithium containing alloy is greater than that required for Al-Zn-Mg alloys.

The fatigue resistance of the Al-Mg-Li alloy in dry

nitrogen is virtually identical to that of the Al-Zn-Mg alloy. However, in aggressive environments, the fatigue lives and fatigue limits were decreased in the Al-Zn-Mg alloy while only the fatigue lives were affected for the Al-Mg-Li alloy. Pre-exposure of the Al-Zn-Mg alloy to humid air followed by testing in dry nitrogen resulted in the same fatigue lives as testing in humid nitrogen. The Al-Mg-Li alloy was unaffected by pre-exposure to humid air. The pre-exposure embrittlement of the Al-Zn-Mg alloy could be reversed by storage in vacuum.

These results are consistent with the hypothesis that corrosion fatigue of these alloys in environments containing water or water vapor results from hydrogen assisted fracture. The differences in the behavior of the alloys is attributed to either reduced hydrogen absorption or to reduced susceptibility to hydrogen assisted fracture.

I. INTRODUCTION

Commercial application of high strength aluminum alloys has been limited because of their low ductility at high strength levels and their susceptibility to environmental assisted fracture. As a result, a great deal of research on these alloys has focussed on these problems. This dissertation is an investigation into the mechanism of environmental assisted fatigue fracture of two high strength aluminum alloys.

Most of the research on the fracture properties of aluminum alloys has centered on the Al-Zn-Mg system (7000 series) because these alloys exhibit the highest strength levels and are the most susceptible to environmental assisted fracture. Investigators have modified metallurgical variables such as grain size, precipitate size, precipitate distribution and surface finish as well as loading and environmental variables. Then, by carefully observing the changes in the crack growth and failure of the samples, the investigators have attempted to explain the results in terms of simple models of the chemical and mechanical interactions at the crack tip. However, for aluminum alloys, the models usually depend on either anodic dissolution of metal at the crack tip or on hydrogen embrittlement of the metal at the crack tip for the actual

process of crack extension.

For this investigation, a similar approach was taken except that instead of varying the metallurgical, environmental, or loading conditions for a single alloy, comparison has been made between two similar but significantly different alloys of aluminum in identical tests. The purpose of this is not to develop a new improved class of alloys any more than the previous work was to develop improved manufacturing techniques by identifying desirable metallurgical conditions and how to achieve them. Instead, the alloys were chosen because while they are both precipitation hardened alloys of aluminum and accordingly are composed almost entirely of aluminum, they are significantly different both metallurgically and chemically. These differences will allow the evaluation of the importance of these factors in the corrosion fatigue behavior of aluminum alloys. That is, it will make it possible to identify the important parameters in corrosion fatigue of aluminum alloys and accordingly assist in the identification of the actual physical mechanism of accelerated fatigue failure.

Two pure ternary alloys were chosen for this work. The first is an Al-5.5% Zn-2.5%Mg alloy similar to the 7000 series alloys that most of the work in the literature has concentrated on. The second is an Al-4.2% Mg-2.2% Li alloy.

Bending fatigue tests were performed on thin sheets of the alloys in dry nitrogen, humid nitrogen, pure water, a sodium sulfate solution and a sodium chloride solution.

II. HISTORICAL REVIEW

A. The Role of Environment on Crack Growth

Gaseous as well as aqueous environments are known to accelerate time dependent crack growth under either static loading (SCC or HE) or dynamic loading conditions. In some cases, the rate controlling processes of these phenomena have been related to surface controlled reactions, while in other cases bulk reactions such as diffusion appear to be rate limiting. It is not entirely clear that the mechanisms of time dependent crack growth are identical for different environment/alloy couples, or for different ranges of loading conditions.

While it is generally accepted that aggressive environments accelerate crack propagation in cyclically loaded metals and alloys, the specific environmental reactions or chemico-mechanical processes which control the rates of crack propagation are not always understood.

The role of the environment is usually evaluated by conducting standardized tests under various controlled environmental conditions and comparing the results to those obtained in "neutral" environments (e.g. vacuum or inert gases) (1-4). The goal is to avoid failures by controlling or at least accurately predicting crack growth or initiation. The advent of fracture mechanics has lead to

the development of a semi-quantitative approach to these determinations. In this approach, the usable lifetime of a component is estimated by determining the time required for a pre-existing flaw to propagate to critical failure. The crack growth rate, and accordingly the service life, may be determined by the maximum possible rate of the environmental fracture mechanism, however, usually some slower environmental interaction, which must precede the actual fracture and is required by the fracture mechanism, is the rate determining step. Thus, changes in the crack propagation rate resulting from altering the aggressiveness of the environment may reflect the effect of these alterations on the rate determining step(s) and not on the actual fracture process.

Mechanisms of Environmental Assisted Fracture

There are a large number of different fracture mechanisms which have been proposed to explain environmental assisted crack propagation. The details of each specific mechanism will not be discussed in this paper. However, the mechanisms which have been proposed are based on either:

1. Active corrosion of material at the crack tip
2. Adsorption of environmental species
3. Reactions in the bulk material ahead of the advancing crack
4. The formation of oxide films

Specific mechanisms differ in the process by which environmental factors combine with the strained metal to result in the actual fracture processes of crack extension. This combined effect occurs at the crack tip or in the plastic zone ahead of the crack tip. A series of events and/or reactions provide the required environmental influence to this fracture, and usually, these steps determine the rate of propagation and not the actual fracture process.

Rate Limiting Steps

All of the proposed mechanisms require a sequence of generally discrete events or reactions for crack growth to occur. The rate determining step of a mechanism is, of course, the slowest step in the sequence of reactions or events required by the mechanism. Due to the similarities of the different mechanisms, there are only a few specific possible rate determining steps for a given fracture event.

Figure 1 schematically shows a crack tip exposed to an environment. This figure shows that there are at least seven separate types of processes which may occur, any one of which may be rate determining. These include:

1. Mass transport of the environment to the crack tip
2. Surface adsorption at and near the crack tip
3. Surface diffusion to the crack tip
4. Surface chemical reaction(s)
5. Volume diffusion ahead of the crack tip

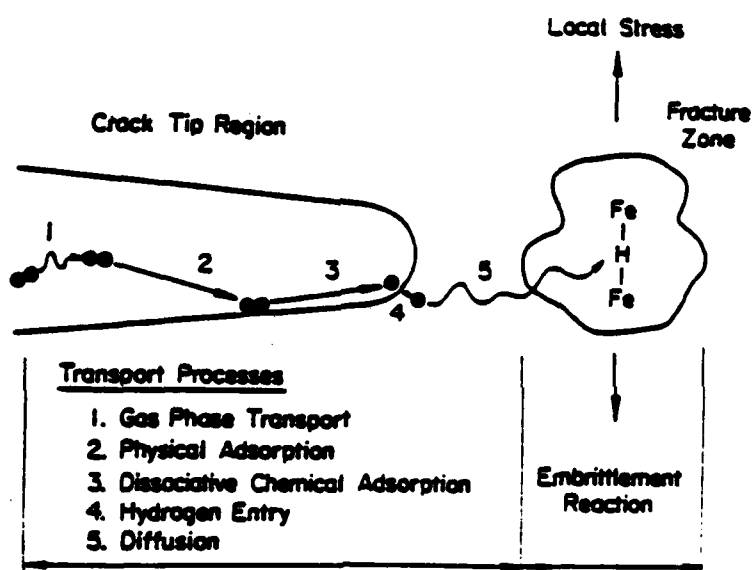


Figure 1

Schematic diagram of various sequential processes which may be required for crack propagation (illustration depicts embrittlement of iron by hydrogen) (39).

6. Embrittling reaction(s) in the bulk
7. The separation (fracture) process

It is generally accepted that environments at crack tips often differ from the external environment. This may result from limited mass transport to this region. If this is the rate limiting step, propagation will vary with crack length, specimen thickness and loading frequency for fatigue tests (8,9).

The rate of adsorption of atoms of environmental species at the crack tip also may be a rate limiting step. In gaseous environments this can be the rate of atoms impinging on the crack tip surfaces. In aqueous environments the rate of adsorption is generally considered to be fast. If a film forms which blocks the adsorption, the rate of the mechanical process of generating fresh crack surfaces may become the rate limiting step (10,11).

If the atoms adsorbed must migrate to locations to affect crack propagation, then surface diffusion could be the rate determining step. This often occurs in gaseous environments, particularly in poor vacuums (5).

A reaction on the surface also may be the rate limiting step if such a reaction occurs. The formation of oxide layers or the dissociation of environmental molecules would require such reaction steps (18,20).

Species in the local environment or liberated by

chemical reactions may diffuse into a sample ahead of the advancing crack. In the highly strained region at the crack tip, the diffusing species may react with either the alloying elements of the sample or impurities in the sample. Also, if a supersaturation results in the plastic zone, the diffusing species may precipitate. Either the diffusion process or a chemical reaction step may be rate controlling. For example, these steps may be rate controlling for hydrogen embrittlement, internal oxidation, carburization, nitriding, or hydrogen attack (12,13). Diffusion can also be rate limiting for dealloying effects such as preferential oxidation, preferential dissolution (ie. dezincification), or evaporative losses of high vapor pressure alloy constituents (13).

The actual separation process could be the rate determining step, but no investigator has found this to be the case. Wei (5) estimated that for AISI 4340 steel the activation energy for the actual fracture process is less than 5 kJ/mole. This is considerably lower than the activation energies found for environmental assisted crack growth (5). The rate determining step in crack propagation is generally not the actual separation process, but usually some environmental interaction which is required for fracture.

Environmental Parameters

Several different environmental parameters are known to affect crack growth rates (14,15). These parameters include, but may not be limited to:

- I. Temperature
- II. Type of environment (bulk and local)
 - A. Gaseous
 - 1. Specific components
 - 2. Partial pressure
 - 3. Reactivity
 - B. Aqueous
 - 1. Solution species
 - 2. Solute concentration
 - 3. pH
 - 4. Electrode potential
 - 5. Solution viscosity
 - C. Others
 - 1. Liquid metals
 - 2. Organic solvents

Systematically altering any of these parameters or combinations of them may help to identify either the rate controlling step(s) or the environmental species responsible for crack propagation. Altering the temperature may allow the activation energy of crack propagation to be determined.

Static Loading Crack Growth

Time dependent or sub-critical crack growth under static loading conditions is classified as either creep, stress corrosion cracking (SCC), liquid metal embrittlement

(LME), or hydrogen embrittlement (HE). Delayed failure phenomena are influenced by the following parameters:

1. Applied stress or stress intensity factor
2. State of stress or loading mode
3. Metallurgical history
4. Crack geometry
5. Alloy composition
6. The environmental parameters listed above.

Tests are performed by placing either smooth samples or precracked samples into the environment and measuring either the time to failure or the actual crack propagation rates. The results of the tests are then plotted as shown in figure 2. Figure 2(a) shows a typical plot of crack propagation rate against the stress intensity factor for a precracked sample (15). From this it can be seen that there are three distinct stages of crack growth. In the first stage, the crack propagation rate increases rapidly with the stress intensity factor beginning at some stress intensity factor usually designated as the threshold stress intensity factor (K_{th} or K_{ISCC}). In the second stage, crack growth is essentially independent of the stress intensity factor. In the final stage, crack propagation is again a strong function of the stress intensity as the crack approaches the critical flaw size (this stage is not always observed). In the first and third stages, crack propagation is strongly influenced by the stress intensity factor. In the second stage or the steady state stage, the crack propagation rate

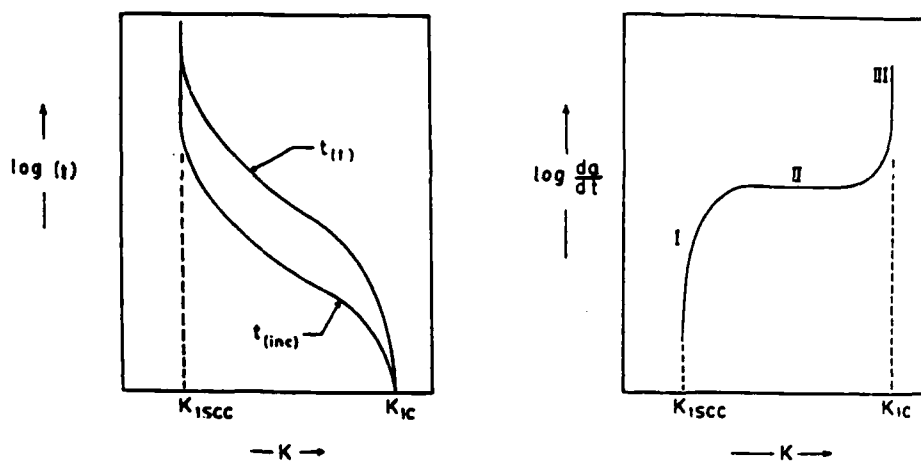


Figure 2

Schematic of crack growth rate (A) and time to failure curves (B) for static loading (14).

is generally believed to be determined by a rate limiting step.

Figure 3 shows the subcritical crack growth behavior of three different steels in hydrogen gas (14). In this figure, two of the steels demonstrate stage 2 propagation which is independent of the mechanical driving force (as measured by the stress intensity factor). Since crack propagation is the result of combined mechanical and environmental factors, and since stage 2 propagation is independent of the magnitude of the mechanical contribution, then it is logical to assume that the rate of stage 2 growth is, in fact, determined by a rate controlling environmental reaction. By varying the temperature and measuring the rate of stage 2 propagation, the activation energy of crack propagation was evaluated (16). If this rate is determined by a single rate determining step, then the activation energy of crack propagation should be a measure of the activation energy of this reaction.

Figure 4 is a plot of the reciprocal of temperature against the rate of crack growth for a AISI 4130 steel in hydrogen gas (17). In this figure, three different regions of behavior are shown. At low temperatures ($<0^{\circ}\text{C}$) the mean stage 2 growth rate increases with increasing temperature (region 3 in figure 4). At higher temperatures ($>40^{\circ}\text{C}$), the crack growth rate decreases with increasing temperature

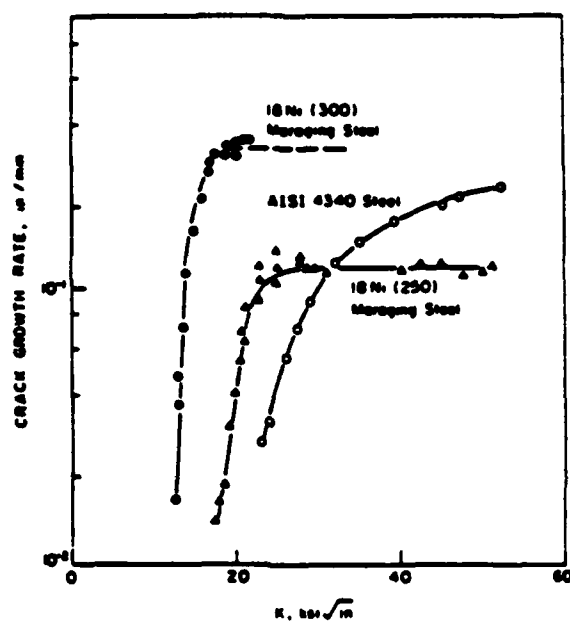


Figure 3

Influence of gaseous hydrogen on the static loading crack growth rate of three steels (14).

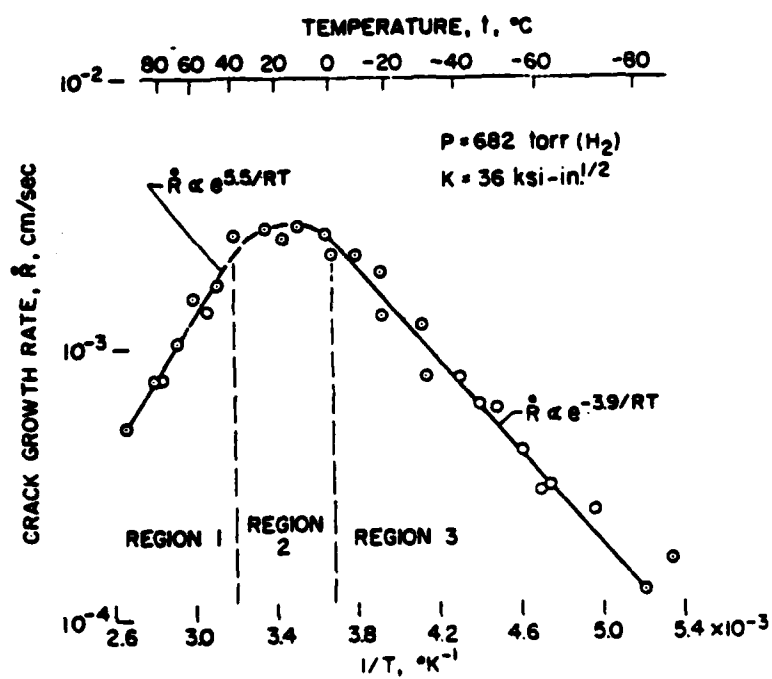


Figure 4

Arrhenius plot of the temperature dependence of the static loading steady state crack growth rate for AISI 4130 steel in gaseous hydrogen (17).

(region 1 in figure 4). Between these two regions is a transition region where crack growth is almost independent of temperature (region 2 in figure 4). Both regions 1 and 3 show Arrhenius type temperature dependence with activation energies of -23 and +18 kJ/mole respectively (17,20).

Figure 5 shows the pressure dependence of the crack growth rate at constant stress intensity in each of the three regions of temperature behavior discussed above. A different pressure dependence was found for each of the three regions. At low temperatures (region 3), the crack growth rate varied with the square root of the hydrogen gas pressure. At high temperatures (region 1), the crack growth rate varied directly with the pressure. At intermediate temperatures, region 2, the growth rate varied with the hydrogen gas pressure to the 1.5 power. Since the activation energy for hydrogen permeation (36 kJ/mole) is very different from the activation energy measured for crack propagation (18 kJ/mole), this is not the rate controlling step of hydrogen embrittlement under these conditions. Williams and Nelson (17) recognized that the shape of the crack growth rate vs. reciprocal temperature curve, figure 4, is of the same basic shape as an adsorption rate vs. reciprocal temperature curve for thermally activated adsorption. Accordingly, they developed a model for the crack growth rate using the hydrogen adsorption results of

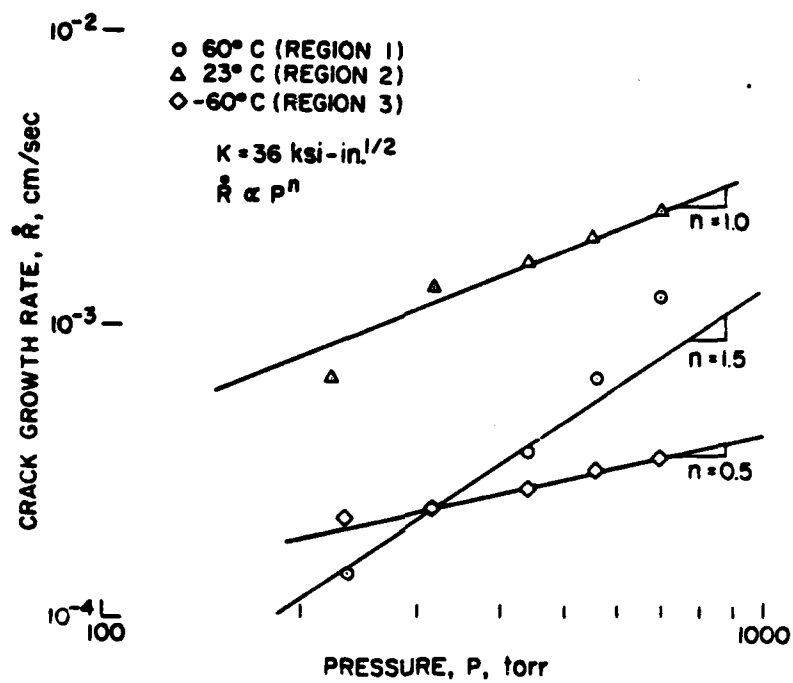


Figure 5

The effect of hydrogen gas pressure on the static loading steady state crack growth rate of AISI 4130 steel (17).

Porter and Tompkins (38). This model explains both the temperature dependence of figure 4 and the pressure dependence of figure 5. According to this model, the activation energy of the low temperature region, region 3, is the energy of migration from the "initial" adsorption sites. Also, according to this model, the activation energy measured for the high temperature region, region 1 in figure 4, is the sum of the heat of adsorption and the energy of migration. The activation energies found in figure 4 are in the range of values found by Porter and Tompkins (38). Williams and Nelson concluded that the crack growth rate in this environment is controlled by a heterogeneous reaction involving the transition of hydrogen from its molecular form in the gas phase to its atomic form on the crack surface (21). To circumvent this slow step, Nelson et. al. tested samples in a partially dissociated hydrogen gas environment (21). They found, as shown in figure 6, that the three distinct regions of thermally activated crack growth no longer existed, that the activation energy for propagation changed, and that the rate of crack propagation was greatly accelerated as compared to that observed for the same pressure of molecular hydrogen gas (17). They determined the apparent activation energy for this environment to be +28.5 kJ/mole (21). Comparing this to the activation energies of permeation, +35.6 kJ/mole, lattice diffusion,

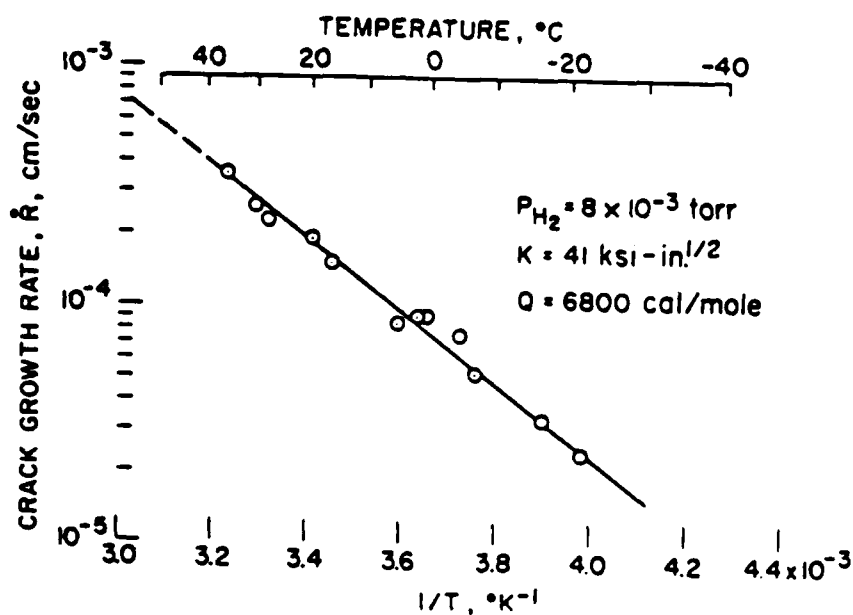


Figure 6

Arrhenius plot of the temperature dependence of the static loading crack growth rate in a dissociated hydrogen gas environment (21).

+7.9 kJ/mole, and the apparent heat of solution, +27.2 kJ/mole, they concluded that the rate controlling reaction was the establishment of a hydrogen population in the ferrous lattice just below the crack tip surface (21). The morphology of the fracture surfaces in this environment was virtually unchanged from that observed in the molecular hydrogen gas environment. These investigators concluded that the specific mechanism of hydrogen induced cracking did not change as a function of molecular or atomic hydrogen atmosphere but that only the rate determining step changed (21).

A change of environment from a gas to an aqueous solution adds significantly to the complexity of the problem. In addition to the effects of solute type and concentration in the solution, there is also the possibility of reactions with the water itself to produce hydrogen gas, oxide films, and/or pH changes in the growing cracks.

Van Der Sluys studied the effect of varying electrochemical potential and pH on the crack growth rate of cracks in an AISI 4340 steel (22). Figure 7 shows the potential vs. crack growth rate in three different pH solutions. The curves show basically three different regions of potential vs. growth rate behavior. First, at potentials active compared to the hydrogen evolution potential, the growth rate increases with decreasing

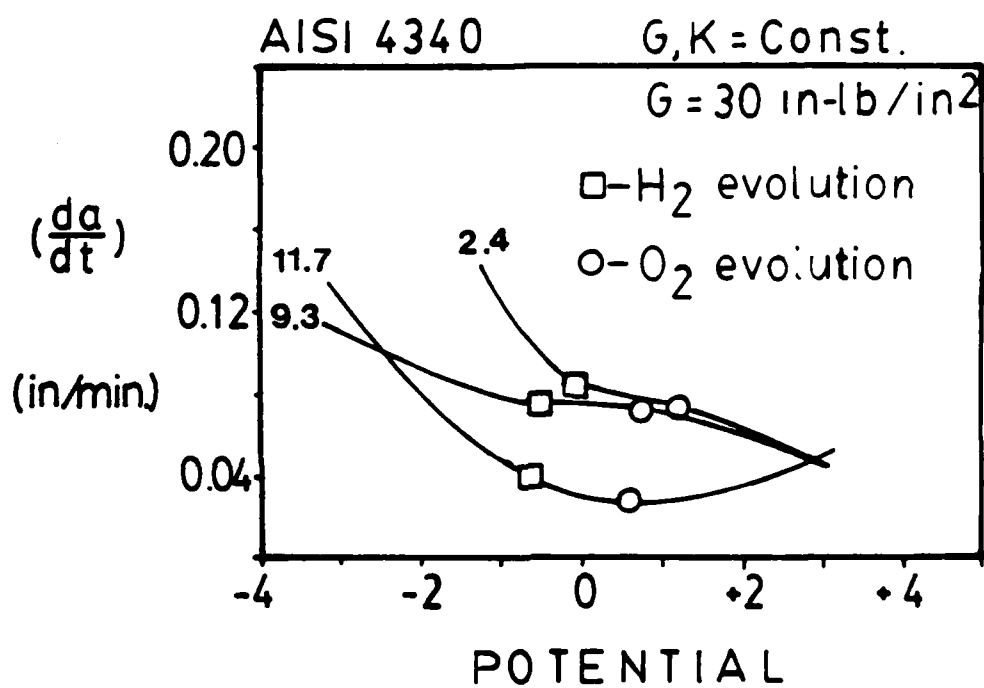


Figure 7

Crack growth rate under static loading at constant stress intensity vs. the electrochemical potential in solutions of $\text{pH}=2.4, 9.3$ and 11.7 (22).

potential and accordingly increasing hydrogen fugacity. Second, a plateau is observed in the region of water stability (above the potential for cathodic hydrogen evolution and below the potential where oxygen evolution begins) and third, the growth rate decreases with increasing potentials above the oxygen evolution potential (22). The drop off at passive potentials was not very great. In the pH 2 solution, the growth rate actually increased with potentials above the oxygen evolution potential (figure 7). Van Der Sluys (22) concluded that at cathodic potentials hydrogen embrittlement is the dominant mechanism of crack growth and at anodic potentials dissolution is the dominant mechanism of crack growth.

Bala and Tromans studied the crack growth rate of HY-180M steel in a 3.5% NaCl solution (23,24). They found a strong dependence of crack growth rate on potential. No crack growth occurred at -0.52 V_{she} but, crack growth did occur at potentials both above and below this value (The reversible potential for iron in this solution is -0.53 V_{she}) (23,24). They also concluded that hydrogen embrittlement was responsible for cracking at active potentials while anodic dissolution was involved at noble potentials. However, while studying the effects of temperature on the crack growth rate, these authors observed the same effect of increasing temperature in promoting more

transgranular SCC at a cathodic potential (-1.0 V Ag/AgCL) and at an anodic potential (-0.48 V Ag/AgCl). As a result, they altered their earlier conclusion and concluded that the same mechanism, hydrogen embrittlement, was responsible for fracture in both potential ranges (24). The activation energy of a rate determining process could not be determined from an Arrhenius type analysis as shown in figure 8. This result indicates that crack growth, which is much slower than that shown for the AISI 4130 steel shown in figure 4, is under mixed rate control. Processes which may contribute to the control of the growth rate are hydrogen ion discharge, surface adsorption and migration, and lattice transport of atomic hydrogen. At anodic potentials, the kinetics of anodic dissolution and subsequent hydrolysis reactions, which lower the pH, thus making hydrogen evolution possible, may further limit the crack growth rate (Figure 8) (24).

Cyclic Loading Crack Growth

Crack growth processes under cyclic loading conditions are more complex than for static loading conditions. In addition to the parameters discussed above, crack growth under cyclic loading is influenced by the following variables:

1. Peak Stress Intensity ($K(\max)$)

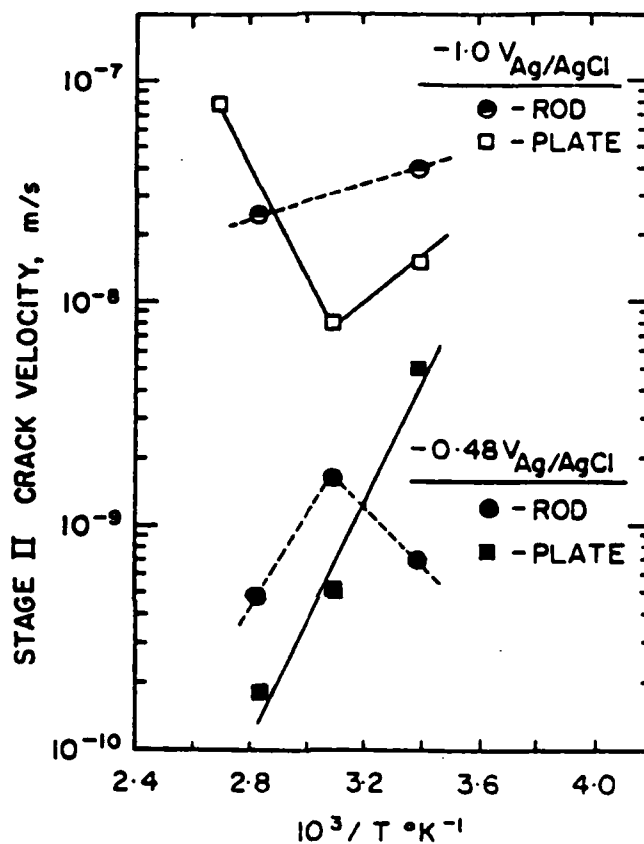


Figure 8

Arrhenius plot of the temperature dependence of the static loading crack growth rate of HY-180M steel in 3.5% sodium chloride at two electrochemical potentials (23).

2. Stress Intensity Range (ΔK)
3. Stress Ratio (R)
4. Frequency (f)
5. Load Waveform

Figure 9 shows three different types of crack propagation curves typical of corrosion fatigue (15). Type A is typical of a material in an aggressive environment where stress corrosion cracking does not occur. The environment reduces the threshold stress intensity factor for the initiation of crack propagation. Also, the relative influence of the environment on the crack growth rate is reduced as the rate of crack growth increases. This is typical of materials such as aluminum in pure water (15,25).

The second type of propagation shown in figure 9, type B, is for an environment which causes stress corrosion cracking. At stresses below the stress corrosion threshold, the environment has no effect on crack propagation. However, as the maximum stress intensity in the load cycle increases, it eventually reaches and exceeds the stress corrosion threshold. When this occurs the crack growth rate increases sharply. This type of propagation is observed in steels in aqueous environments (18-20). The third type, type C, is more representative of what is commonly observed in service; a combination of the two previous types.

Air is, of course, the most commonly encountered gaseous environment and has a significant effect on the

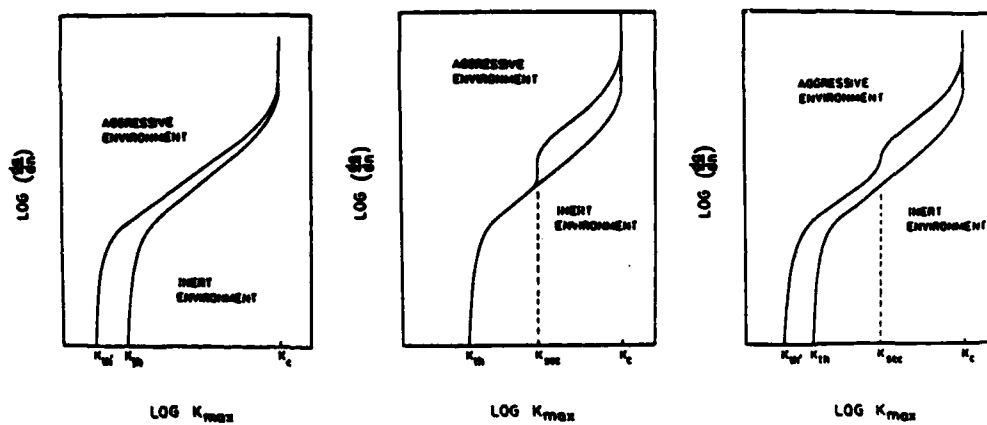


Figure 9

Three basic types of corrosion fatigue crack growth behavior (27).

fatigue properties of most engineering alloys. Usually, fatigue crack propagation in air is increased with respect to vacuum at the same temperature. Oxygen and water vapor are usually responsible for this detrimental effect. However, under certain conditions, exposure to air can retard or even arrest crack propagation (29-31).

Figure 10 shows the effects of gaseous environments on fatigue crack propagation of two aluminum alloys (26). Water vapor is the most detrimental component in the gaseous atmosphere for these alloys. However, for nickel alloys, oxygen is the most detrimental species, and for high strength steels both water vapor and oxygen are equally detrimental.

The effect of gas pressures on crack propagation usually follows a step or "S" type behavior with some critical pressure range separating a plateau of no effect from a plateau where saturation of the effect occurs. This type of behavior is shown in Figure 11 (27) where the crack growth rate for three stress intensity ranges are plotted against the partial pressure of water vapor for aluminum alloy 2219-T851 (27,25). At pressures below the critical pressure, the crack growth rate rapidly approaches that observed in vacuum or in argon gas. Pao et. al. (39) found that, for an AISI 4340 steel in water vapor, the frequency where the minimum in crack growth rate was reached

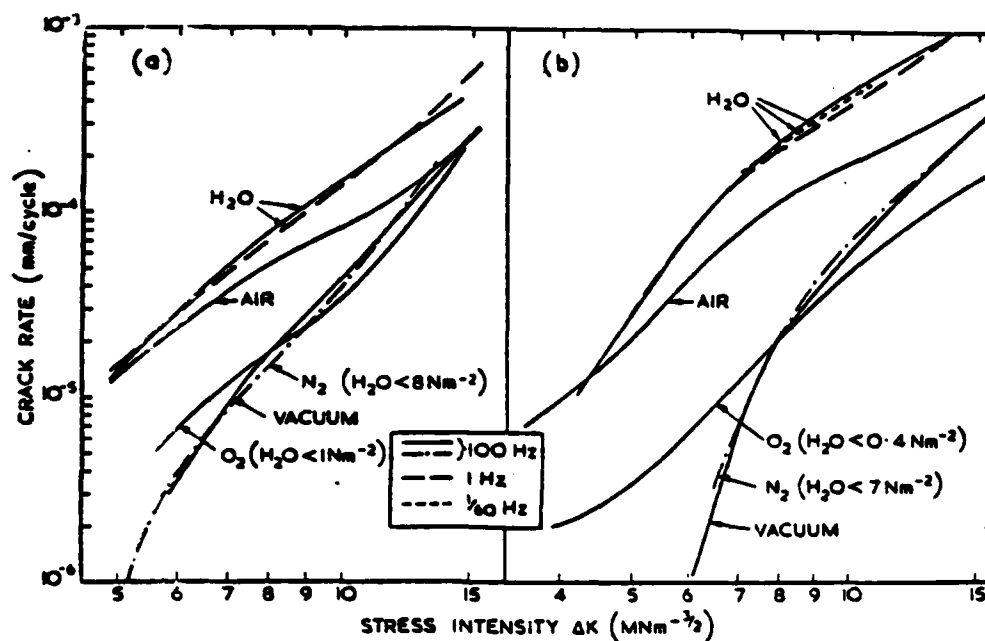


Figure 10

Fatigue crack growth rates of two aluminum alloys in various environments and vacuum at a loading frequency of 100 Hz (26).

- (a). Al-2.5%Cu-1.5%Mg-1.2%Ni
- (b). Al-5.8%Zn-2.7%Mg-1.3%Cu

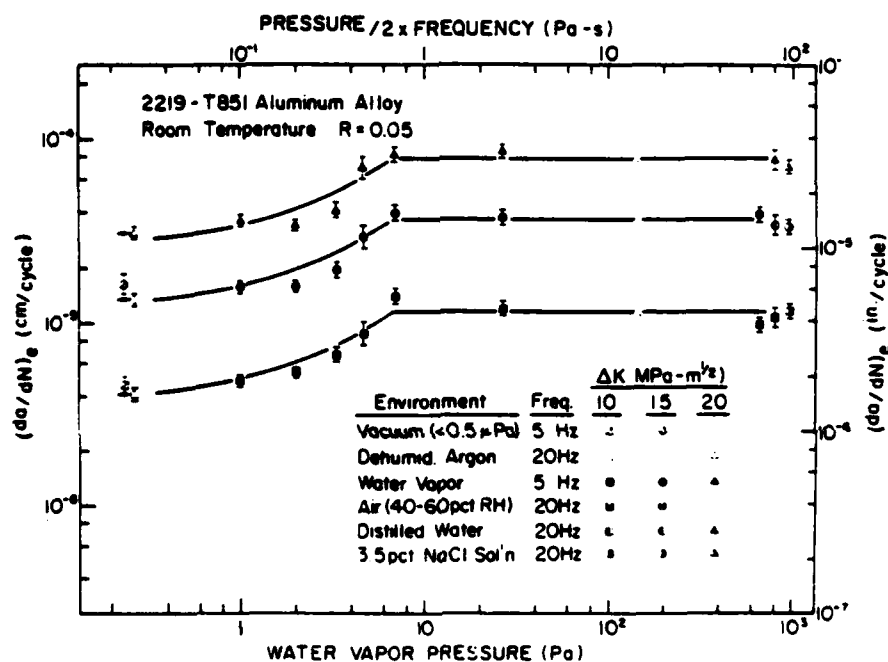


Figure 11

Influence of water vapor on fatigue crack growth rate in 2219-T851 aluminum alloy (25).

corresponded to the point where the exposure per cycle (pressure/2xfrequency) was not great enough for the onset of oxidation. Also, they found that the maximum crack growth rate per cycle corresponded to the exposure per cycle where the oxidation of the steel surface at the crack tip was essentially complete (39). However, Wei et. al. (25,27) found that this approach required an adjustment of three orders of magnitude to fit the data of figure 11. As a result, they assumed that the rate of mass transport must be the crack growth rate limiting step. The limited transport of water vapor to the crack tip and the rapid reaction rate of aluminum and water vapor results in an effectively reduced gas pressure at the crack tip. Therefore, the exposure of the metal at the crack tip to the damaging environment for this aluminum alloy is less than that assumed by the model of Pao et. al. (39). By using reaction rate data and assuming Knudsen flow up the crack, Wei et. al. (27) estimated that an essentially constant reduced pressure develops at the crack tip and then used this pressure in the previous model to derive the line shown in figure 12 (27,25).

Environment also has significant effects at elevated temperatures. For example, figure 13 shows the effect of oxygen pressure on the crack growth rate of 316 stainless steel at 500°C (28). The same type of critical pressure

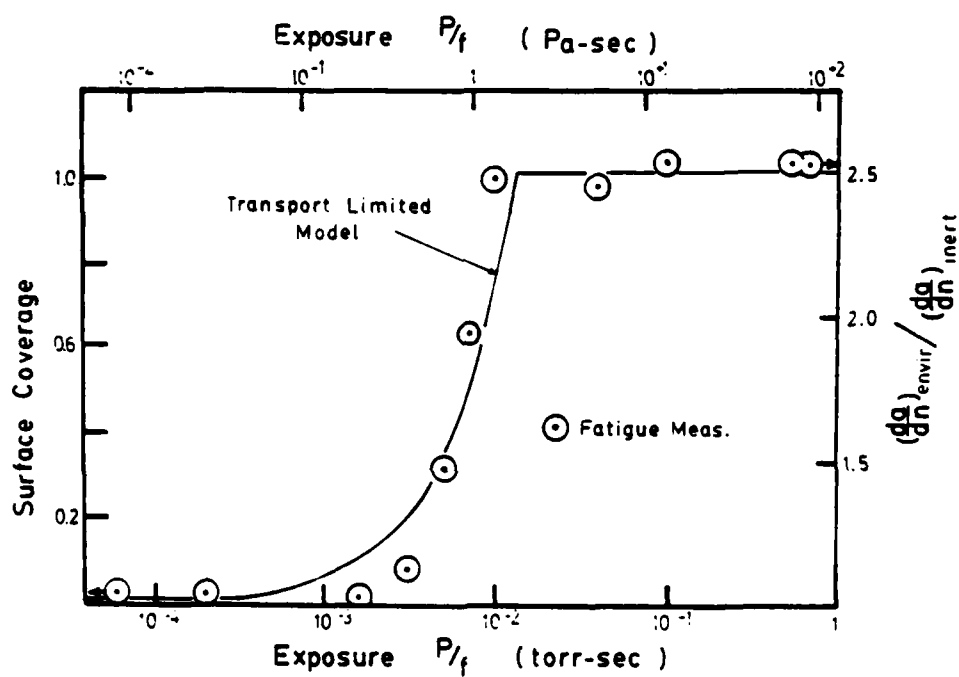


Figure 12

Comparison of the observed fatigue crack growth response for 2219-T851 aluminum alloy in water vapor and a transport-limited rate model (25).

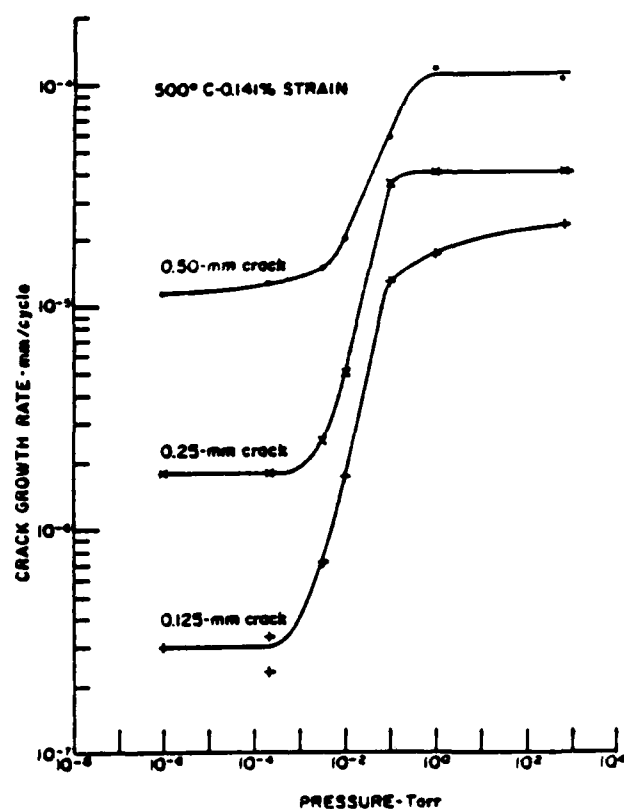


Figure 13

Effect of oxygen pressure on fatigue crack growth rate of type 316 stainless steel at 500°C (28).

effect is observed at this temperature as is typically found at lower temperatures. The fatigue lives of a nickel base superalloy (MAR-M200) at three different temperatures in air and vacuum are shown in figure 14 (1,2,29). From this it can be seen that at two temperatures, air accelerated failure, while at 760°C (1400°F) air has no effect and at 925°C (1700°F) air retards failure. Austin (31) found that at room temperature a directionally solidified cobalt-base eutectic (COTAC) demonstrated accelerated crack propagation and a reduced threshold in air as compared to vacuum (figure 15a). At elevated temperatures, crack propagation in vacuum increased compared to room temperature vacuum tests (figure 15b). However, at temperatures above approximately 600°C crack propagation did not occur in air for the medium and low stress intensities shown in figure 15. Introduction of air into the vacuum chamber of a propagating fatigue crack at 750°C resulted in immediate arrest and increasing the stress range resulted in propagation followed by another arrest (31). Alternating stress intensity levels which resulted in continued propagation caused failure in less than a thousand cycles (31). It was concluded that, the positive volume change of oxidation at the crack tip results in reducing the effective alternating stress intensity and increasing the mean stress intensity (31).

Aqueous solutions are generally aggressive and, as with

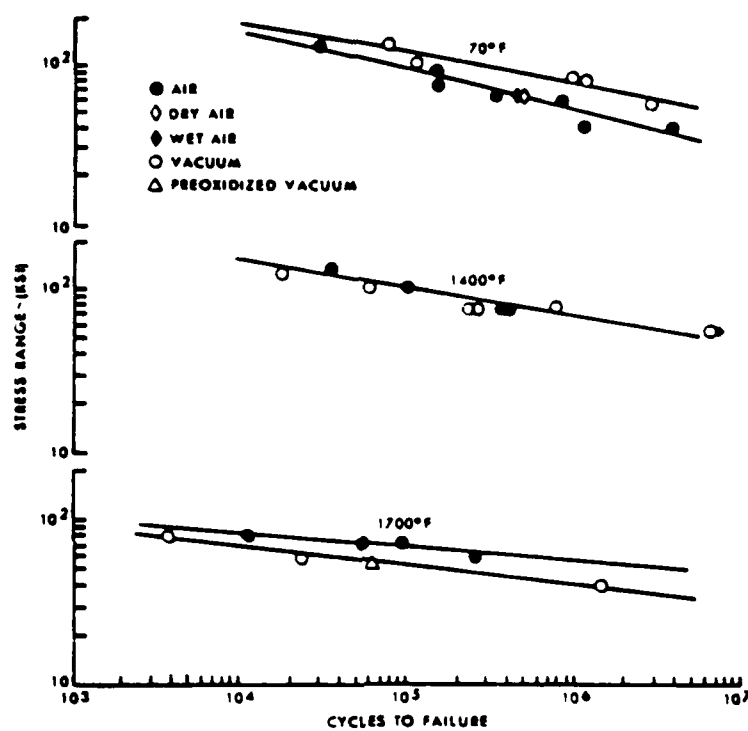


Figure 14

Fatigue life of nickel superalloy single crystals (low carbon MAR-M200) in air and vacuum at 20°C, 760°C and 925°C (1).

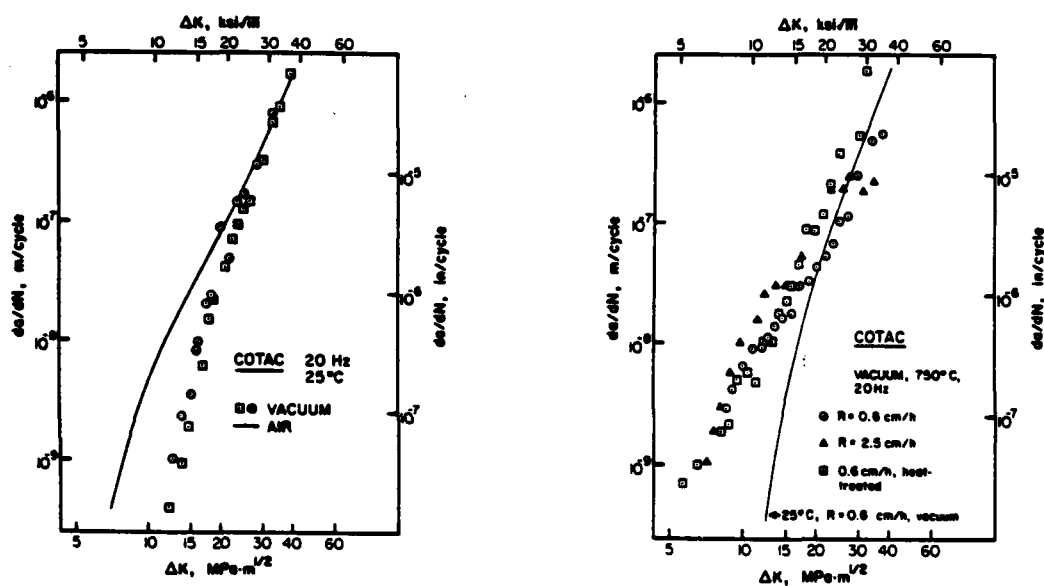


Figure 15

Fatigue crack growth in a cobalt base directionally solidified eutectic in air and vacuum at 25°C (a) and 750°C (b) (31).

static loading, aqueous solutions are more difficult to analyze than are single component gaseous environments. The effect of frequency and waveform in aqueous solutions have been studied by many different investigators. For example, Barsom (32,33) studied the effects of these variables on steels below the stress corrosion cracking threshold. Figure 16(a) shows the effect of frequency on the crack growth rate (32). Barsom found that the propagation followed the Paris-Erdogan (34) equation at all frequencies: $da/dN = D(t)(\Delta K)^2$. Only the pre-exponential coefficient $D(t)$ varied with the environment and frequency. In air, $D(t)$ was a constant, independent of frequency. In sodium chloride solution, $D(t)$ increased with decreasing frequency (figure 16(a)). By changing the waveform at a constant frequency (6 Hz), it was found (Figure 16b), that the rising portion of the load wave form was responsible for the environmental damage observed (Figure 16(b)). Sinusoidal, triangular, and positive sawtooth waves all had the same crack growth rates. However, fast rise time square waves and negative sawtooth forms had the same crack growth rate in the 3% sodium chloride solution as all of the waveforms had in air.

Figure 17 shows the behavior of a Ti-6% Al-6% V-2% Sn alloy in an aqueous environment which causes stress corrosion cracking (0.6 M NaCl) (35). This shows the

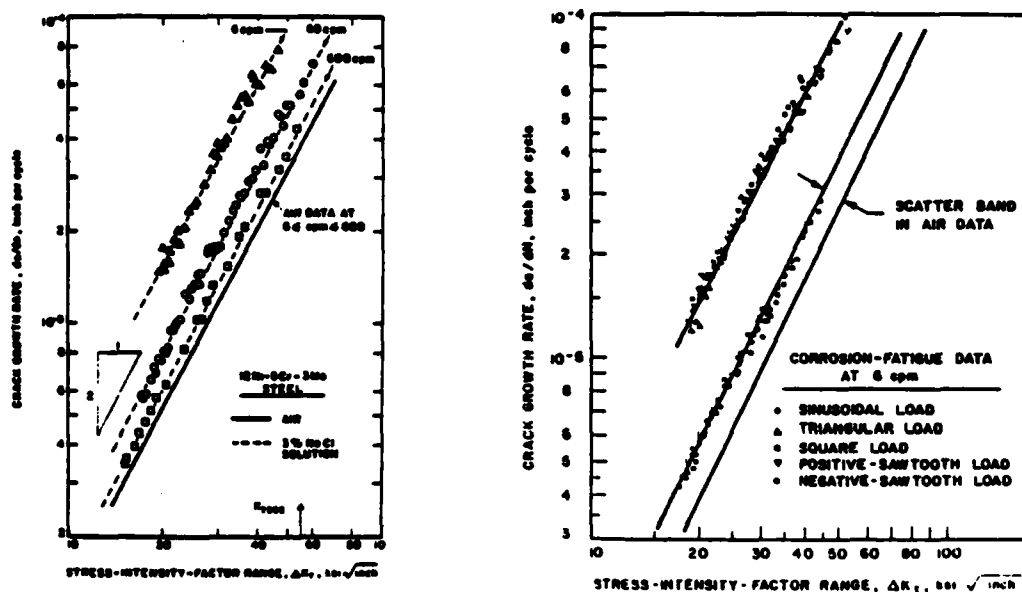


Figure 16

Effect of loading variables on the corrosion fatigue crack growth of a 12Ni-5Cr-3Mo steel in 3.0% sodium chloride solution: (a) Frequency Effect and (b) Load Waveform Effect (32).

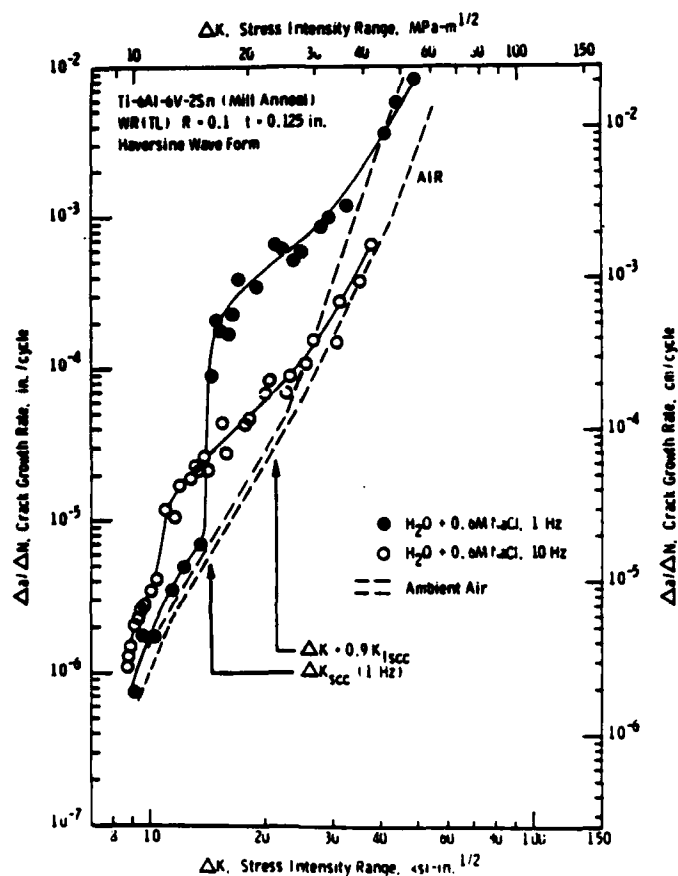


Figure 17

Effect of loading frequency on the fatigue crack growth rate of a 6Al-6V-2Sn titanium alloy in 0.6 N sodium chloride solution (35).

typical crack propagation behavior for this type of corrosion fatigue system as shown above in figure 9. However, the stress intensity range where stress corrosion cracking apparently begins is below that where the peak stress intensity ($K(\max)$) is equal to the statically measured threshold. Above this apparent stress corrosion cracking level, decreasing the frequency increased the crack propagation rate. Below this level, the opposite frequency effect was found. The level of the transition, the stress intensity range for stress corrosion cracking, increased with decreasing frequency approaching the statically measured value. Methanol causes intergranular corrosion of this alloy and, if a load is applied, intergranular cracking. Figure 18 shows the effect of combining two corrosive environments in different ratios (36). Apparently repassivation of the surface cannot occur in pure methanol and adding water allows passivation to occur below the level for stress corrosion cracking. Above the stress corrosion cracking threshold, the crack propagation rate is greater than the beneficial repassivation rate. This explains the shift in the observed stress intensity range for stress corrosion cracking with frequency and the cross over in frequency effect. That is, above the apparent stress corrosion threshold, slower frequencies allow more dissolution and hydrogen evolution per cycle resulting in

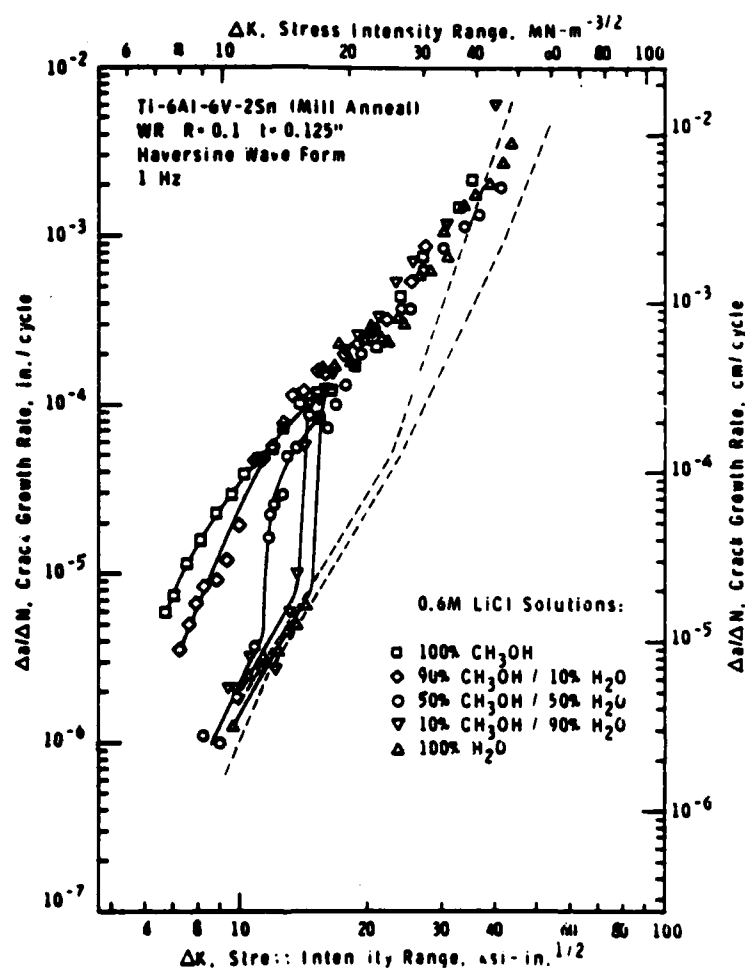


Figure 18

Effect of water additions on the fatigue crack growth rate of a titanium alloy in a 0.6 N lithium chloride methanol solution (36).

more crack growth per cycle. However, below the critical level, slower frequencies allow a thicker protective layer to form resulting in less crack growth per cycle. Since repassivation occurs at a relatively fixed rate, the critical stress intensity range where complete repassivation of the metal at the crack tip cannot occur in each cycle, decreases with increasing frequency (36).

B. Metallurgy of Aluminum Alloys

Aluminum alloys are usually composed almost entirely of aluminum with less than 15% alloying additions. Alloys are grouped into numerical classes depending upon the alloying elements present. For example, precipitation hardened alloys containing zinc and magnesium, such as one of the alloys used in this investigation, are in the 7XXX series (where the last three digits specify the exact composition) while the lithium containing alloys do not yet have a series designation.

Metallurgy of the Al-Zn-Mg System

The strengthening of these alloys is due to the formation of the η' phase (HCP MgZn_2), however, the "T" phase (cubic $\text{Mg}_3\text{Zn}_3\text{Al}_2$) will form at aging temperatures above 150°C or if quenching from solutionizing temperature is too slow (42-46). Nine different orientation

relationships have been observed for the precipitate and table I is a list of these relationships (42). Table II shows the relative predominance of the different orientation relationships found in samples solutionized at 485°C and aged between 130°C and 150°C. The general precipitation sequence for this system is (42-46):



The initial G.P. zones are coherent but coherency diminishes as aging proceeds. At peak hardness, a homogenous distribution of semi-coherent precipitates (with the orientations and frequency distributions given in Tables I and II) block cross slip making deformation very planar. Overaging results in increasing cross slip.

During either quenching or aging precipitates will nucleate heterogeneously at the grain boundaries. These grain boundary precipitates nucleate early and grow rapidly depleting the adjacent region of the grain of solute and vacancies. This results in a precipitate free zone (PFZ) in the grain adjacent to the grain boundary. These soft zones tend to deform preferentially and they can dominate the deformation and failure modes of the alloy. It is not uncommon for these alloys to fail intergranularly in tensile tests in inert environments. These ductile intergranular

Table I: The Orientation Relationships Observed between the MgZn_2 (η) Precipitates and the Aluminum Lattice (42).

<u>Type No.</u>	<u>Orientation Relations</u>
1	$(10\bar{1}0)_\eta \parallel (001)_{\text{Al}}; (001)_\eta \parallel (110)_{\text{Al}}$
2	$(0001)_\eta \parallel (1\bar{1}\bar{1})_{\text{Al}}; (10\bar{1}0)_\eta \parallel (110)_{\text{Al}}$
3	$(0001)_\eta \parallel (1\bar{1}\bar{1})_{\text{Al}}; (11\bar{2}0)_\eta \parallel (110)_{\text{Al}}$
4	$(0001)_\eta \parallel (110)_{\text{Al}}; (\bar{1}2\bar{1}0)_\eta \parallel (1\bar{1}\bar{1})_{\text{Al}}$
5	$(1210)_\eta \parallel (1\bar{1}\bar{1})_{\text{Al}}; (30\bar{3}2)_\eta \parallel (110)_{\text{Al}}$
6	$(\bar{1}2\bar{1}0)_\eta \parallel (111)_{\text{Al}}; (20\bar{2}1)_\eta \parallel (1\bar{1}2)_{\text{Al}}$
7	$(\bar{1}2\bar{1}0)_\eta \parallel (1\bar{1}\bar{1})_{\text{Al}}; (10\bar{1}4)_\eta \parallel (110)_{\text{Al}}$
8	$(\bar{1}2\bar{1}0)_\eta \parallel (1\bar{1}2)_{\text{Al}}; (0001)_\eta \parallel (31\bar{1})_{\text{Al}}$
9	$(\bar{1}2\bar{1}0)_\eta \parallel (001)_{\text{Al}}; (0001)_\eta \parallel (110)_{\text{Al}}$

Table II: Relative Predominance of the Various Precipitate-Matrix Orientation Types of Table I in an Al-5.8% Zn-1.1% Mg Alloy After Solution Treatment at 485°C and Aging Between 130°C and 150°C to Peak Hardness (42).

<u>Percent of the Precipitates in the Sample</u>	<u>Precipitate and Orientation Type Listed in Table I</u>
70%	η' (type 1)
16%	η type 1
10%	η type 2
4%	η type 4
<1%	other types

failures are characterized by dimples on the grain facets resulting from micro-void coalescence (MVC) in the soft zones adjacent to the grain boundary.

Metallurgy of the Al-Mg-Li System

When lithium is added to aluminum alloys the density is reduced and the modulus of elasticity is increased. The density decreases approximately 3% for each weight percent of lithium added while the modulus increases approximately 6% for the the same increment (47).

Strengthening of Al-Mg-Li alloys is achieved through the precipitation of δ' (Al_3Li) and the "S" phase (Al_2MgLi) (47-54). The precipitation sequence is:

Solid Soln.- δ' (Al_3Li)-"S" (Al MgLi)

Fridlyander et. al. reported that the maximum hardness in the Russian alloy O1420 (Al-6% Mg-2% Li-0.25% Mn) resulted from the formation of "S" phase precipitates (54). Thompson and Noble reported that the maximum in hardness for these alloys results from the precipitation of an even distribution of the δ' precipitates (50,51). They reported that the "S" phase formed at the grain boundaries resulting in precipitate free zones and a decline in mechanical properties (50,51).

The δ' phase is a superlattice precipitate similar to the γ' (Ni_3Al) precipitates used to strengthen nickel base superalloys. Reportedly, there is little precipitate/matrix mismatch and most of the strengthening comes from the resistance of the precipitates to dislocations cutting through them. This resistance is due to the anti-phase domain boundary (APDB) energy of the precipitates(47-56). As successive dislocations pass through a precipitate on a slip plane, the order of the precipitate is diminished and slip becomes easier resulting in the formation of a persistent slip band (PSB).

The development of lithium containing alloys has been hampered by their low fracture toughness which is believed to be the result of tramp elements brought in with the lithium such as sodium, potassium, sulfur and hydrogen which segregate to the grain boundaries reducing the grain boundary cohesion (48,57). This coupled with concentration of strain where persistent slip bands intersect the grain boundaries, results in a tendency for intergranular fracture (48,57).

C. Corrosion of Aluminum Alloys

Aluminum is an active metal ($E^\circ=1.71$ V vs. she) and derives its corrosion resistance from an adherent continuous passive film of oxides or hydroxides (58). As a

result, the corrosion behavior of aluminum and its alloys is completely determined by the stability of this layer and the rate at which it reforms when ruptured (59). Figure 19 shows the electrochemical equilibrium (Pourbaix) diagrams for aluminum and the alloying elements in the alloys used in this experimental program (59). The aluminum diagram shows that the passive film on aluminum is amphoteric and will protect aluminum from corrosion in the pH range from about 4 to 9.5. However, these diagrams are for the metals in water only and they do not take into account ionic species in the environment which can either extend reduce or shift the range of passivity (60). Halide ions in the environment will attack the passive film and can cause pitting of aluminum alloys.

Lithium is a very active element ($E^0=3.05$ V vs. she) and therefore could have dramatic effects on the corrosion properties of an alloy even in small concentrations. Niskanen et. al. studied the effect of heat treatment and microstructure on the corrosion of various Al-Li-X alloys (53,61). They found that overaging, resulting in the precipitation of the equilibrium phase AlLi, had a deleterious effect on the corrosion properties of the alloys studied. However, in the Al-Li-Mg alloys the formation of Al_2MgLi prevented the formation of the anodic AlLi phase and resulted in improved corrosion properties. A similar study

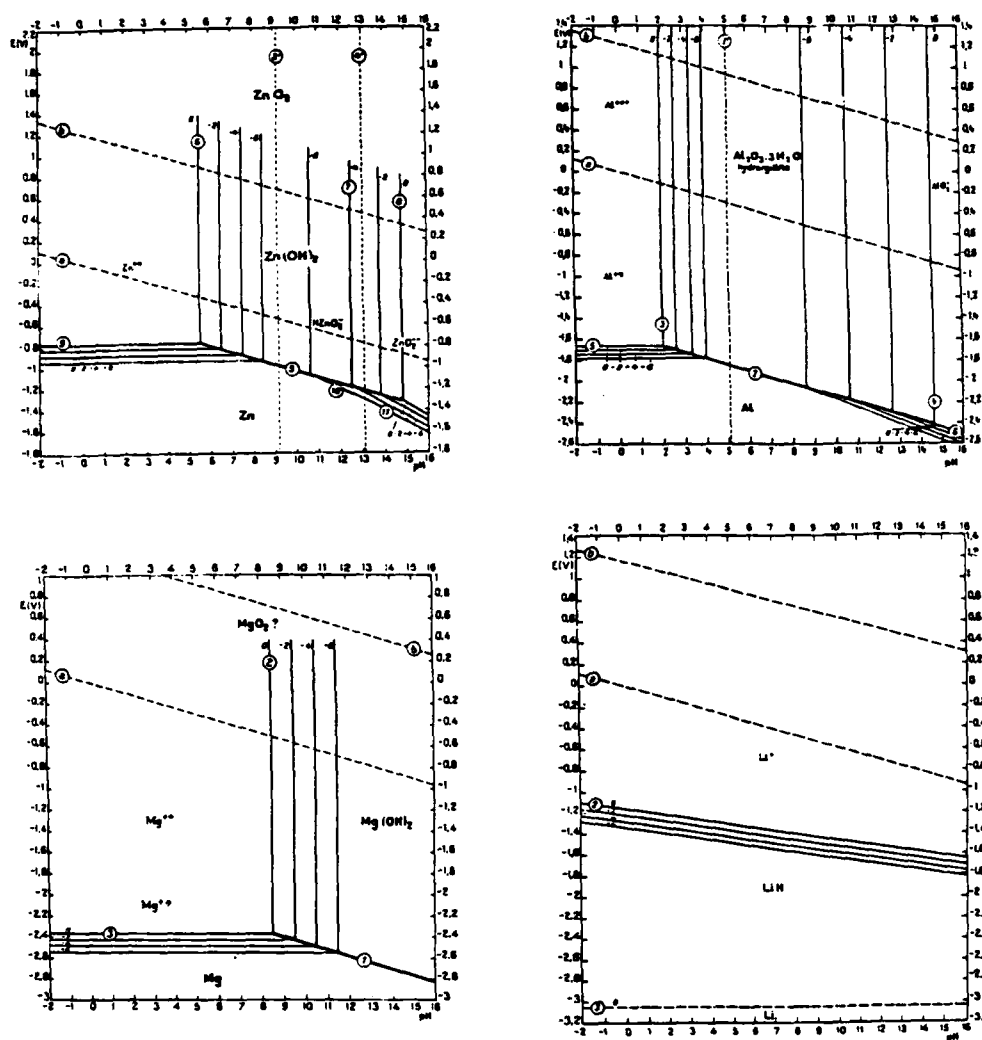


Figure 19

Electrochemical equilibrium or Pourbaix diagram for aluminum and the alloying elements used for this investigation (59).

on an Al-Li-Cu-Mg alloy also showed no deleterious effect of overaging (62).

D. Stress Corrosion Cracking of Aluminum Alloys

Al-Zn-Mg(7000 series) alloys are the most susceptible aluminum alloy to stress corrosion cracking (SCC) and pitting (63). However, only a few studies have been conducted on the stress corrosion behavior of alloys containing lithium.

Stress corrosion cracking of the Al-Zn-Mg alloys is usually intergranular and accordingly, the short transverse direction is the most susceptible orientation. Both the soft precipitate free zone (PFZ) and magnesium segregation to the grain boundaries as well as to the free surface have been linked to SCC susceptibility (63-70). Also, the concentration of magnesium, zinc and the Mg/Zn ratio have been linked to susceptibility (64,69). Probably the most effective means of reducing susceptibility is to overage the alloy (ie. 7075-T73) but it is not known whether this beneficial effect results from promoting a finer slip distribution or from modifying the the grain boundary chemistry or structure (69).

Stress corrosion cracking of aluminum alloys has been shown to occur in water vapor (69). In fact, water vapor is the only common gaseous species that is known to cause

cracking (69,70). Figure 20(a) shows the stress corrosion crack velocity vs. stress intensity measurements for different relative humidities and figure 20(b) shows the linear dependence of the stage 2 velocity plateau on the relative humidity (69). This shows that chloride ions or any other halide ions are not required to produce stress corrosion cracking in Al-Zn-Mg alloys. Also, since it is unlikely that capillary condensation could occur down to relative humidities as low as 1%, bulk dissolution is not responsible for crack growth in this environment. As a result, hydrogen embrittlement was proposed as an alternative explanation of the stress corrosion cracking of these alloys (68).

Hydrostatic stresses promote hydrogen embrittlement by increasing the hydrogen solubility and accordingly the hydrogen concentration at the crack tip. If loading is done in torsion (mode 3) where a biaxial state of stress exists, then there is no hydrostatic component of stress to promote embrittlement. Green et. al. (71,72) performed these tests on an aluminum alloy, titanium and brass. They found, as shown in figure 21, no change in cracking susceptibility for brass where SCC is generally believed to be caused by anodic dissolution. However, they found that titanium, where hydrogen embrittlement is believed to be responsible for SCC, was not susceptible to cracking in mode 3 loading. The

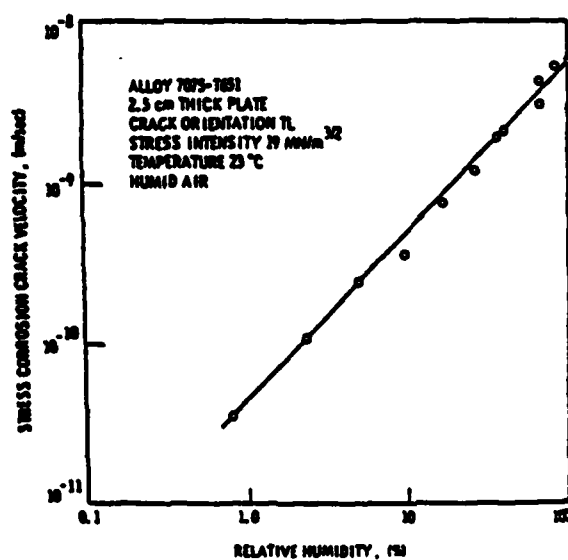
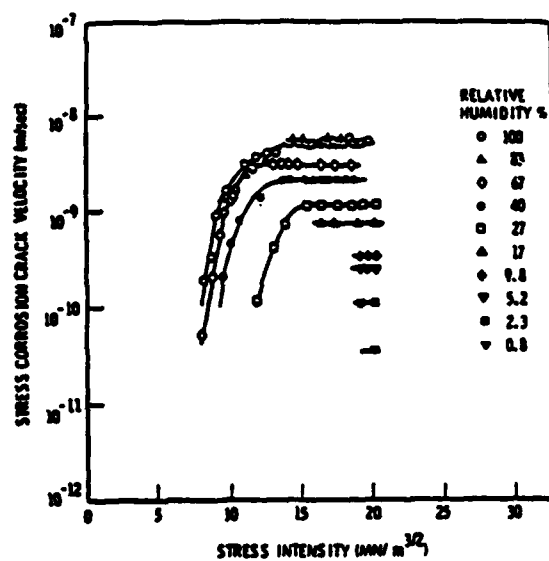


Figure 20

The effect of humidity and stress intensity on the stress corrosion crack velocity of alloy 7075-T651 (69).

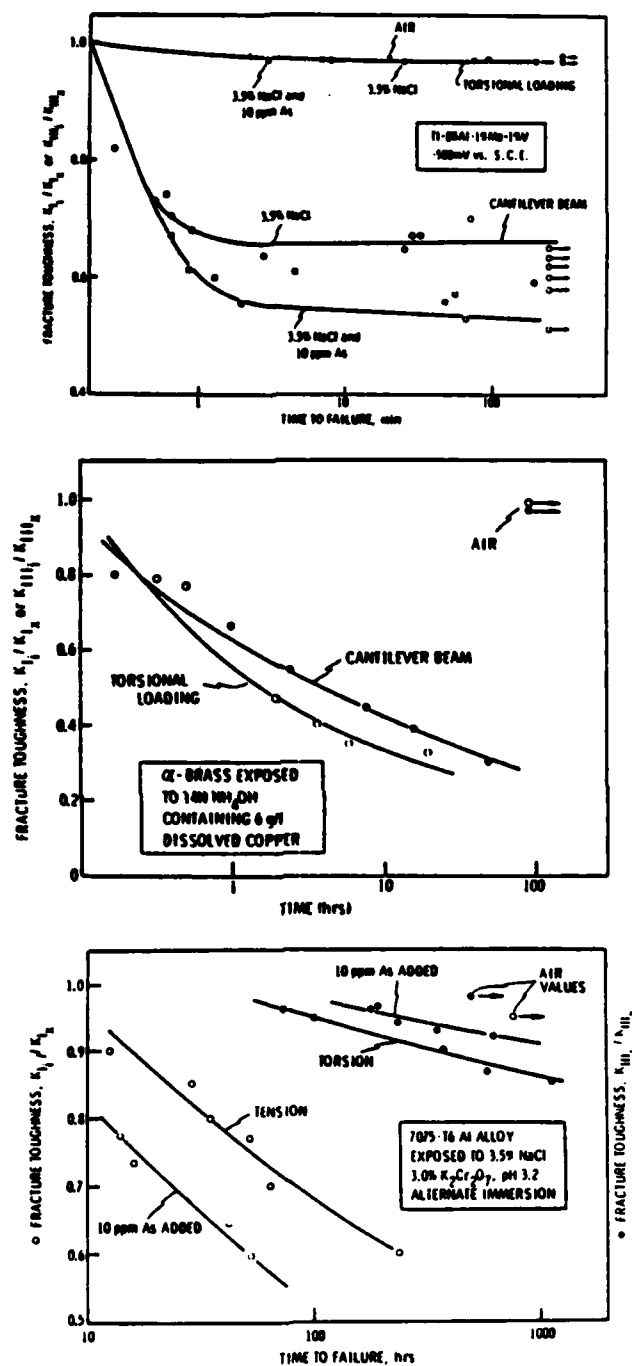


Figure 21

The effect of loading mode on the stress corrosion cracking of (a) Ti-8% Al-1% Mo-1% V, (b) Alpha brass, and (c) 7075-T6 (65,66).

aluminum alloy, however, demonstrated improved behavior for torsional loading but not complete elimination of SCC susceptibility. They concluded that dissolution contributes to stress corrosion cracking, but that hydrogen embrittlement was the rate controlling step for crack propagation in the aluminum alloy for mode I loading (71,72).

Only a few studies have been conducted into the stress corrosion behavior of aluminum alloys containing lithium (73-75). Early experiments were on alloy 2020 (Al-4.5% Cu-1.0% Li-0.8% Mn-0.15% Cd) which is a Al-Cu alloy with lithium added to reduce density that was commercially produced. Rinker (73) measured the crack growth rates and the times to failure for alloy 2020 in 3.5% sodium chloride solutions. He obtained varying results but it is obvious that while SCC will occur in 2020, it is not especially susceptible to SCC (73). Pizzo (74) tried to study the SCC behavior of an Al-Li-Cu and an Al-Li-Mg alloy but general corrosion obscured the results. Recently, Christodoulou et. al. (75) studied the SCC of two Al-Li binary alloys. They reported that the alloys were susceptible to SCC if and only if the anodic phase AlLi was present at the grain boundaries. However, they concluded that the most probable mechanism was hydrogen embrittlement of the highly strained matrix around the precipitates rather than the anodic attack

of the precipitates (75).

E. Pre-exposure Embrittlement

Studies on pre-exposure of Al-Zn-Mg alloys to aqueous environments have shown that the alloys are reversibly embrittled by cathodically charging or by exposure to water or water vapor (76-81). Ciaraldi (80) has demonstrated that exposure of alloy 7075 and high purity analogs of this alloy to water vapor saturated air or to water by continuous abrasion of the sample in an aqueous slurry for several days, results in brittle intergranular fracture of samples when tested in tension in argon. Ciaraldi observed a fractured layer on some of the intergranular facets. He identified these thin layers as aluminum hydride by reflection electron diffraction immediately after testing (80). Diffraction experiments 24 hours later on the same samples failed to produce the same evidence of a hydride phase. Ciaraldi concluded that stress induced precipitation of a meta-stable hydride which was responsible for the embrittlement of these alloys (80).

Tests have shown that there is a strong relationship between pre-exposure, test environment, strain rate and ductility (77-79). Figure 22 shows the effect of strain rate on alloy 7049 in various environments and figure 23 shows the same alloy in the same environments after a three

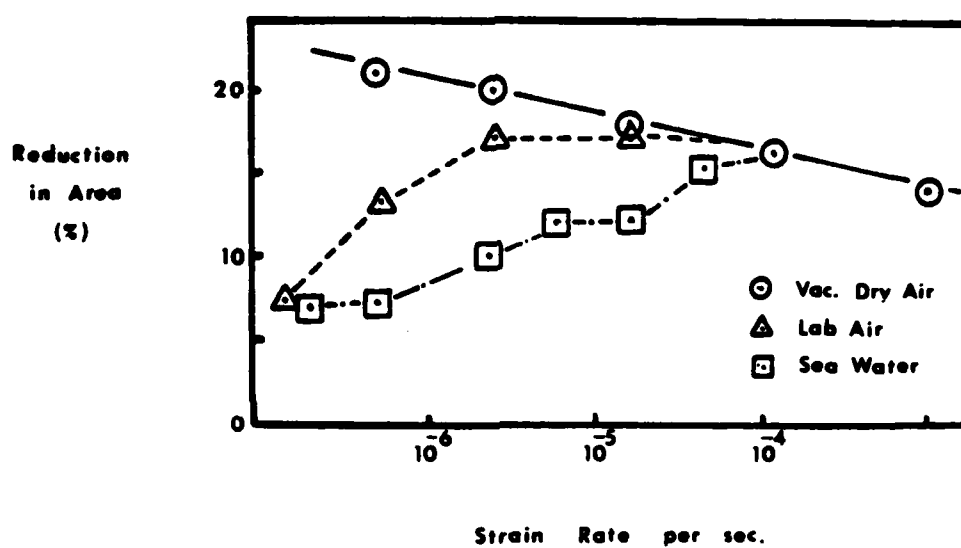


Figure 22

The effect of strain rate on the ductility of alloy 7049 in different environments (78).

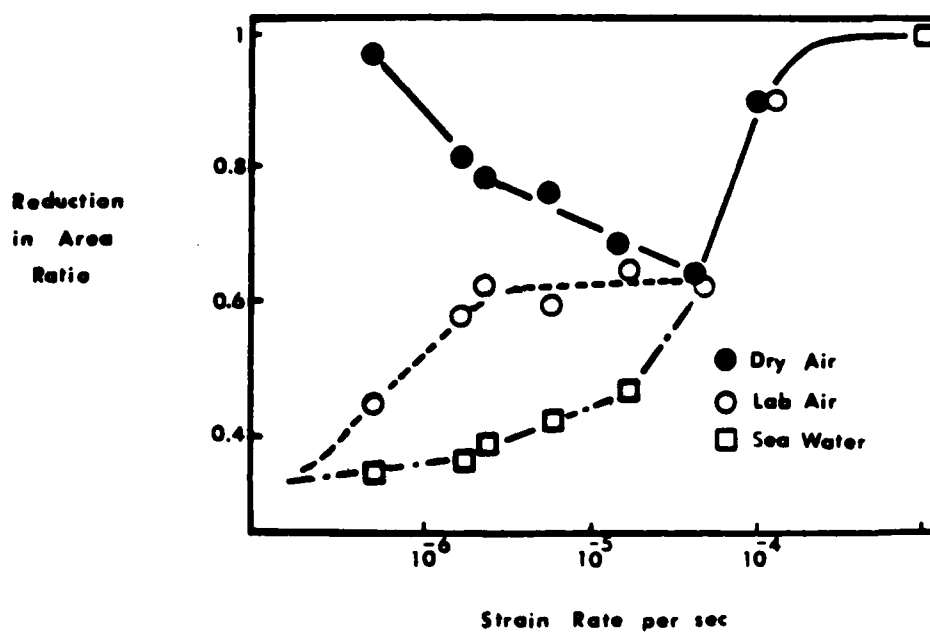


Figure 23

The effect of strain rate on the ductility of alloy 7049 in different environments after a three day pre-exposure to seawater (79).

day pre-exposure to seawater. The pre-exposed and tested in dry air curve shows decreasing ductility with decreasing strain rate to about 1×10^{-4} /second and then increasing ductility with slower strain rates. Holroyd et. al. (79) attributed this effect to the outgassing of hydrogen which was absorbed during the pre-exposure. They reported that storage of the samples in a vacuum was not as effective as slow straining in dry air at restoring the ductility. They concluded that dislocation motion was required to effectively remove the hydrogen(79). Similarly, Swann et. al. (82,83) performed tensile tests on samples of a high purity Al-Zn-Mg alloy that had been pre-exposed to moist air in a vacuum chamber equipped with a mass spectrometer. They found that hydrogen was emitted from samples that were pre-exposed to moist air during elastic loading and during fracture. No hydrogen was detected during testing of similar samples that were not exposed to water vapor (82,83).

Scamans et. al. (87-89) conducted careful examinations of surfaces exposed to water vapor and permeation experiments through aluminum alloy membranes exposed to water vapor to determine how hydrogen enters the metal, how much hydrogen can enter the metal and to determine the diffusivity of hydrogen in the alloys. They found that Al-Zn-Mg alloys were more permeable to hydrogen than either

Al-Mg-Si or pure aluminum. Also, they determined that water vapor attacked the passive film, as shown in figure 24, by first permeating through the passive film to reach the aluminum metal underneath. Then, the water reacts with the metal to form hydrogen gas and aluminum oxides or hydroxides. The gas pressure builds and a blister forms in the passive film. Finally the blister breaks exposing the underlying layer. Scamans et. al. (87-89) reported that these blisters occurred most frequently at the grain boundaries/free surface intersection and they postulated that the tendency for intergranular cracking may be the result of preferential hydrogen absorption at these sites and not necessarily to any greater metallurgical susceptibility of the boundaries (87-89).

Holroyd and Hardie (79) found three types of fracture morphology in the tests of Figures 22 and 23 First, they found normal ductile fracture where little or no embrittlement was found. Second, they found brittle transgranular cleavage-like fracture at intermediate levels of embrittlement. Finally, they found intergranular cracking where hydrogen absorption and embrittlement would be the most severe (78,79). Albrecht et. al. (77) cathodically charged samples in a hydrochloric acid solution of pH=1, where hydrogen absorption would not be as great (84,85), and found fracture surfaces composed almost

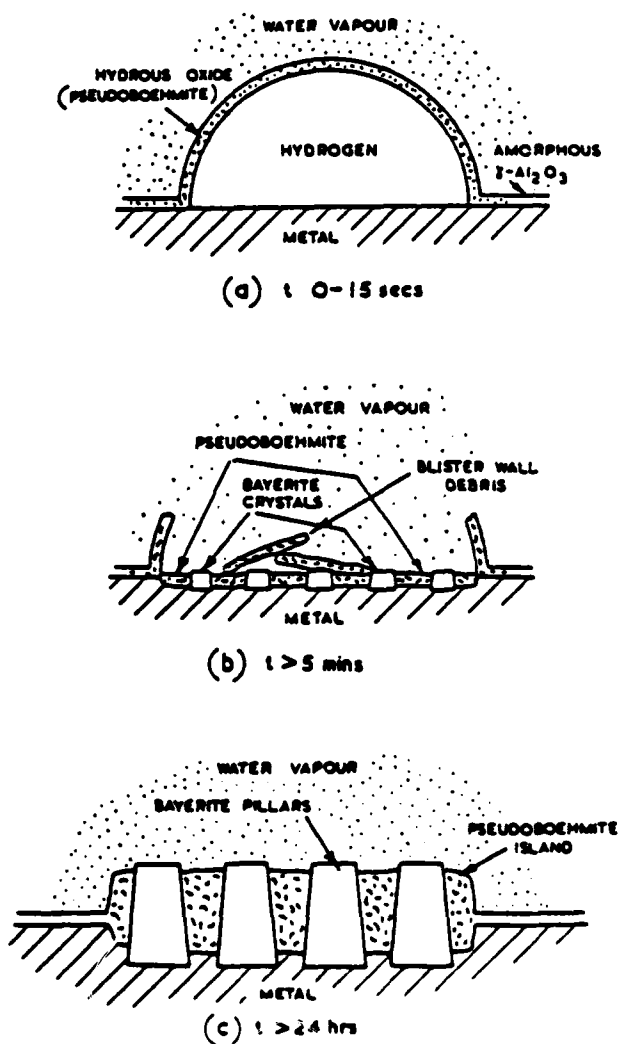


Figure 24

Schematic illustration of the aluminum-water vapor reactions on the surface of aluminum alloys (87).

entirely of ductile dimples even though there was a significant reduction in ductility. (They also tested in the longitudinal direction where the stresses on the grain boundaries would be diminished.) They found that the cathodically charged samples had significantly larger dimples than the uncharged samples did and concluded that hydrogen did not assist nucleation of micro-voids but assisted micro-void growth (77). Ciaraldi (80), as discussed above, used exposure conditions which resulted in greater hydrogen absorption and found predominately intergranular cracking with some transgranular cleavage-like cracking.

F. Fatigue of Aluminum Alloys

Fractography and fracture mechanics has lead to a three stage understanding of the fatigue process as shown in figure 25 (90). The first stage is is characterized by a rapid increase in the crack propagation rate with stress intensity and, in Al-Zn-Mg alloys, by fracture along favorably oriented planar slip bands (90-98). However, in polycrystalline samples intergranular crack nucleation is observed at high stresses. In the second stage, the crack growth rate increases with the alternating stress intensity factor according to the Paris-Erdogan equation and propagation is perpendicular to the applied stress as shown

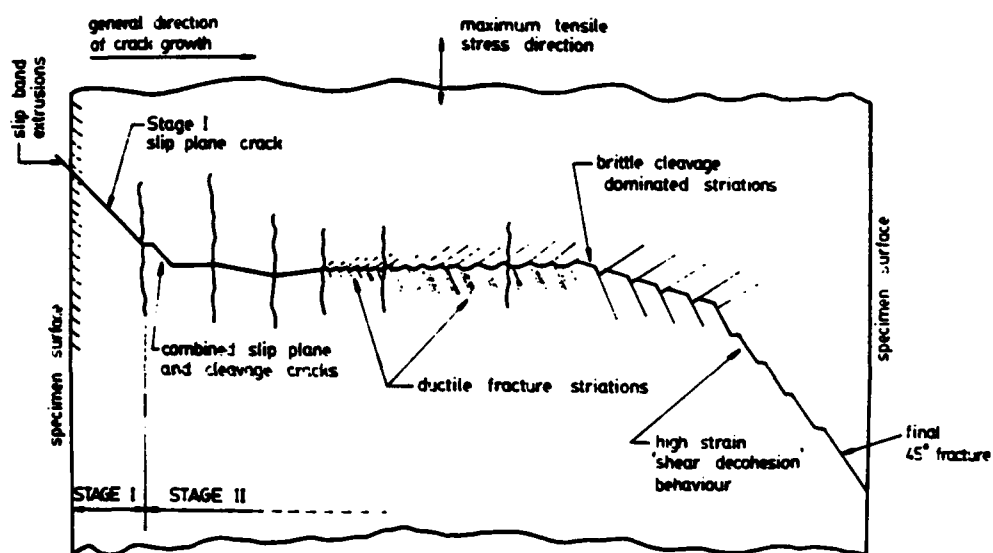


Figure 25

A schematic illustration of the various modes of fatigue fracture observed in age hardened aluminum alloys. This is a composite of the various modes and not a strict sequence of events (90).

in figure 25. Stage 3 is ductile failure of the remaining ligament holding the sample together.

Fatigue Crack Nucleation

Laird and Duquette (91) have reviewed mechanisms of fatigue crack nucleation and their work will not be duplicated here but will be briefly summarized. Basically, the exact mechanism of crack nucleation can vary with material composition, purity, heat treatment, loading conditions, or environment. However, some generalizations can be made. Planar slip materials tend to form intense slip offsets where slip cannot be fully reversed. This results in a notch-peak topography where the notches act as stress concentrators which eventually grow into fatigue cracks (91,92). In materials where cross slip can occur, persistent slip bands form which lead to the growth of intrusions and extrusions. The intrusions grow until they become fatigue crack nuclei (6,91-93). In materials where deformation is more homogeneous, cyclic loading leads to a general rumpling of the surface which eventually leads to the formation of critical size flaws (91,92).

In aged Al-Zn-Mg alloys, crack nucleation is believed to occur by the formation of persistent slip bands (PSB's) and intrusion/extrusion growth as shown in figure 26. The formation and structure of these persistent slip bands has

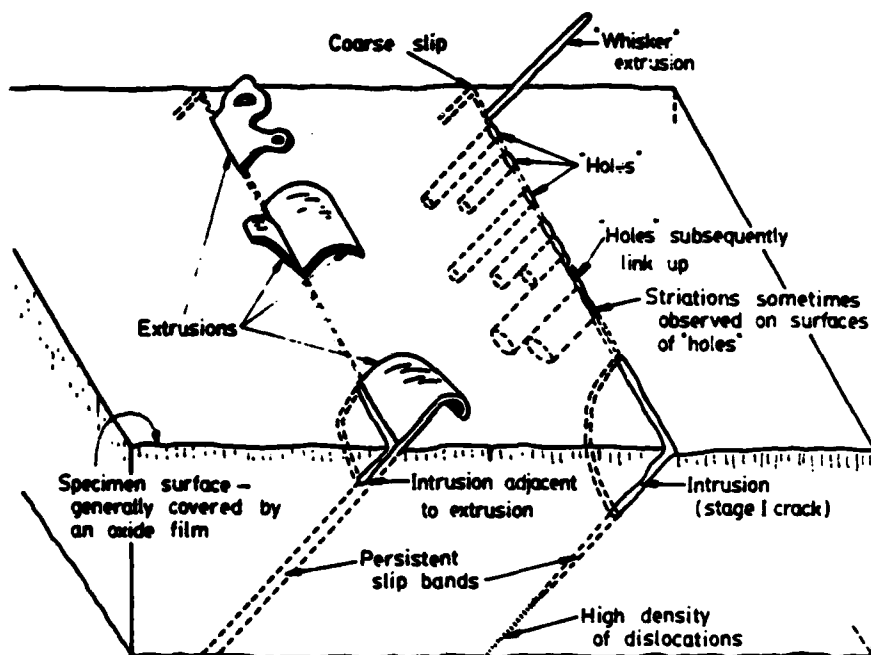


Figure 26

Diagrammatic summary of the important slip-band intrusion and extrusion features commonly observed (93).

been studied (90,93-100). In these alloys the persistent slip bands are not observed initially but, after some cycling, they form and grow rapidly. This led Forsyth (90) to conclude that some microstructural change, such as deformation induced dissolution of the precipitates, occurred in the slip bands. This results in a soft region which deforms preferentially. Several investigators have since studied stage 1 crack nucleation and growth and have found that stage 1 cracks always follow PSB's, that the PSB's do not contain any precipitates observable by transmission electron microscopy and that a supersaturation of solute exists in the PSB's (6,95-99).

Duquette and Swann (102) studied the initiation of fatigue cracks in an Al-Zn-Mg alloy and proposed a model of fatigue crack initiation which does not require the formation of intrusions at persistent slip bands. They removed samples from bending fatigue tests at various intervals before crack initiation and examined them in the transmission electron microscope. They found that dislocation dipoles, loops and other dislocation debris accumulated on the slip planes. They postulated that the accumulation of these defects resulted in an increasing stress perpendicular to the slip plane which, when added to the stress from the applied load, resulted in localized cleavage of the slip plane (102).

Stage 1 Crack Propagation

Stage 1 crack propagation is influenced by the environment and the microstructure (91-98). Stage 1 propagation is usually crystallographic and in the slip direction on the slip planes. Accordingly, it is greatly influenced by slip character, grain size, precipitate morphology, stacking fault energy, etc.

Different mechanisms have been proposed for the actual micro-mechanical process of fracture or crack extension in stage 1. Nageswararao and Gerold (95,96) studied the stage 1 slip plane fracture surfaces of Al-Zn-Mg single crystals tested in dry nitrogen and humid air. They found cleavage like features at low stress intensities and dimples on the facets at higher stress intensities. Similar features were found on stage 1 fractures of a nickel-base super alloy by Duquette and Gell (29). Duquette and Gell (29) postulated that the accumulation of dislocation dipoles in the slip band resulted in a stress across the slip plane and localized cleavage of the slip plane (103-105). This is similar to the mechanism proposed by Duquette and Swann (102) for the initiation of fatigue cracks as illustrated schematically in figure 27. At higher stresses or stress intensities, plastic deformation ahead of the crack increases and results in the formation of micro-cracks in

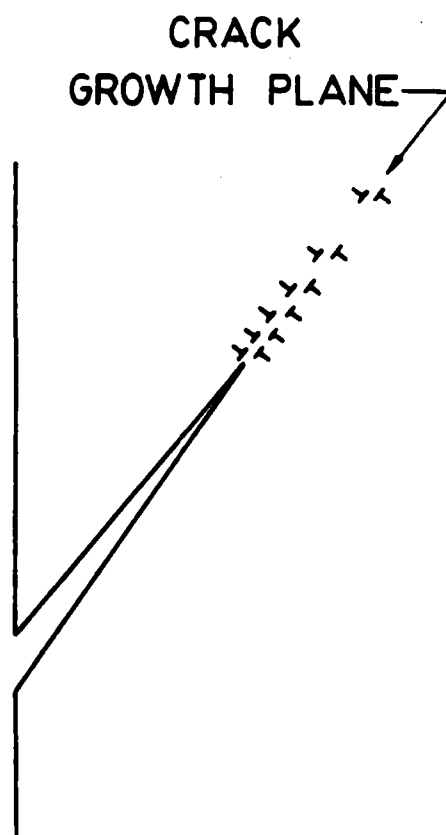


Figure 27

Schematic diagram of a stage 1 crack and associated dipole array (29).

the slip plane ahead of the crack tip which grow into the observed dimples as illustrated in figure 28. When the stress intensity increases to the point where blunting of the crack tip can occur, then stage 2 crack propagation begins.

Lynch (6,93) has proposed an alternate model for the propagation of stage 1 fatigue cracks based on investigations on polycrystalline samples of a high purity Al-Zn-Mg alloy. This is basically an extension of intrusion and extrusion growth to the tip of a propagating fatigue crack. Lynch proposed that fatigue cracks developed from intrusions and propagate by the progressive development and linking up of holes intruded into the persistent slip bands as shown in figure 29 (93).

Stage 2 Crack Propagation

Stage 2 propagation is influenced by the environment and microstructure. Stage 2 propagation is characterized by the formation of striations or crack arrest marks. Each striation corresponds to a single load cycle. In aluminum alloys, there are two types of striations observed(7-9). These have been classified as being either ductile (type A) or brittle (type B)(9). The ductile striations propagate perpendicular to the loading axis and are characterized by a general rumpling of the surface. The brittle striations are

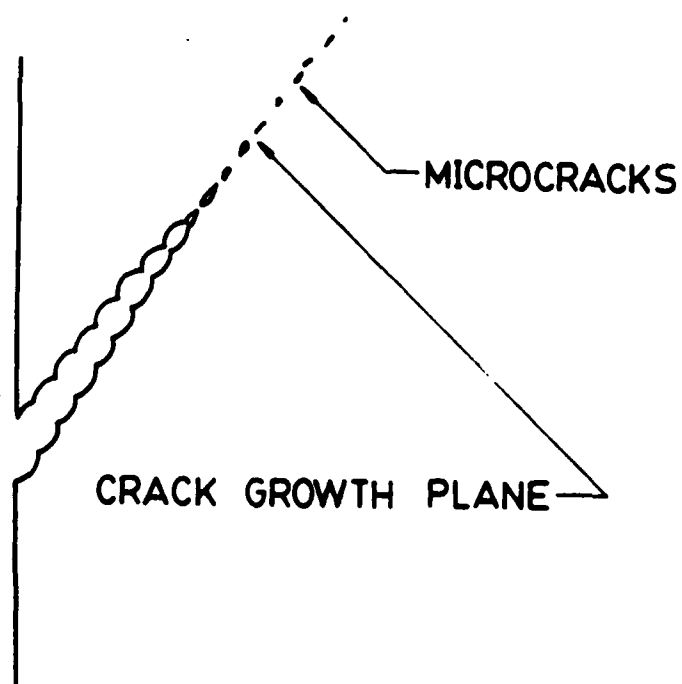


Figure 28

Schematic diagram illustrating micro-cracking ahead of the crack tip and the growth of dimples as the crack progresses (29).

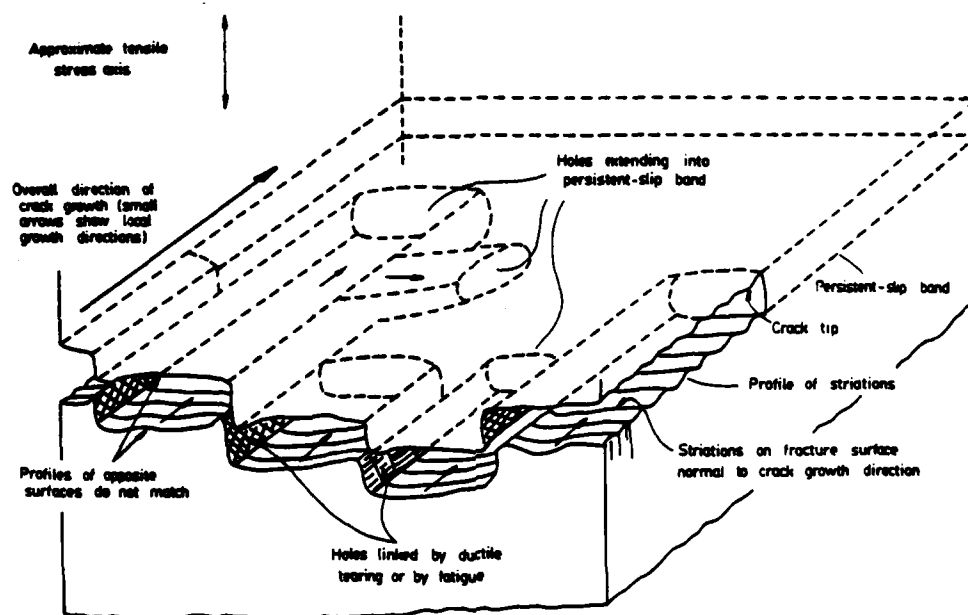


Figure 29

Schematic of intrusions at a crack tip showing regions of ductile tearing (93).

characterized by flat facets and river lines and they tend to propagate parallel to the {100} planes (10,108) Both types of striations are the result of environmental effects as no striations are formed during fatigue in vacuum (26,109,110).

Several mechanisms have been proposed for the formation of striations during stage 2 fatigue crack propagation. However, the slip plane decohesion mechanism of Pelloux (101,109) or a variation of this appears to be the most probable mechanism. In this model, crack propagation is the result of slip displacements on more than one intersecting slip system. Slip may occur either simultaneously or alternately on the active systems. This results in the blunting and resharpening of the crack during each load cycle and the formation of the striations when slip cannot be fully reversed (except in vacuum where it is more completely reversed). Propagation can always occur perpendicular to the applied load by adjusting the relative displacements on the different slip planes as illustrated in figure 30.

G. Environmental Assisted Crack Propagation in Aluminum Alloys

In corrosion fatigue, crack initiation and propagation are usually transgranular. However, at high mean stresses

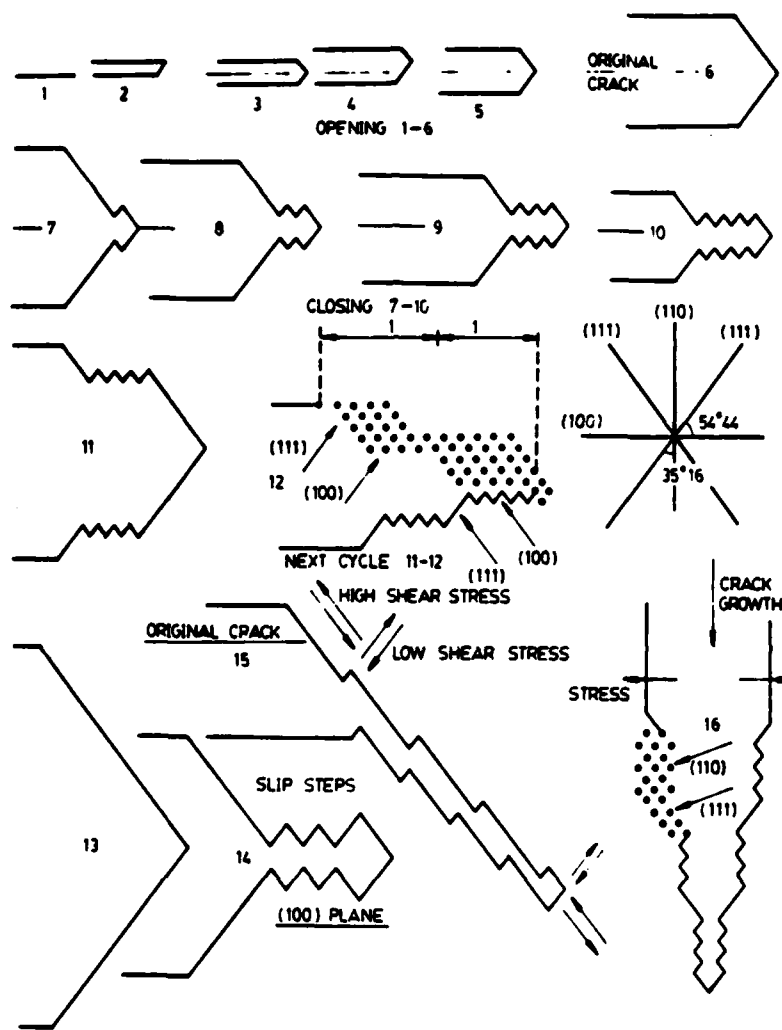


Figure 30

Schematic of the mechanism of striation formation and the planes of propagation showing how propagation can occur on different crystallographic planes (101).

and anodic potentials crack initiation and propagation will become intergranular (112).

Stage 1 Crack Propagation

Nageswararao et. al. (95,96) and Vogel et. al. (97,98) studied stage 1 fatigue crack propagation in Al-Zn-Mg single crystals in dry and humid air. They found that moisture in the environment effected stage 1 fatigue while oxygen had little effect in spite of the fact that the reaction with oxygen is energetically more favorable. They reported that moisture effects stage 1 propagation in five ways (95-98).

These are:

1. The crack propagation velocity increases 4 to 5 times.
2. The fracture surface becomes smoother.
3. The influence of moisture decreased as the crack propagation rate increased.
4. At low frequencies, the crack propagation mode changes to stage 2.
5. The width of the slip bands, as measured in the transmission electron microscope, is reduced for the same stress intensity.

These investigators concluded that moisture embrittled the material ahead of the crack making crack propagation easier (requiring less deformation in the slip plane). At lower frequencies, the material is embrittled more and the crack propagates into more homogeneously deformed material. This results in the change to mode 2 crack propagation.

Stage 2 Crack Propagation

Stoltz and Pelloux (108) studied the formation of striations under conditions of alternating cathodic and anodic potentials. They found ductile striations at cathodic potentials and brittle striations at anodic potentials. Since Stubbington (94) had determined from etch pit experiments that the cracks propagated macroscopically on the {100} planes and since the {100} planes would be the cleavage planes for aluminum, Stoltz and Pelloux (108) concluded that the brittle striations were the result of cleavage and that anodic potentials promoted cleavage. They concluded from this that a surface film must be forming at the crack tip blocking slip and causing the cleavage. Cathodic potentials prevent this film growth and therefore promote ductile striations (108).

Lynch (6,93) proposed an alternate explanation for the transition from ductile to brittle striations in Al-Zn-Mg alloys. Lynch conducted tests in inert environments, water vapor, aqueous solutions, and liquid metals. He found brittle striations in liquid metal environments where no surface film would form. Lynch concluded that the formation of brittle striations was not the result of cleavage but resulted from localization of the alternate shear processes on the slip planes intersecting the crack tip as shown in figure 31. Since slip occurs in the $\langle 110 \rangle$ directions in the

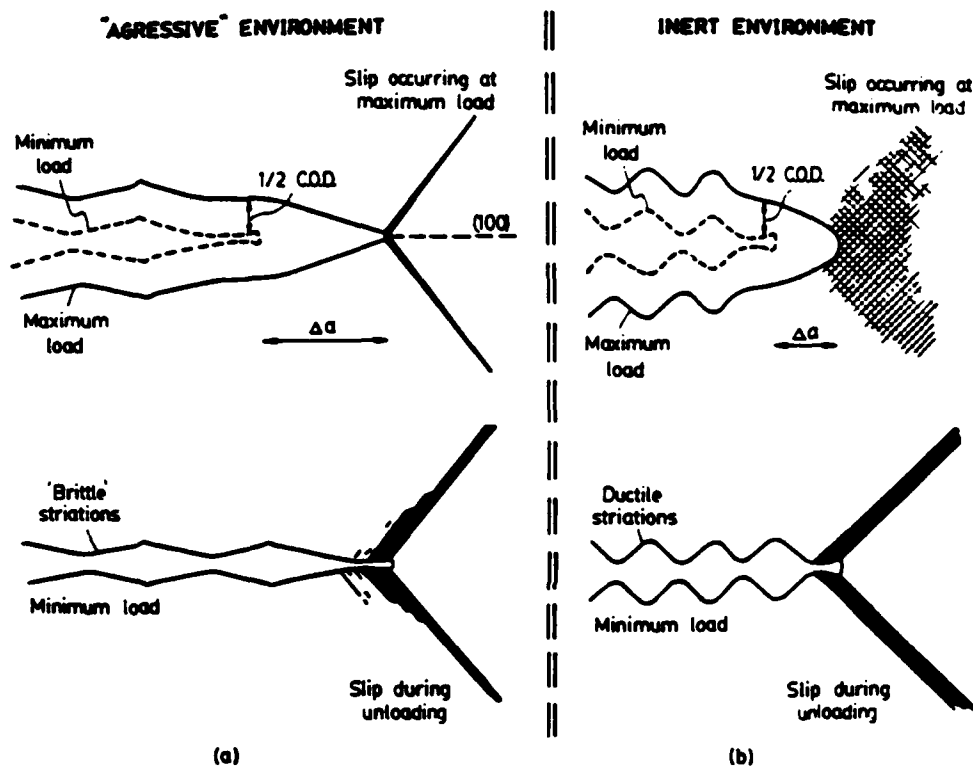


Figure 31

Schematic of proposed difference between "brittle" and "ductile" striation formation (6).

{111} planes, then as the homogeneity of deformation at the crack tip decreased propagation would tend to the {100} planes where the shear displacements would be more equally shared by the slip planes intersecting the crack tip.

H. Corrosion Fatigue Performance of Aluminum Alloys

Effect of Surface Oxide Thickness and Modulus

Beitel and Bowles (113) studied the effect of oxide thickness and modulus of elasticity on the cycles to crack initiation and to failure of aluminum in bending fatigue. They found, as shown in figure 32, that the oxide film thickness had no effect on the measurements. Water vapor reduced the cycles to crack initiation and cycles to failure but this effect was independent of the oxide thickness. As a result, Beitel and Bowles (113) concluded that the reductions were the result of some environmental effect not attributable to the oxide film properties or thickness (over the range of thicknesses studied).

Effect of Potential

Figure 33 shows that cathodic polarization to potentials just below the free corrosion potential increases fatigue life, but greater polarization reduces the fatigue life of smooth specimens(4). If this effect is due to

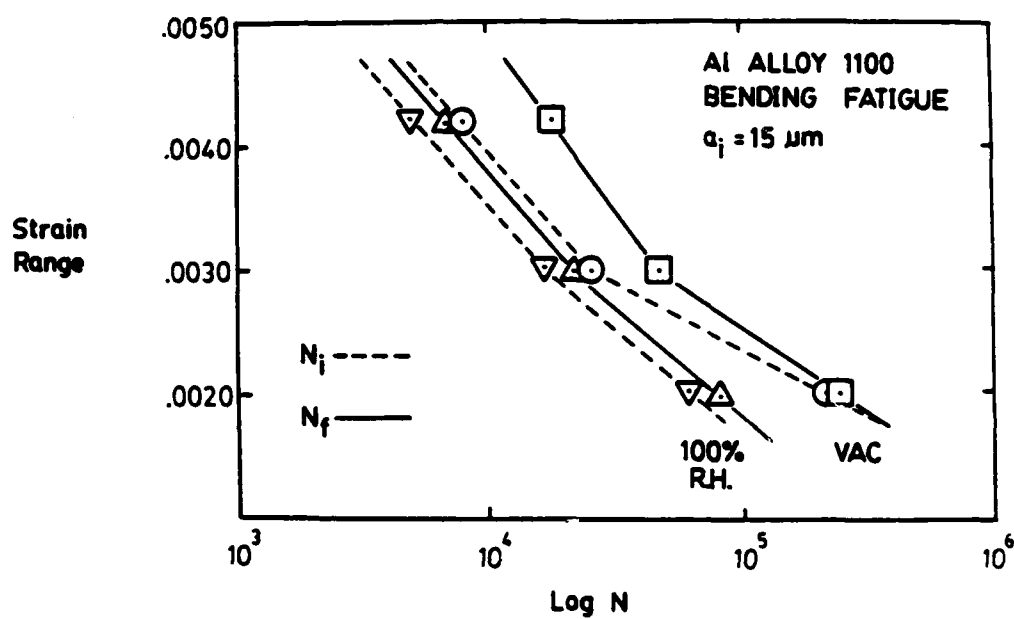


Figure 32

Effect of oxide surface layer thickness on the cycles to crack initiation (defined as the cycles to form a micro-crack 15 microns long) and cycles to failure (113).

AD-A162 627

CORROSION FATIGUE OF Al-Zn-Mg AND Al-Mg-Li ALLOYS

2/3

(U) RENSSELAER POLYTECHNIC INST TROY NY DEPT OF

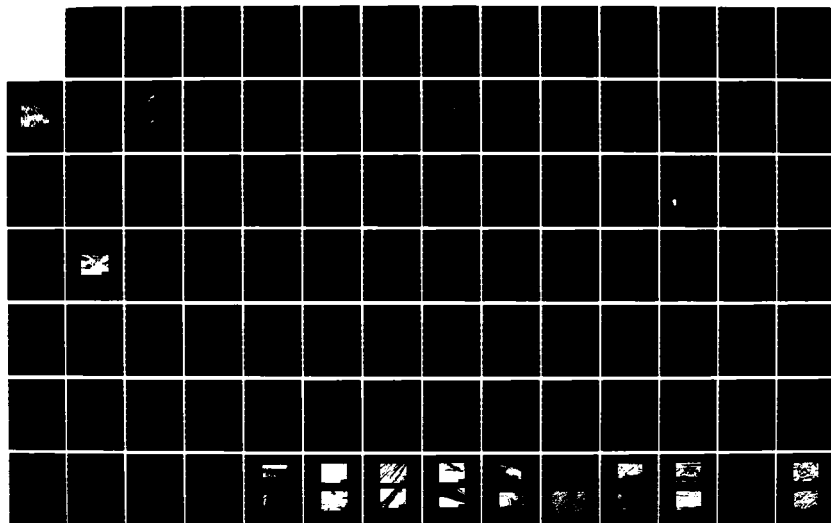
MATERIALS ENGINEERING R E RICKER ET AL. JAN 86

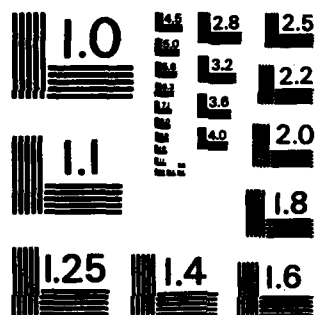
UNCLASSIFIED

N00014-67-A-0117-0012

F/G 11/6

NL





MICROCOPY RESOLUTION TEST CHART
NATIONAL BUREAU OF STANDARDS-1963-A

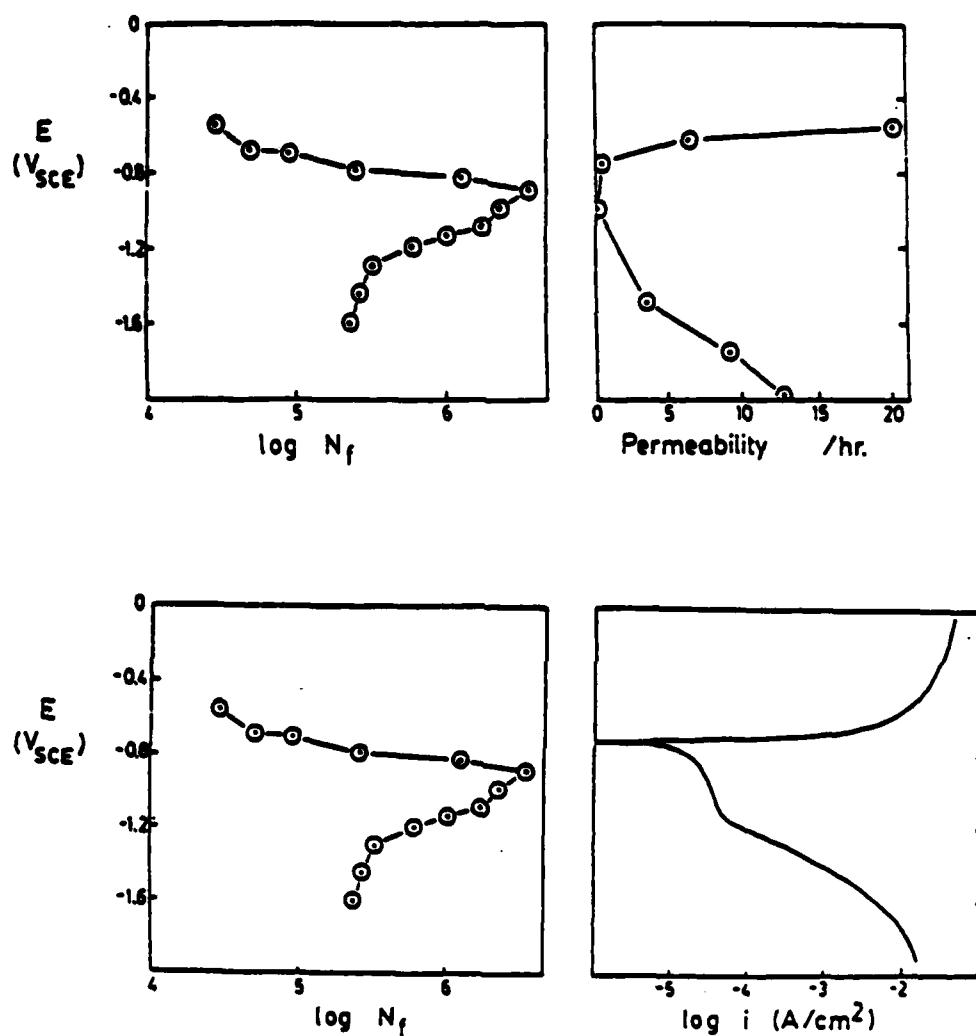


Figure 33

Effect of electrochemical potential on the cycles to failure (a) the hydrogen permeation flux (b) and the polarization current density (c) of alloy 7075 (120,116).

hydrogen, it is the result of either increasing hydrogen fugacity or increased absorption of hydrogen through the surface layer. Hydrogen absorption would be increased by the cathodic removal of the surface oxide layer which acts as a barrier to hydrogen absorption.

Effect of Loading Mode

As discussed above, hydrogen embrittlement requires hydrostatic stresses. If hydrogen embrittlement is the rate determining step for corrosion fatigue, then there will be a significant change in fatigue behavior with a change in loading mode. Figure 34 shows the results of these tests which indicate that a hydrogen mechanism is responsible for the observed corrosion fatigue behavior in mode 1 loading(4).

Effect of Mean Stress

Jacko(4) found no effect of mean stress as shown in figure 35. This indicates that the cyclic stress range and not the mean stress is the controlling parameter for corrosion fatigue. This could be due to either dislocation transport of the embrittling hydrogen or to an increase in the number of dislocations moving to the surface breaking the oxide layer and allowing hydrogen entry. Wei(28) similarly reported that the rate controlling step for

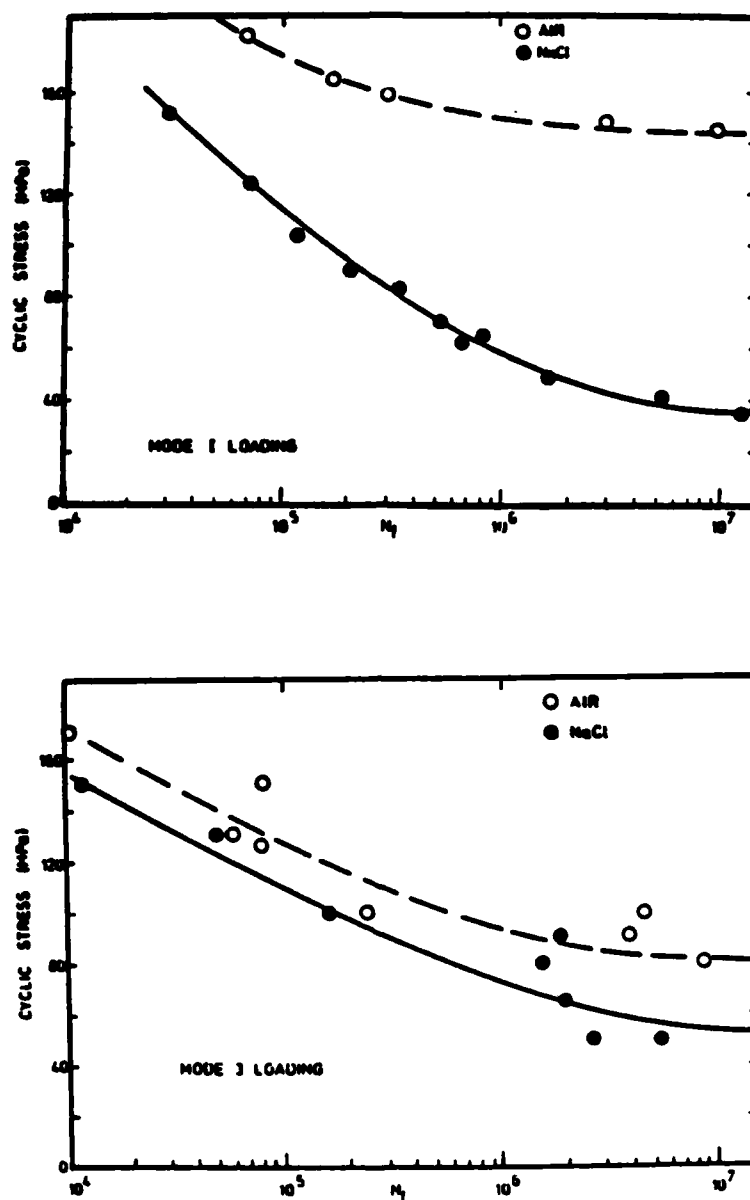


Figure 34

The effect of loading mode on the fatigue lives of alloy 7075 in air and aerated 0.5 N sodium chloride (120).

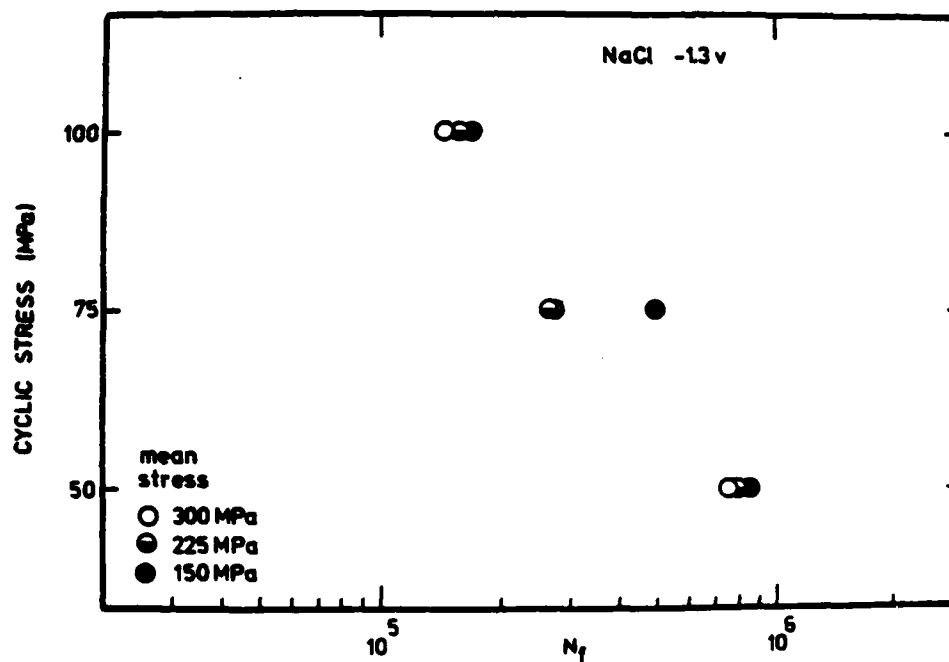


Figure 35

The effect of mean stress on the fatigue lives of alloy 7075 in aerated 0.5 N sodium chloride at different cyclic stress ranges (76).

fatigue crack propagation between 2.5×10^{-8} and 2.5×10^{-6} meters/cycle was the mechanical process of generating fresh crack surface.

Effect of Heat Treatment

Jacko(4) has demonstrated, as shown in figure 36, that overaging alloy 7075 does not improve the resistance to corrosion fatigue. Overaging does reduce the susceptibility of this alloy to stress corrosion cracking. The beneficial effect of overaging is usually attributed to either a change in slip character or to a change in nature of the grain boundaries. Since a change in slip character would probably effect transgranular cracking as well as intergranular cracking, it is logical to assume that the change in slip character is not responsible for the beneficial influence of overaging on stress corrosion cracking.

Stoltz and Pelloux (108) investigated the effect of thermal mechanical treatments to refine grain size on the corrosion fatigue properties of Al-Zn-Mg alloys. They found that grain refinement resulted in increased corrosion fatigue crack propagation rates (108).

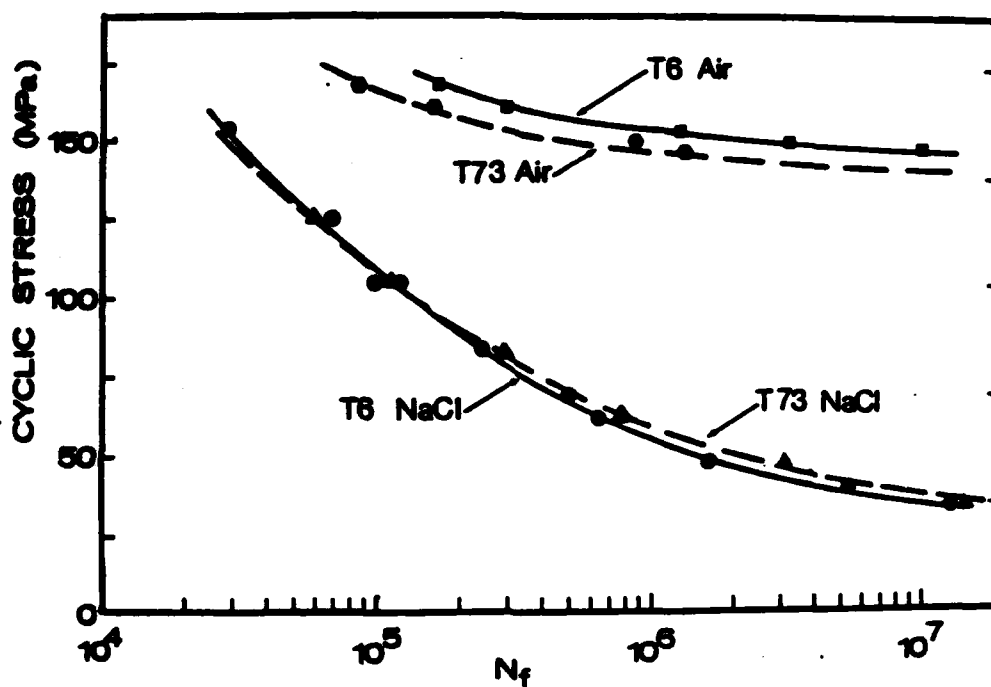


Figure 36

Comparison of the fatigue lives of peak aged (T6) and overaged (T7) samples of alloy 7075 in air and in aerated 0.5 N sodium chloride (76).

III. EXPERIMENTAL

A. Objective and Hypothesis

There were three main objectives of this program.

First, to determine the important parameters influencing the fatigue lives of high strength aluminum alloys in aggressive environments. Second, to determine if the actual mechanism(s) of corrosion fatigue fracture can be attributed to hydrogen embrittlement or not. And third, to identify how the metallurgical and chemical properties of high strength aluminum alloys influence hydrogen absorption and embrittlement.

As mentioned in the introduction, these objectives were approachable by utilizing two significantly different high strength alloys of aluminum. In this way, alloys which have similar mechanical properties but are chemically and metallurgically different are used to assess the importance of these properties on corrosion fatigue behavior. Thus, the goal of this work is to exploit the metallurgical and chemical differences between two alloys to learn something about the basic physics and chemistry of corrosion fatigue of high strength aluminum alloys.

To achieve these goals, three types of tests were employed. First, various examinations were performed to evaluate the chemical and metallurgical differences of the

alloys. Since considerable information is available on this subject in the literature, these examinations were kept to a minimum. Second, electrochemical polarization tests and corrosion rate (weight loss) measurements were performed to evaluate the corrosion behavior of the alloys. And third, corrosion fatigue tests were performed in various environments and at different electrochemical potentials.

B. Materials

A high purity Al-Zn-Mg alloy and a high purity Al-Mg-Li alloy were selected for the fatigue tests of this program. However, electrochemical polarization tests were conducted on a commercial Al-Zn-Mg alloy (7050). Table III gives the chemical composition of each of the alloys.

The high purity Al-Zn-Mg ternary alloy was supplied by the Olin Metals Research Laboratories and was made from elemental components of 99.995 % purity. The ingot was homogenized and hot rolled to approximately 0.65 cm (0.25 in) thick. Then, it was cold rolled to approximately 0.10 cm (0.04 in) thick sheet and machined into samples. The samples were solutionized for half an hour, quenched, straightened, and resolutionized at 465°C for an hour. Solutionizing was done in a fluidized bed furnace at 465°C in flowing argon. After quenching in cold tap water, the samples were cleaned, dried and aged in silicone oil for 24

Table III: Chemical Composition of Alloys

Element	7050 ¹	Al-Zn-Mg	Ternary ¹	Al-Mg-Li	Ternary ²
	wt%	wt%	At%	wt%	At%
Al	BAL.	BAL.	~95.26	BAL.	~87.69
Zn	6.52	5.64	2.40	0.004	~0
Mg	2.41	1.94	2.23	4.24	4.415
Li	*	*	*	2.13	7.772
Cu	2.20	0.028	0.01	0.030	0.013
Fe	0.147	0.031	0.02	0.01	0.005
Si	0.109	0.039	0.04	0.10	0.091
Mn	*	0.015	0.01	0.002	~0
Ni	*	*	*	0.006	0.003
Cr	0.029	0.049	0.03	<.002	~0
Ti	0.050	0.024	0.01	<.001	~0
Na	*	*	*	<.001	~0
K	*	*	*	<.001	~0
S	*	*	*	0.012	0.010

1. Dirats Testing, Westfield, MA.

2. Bowser-Morner Testing Laboratories, Inc., Dayton, Ohio.
(Analysis after extended thermal mechanical treatment and aging.)

* Not analyzed for.

hours at 120°C to achieve peak hardness as shown in the aging curve of figure 37.

The commercial Al-Zn-Mg alloy was supplied by the Alcoa Corporation as four inch thick plate. The electrochemical polarization tests were performed on this alloy because preliminary tests showed that the difference between the polarization behavior of this alloy and the high purity alloy was insignificant compared to the accuracy of the measurements and because more of this material was available for specimen fabrication.

The Al-Mg-Li ternary was supplied by the Naval Air Development Center (NADC) in Warminster Pa. The alloy was fabricated from pre-alloyed powders. The properties of this alloy, as determined by NADC, are given in Table IV (125). As received, the alloy was subject to intergranular failure at the powder particle boundaries and samples could not be readily fabricated without introducing cracks at these boundaries. Cold rolling less than 10% caused extensive cracking of an entire piece even after extensive solution heat treatment. Figure 38 is a scanning electron fractograph of cracks in a piece cold rolled 4% immediately after solutionizing for several hours. As a result, a thermo-mechanical heat treatment sequence was developed which was intended to break up the continuous network of oxides at the particle boundaries and to assist in

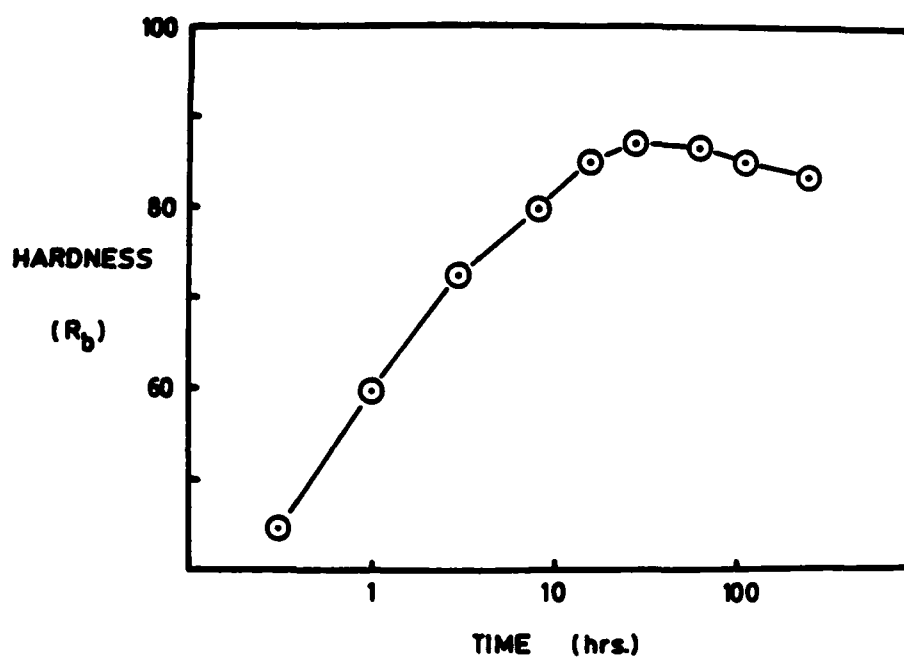


Figure 37

Hardness versus the aging time for the Al-Zn-Mg ternary alloy in silicone oil at 120°C.

Table IV: Properties of the Al-Mg-Li Ternary Alloy,
and of Aluminum Alloy 7075-T6 for Comparison.

<u>Property</u>	<u>Al-Mg-Li</u>	<u>7075-T651</u>
Density	2.50 g/cm ³	2.71 g/cm ³
Modulus of Elasticity	11.3x10 ⁶ psi 77.9 GPa	10.4x10 ⁶ psi 71.7 GPa
Yield Strength (0.2% offset)	51 ksi 351 MPa	72 ksi 496 MPa
Ultimate Tensile Strength	60 ksi 413 MPa	83 ksi 572 MPa
Knotched Tensile Strength	48.5 ksi 334 MPa	
Elongation (2 in)	12%	11%
E _{corr} (3.5% NaCl)	-1200 mV	-790 mV
K _c	~23-25 ksi $\sqrt{\text{in}}$ 25.3-27.5 MPa $\sqrt{\text{m}}$	~25-28 ksi $\sqrt{\text{in}}$ 27.5-30.8 MPa $\sqrt{\text{m}}$

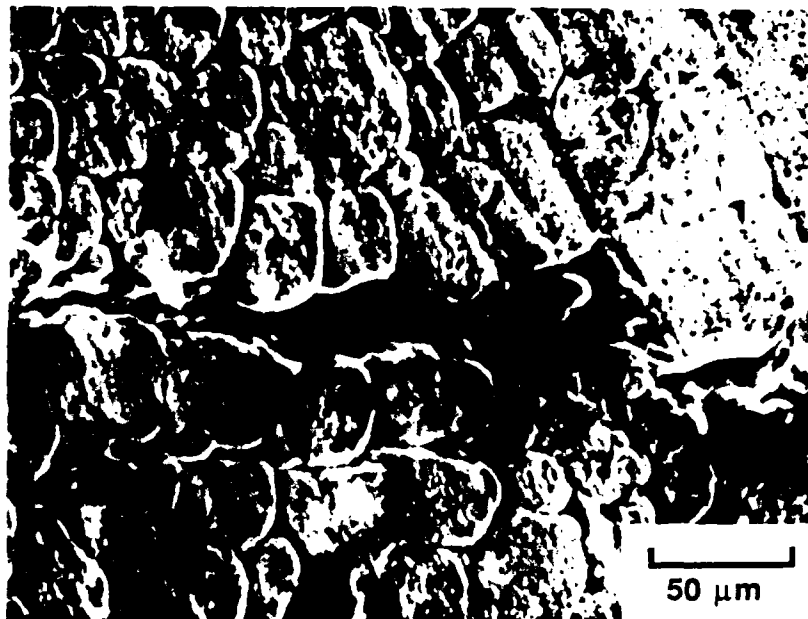


Figure 38

Cracks at the powder particle interfaces for the Al-Mg-Li alloy after cold rolling to 4% reduction in thickness.

homogenizing the material. This heat treatment procedure resulted in an improvement in the ductility and the yield strength of the material. After this treatment, the alloy in the solution treated condition could be cold rolled >60% without cracking. This thermal-mechanical-treatment (TMT) procedure consisted of alternately solutionizing and cold rolling the material. Each solutionizing treatment was performed in a fluidized bed for one hour in flowing argon at 465°C. Solutionizing was performed at 465°C instead of at higher temperatures, because it was found that lower temperatures resulted in less cracking and because the ternary phase diagram of figure 39 shows that the alloy composition is still in the single phase solid solution range at this temperature. It is believed that the lower solutionizing temperature reduced intergranular cracking by reducing residual stresses, segregation, and AlLi nucleation during quenching.

The starting material for this "TMT" process was 0.65 cm (0.25 in) thick and the final thickness was 0.1 cm (0.040 in). The solutionized material was machined into samples and then resolutionized, quenched, cleaned, dried, and aged in silicone oil at 190°C for 5 hours and 45 minutes. This resulted in the peak hardness shown in the results of the aging experiments of figure 40. This figure also gives the aging response of the alloy at 160°C, at 175°C and at 205°C

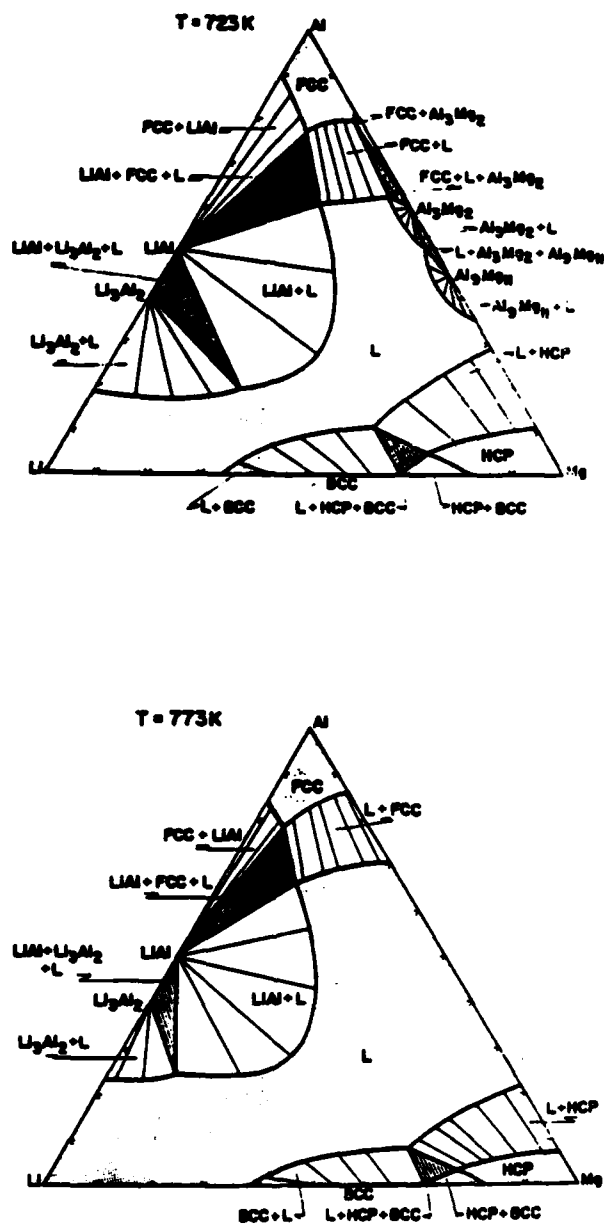


Figure 39

Isothermal sections of the Al-Mg-Li ternary phase diagram at 450°C and 500°C.

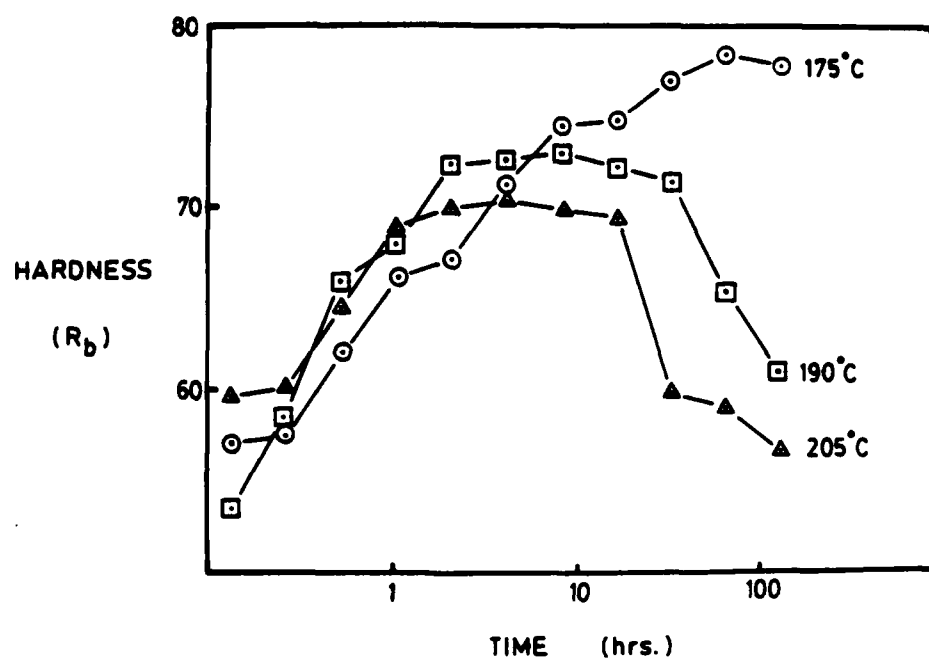


Figure 40

Hardness response as a function of aging time for the Al-Mg-Li alloy in silicone oil at various temperatures.

as well as at 190°C.

C. Examination Techniques

Metallography

Fatigue samples of each of the ternary alloys were sectioned for metallography in each of the three principle axes of the samples. The samples were mounted and polished using standard metallographic practices. They were then etched in Keller's etchant for twenty seconds, examined and photographed.

Slip Character Analysis

To determine the relative deformation characteristics of the Al-Zn-Mg alloy and the Al-Mg-Li alloy in the heat treatment conditions employed for the fatigue tests, the electropolished surfaces of samples were examined by phase contrast microscopy both before and after bending over a mandrel (2.54 cm radius). These samples were selected from the samples prepared for the fatigue tests. Also, fatigue samples were examined after fracture to determine if the slip found in the bend tests was representative of the slip found at fatigue cracks.

Scanning Electron Microscopy

Fracture surfaces of the samples were examined in an

AMR 1000 scanning electron microscope. The fracture surfaces were cut from the gage section of the samples and mounted on standard stubs with silver paint.

Auger Electron Spectroscopy

Samples were prepared for Auger electron spectroscopy by cutting fatigue samples of each alloy into one centimeter square pieces. These pieces were then ground with successively finer grades of silicon carbide paper to 600 grit. Care was taken during this procedure to avoid mixing samples and to use clean grinding papers for each sample. The samples were placed in a dessicator with a beaker of saturated sodium carbonate below the rack holding the samples. The equilibrium partial pressure of water vapor over the sodium carbonate solution is such that the relative humidity is 87% at 25°C (126). One sample of each alloy was removed from this environment after 40 hours of exposure and after 1200 hours of exposure and examined in the scanning Auger microprobe.

D. Evaluation of Corrosion Behavior

Potentiodynamic Polarization Tests

Potentiodynamic polarization tests were compared for the Al-Mg-Li alloy and a commercial Al-Zn-Mg alloy (7050).

These tests were performed on the commercial Al-Zn-Mg alloy because preliminary experiments showed that the differences between the polarization behavior of the commercial alloy and the high purity alloy were small compared to the accuracy of the measurements and because of the availability of the commercial alloy.

The tests were performed in various concentrations of sodium chloride and sodium sulfate solutions as functions of scan rate, pH, temperature, and degree of aeration. Cylindrical samples were machined from each of the alloys. The samples were then ground with successively finer grades of silicon carbide papers to 600 grit and then polished with 9 micron diamond paste. Samples were reconditioned after each test by machining the exposed surface and then repeating the procedure above to produce a fresh surface for each test.

Tests were performed in a standard glass polarization cell with the sample mounted on a steel rod encased in glass and sealed with a teflon gasket as shown in figure 41 (127). Only the totally immersed sample, teflon gasket and glass made contact with the solution. Potentials were measured with a Luggin capillary and a saturated calomel electrode and all reported voltages are versus the saturated calomel electrode ($0.0 V_{sce} = 0.242 V_{she}$). Temperatures were maintained constant utilizing a temperature bath filled with

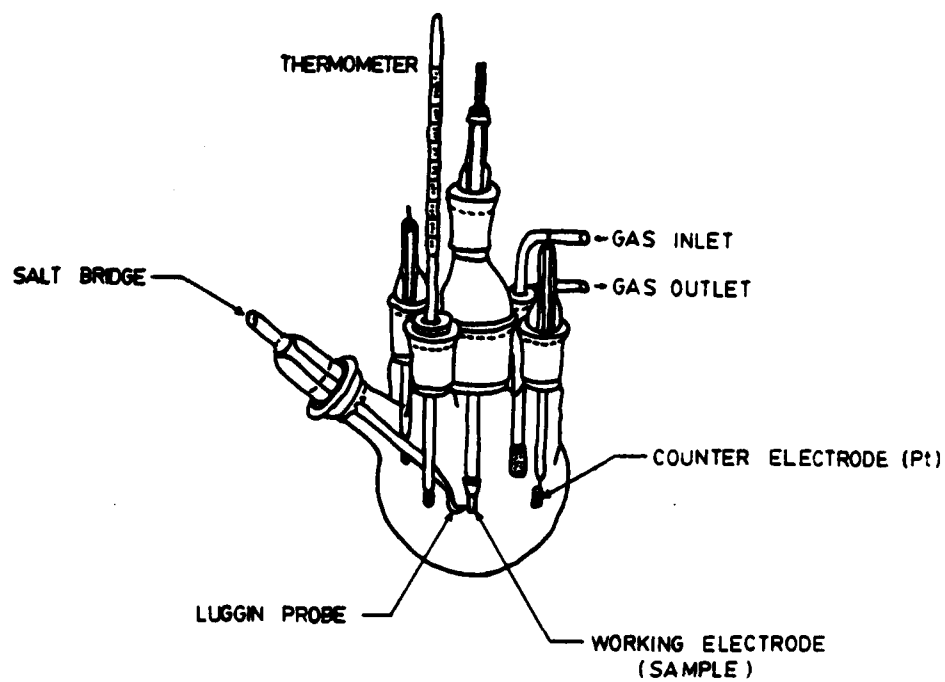


Figure 41

Schematic diagram of the electrochemical polarization cell.

water into which the corrosion cell was immersed. the temperature of the solution in the cell was monitored with a standard laboratory thermometer.

All solutions were mixed, thoroughly deaerated and stored under nitrogen prior to use. The solutions were then deaerated with nitrogen or aerated with air for at least one hour prior to insertion of the sample. Bubbling of either nitrogen or air was continued for the duration of the tests to maintain conditions and to agitate the solutions.

The samples were inserted into the solutions for a period of 30 minutes to reach the steady state or free corrosion potential. Monitoring of the potential during this period and for longer durations indicated that this potential was reached in 10 to 20 minutes. A dynamic potential scan was started at a potential 100 mV active to the corrosion potential and continued to a potential sufficiently noble to cause pitting prior to reversing the scan. If pitting did not occur the scan was halted manually. The scans shown in the figures are active to noble potential scans. If the samples were mounted properly, the reverse scans retraced the original scans.

Corrosion Rate Measurements

Weight loss measurements were conducted at constant electrochemical potentials in 0.5 M sodium chloride and

sodium sulfate solutions. This was done so that a comparison could be made between the fatigue life at a constant potential and the actual rate of dissolution of metal from the alloy surface at the same potential.

The samples were prepared in exactly the same manner as the samples used in the polarization tests except that these samples were not polished with the 9 micron diamond paste. The samples were weighed three times before testing and measured with a micrometer to determine the surface area. The solutions were mixed and deaerated with bubbling argon for 12 hours prior to insertion of the sample. The samples were inserted into the solution, the chamber closed and then deaerated an additional 30 minutes before applying the potential. The potential was maintained constant with respect to a saturated calomel reference electrode by using a Princeton Applied Research Model 173 potentiostat. Exposures varied from one hour to one week depending on the corrosion rate. After the exposure, the samples were cleaned in distilled water and acetone in an ultrasonic cleaner then rinsed with ethanol and dried before weighing again. Weight loss was then converted to a corrosion rate mathematically and is reported as milligrams of weight loss per square decimeter of surface area per day of exposure or "MDD".

E. Mechanical Testing

Sample Preparation

The samples for fatigue testing were machined, according to the diagram of figure 42, prior to the final solution treatment and aging. The samples were solution treated and aged according to the parameters discussed above in the section on materials. They were ground in oil or in a kerosene/paraffin mixture to the equivalent of a 600 grit finish. Then, they were thoroughly cleaned in kerosene, boiling acetone, dried and stored in a dessicator for electropolishing.

The samples were prepared for electropolishing by grinding the edges and rounding the corners with 600 grit silicon carbide paper. Then, they were cleaned again and electropolished in a perchloric acid ethanol solution (No. L1 in reference 124). Electropolishing was done at -35°C with an applied potential of approximately 20 volts. Exact parameters for good polishing varied slightly from time to time and from alloy to alloy.

After electropolishing, the samples were cleaned in acetone rinsed with ethanol, dried with freon and stored in a vacuum. Originally, the samples were periodically removed from the vacuum for fatigue testing. However, after some testing it became obvious that the fatigue lives of the samples in dry nitrogen varied with the time in the vacuum

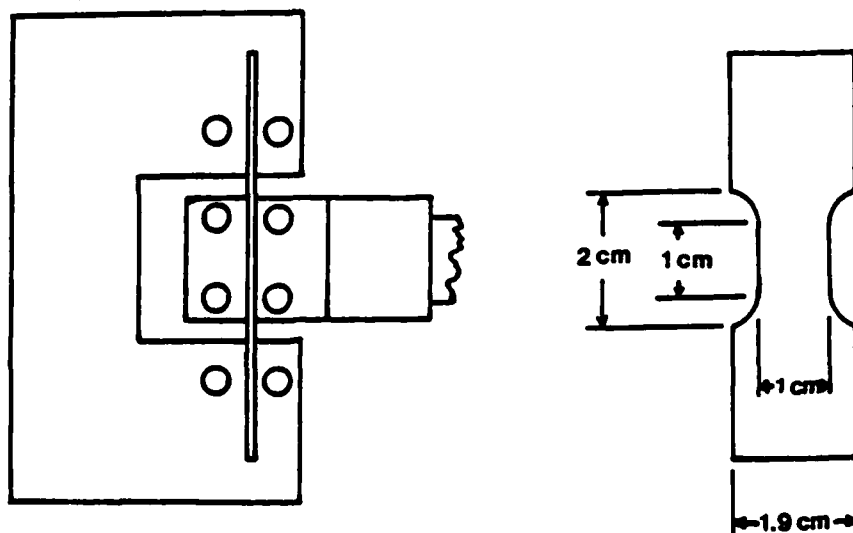


Figure 42

Fatigue sample design and bending fatigue grips.

chamber prior to testing. As a result, a standard vacuum pre-exposure had to be chosen for all subsequent testing.

Testing Apparatus for Fatigue Testing

Fatigue tests were conducted with a four point bend machine that was fabricated from an electro-proportional solenoid and other equipment as shown in figure 43. The solenoid was capable of 33 pounds continuous force with a 0.375 inch stroke.

The solenoid was mounted on a small steel loading frame and the grips, illustrated in figure 42, were placed in a plexiglass environmental chamber. The environmental chamber was used to strictly control the environment of all fatigue tests. A load cell and a LVDT were used to monitor the load and position of the shaft during the tests. The outputs of these transducers were monitored with an oscilloscope and a strip chart.

The strains were determined from the strain-load-displacement equations derived in appendix I. These were derived from the moment equations by the double integration technique assuming a simple model for the specimen geometry (129,130). Before conducting fatigue tests, samples of each alloy with different dimensions were tested with strain gages applied to both surfaces. The strain gages were specially designed for use on high

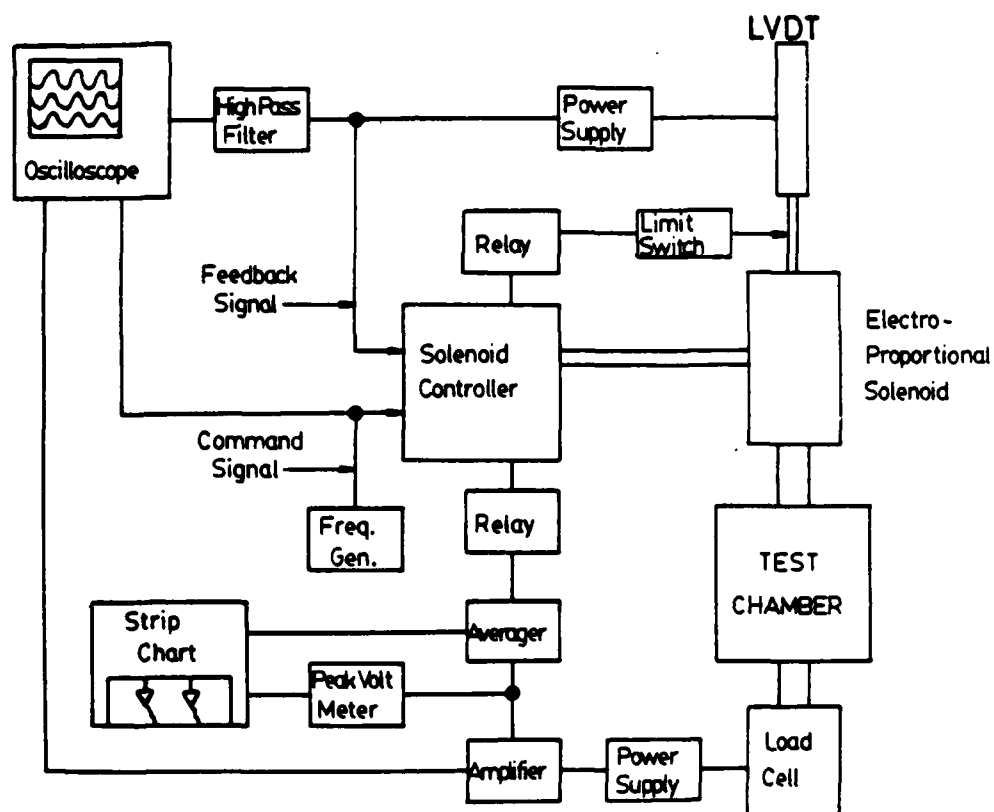


Figure 43

Diagram of the various equipment used to conduct the fatigue tests.

strength aluminum alloys. Tests of these samples were conducted under both cyclic and static loading conditions. From these measurements, the standard deviation of the strain calculated from the sample dimensions, load and the stroke was less than 10^{-4} m/m (0.01%). All strains are reported as meters/meter unless specifically stated otherwise.

Testing Procedures

All of the fatigue tests were conducted under controlled and regulated pre-exposure and test environmental conditions. The specific conditions and procedures for each environment are discussed in the appropriate sections below. The tests were conducted with stroke control four point bending at 2.778 Hz (10,000 cycles per hour). For all tests, the maximum stress at the surface of the sample was below the yield stress of the alloy. As a result, tests were conducted without reversed bending so that the features on the fracture surface would be preserved for fractography. The mean load was monitored for all tests and the minimum to maximum load was monitored for tests without electrolytes. For tests in electrolytes, the corrosion potential (for free corrosion tests) or the current (for constant potential tests) was monitored on the two pen strip chart. When the mean and peak to peak load for the constant stroke decreased

to approximately 10% of their initial values the tests were terminated.

Pre-exposures: Since storage in a vacuum improved the fatigue lives of the samples, a standard pre-exposure to vacuum period had to be established before consistent results could be obtained. To establish this period some assumptions had to be made, first it was assumed that the effect was due to the desorption of hydrogen from the sample. As will be shown, this is a good assumption as the times predicted for removal of hydrogen coincide with the exposures which result in improved properties. Second, several assumptions were required to solve Fick's second law for the test specimen geometry. Finally, a diffusion coefficient had to be determined or assumed for hydrogen in aluminum.

Several authors have attempted to determine the diffusivity of hydrogen in aluminum at room temperature. However, as shown in table V, these results have been inconsistent and extrapolation from high temperatures, also in table V, yields widely different results. However, since Ciaraldi (80) used similar sample geometry for his hydrogen absorption measurements from humid air, then a hydrogen diffusion coefficient could be estimated from the measurements of Ciaraldi (80) and the equations for the absorption or desorption of hydrogen derived in appendix II.

Table V: Diffusion Information for Hydrogen in Aluminum and Aluminum Alloys

Alloy	Method	D_0 (cm^2/sec)	Q (kJ/mole)	$D(T=25^\circ\text{C})$ (cm^2/sec)	Ref.
99.999% Al	Desorp. ^o (400-500°C)	1.2×10^5	-140	$3.5 \times 10^{-20} \text{ cm}^2/\text{sec}$	134
99.999% Al	Desorp. ^o (350-600°C)	1.1×10^{-1}	-41	7.2×10^{-9}	135
99.8% Al	Desorp. ^o (450-590°C)	2.5×10^{-2}	-91	2.8×10^{-18}	136
99.999% Al	Desorp. ^o (450-590°C)	1.9×10^{-1}	-40	1.85×10^{-8}	137
99.995% Al	Desorp. ^o (450-625°C)	1.01×10^{-1}	-47.7	4.39×10^{-10}	138
7075-T651	Electrochem. permeation (~25°C)	--	--	2×10^{-9}	81
Al-4.32Zn-1.5Mg	Permeation (.70°C)	--	--	10^{-10}	87.88

Also, since Scamans and Tuck (128) conducted their diffusion measurements with humid air as the hydrogen source, their measurements provide an independent check of the diffusion coefficient and the equations determined in appendix II. Figure 44 shows the data of Ciaraldi (80) and the predicted hydrogen concentrations for the diffusion coefficient and the equations determined in appendix II. According to these assumptions, calculations and measurements, vacuum pre-exposures of four weeks or more should yield relatively hydrogen free samples for testing. As a result, all fatigue test samples were given a vacuum pre-exposure of four or more weeks except for those which were pre-charged with hydrogen from water vapor. The pre-exposure to water vapor period was also for four or more weeks.

Dry nitrogen environment: The dry nitrogen environment was maintained for the fatigue tests by a continuous flow of nitrogen (<3ppm water) through a dry ice cold trap. The cold trap was made by placing a bubbler filled with small glass beads in a Dewar flask filled with dry ice. The nitrogen flow rate was held constant at 0.22 liters per minute. The volume of the testing chamber is 1.4 liters. This experimental arrangement is illustrated in figure 45.

Humid nitrogen environment: As shown in figure 46, the humid nitrogen environment was maintained constant by bubbling the nitrogen at 0.22 liters per minute through two

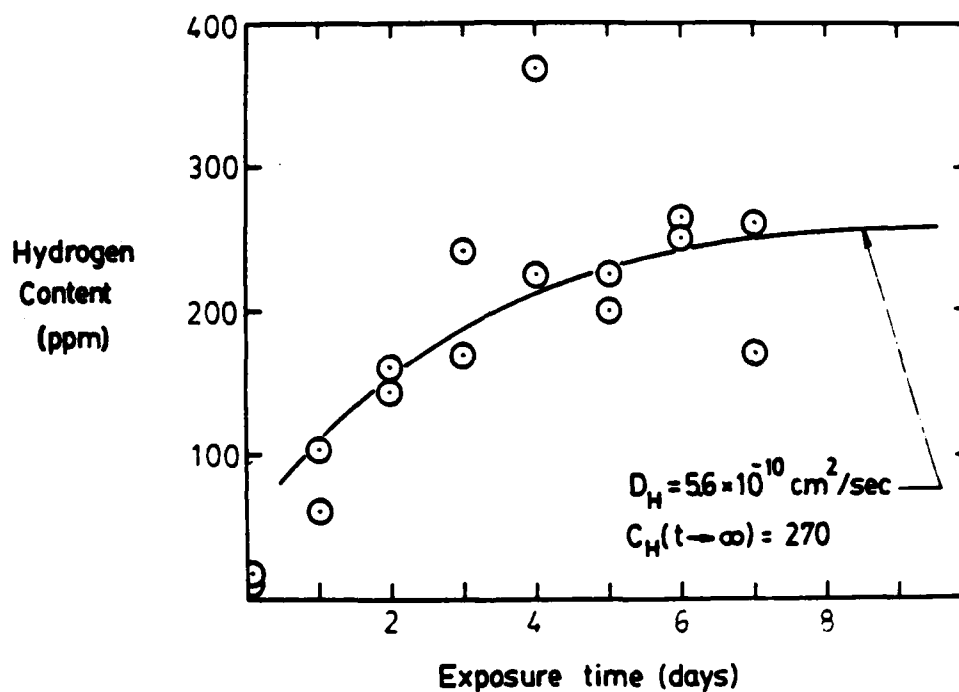


Figure 44

The correspondence of the diffusion equation derived in Appendix II for an estimated diffusion coefficient of $5.6 \times 10^{-10} \text{ cm}^2/\text{sec}$ with the hydrogen content versus exposure to humid air measurements of Ciaraldi (80) for a high purity Al-Zn-Mg ternary alloy.

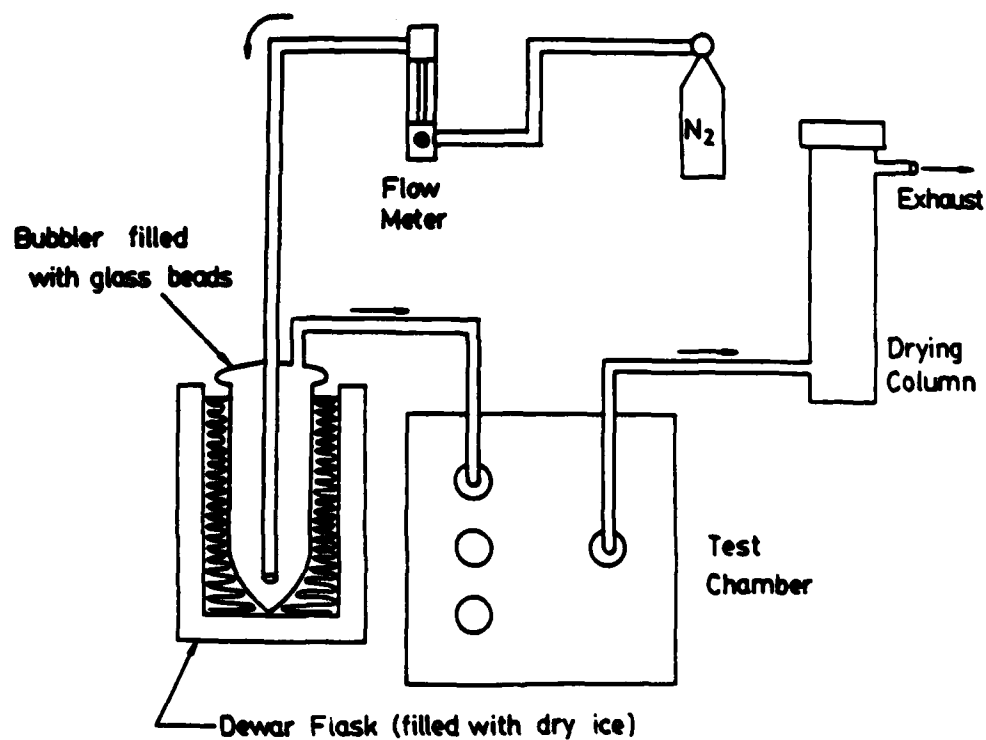


Figure 45

The environmental regulation and maintenance system used for fatigue tests in dry nitrogen gas

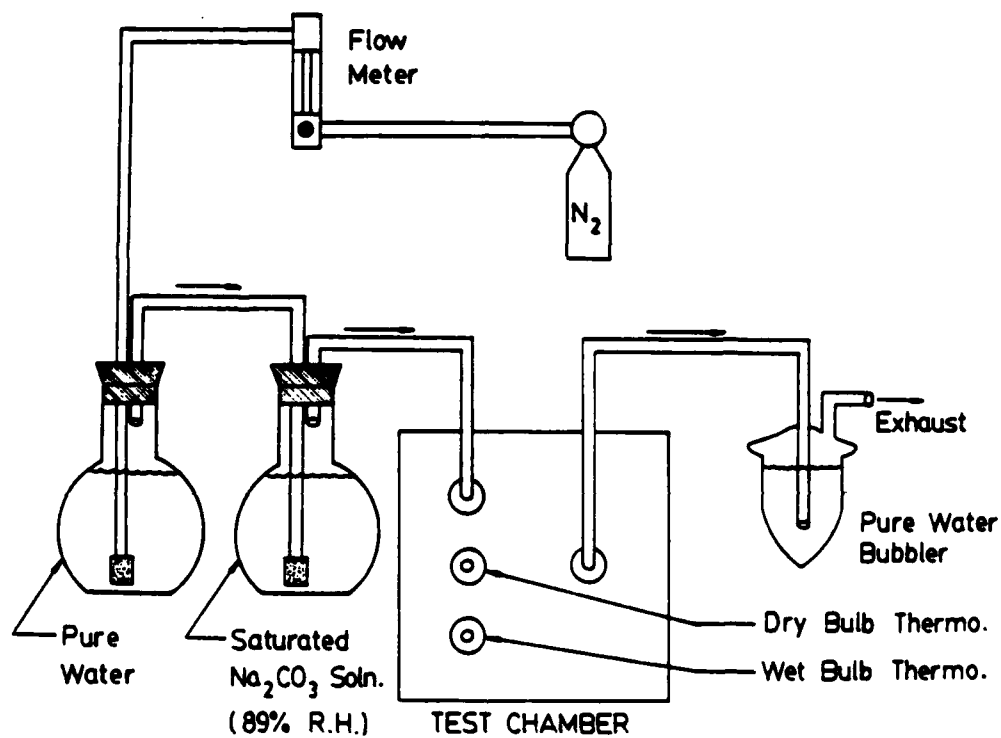


Figure 46

The environmental regulation and maintenance system for fatigue tests in 87% relative humidity nitrogen gas.

flasks one containing pure water and the other containing a solution saturated with sodium carbonate. The equilibrium partial pressure of water vapor over a solution saturated with sodium carbonate at 25°C is such that the relative humidity is 87% (126). The double bubbler arrangement was used to prevent restriction of the nitrogen flow by the precipitation of sodium carbonate solid.

Purified water environment: Distilled and deionized water (<0.5 micro-mhos/cm) was used for these tests and for making the solutions in the tests below. One liter of water was placed into the test chamber and deaerated by bubbling oxygen free grade nitrogen (<0.5 ppm oxygen) through the chamber at 0.22 liters per minute for 12 hours before testing. The samples were placed into the solutions and the chamber resealed for 30 minutes before commencing fatigue loading. Since the resistivity of the solution was so high, no attempt was made to monitor the free corrosion potentials.

Electrolyte solutions: Two types of electrolyte solutions were used for fatigue testing environments. These were 0.5 M sodium sulfate and 0.5 M sodium chloride solutions. The salts were weighed, mixed with pure water (<0.5 micro-mhos/cm) and deaerated in the same manner as employed for the corrosion tests above. The nitrogen flow rate was maintained constant at 0.22 liters per minute. The

samples were placed into the solutions for 30 minutes before commencing the fatigue loading.

Tests were conducted under either free corrosion conditions or with the electrochemical potential of the sample held constant. The electrochemical potential of the sample was recorded on the strip chart for the free corrosion tests and the current required to maintain the sample at the desired potential recorded in the constant potential tests. The potentials were maintained constant with respect to a saturated calomel electrode with a Wenking potentiostat and a platinum counter electrode. Figure 47 illustrates the test cell arrangement and Luggin capillary to the reference electrode.

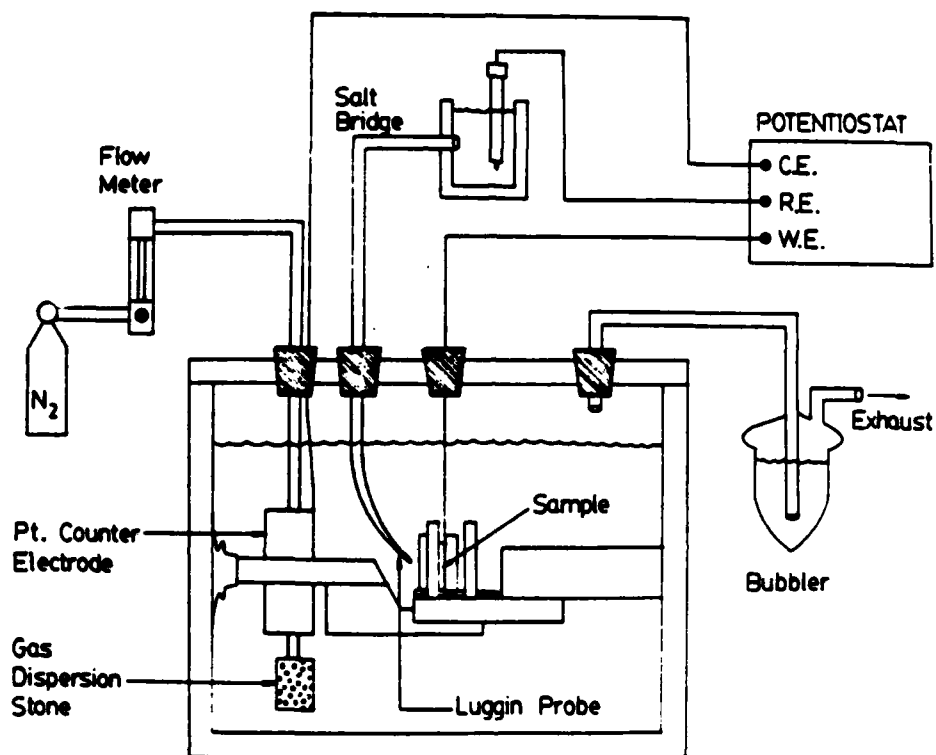


Figure 47

Test cell and electrochemical instruments used for conducting tests in 0.5 M sodium sulfate and 0.5 M sodium chloride.

IV. RESULTS

A. Material Evaluation Examinations

Metallography

Fatigue samples of each alloy were sectioned and examined along each of the three principal axes. Figure 48 shows a section in each of the axes for a sample of the Al-Zn-Mg alloy at 100X. The grain size of this sample was determined from the three sections by the Heyn intercept technique to be ASTM grain size number 3. This means that a typical cross section through the gage section of the fatigue sample should intersect approximately 500 grains. Figure 49 shows metallographic sections along each of the principle axes for a sample of the Al-Mg-Li alloy at 100X. It can be seen that this alloy has a finer grain size and, by the same technique, the grain size is determined to be ASTM grain size number 7.5. A cross section through the gage section of a fatigue sample should intersect approximately 11,000 grains.

Slip Character

Fatigue samples of each alloy were chosen from those prepared for fatigue testing and bent over a 2.54 cm radius mandrel. The surfaces were examined and photographed by phase contrast optical microscopy. Figure 50 compares typical areas of each sample. From this figure it can be

Figure 48

Metallographic sections in the short transverse, long transverse and the rolling direction of a fatigue sample of the Al-Zn-Mg ternary alloy.

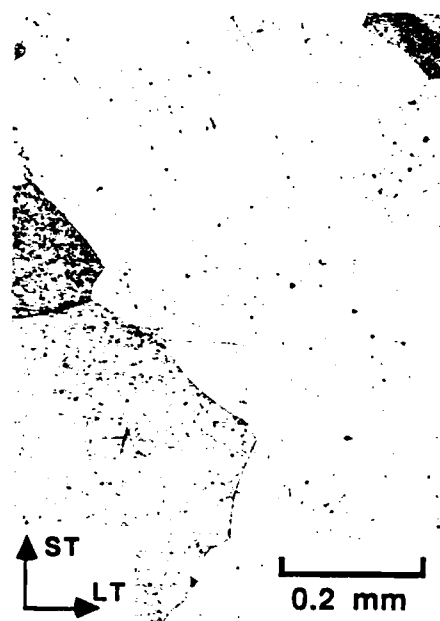
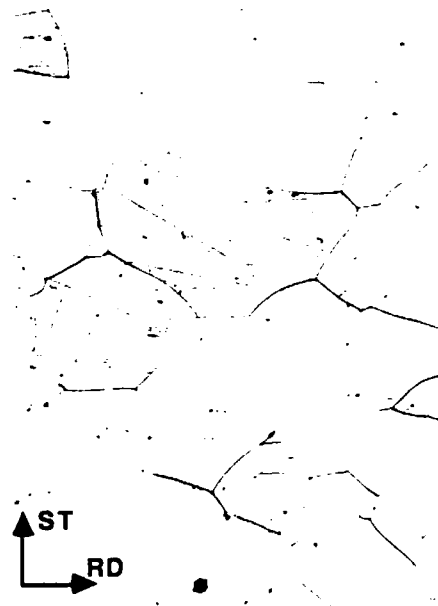
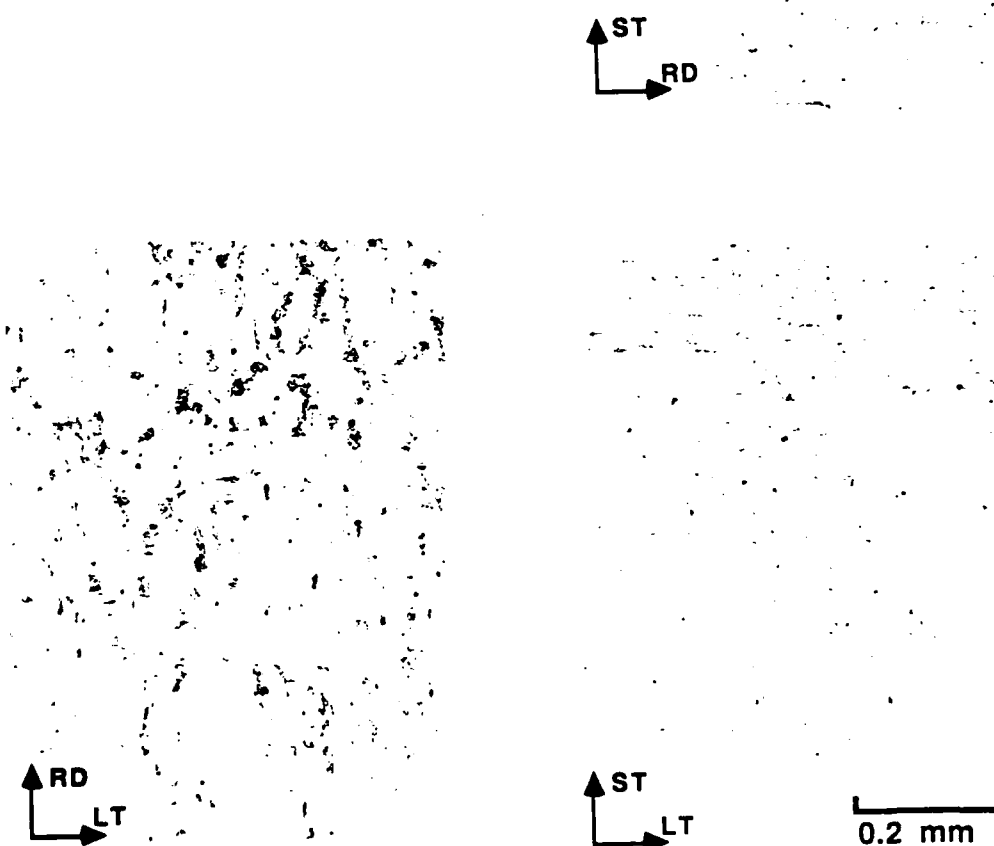
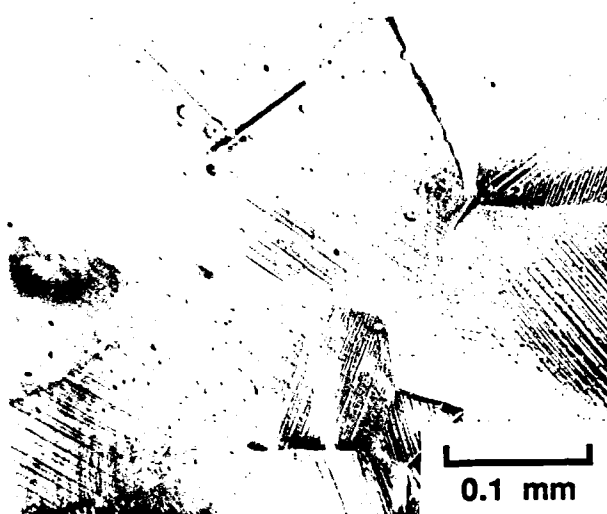


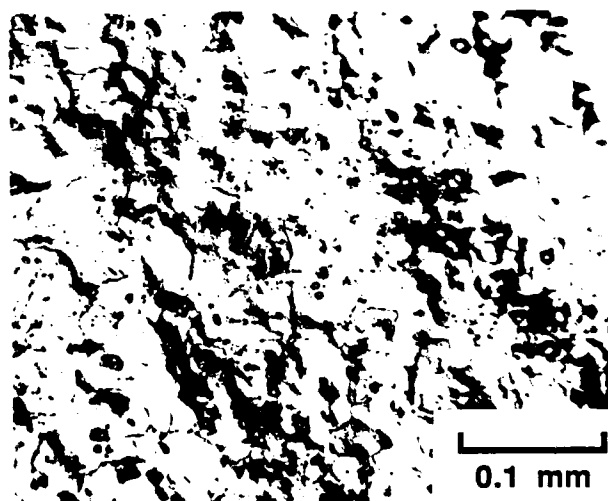
Figure 49

Metallographic sections in the short transverse, long transverse and the rolling direction of a fatigue sample of the Al-Mg-Li ternary alloy.





[A]



[B]

Figure 50

Phase contrast micrographs of the electropolished surfaces of an Al-Zn-Mg alloy sample (A) and an Al-Mg-Li alloy sample (B) after bending to a surface strain of approximately 1.5%.

seen that the Al-Zn-Mg ternary alloy demonstrates considerably more planar deformation character than the Al-Mg-Li alloy. Similar bend tests were conducted on samples exposed to humid air for greater than four weeks but no significant change in character with exposure to humid air could be detected. Figure 51 shows the deformation about a fatigue crack tip in a Al-Zn-Mg sample.

The reduced grain size of the Al-Mg-Li alloy contributes to the increased homogeneity of deformation in this alloy. To determine if the difference in the slip character of the alloys was due only to the difference in grain size, regions of larger and smaller grains were examined in each alloy to evaluate how slip character of the alloys varied with grain size. As a result, it was concluded that the reduced grain size of the Al-Mg-Li alloy was not the only factor contributing to the increased homogeneity of deformation of this alloy but that there was an intrinsic difference in the slip character of the alloys.

Auger Electron Spectroscopy

Samples of each alloy were examined after varying exposures to humid air. The samples were examined by a scanning Auger microprobe before and after sputtering the surface. The surface was sputtered to determine if the film compositions varied with depth. No significant difference was found between the Al-Mg-Li alloy and the Al-Zn-Mg alloy

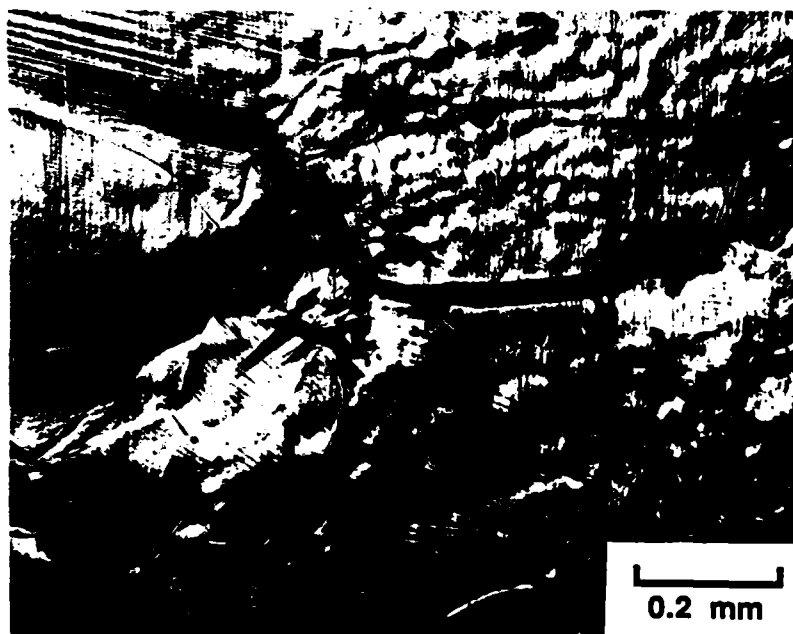


Figure 51

Phase contrast image of the deformation at at a fatigue crack tip in an Al-Zn-Mg alloy sample.

in any scan of electron energies at any depth into the surface films. Figure 52 compares typical scans for the alloys. As a result, a lithium standard made from lithium chloride was examined in the instrument. The lithium peaks were located and identified. However, the lithium peaks still could not be detected in the surface films of the samples. This does not mean that lithium is not present in the passive layer but, only that the atomic concentration of lithium on the surface was never great enough to detect with the Auger electron spectrometer.

B. Corrosion Behavior Evaluation

Two types of tests were conducted to determine the relative corrosion behavior of the two types of alloys. First, potentiodynamic polarization tests were conducted in a variety of environments and environmental conditions on the Al-Mg-Li ternary alloy and on a commercial Al-Zn-Mg alloy (7050). Second, the dissolution rates of the Al-Mg-Li ternary alloy and the Al-Zn-Mg ternary alloy in 0.5 M sodium chloride and 0.5 M sodium sulfate at constant electrochemical potentials were calculated from weight loss measurements.

Potentiodynamic Polarization Tests

Scan Rate: Figure 53 shows the effect of scan rate on

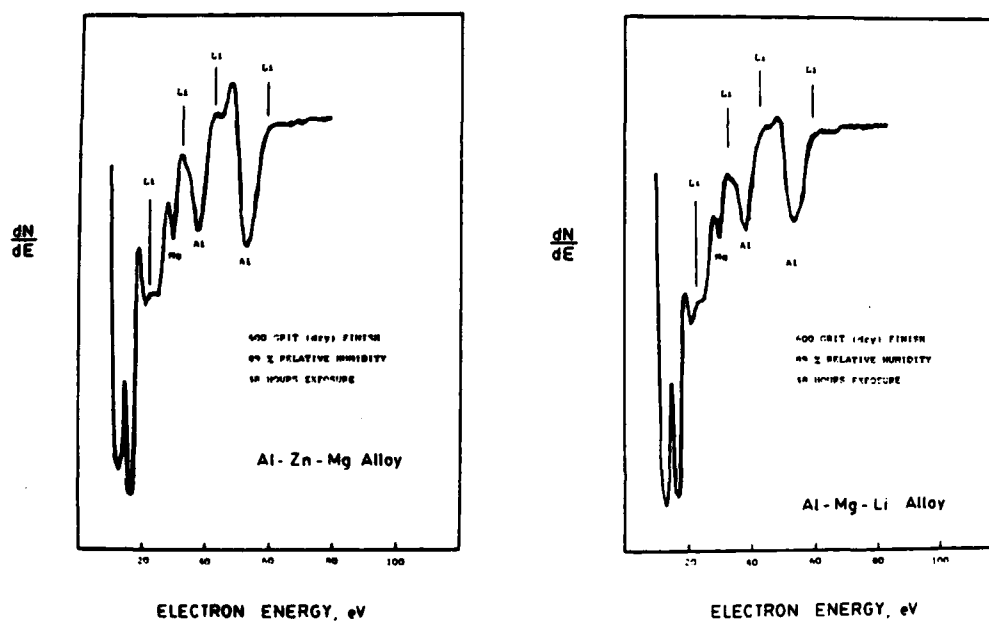


Figure 52

Auger electron spectroscopy of the surfaces of an Al-Zn-Mg alloy and an Al-Mg-Li alloy sample after exposure to humid air.

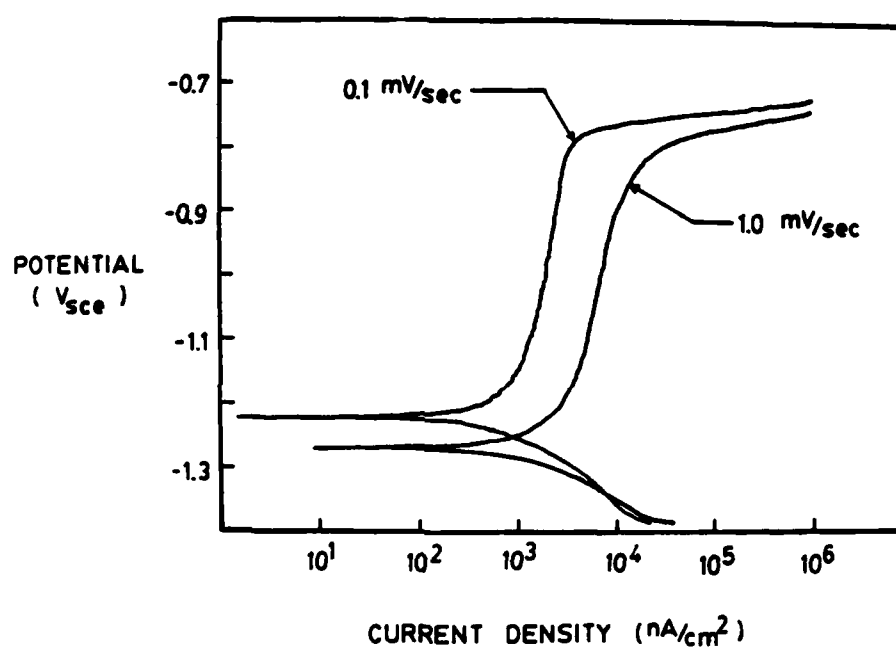


Figure 53

Effect of potentiodynamic scan rate on the polarization behavior of the Al-Mg-Li alloy in deaerated 0.5 M sodium chloride at 23°C.

the measured pitting and corrosion potentials of the alloys. The slower scan rate resulted in reproducibly lower current densities at a given potential, indicating that the achievement of a steady state passive film is time dependent. That is, the steady state thickness of the passive layer increases with increasingly noble potentials and film growth is time dependent. However, figure 53 shows that the pitting potential is not significantly altered by the increased scan rate.

Aeration: Aeration of the solutions reduced the passive current density and increased the free corrosion potential of the alloys to more noble potentials. The pitting potentials were essentially unchanged. Figure 54 shows the effect of aeration on the Al-Mg-Li alloy in 0.5 M sodium chloride solution. In the 7050 alloy this resulted in pitting either during the 30 minute exposure before the test or on passing the open circuit potential during the scan. The Al-Mg-Li alloys free corrosion potential also increased but not enough to result in pitting. Table VI lists the results of aeration tests compared to deaerated tests for sodium chloride solutions with varying pH.

pH: Increasing the pH of the solution reduced the corrosion potential of both alloys to more active potentials while not significantly altering the pitting potential for a fixed chloride ion concentration and temperature. The free

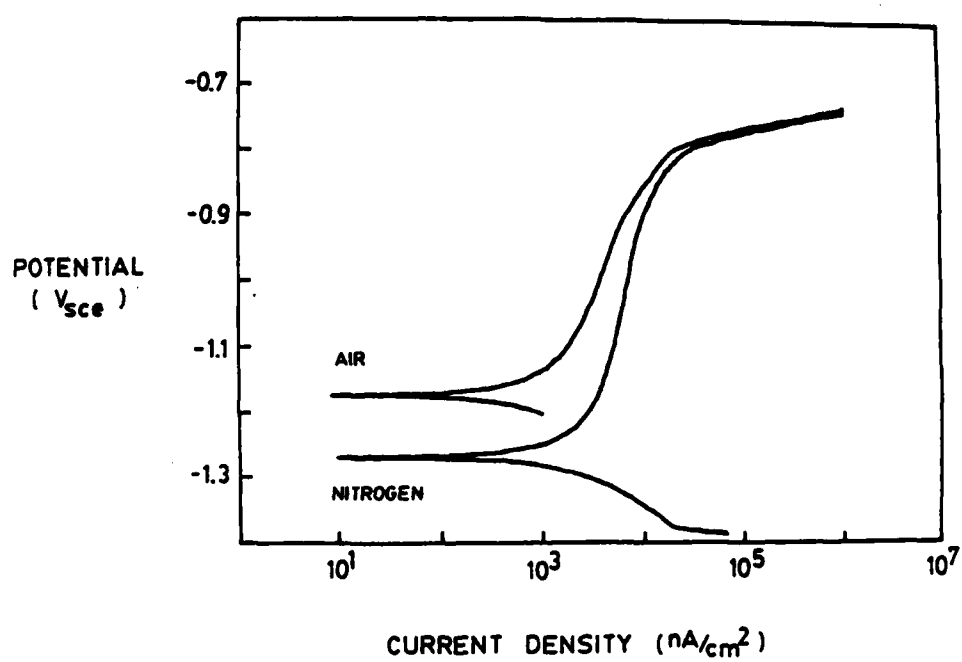


Figure 54

Effect of solution aeration on the polarization behavior of the Al-Mg-Li alloy in 0.5 M sodium chloride at 23°C and 1 mV/sec scan rate.

corrosion potential for the alloys in 0.5 M sodium chloride of pH 10, table VI, were similar. The free corrosion potentials were considerably different in neutral solutions and were closer again in aerated acidic solutions. Figure 55 shows the effect of varying the pH in 0.5 M sodium chloride solutions under deaerated and aerated conditions.

Temperature: Increasing the temperature reduced both the free corrosion potential and the pitting potential to more active potentials while increasing the passive current density. Figure 56 shows the effect of temperature on the polarization behavior of the alloys. In this figure, it can be seen that altering the temperature affected the alloys similarly, but that the pitting potential of the 7050 alloy shifted more as a function of temperature. Figure 57 shows the open circuit corrosion potential and pitting potential versus temperature for the alloys.

Chloride Ion Concentration: Chloride ions or other ionic species in the environment can cause pitting of these as well as other alloys. Accordingly, the pitting potential of the alloys varies with the concentration or activity of the ionic species present. Figure 58 shows the effect of chloride ion concentration on the polarization behavior of the Al-Mg-Li alloy. In figure 59, the chloride ion activity is plotted against the pitting and corrosion potentials. For this figure, the activities were calculated from the

Table VI: Effect of Aeration and pH on the Electrochemical Behavior of Aluminum Alloy 7075 and an Al-Mg-Li Alloy.

Alloy	Aeration	E_{corr}^1 (Vsce)	E_{pit}^2 (Vsce)	I_{pass}^3 ($\mu\text{A}/\text{cm}^2$)
(a) pH=2, 0.5 N sodium chloride				
7050	Nitrogen	-0.745	-0.738	---
	Air	-0.724	-0.709	---
Al-Mg-Li	Nitrogen	-1.052	-0.770	110
	Air	-0.798	-0.766	18
(b) Neutral pH, 0.5 N sodium chloride				
7050	Nitrogen	-0.728	-0.699	---
	Air	-0.726	-0.708	---
Al-Mg-Li	Nitrogen	-1.236	-0.805	7.3
	Air	-1.160	-0.789	4.4
(c) pH=10, 0.5 N sodium chloride				
7050	Nitrogen	-1.240	-0.712	4.3
Al-Mg-Li	Nitrogen	-1.342	-0.795	20
	Air	-1.364	-0.782	33

1. Free corrosion potential, measured before initiation of scan.
2. Breakdown potential, measured at intersection of extrapolated linear regions.
3. Measured at a potential half way between E_{corr} and E_{pit} .

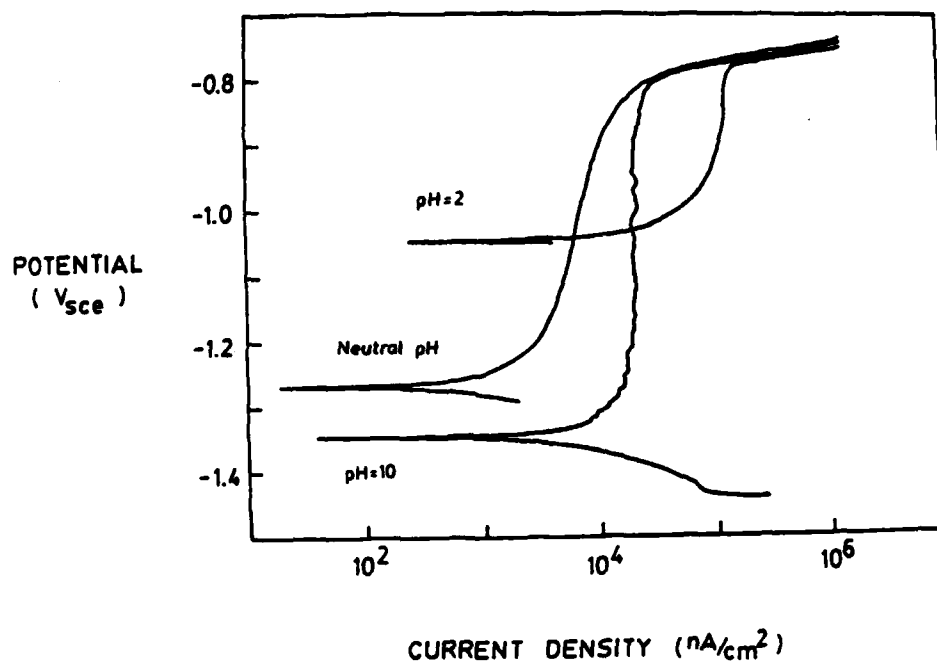


Figure 55(A)

Effect of pH on the polarization behavior of the Al-Mg-Li alloy in deaerated 0.5 M sodium chloride at 23°C and 1 mV/sec scan rate.

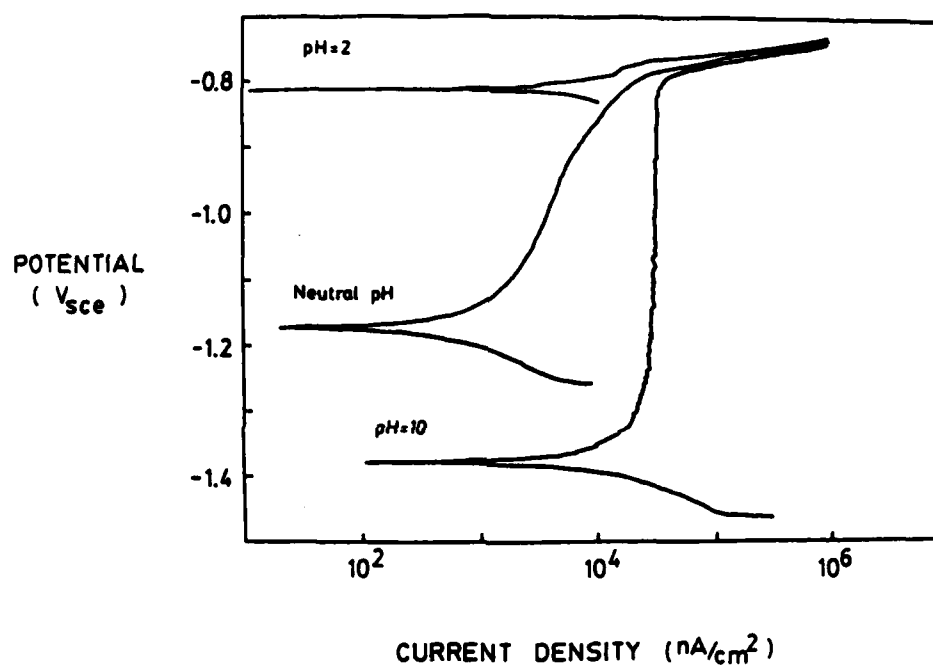


Figure 55(B)

Effect of pH on the polarization behavior of the Al-Mg-Li alloy in aerated 0.5 M sodium chloride at 23°C and 1 mV/sec scan rate.

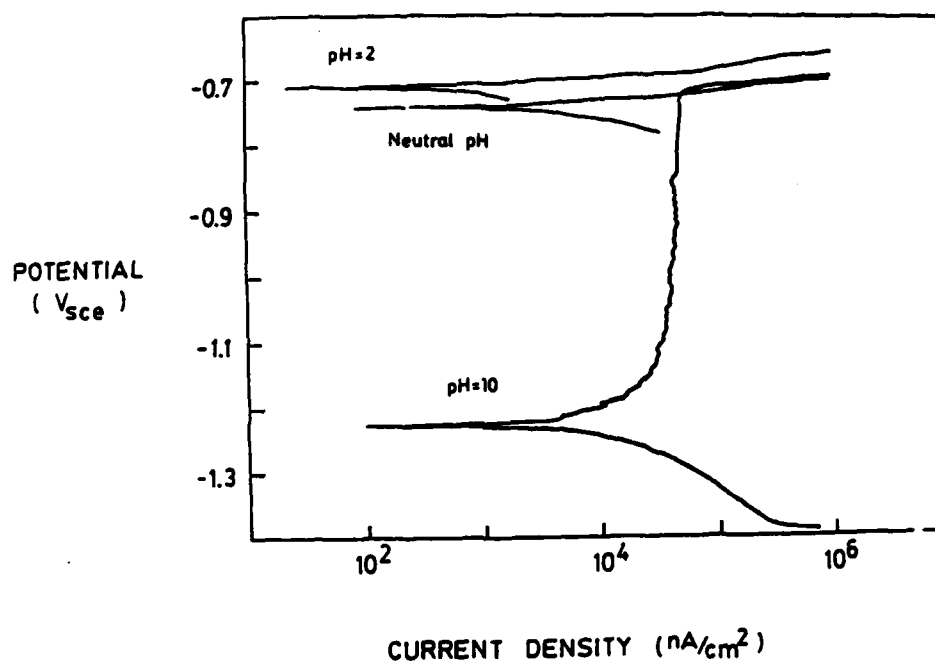


Figure 55(C)

Effect of pH on the polarization behavior of alloy 7050 in deaerated 0.5 M sodium chloride at 23°C and 1 mV/sec scan rate.

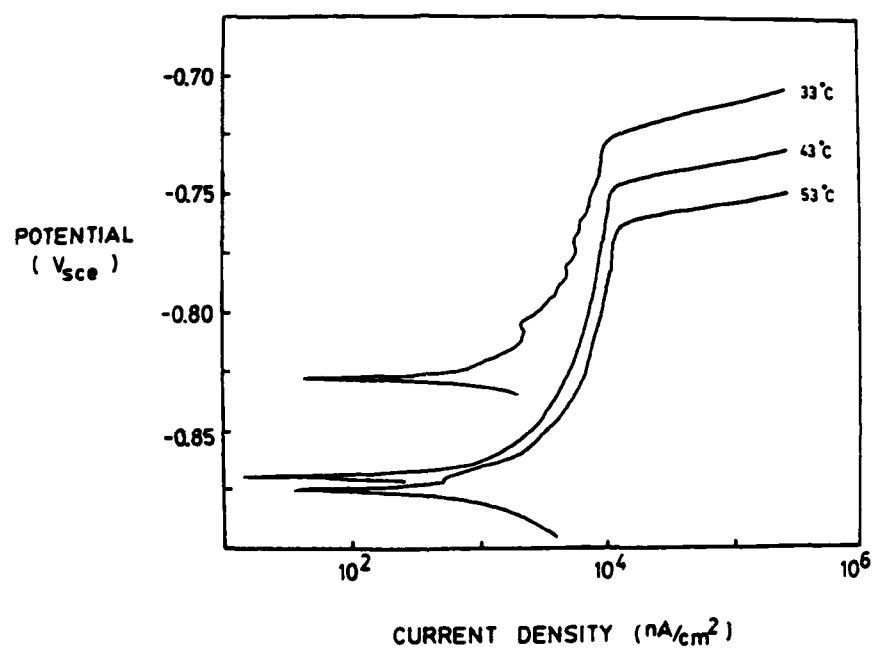


Figure 56(A)

Effect of temperature on the polarization behavior of alloy 7050 in deaerated 0.5 sodium chloride at 1 mV/sec scan rate.

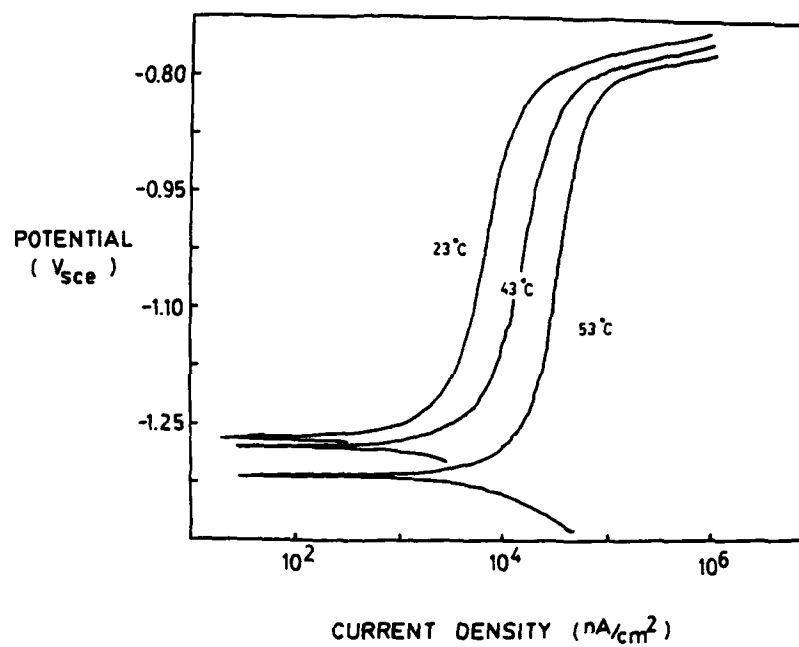


Figure 56(B)

Effect of temperature on the polarization behavior of the Al-Mg-Li alloy in deaerated 0.5 M sodium chloride at 1 mV/sec scan rate.

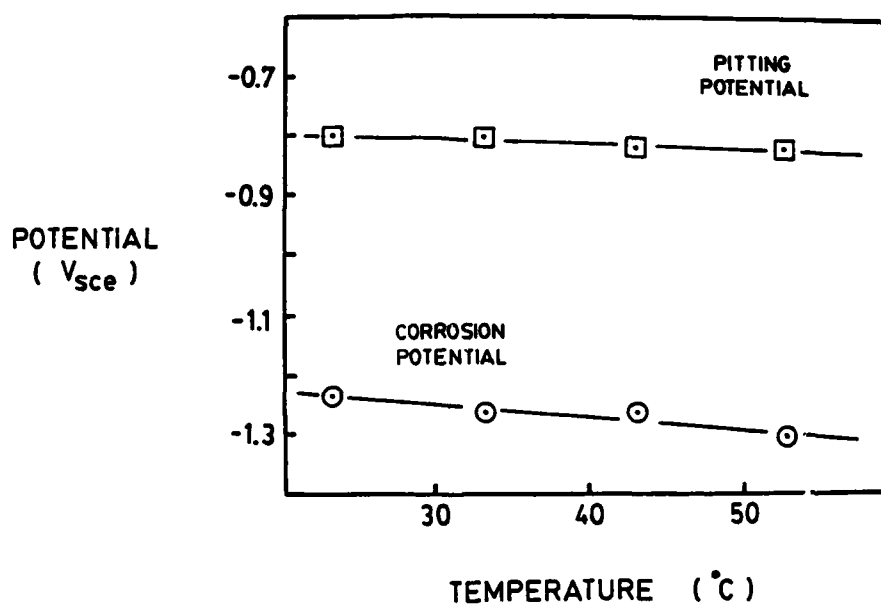


Figure 57(A)

Temperature versus the corrosion and pitting potentials for the Al-Mg-Li alloy in deaerated 0.5 M sodium chloride.

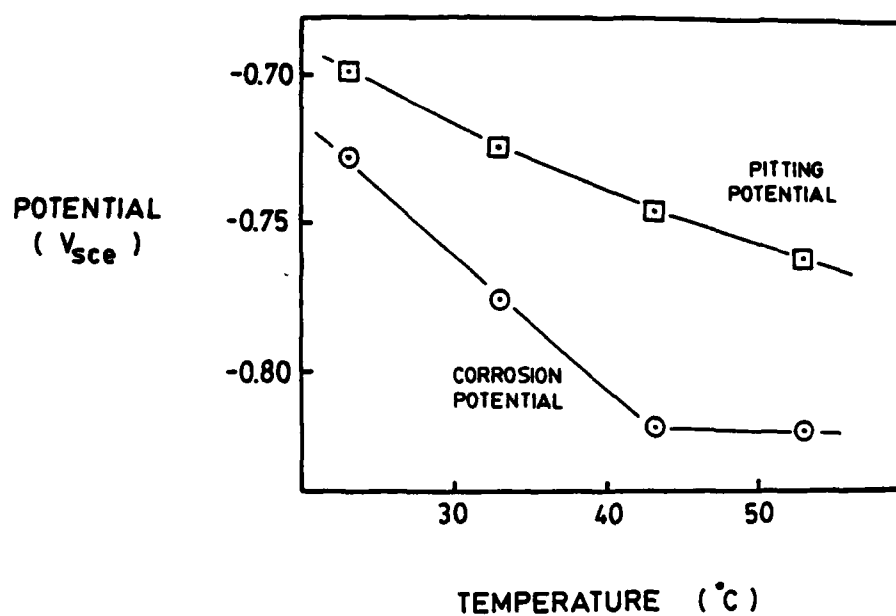


Figure 57(B)

Temperature versus the corrosion and pitting potentials for alloy 7050 in deaerated 0.5 M sodium chloride.

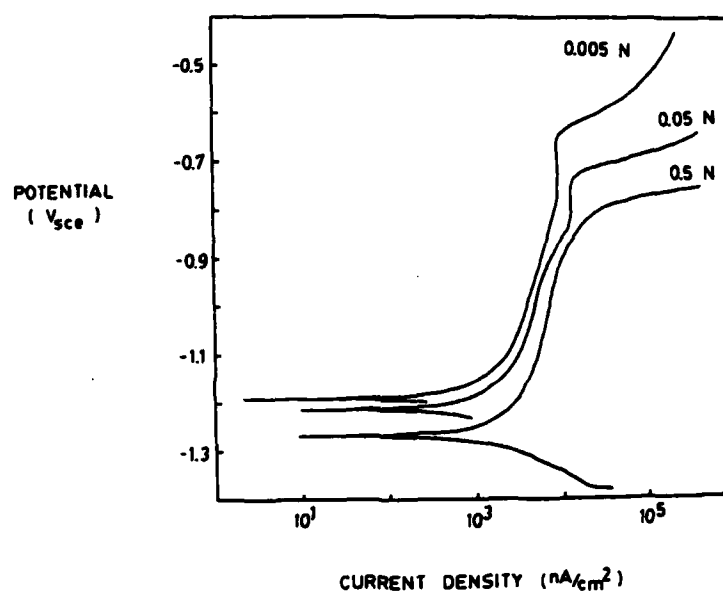


Figure 58(A)

Effect of chloride ion concentration on the polarization behavior of the Al-Mg-Li alloy in deaerated sodium chloride at 23°C and 1 mV/sec scan rate.

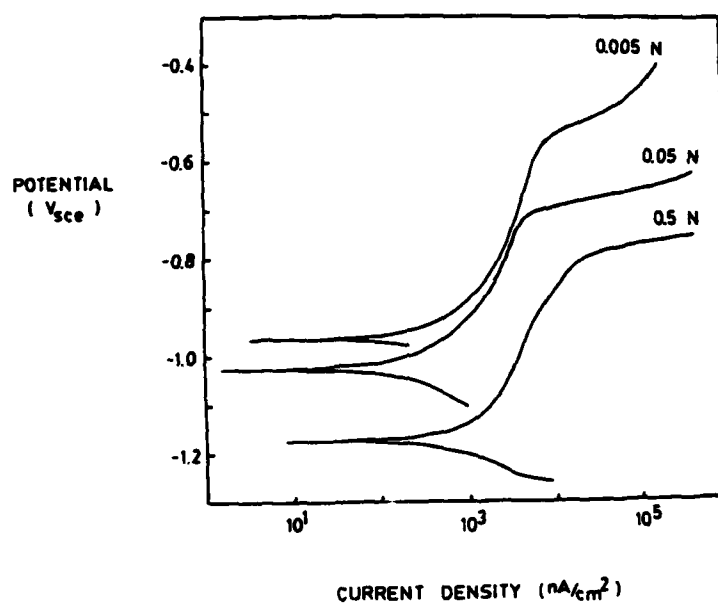


Figure 58(B)

Effect of chloride ion concentration on the polarization behavior of alloy 7050 in deaerated sodium chloride at 23°C and 1 mV/sec scan rate.

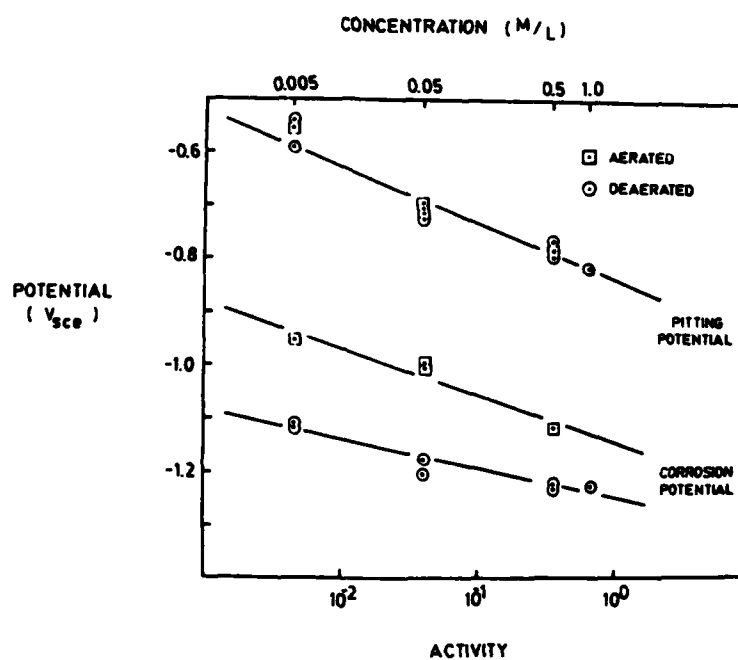


Figure 59

Chloride ion activity versus the pitting and corrosion potentials of the Al-Mg-Li alloy in aerated and deaerated sodium chloride solutions at 23°C.

concentrations using the activity coefficients of Latimer (141).

Dissolution Rates at Constant Potentials

The dissolution rates were determined from the weight loss measurements and are given in table VII. Figure 60 is a plot of the calculated dissolution rates versus the potentiostatically held constant electrochemical potential of the Al-Zn-Mg alloy in 0.5 M sodium sulfate and 0.5 M sodium chloride. From this figure, it can be seen that both anodic and cathodic polarization results in increased dissolution rates.

Figure 61 is a plot of the calculated dissolution rate versus the constant electrochemical potential of the measurements for the Al-Mg-Li ternary alloy. This alloy exhibits similar behavior to that of the Al-Zn-Mg ternary alloy except that the anodic and cathodic potentials where the corrosion rates increase rapidly were shifted slightly to more active potentials. This shift is in the direction but not in proportion to the shift in the free corrosion potentials. The difference in the free corrosion potentials of the two alloys is 400 to 500 mV but by comparing the two figures the difference in the potentials where the corrosion rate increases is less than 200 mV.

Table VII: Wt. Loss Measurements

(I) Al-Mg-Li Alloy in 0.5 N Na_2SO_4 , deaerated

$E(V_{sce})$	MDD	$E(V_{sce})$	MDD
-2.0	2860	-1.0	-9
-1.7	73.5	-0.2	53.5
-1.5	8.4	0	346

(II) Al-Mg-Li Alloy in 0.5 N NaCl, deaerated

$E(V_{sce})$	MDD	$E(V_{sce})$	MDD
-0.2	2370	-1.0	3.8
-1.8	156	-0.8	3.2
-1.6	10	-0.6	37820
-1.4	-36		

(III) Al-Zn-Mg Alloy in 0.5 N Na_2SO_4 , deaerated

$E(V_{sce})$	MDD	$E(V_{sce})$	MDD
-1.8	2785	-0.8	-4
-1.6	272	-0.4	47
-1.2	1.0	-0.2	64.3

(IV) Al-Zn-Mg Alloy in 0.5 N NaCl, deaerated

$E(V_{sce})$	MDD	$E(V_{sce})$	MDD
-0.2	4377.0	-1.0	2.04
-1.8	3219.6	-0.8	36,296
-1.6	167.8	-0.6	117,232
-1.4	3.815		

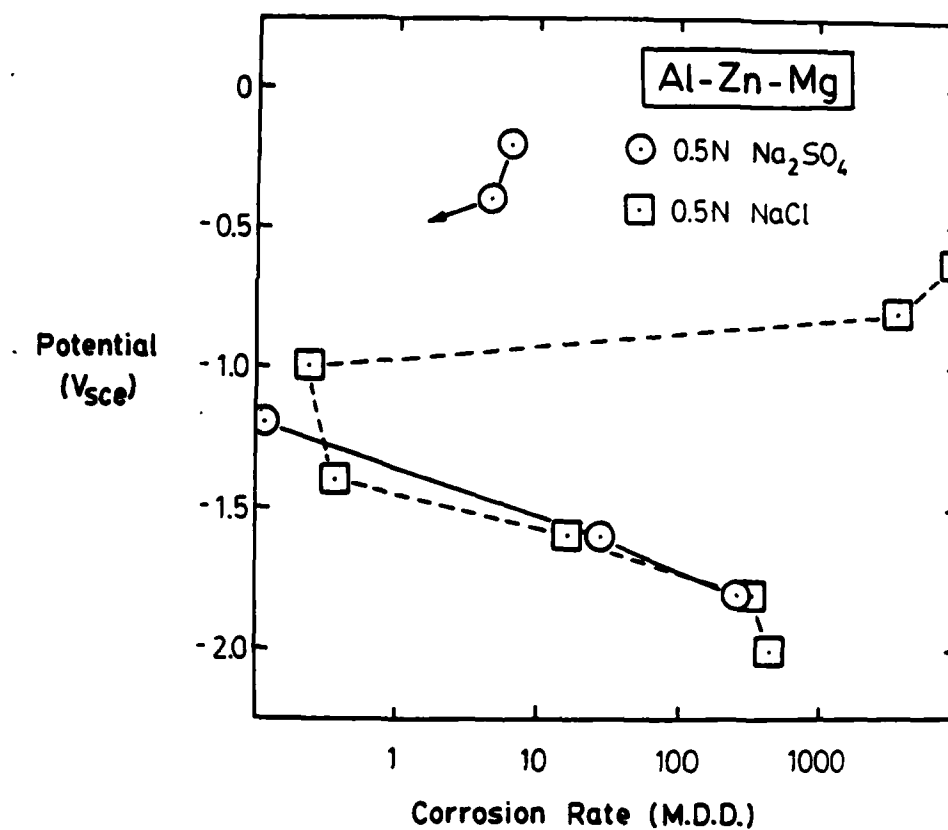


Figure 60

The dissolution rate determined from weight loss measurements for the Al-Zn-Mg ternary alloy in 0.5 M sodium sulfate and 0.5 M sodium chloride at constant electrochemical potentials.

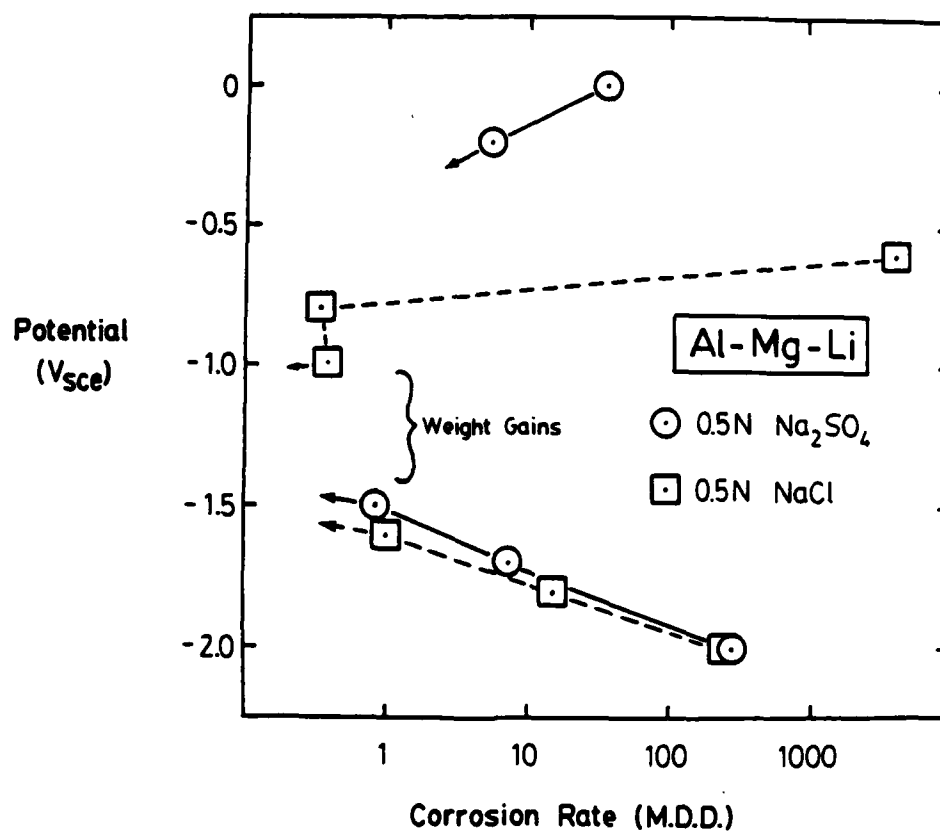


Figure 61

The dissolution rate determined from weight loss measurements for the Al-Mg-Li ternary alloy in 0.5 M sodium sulfate and 0.5 M sodium chloride at constant electrochemical potentials.

C. Corrosion Fatigue Tests

Corrosion fatigue tests were conducted in five different environments. All samples were stored in vacuum for at least one month prior to all tests except for those given special pre-exposure treatments which will be discussed in the appropriate sections.

Fatigue Tests in Dry Nitrogen Gas

Figure 62 is a plot of the cyclic strain range versus the cycles to failure of the Al-Zn-Mg ternary alloy and the Al-Mg-Li alloy in dry nitrogen after the standard vacuum pre-exposure. It is interesting that the two alloys fall into the same scatter band on the curve even though the yield strengths and the precipitate morphologies of the two alloys are different.

Fatigue Tests in Humid Nitrogen

Fatigue tests were conducted in humid nitrogen where the relative humidity was held at 87% after pre-exposure for at least a month to humid air at 87% relative humidity. The fatigue tests were performed in humid nitrogen so that the only difference between this test environment and the inert reference environment was one species (water vapor). The precharging was performed in air because special equipment would not be required for the extended exposure periods.

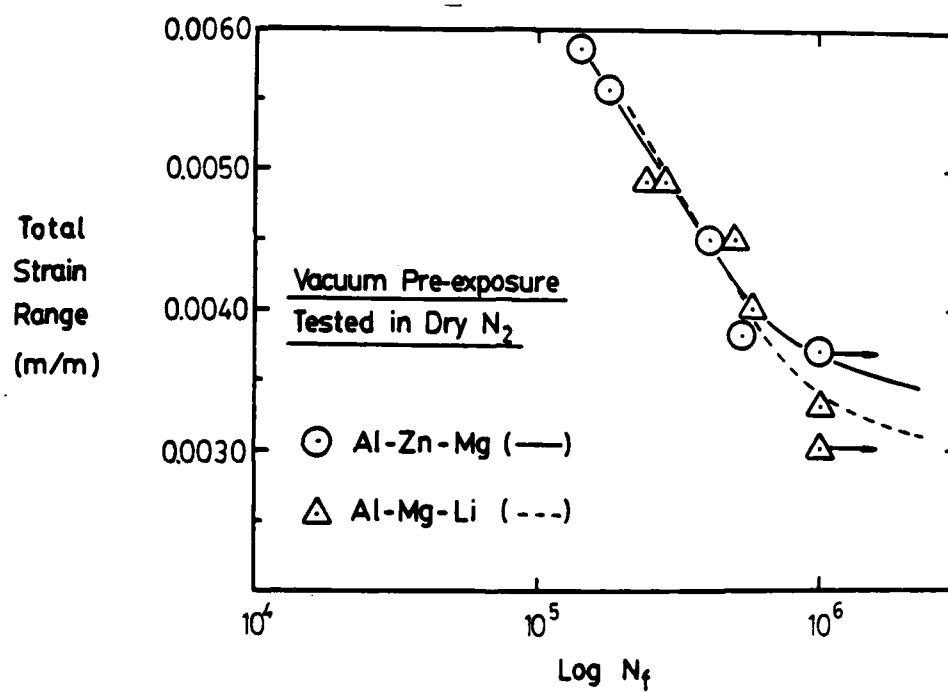


Figure 62

Cyclic strain range versus the cycles to failure for the Al-Zn-Mg alloy and the Al-Mg-Li alloy in dry nitrogen after vacuum pre-exposure.

The results of these tests are shown with the results of the tests in dry nitrogen for comparison in figure 63 for the Al-Zn-Mg ternary alloy and in Figure 64 for the Al-Mg-Li ternary alloy. In these figures a significant difference is noted in the behavior of the two alloys. The fatigue lives and the apparent fatigue limit were reduced for the Al-Zn-Mg alloy while the fatigue lives were reduced for the Al-Mg-Li alloy without any significant change in the apparent fatigue limit. It should be noted that these tests were conducted under strain control conditions and there is no true fatigue limit.

Effect of Pre-Exposure to Humid Air

The tests above were conducted after pre-exposure to humid air. As a result, experiments were performed on the Al-Zn-Mg alloy to determine if the pre-exposure to water vapor or if water vapor in the test environment was responsible for the reduced fatigue lives. First, a sample was tested in humid nitrogen which had not been exposed to water vapor and, as shown in figure 65, the same fatigue life was found for this sample as was found for samples tested after pre-exposure to humid air (represented by the dashed line in figure 65). Then, to determine if the pre-exposure step had any effect on fatigue lives, four samples were tested in dry nitrogen after a pre-exposure to

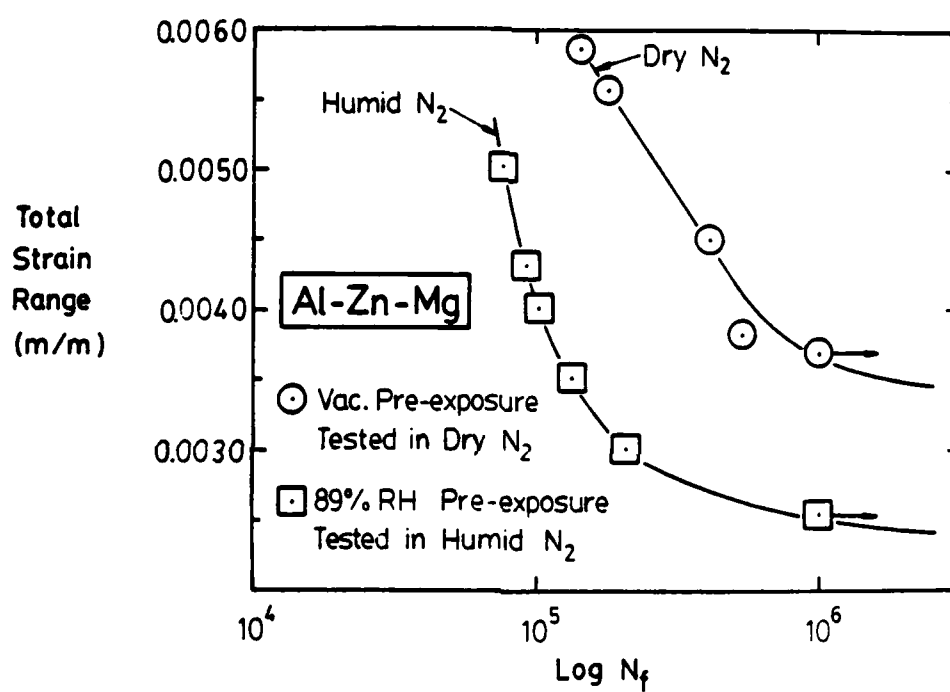


Figure 63

Cyclic strain range versus the cycles to failure for the Al-Zn-Mg alloy in humid and dry nitrogen.

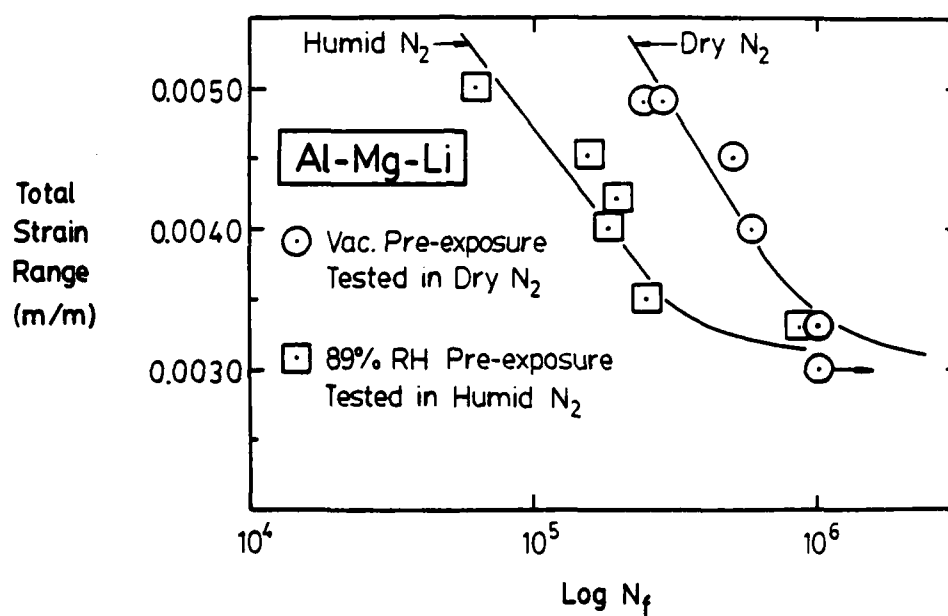


Figure 64

Cyclic strain range versus the cycles to failure for the Al-Mg-Li alloy in humid and dry nitrogen.

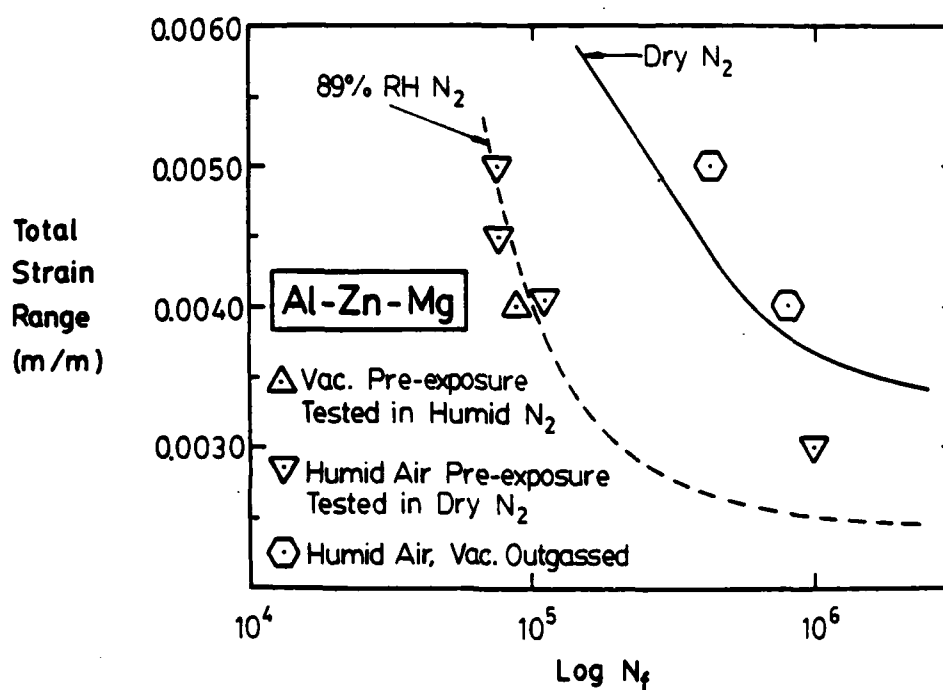


Figure 65

The effect of different pre-exposure and test environments on the fatigue lives of Al-Zn-Mg alloy samples as compared with testing in dry nitrogen after a vacuum pre-exposure (solid line) and with testing in humid nitrogen after a humid air pre-exposure (dashed line).

water vapor. These fatigue lives, illustrated by the triangles pointing upward in figure 65, were the same as the samples tested in humid nitrogen except for the lowest strain range where the time to failure becomes large enough for hydrogen desorption to occur. To determine if this pre-exposure effect was reversible, samples which had been exposed to humid air were placed in a vacuum for at least a month and tested in dry nitrogen. The fatigue lives of these samples, represented by the hexagons in figure 65, were the same as those of samples which had not been exposed to water vapor as represented by the solid line in figure 65. Therefore, the fatigue lives of the Al-Zn-Mg alloy are reversibly reduced ("embrittled") by exposure to water vapor either prior to fatigue loading or during loading.

Similar tests, as shown in figure 66, were conducted on the Al-Mg-Li alloy. As found in the Al-Zn-Mg alloy and represented by the triangles pointing upward in figure 66, the same fatigue lives were obtained in humid nitrogen when the pre-exposure to humid air was omitted. However, the samples tested in dry nitrogen after a pre-exposure to water vapor, represented by the downward pointing triangles of figure 66, had almost the same fatigue lives as those not pre-exposed to humid air as represented by the solid line in figure 66. Thus, the fatigue lives of the Al-Mg-Li alloy, in contrast to the Al-Zn-Mg alloy, are reduced by water

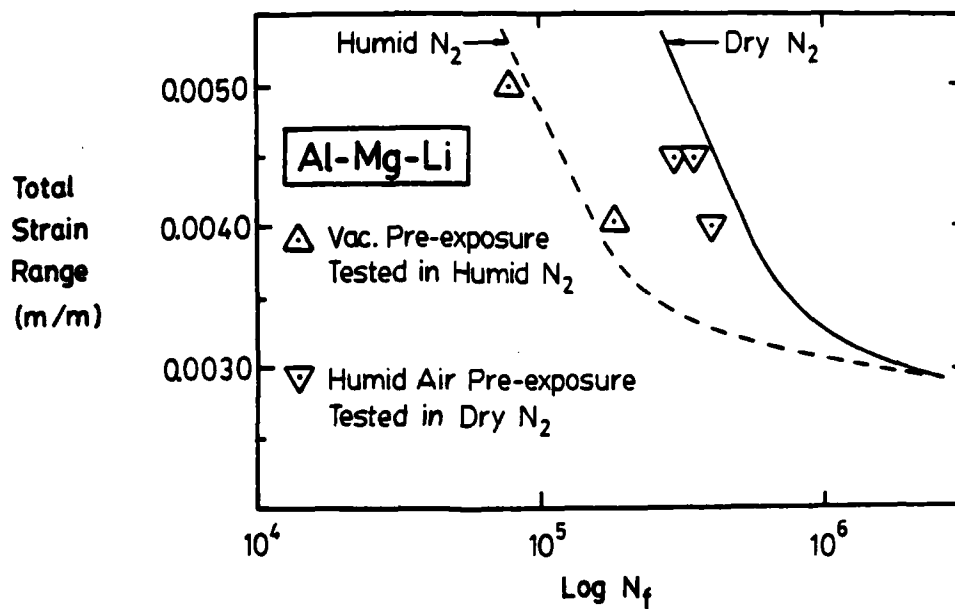


Figure 66

The effect of different pre-exposure and test environments on the fatigue lives of Al-Mg-Li alloy samples as compared with testing in dry nitrogen after a vacuum pre-exposure (solid line) and with testing in humid nitrogen after a humid air pre-exposure (dashed line).

vapor in the testing environment and not significantly influenced by pre-exposure.

If it is assumed that the initial variations in the fatigue lives of the Al-Zn-Mg samples with storage time in vacuum prior to testing in dry nitrogen was due to desorption of hydrogen from the samples, then these results can be reexamined. If a percent recovered fatigue life is calculated for these samples and plotted against the storage time in vacuum as shown in figure 67, a sigmoidal shape is observed. On this same figure is plotted the percent of hydrogen desorbed assuming different diffusion coefficients for hydrogen and using the desorption equations derived in appendix II. By comparing the curves and assuming that diffusion of hydrogen is the rate controlling parameter in the recovery process, it can be seen that the fatigue results indicate that the diffusion coefficient of hydrogen in the Al-Zn-Mg ternary alloy is approximately 1×10^{-9} cm.²/second. This compares well with the results of hydrogen diffusion coefficient determinations summarized in table V and with the adsorption data of Ciaraldi shown in figure 44 (80).

Free Corrosion Fatigue Tests

Figure 68 shows the fatigue lives of samples of the Al-Zn-Mg alloy under free corrosion conditions in pure

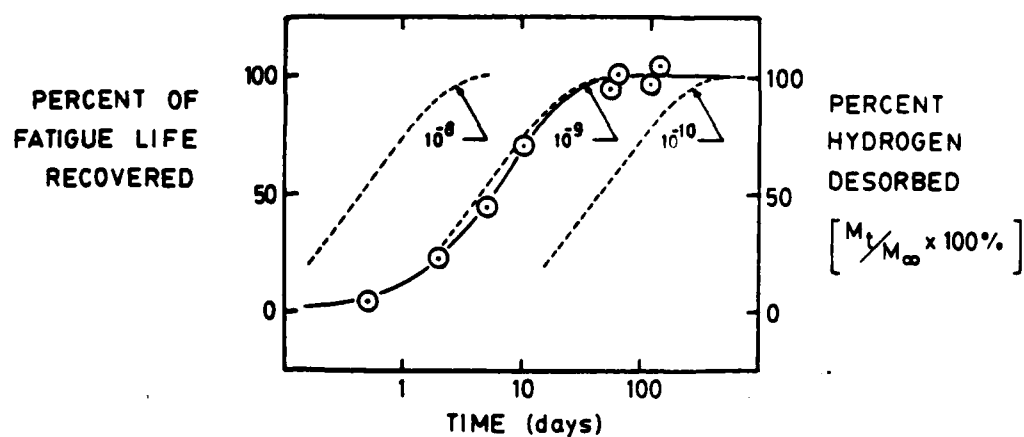


Figure 67

The effect of varying vacuum pre-exposure times on the percent of recovered fatigue life of samples of the Al-Zn-Mg ternary alloy.

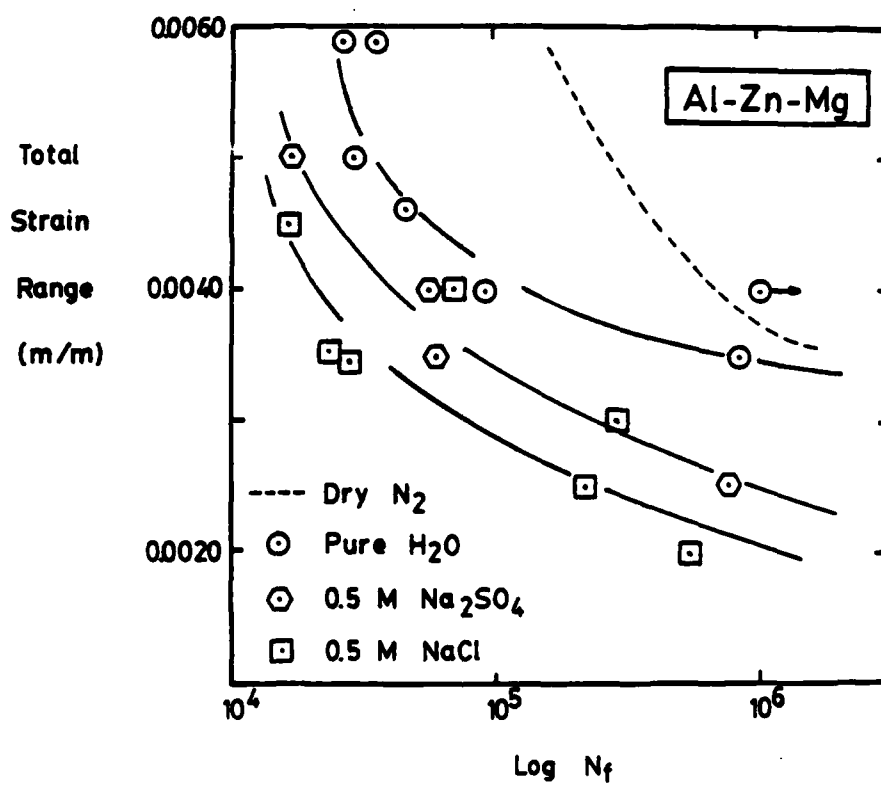


Figure 68

Cyclic strain range versus the cycles to failure for samples of the Al-Zn-Mg alloy in pure water, 0.5 M sodium sulfate and 0.5 M sodium chloride.

water, 0.5 M sodium sulfate and 0.5 M sodium chloride. From this figure, it can be seen that the greatest reduction in fatigue lives occurred in 0.5 M sodium chloride while the least reduction occurred in distilled water. However, for the Al-Mg-Li alloy, as shown in figure 69, the greatest reduction in the fatigue lives was observed in 0.5 M sodium sulfate and the least in distilled water.

Constant Electrochemical Potential Fatigue Tests

Fatigue tests were conducted on the two ternary alloys under constant electrochemical potentials in 0.5 M sodium chloride and sodium sulfate solutions. Figure 70 is a plot of the fatigue lives versus potential for samples of the Al-Zn-Mg alloy at a constant cyclic strain range of 0.0045 m/m (0.45%). This figure shows that anodic polarization was detrimental to the fatigue lives of the samples. The fatigue lives in the sodium chloride solution were reduced by more than an order of magnitude below the fatigue lives in the sodium sulfate solution. Cathodic polarization relative to the free corrosion potential initially extended the fatigue lives, but, greater polarization reduced the fatigue lives in both solutions. During cathodic polarization, essentially the same fatigue lives were measured in both solutions.

Figure 71 is a plot of the fatigue lives versus

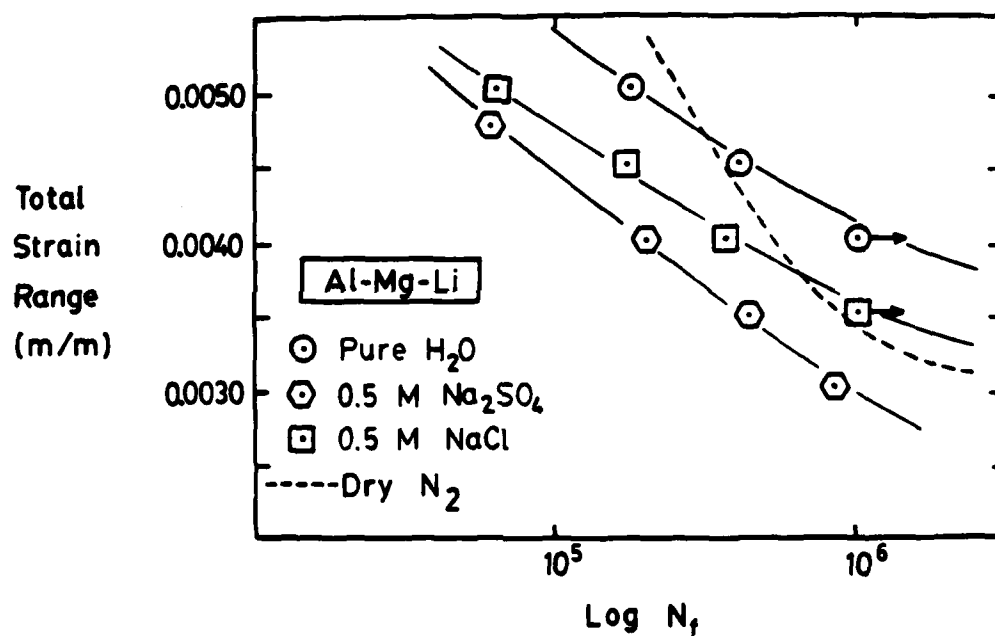


Figure 69

Cyclic strain range versus the cycles to failure for samples of the Al-Mg-Li alloy in pure water, 0.5 M sodium sulfate and 0.5 M sodium chloride.

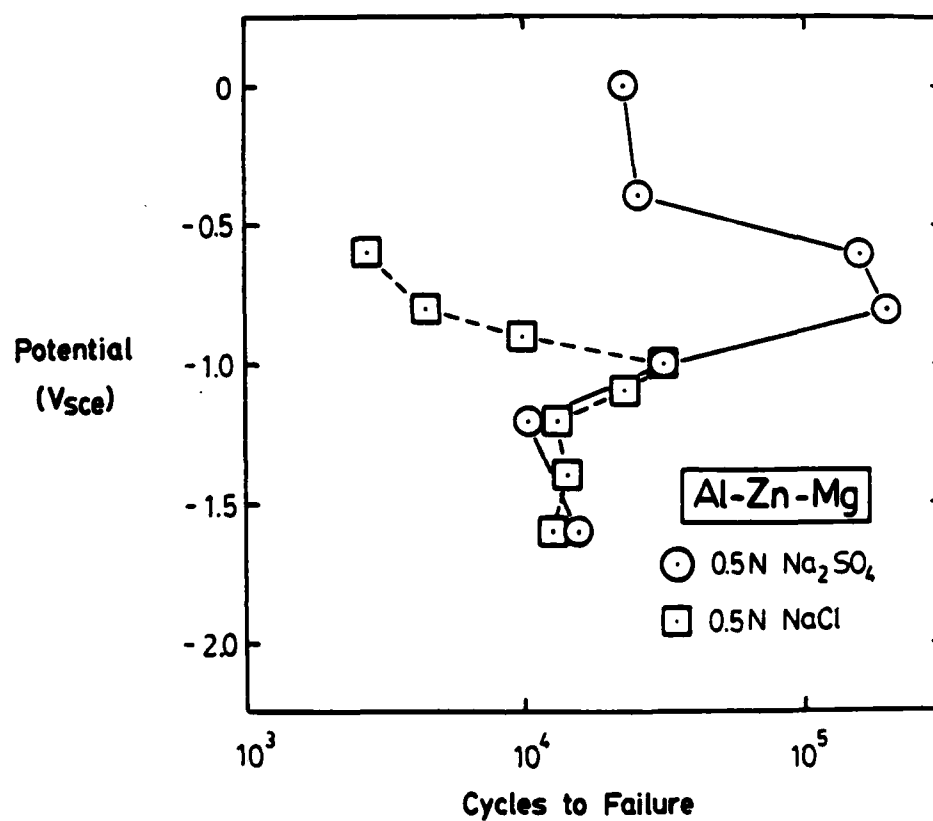


Figure 70

Fatigue life at a cyclic strain range of 0.0045 m/m (0.45%) versus the potentiostatically held constant electrochemical potential for samples of the Al-Zn-Mg alloy in 0.5 M sodium sulfate and 0.5 M sodium chloride.

potential for samples of the Al-Mg-Li alloy at a constant cyclic strain of 0.0045 m/m (0.45%). Similar to the Al-Zn-Mg alloy, anodic polarization reduced the fatigue lives in both solutions and sodium chloride was the more detrimental electrolyte. However, the difference between the fatigue lives in the two solutions was not as great for this alloy. Again, cathodic polarization initially improved fatigue lives but greater cathodic currents and lower potentials resulted in reduced fatigue lives.

It was reported earlier that at the free corrosion potential the Al-Mg-Li alloy demonstrated greater fatigue lives in 0.5 M sodium chloride than in sodium sulfate. The potential was monitored during the free corrosion tests and was found to fall between -1.05 Vsce and -1.25 Vsce for both the sodium chloride solution and the sodium sulfate solution. This is in the region where the fatigue lives versus electrochemical potential curves for each electrolyte converge. Sodium chloride could have caused the improvement in fatigue lives by either promoting passivation, by the formation of insoluble salts, or by blunting crack tips and removing crack nuclei by dissolution. In this potential range, fatigue lives are very sensitive to the electrochemical potential. If sodium chloride increased anodic activity at inclusions and/or other sites, the remainder of the sample would have been slightly

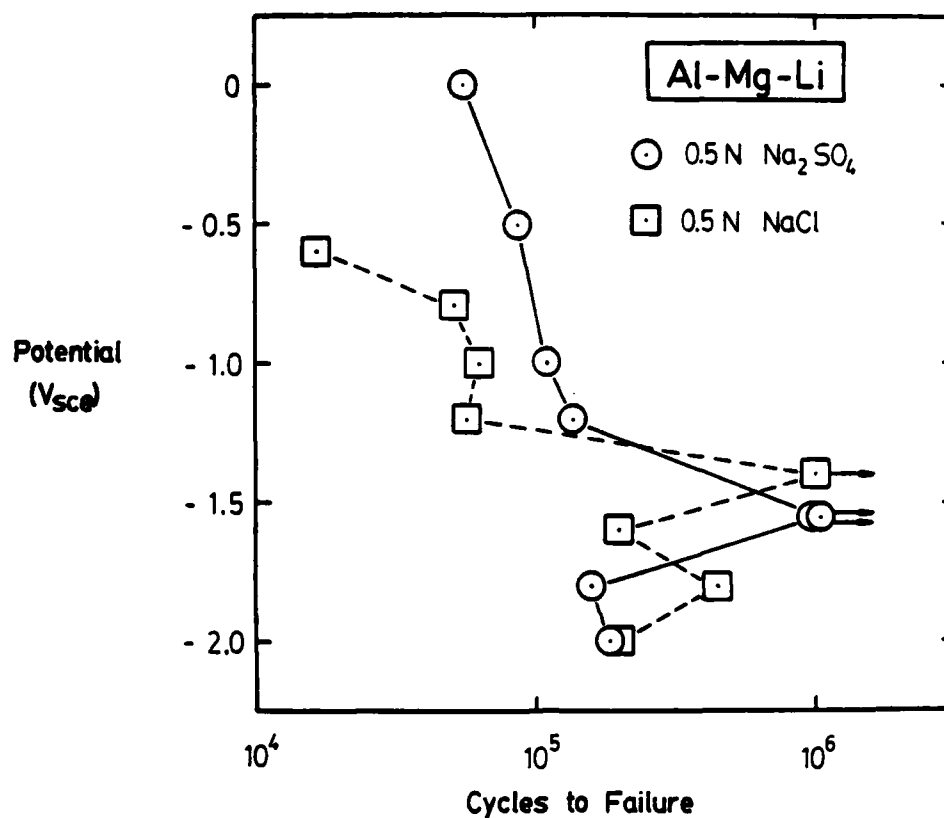


Figure 71

Fatigue life at a cyclic strain range of 0.0045 m/m (0.45%) versus the potentiostatically held constant electrochemical potential for samples of the Al-Mg-Li alloy in 0.5 M sodium sulfate and 0.5 M sodium chloride.

cathodically polarized. If the increased anodic activity did not contribute to fatigue process, then the slight cathodic polarization would have increased the fatigue lives of the samples.

Linear Regression Analysis

Strain control fatigue lives are frequently plotted against the logarithm of the cyclic strain range to yield straight lines. This type of analysis had been studied by Coffin (150-153) and Manson (154-156). This work has resulted in an equation for representing the fatigue lives in terms of the summation of elastic and plastic strain contributions to the total cyclic strain which is given in Appendix III. Since the maximum bending stresses of the fatigue tests were below the yield stress of each alloy, the plastic strains can be approximated as zero and the results analyzed in terms of the low strain amplitude or elastic part of the summation sometimes called the Basquin equation (149-162). The technique used for this analysis is explained more completely in Appendix III.

Figure 72 shows the results of plotting the log of the strain range versus the log of the cycles to failure of the Al-Zn-Mg alloy in the test environments with the linear regression lines through the data points. Similarly, figure 73 shows the results of the tests on the Al-Mg-Li alloy

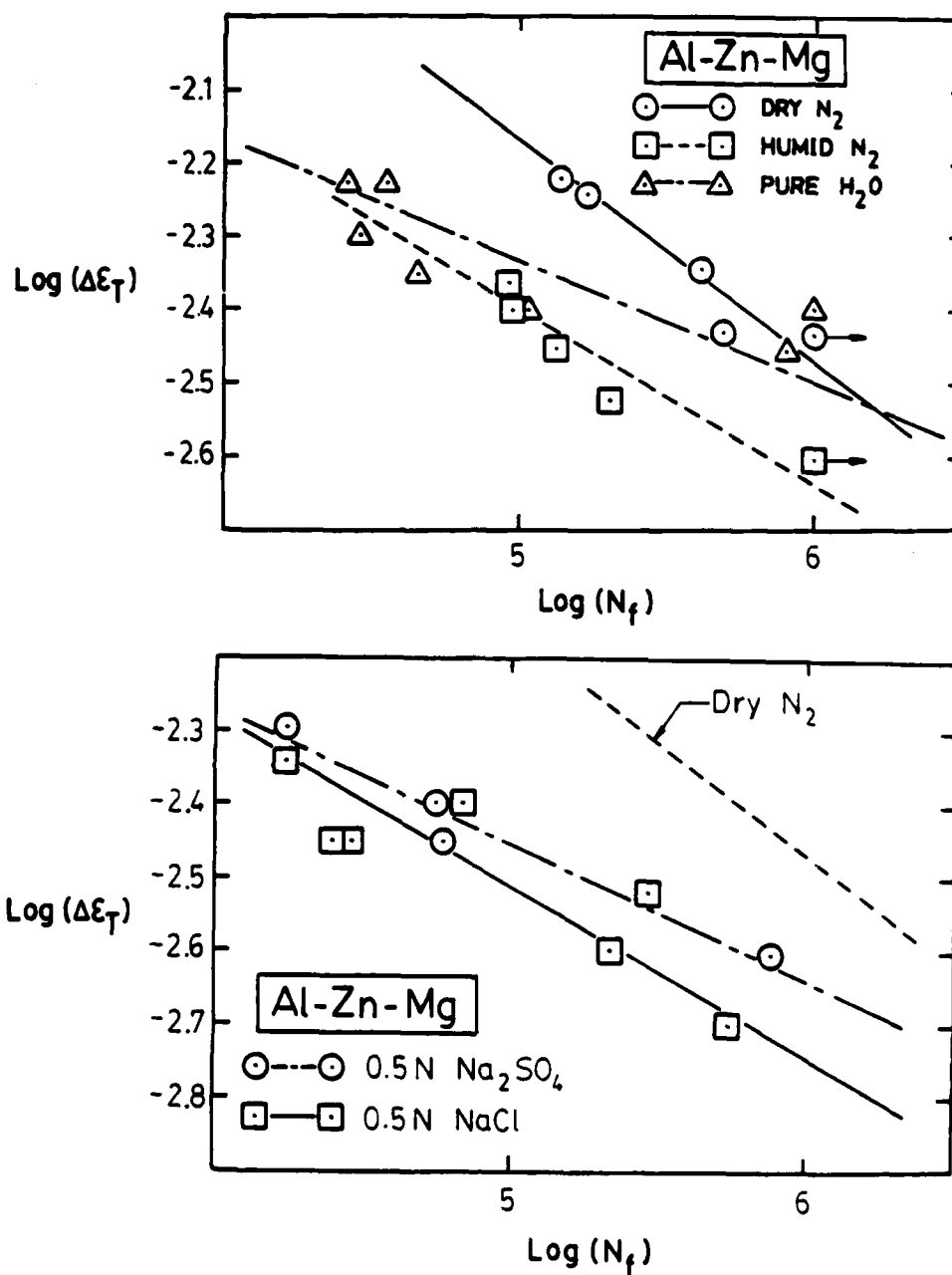
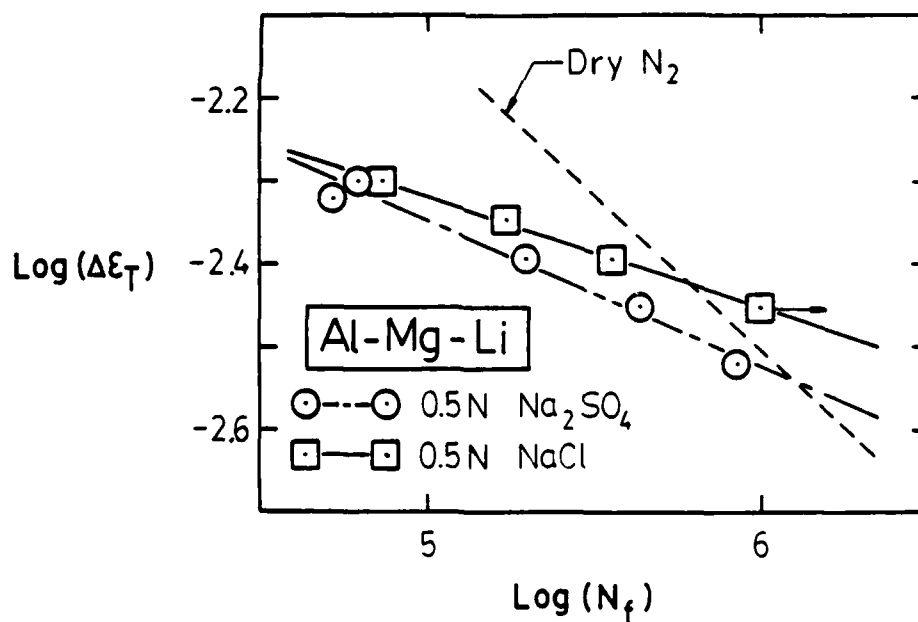
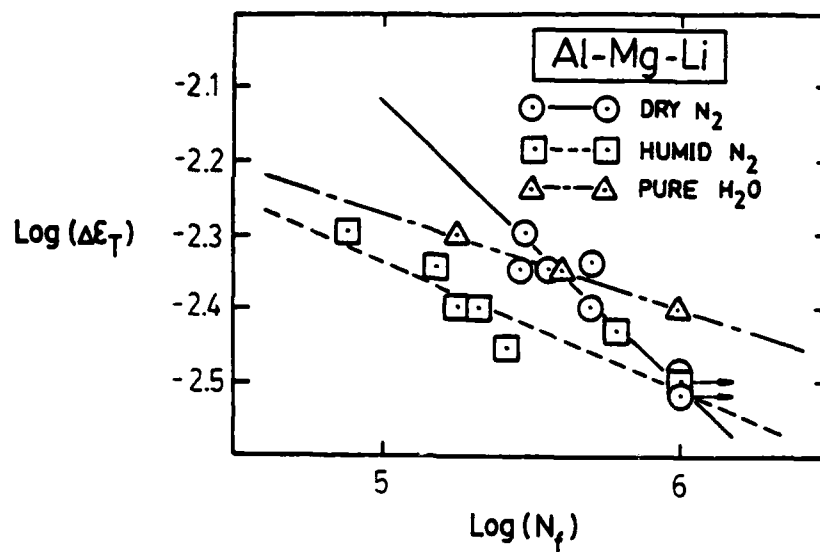


Figure 72

Linear regression analysis of the logarithm of the cyclic strain range versus the logarithm of the cycles to failure for the Al-Zn-Mg alloy in dry nitrogen, humid air, pure water, 0.5 M sodium sulfate and 0.5 M sodium chloride.



Linear regression analysis of the logarithm of the cyclic strain range versus the logarithm of the cycles to failure for the Al-Mg-Li alloy in dry nitrogen, humid air, pure water, 0.5 M sodium sulfate and 0.5 M sodium chloride.

plotted this way with the lines of linear regression for the data.

Table VIII gives the results of the linear regression analysis and the values determined for the fatigue strength coefficient and the strain axis intercept. Morrow et. al. (157,158) mathematically modeled the strain controlled fatigue lives and related the fatigue strength exponent (b) to the cyclic strain hardening coefficient (n') as:

$$b = \frac{-n'}{1+5n'} \quad [1]$$

Similarly, the fatigue strength coefficient (σ_f') is determined from the one cycle strain axis intercept ($\Delta\epsilon_{0.1}$) with the modulus of elasticity (E) according to the relationship:

$$\Delta\epsilon_{0.1} = \frac{\sigma_f'}{E} \quad [2]$$

This fatigue strength coefficient (σ_f') has been found to be approximately equal to the monotonic fracture strength (σ_f) of the sample. Also, the cyclic strain hardening coefficient (n') is approximately the same as the monotonic strain hardening coefficient (n). According to this generally accepted interpretation of the coefficient and

Table VIII: Linear Regression Analysis of the Low Amplitude Strain Controlled Corrosion Fatigue Results (see Appendix III).

Al-Zn-Mg TERNARY ALLOY

ENVIRONMENT	DATA POINTS	CORRELATION COEFFICIENT	SLOPE	INTERCEPT	FATIGUE STRENGTH EXPONENT "b"	FATIGUE STRENGTH COEFFICIENT σ_f'	ESTIMATED n'	Δc for $N_f \sim 10^5$
Dry N_2	5	-.9498	-3.317	-2.204	+3.015	15.5 GPa	0.1202	.00676
Humid N_2	5	-.9386	-4.213	-5.124	+2.374	4.36	0.1086	.00396
Water	7	-.8133	-6.091	-9.223	+1.642	2.19	0.0902	.00463
0.5M Na_2SO_4	4	-.9756	-5.383	-8.223	+1.858	2.13	0.0963	.00350
0.5M NaCl	7	-.8690	-4.248	-5.682	+2.354	3.30	0.1081	.00305

Al-Mg-Li TERNARY ALLOY

ENVIRONMENT	DATA POINTS	CORRELATION COEFFICIENT	SLOPE	INTERCEPT	FATIGUE STRENGTH EXPONENT "b"	FATIGUE STRENGTH COEFFICIENT σ_f'	ESTIMATED n'	Δc for $N_f \sim 10^5$
Dry N_2	7	-.9211	-2.595	-.5052	+3.854	49.8 GPa	.1317	.00756
Humid N_2	7	-.8909	-5.749	-8.429	+1.739	2.67	.0930	.00462
Water	3	-.9998	-7.730	-12.536	+1.294	1.86	.0786	.00538
0.5M Na_2SO_4	5	-.9893	-5.668	-8.330	+1.764	2.64	.0937	.00445
0.5M NaCl	4	-.9974	-7.522	-12.467	+1.329	1.72	.0798	.00476

exponent of the Basquin equation, the results of the fatigue tests demonstrate that the aggressive environments are simultaneously reducing the fracture strength and the work hardening rate of the samples. The scatter of the results, as indicated by the correlation coefficients, is increased in environments where crack initiation is more random. More testing would reduce the error in the estimates of the fatigue strength exponents and coefficients; however, the trend to reduced fracture strengths and reduced work hardening coefficients with testing in aggressive environments is firmly established.

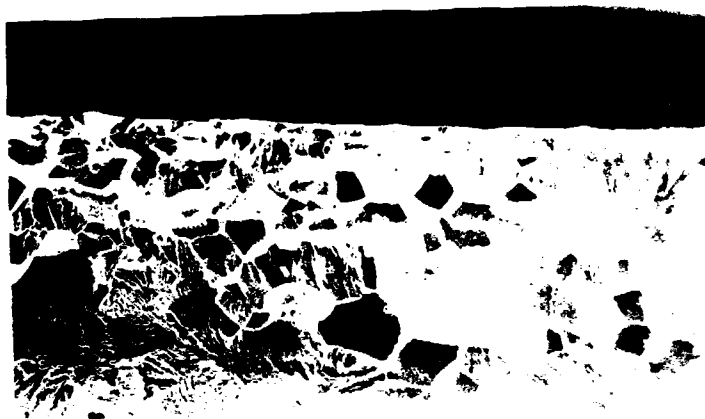
D. Fractography

A scanning electron microscope was used to examine the fracture surfaces of the specimens. In each of the figures, the macroscopic direction of crack propagation is from the bottom of the page to the top unless specified otherwise.

Al-Zn-Mg Ternary Alloy

The fracture surfaces of the Al-Zn-Mg alloy samples were examined and regions of both intergranular and transgranular crack propagation were observed on samples tested in each environment. The relative percentage of each type of fracture morphology varied with the aggressiveness of the environment and the magnitude of the cyclic strain range.

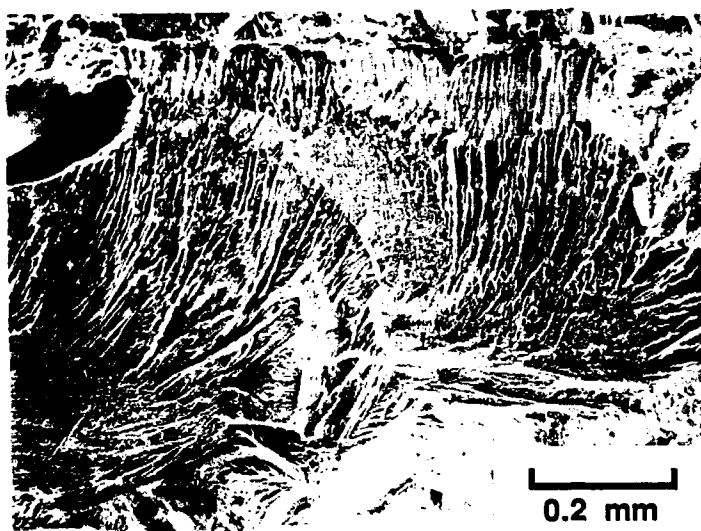
Dry Nitrogen: Figure 74 shows regions of both intergranular and transgranular crack propagation on the fracture surface of a sample tested in dry nitrogen. This mixed propagation was typical of samples tested in this environment. However, some trends could be distinguished. The transgranular cleavage-like ("TCL") crack propagation was more common in areas of above average grain size and lower stress intensities (smaller crack lengths and lower alternating strains). Figure 75 shows an area which demonstrates almost entirely this type of propagation. In this figure, the individual grains can be identified where crack propagation changed from grain to grain. Figure 76 shows a transition from one grain with small cleavage-like facets to a grain with large cleavage-like facets. The facets are shown at a higher magnification in figures 77 and 78. In the region of small facets, figure 77, the surface appears as small hillocks with very small striations. These striations are 80 to 190 nm apart which corresponds to a crack propagation velocity for this region of about 1.4×10^{-7} meters/cycle. In the area of large facets, shown in figure 78, the surface is composed of large, flat, and parallel cleavage like areas which are covered with very small striations. These striations are similar to those shown in figure 77 and are 100 nm apart which corresponds to a crack propagation velocity of 1×10^{-7} meters/cycle. The regions



0.3 mm

Figure 74

The fatigue fracture surface of a sample of the Al-Zn-Mg alloy tested in dry nitrogen (50X).



0.2 mm

Figure 75

The transgranular cleavage-like fracture morphology of the Al-Zn-Mg alloy tested in dry nitrogen (100X).



Figure 76

Comparison of the transgranular cleavage-like fracture in two grains of an Al-Zn-Mg alloy sample tested in dry nitrogen (500X).

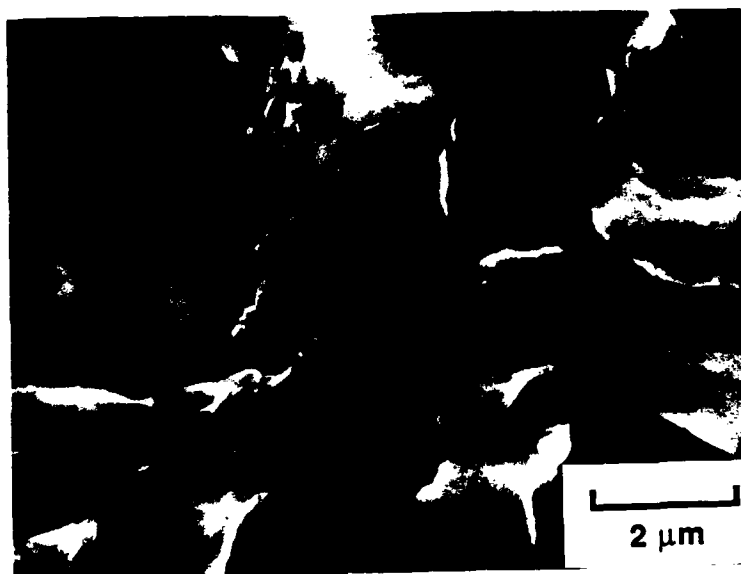


Figure 77

A region of transgranular cleavage-like fracture of an Al-Zn-Mg alloy sample tested in dry nitrogen (10,000X).

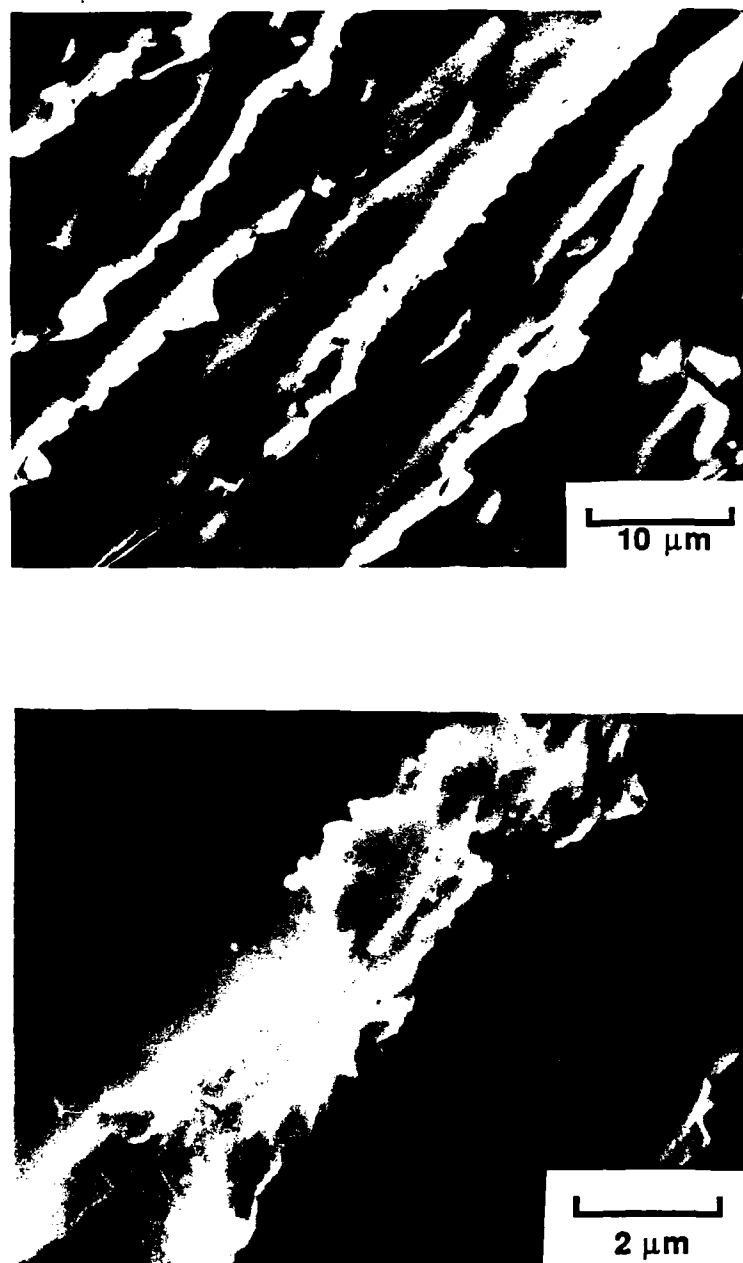
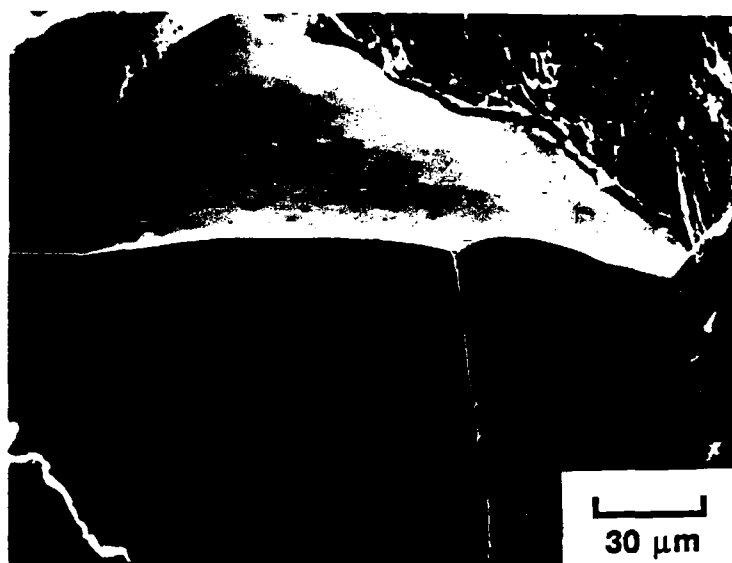
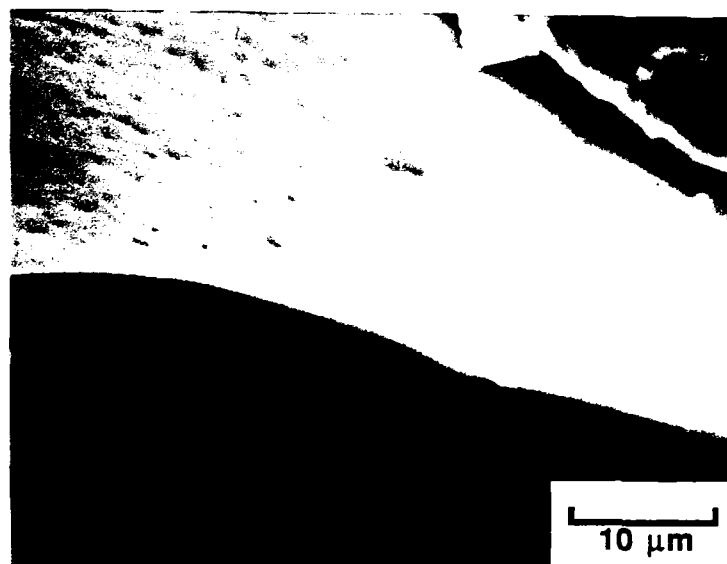


Figure 78

A region of transgranular cleavage-like fracture of an Al-Zn-Mg alloy sample tested in dry nitrogen; A) 2,000X, B) 10,000X.



[A]



[B]

Figure 79

The intergranular fracture surface of a sample of the Al-Zn-Mg alloy tested in dry nitrogen; A) 500X, B) 2,000X.

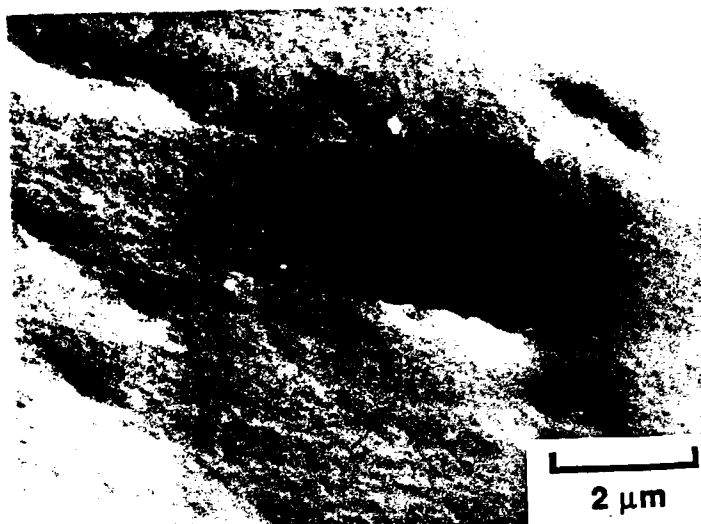


Figure 80

The intergranular fracture surface of a sample of the Al-Zn-Mg alloy tested in dry nitrogen (10,000X).

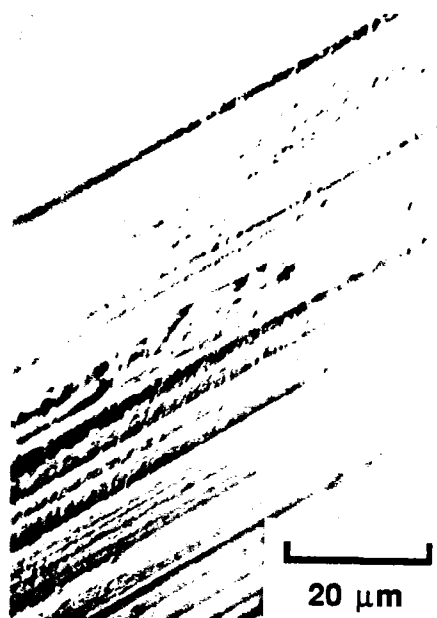


Figure 81

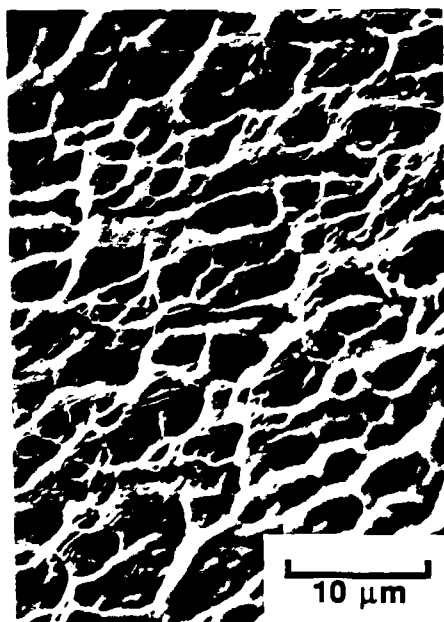
Stage 1 crack propagation of a sample of the Al-Zn-Mg alloy tested in dry nitrogen (50X).

Figure 82

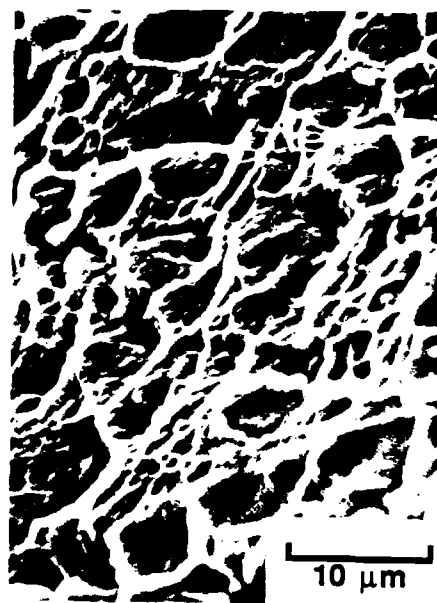
The morphology of three regions of stage 1 propagation in an Al-Zn-Mg alloy sample tested in dry nitrogen; A) 1,000X, B) 2,000X, C) 2,000X.



[A]



[B]



[C]



Figure 83

A crack initiation site for the fatigue fracture of a sample of the Al-Zn-Mg alloy tested in dry nitrogen (1,000X).



Figure 84

An intergranular region at the initiation site of the fatigue fracture of an Al-Zn-Mg alloy sample tested in dry nitrogen (500X).

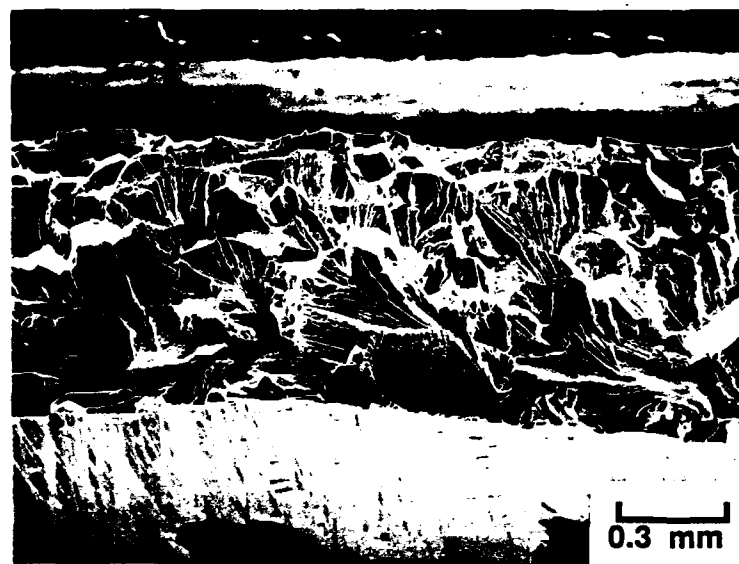


Figure 85

The fracture surface of a sample of the Al-Zn-Mg alloy tested in humid nitrogen (50X).

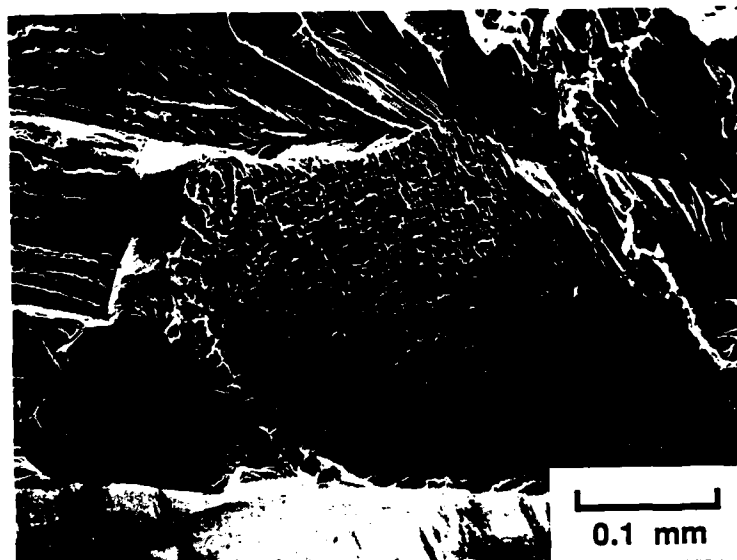


Figure 86

The fracture surface of a sample of the Al-Zn-Mg alloy tested in humid nitrogen (200X).

figure 74. However, an increase was observed in the intergranular cracking at low stress intensities and near crack initiation as shown in figure 86.

The transgranular cleavage-like fracture is similar to that observed in dry nitrogen except that, as shown in figure 87 and 88, the surfaces are flatter and smoother indicating increased cleavage. It is difficult to compare these figures to figures 87 and 88 because of unknown changes in the orientation, stress intensity, and propagation rate, but the impression is that the crack propagation in this environment was less ductile. The intergranular fractures surfaces in this environment appeared identical to the intergranular fracture surfaces in dry nitrogen, figure 89.

The external surface of an Al-Zn-Mg alloy fatigue sample tested in humid nitrogen is shown in figure 90. From this figure, it can be seen that water vapor causes cracking and blistering of the surface film. These ruptures in the surface film are essentially the same as those reported by Scamans et. al. (97-89) and shown in figure 24. Presumably, this behavior was responsible for allowing hydrogen entry into the metal.

Pure Water: The tests in the pure water environment resulted in fractures with increased intergranular cracking and secondary intergranular cracks as shown in figure 91.

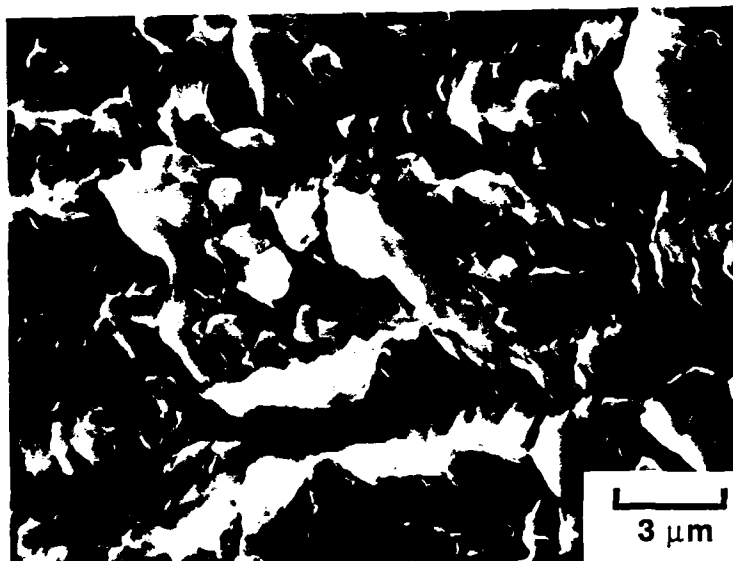


Figure 87

The transgranular cleavage-like fracture surface of a sample of the Al-Zn-Mg alloy tested in humid nitrogen (5,000X).

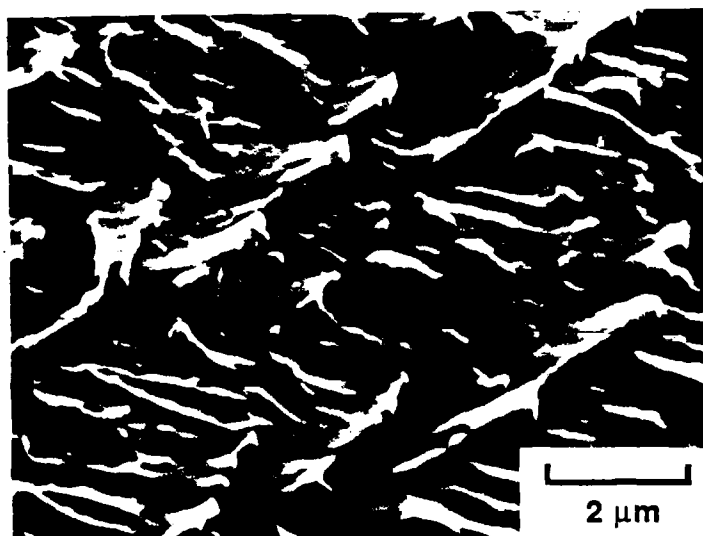


Figure 88

A region of transgranular fracture of a sample of the Al-Zn-Mg alloy tested in humid nitrogen (10,000X).

AD-A162 627 CORROSION FATIGUE OF Al-ZN-MG AND Al-MG-LI ALLOYS

3/3

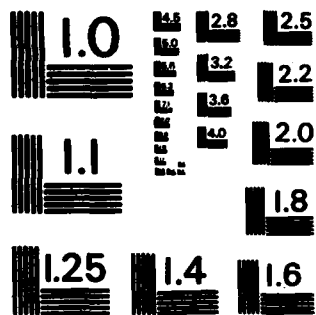
**CORROSION FATIGUE OF Al-ZN-MG AND AND Al-MG-LI
(U) RENSSELAER POLYTECHNIC INST TROY NY DEPT OF
MATERIALS ENGINEERING R E RICKER ET AL. JAN 86**

UNCLASSIFIED N00014-67-A-0117-0012

F/G 11/6

NL

2	1	17	1		17	17	17	17	17	17	17			
2	1	17	17		17									
														</



MICROCOPY RESOLUTION TEST CHART
NATIONAL BUREAU OF STANDARDS-1963-A



Figure 89

A region of intergranular fracture on the fracture surface of a sample of the Al-Zn-Mg alloy tested in humid nitrogen (1,000X).

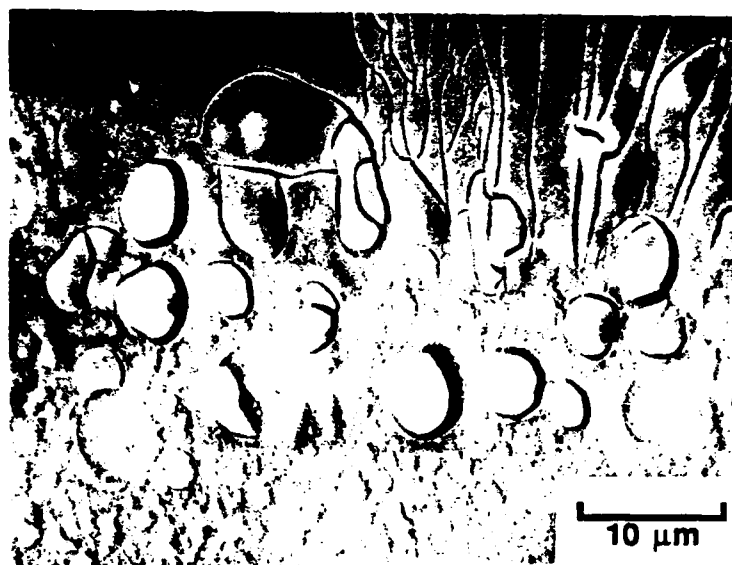


Figure 90

The external surface of a fatigue sample of the Al-Zn-Mg alloy after testing in humid nitrogen (2000X).



Figure 91

The intergranular fracture and secondary intergranular cracks on the fracture surface of a sample of the Al-Zn-Mg alloy tested in pure water (100X).



Figure 92

A region of transgranular cleavage-like fracture of an Al-Zn-Mg alloy sample tested in pure water (1,000X).

The morphology of the transgranular fracture regions resembled that observed in the previous environments except that the cleavage-like facets were flatter and the edges between facets were sharper as shown in figure 92.

0.5 M Sodium Sulfate: Figure 93 shows the fracture surface of a sample tested in 0.5 M sodium sulfate. This figure shows the mixed transgranular and intergranular cracking found on the fracture surfaces of samples tested in this environment. Figure 94 shows the transgranular crack propagation at a higher magnification.

The percentage of intergranular crack propagation increased with both anodic and cathodic polarization. Figure 95 shows the fracture surface of a sample tested with anodic currents applied to maintain the potential at $-0.8 V_{sce}$. In this figure, the fracture is almost entirely intergranular. Figure 96 shows the fracture surface of a sample tested with cathodic currents applied to maintain the potential constant at $-1.6 V_{sce}$. There is a fragmented surface layer on the intergranular facet shown in this figure similar to those found and identified as aluminum hydride by Ciaraldi (80).

0.5 M Sodium Chloride: Testing in 0.5 M sodium chloride resulted in fractures which were almost entirely intergranular. The fractures of samples tested with anodic polarization, shown in figure 97, were almost entirely



Figure 93

Mixed intergranular and transgranular fracture of a sample of the Al-Zn-Mg alloy tested in 0.5 M sodium sulfate (50X).

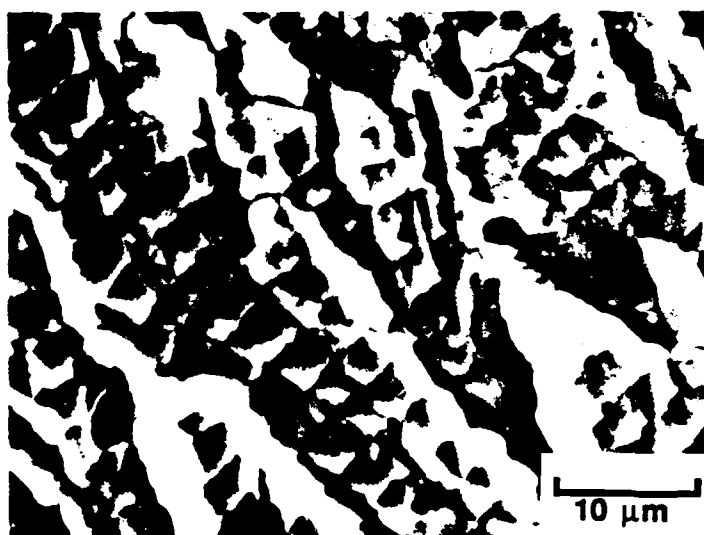


Figure 94

A region of transgranular cleavage-like fracture of a sample of the Al-Zn-Mg alloy tested in 0.5 M sodium sulfate (2,000X).



Figure 95

Regions of transgranular and intergranular fracture of a sample of the Al-Zn-Mg alloy tested in 0.5 M sodium sulfate at a constant potential of -0.8 Vsce (100X).



Figure 96

The fragmented surface layer found on the intergranular fracture surface of an Al-Zn-Mg alloy sample tested in 0.5 M sodium sulfate at a constant potential of -1.6 Vsce (1,000X).

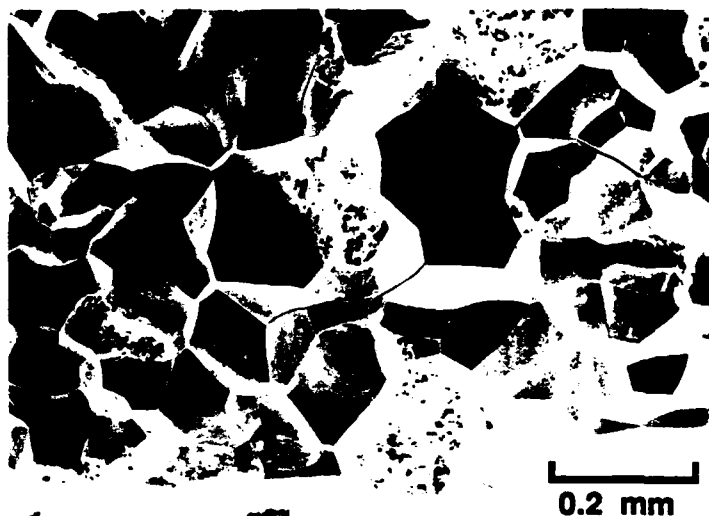


Figure 97

The fracture surface of a sample of the Al-Zn-Mg alloy tested in 0.5 M sodium chloride at a constant potential of $-0.8 \text{ V}_{\text{SCE}}$ (100X).

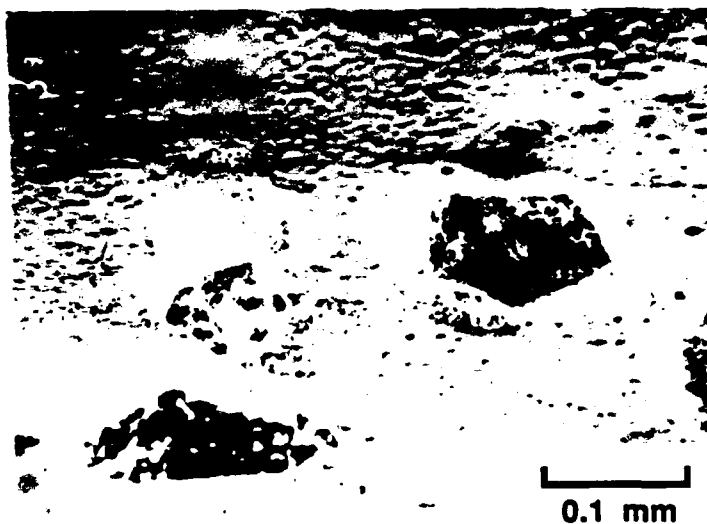


Figure 98

Pitting of the external surface of an Al-Zn-Mg alloy tested in 0.5 M sodium chloride at a constant potential of $-0.8 \text{ V}_{\text{SCE}}$ (200X).

intergranular and corrosion pits can be seen in the intergranular facets. These pits are essentially identical to those found in the samples external surface as shown in figure 98. At the potential which yielded the longest fatigue life, $-1.0 V_{sce}$, the fracture surface was mixed intergranular and transgranular, figure 99. This potential is slightly active (cathodic) to the free corrosion potential. With increased polarization to more active potentials the fracture surfaces demonstrated more secondary cracking and more of the fragmented layer shown in figure 100.

Al-Mg-Li Ternary Alloy

The fracture surfaces of the Al-Mg-Li ternary alloy fatigue samples were examined and both intergranular and transgranular crack propagation was observed. However, transgranular cleavage-like crack propagation, similar to that observed in the other alloy, was the dominant mode of crack propagation in each environment.

Dry Nitrogen: Figure 101 shows the fracture surface of a sample tested in dry nitrogen after storage in vacuum. In this figure, it can be seen that most of the crack propagation was transgranular. Figure 102 and 103 are higher magnification fractographs of samples tested in this environment and they show regions of stage 1 crack



Figure 99

The fracture surface of a sample of the Al-Zn-Mg alloy tested in 0.5 M sodium chloride at a constant potential of -1.0 Vsce (20X).



Figure 100

The fracture surface of a sample of the Al-Zn-Mg alloy tested in 0.5 M sodium chloride at a constant potential of -1.6 Vsce (100X).

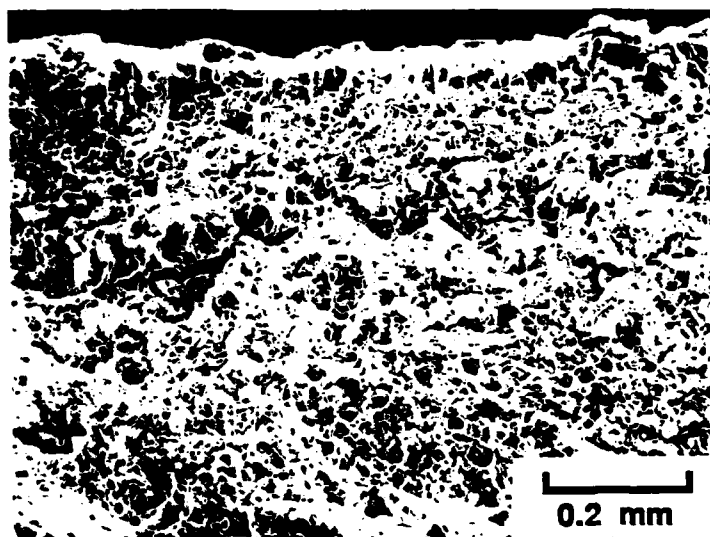


Figure 101

The fracture surface of a sample of the Al-Mg-Li alloy tested in dry nitrogen (100X).

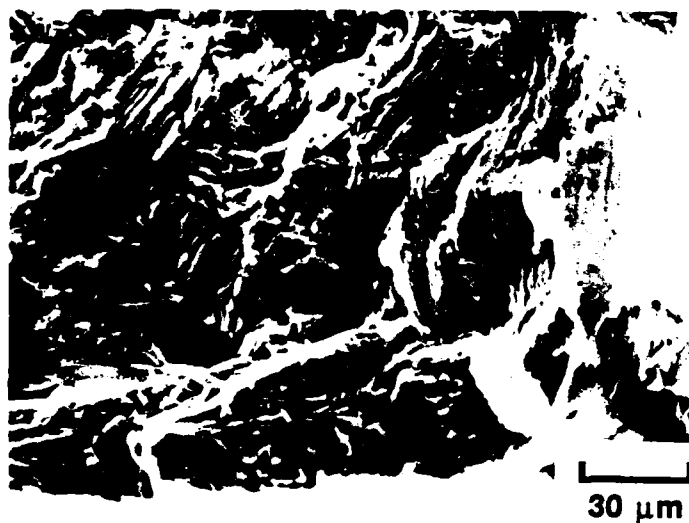


Figure 102

The crack initiation and stage 1 crack propagation regions of the fracture surface of an Al-Mg-Li alloy sample tested in dry nitrogen (500X).

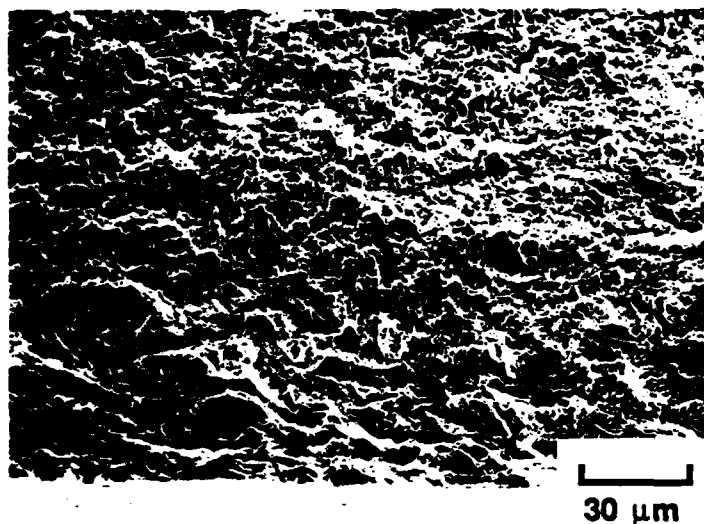


Figure 103

The crack initiation and stage 1 crack propagation regions of the fracture surface of an Al-Mg-Li alloy sample tested in dry nitrogen (500X).

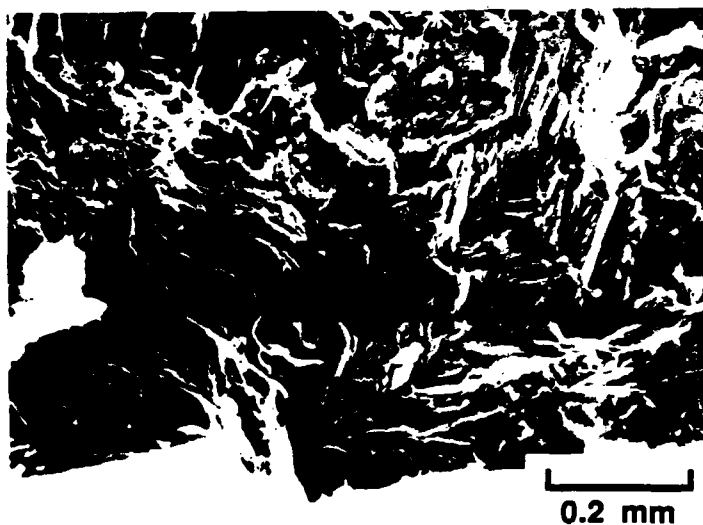


Figure 104

The fracture surface of a sample of the Al-Mg-Li alloy tested in humid nitrogen (100X).

initiation and propagation.

Humid Nitrogen: In humid nitrogen, crack propagation was essentially the same as in dry nitrogen, figure 104.

Pure Water: The fracture surfaces of samples tested in pure water resembled the fracture surfaces of samples tested in humid and dry nitrogen, figures 105 and 106. However, closer examination reveals secondary intergranular and transgranular cracking as shown in figures 107 and 108.

0.5 M Sodium Sulfate: Examination of the fracture surface shown in figure 109 shows that, in this environment, the morphology of the fracture surface resembles that of the other environments. Closer examination of the fracture surfaces in figures 110 and 111 shows that there are deposits on the surfaces similar to those found on the surfaces of the Al-Zn-Mg alloy tested in sodium chloride, figure 100. Figure 111 shows flake like deposits on the outside exposed surfaces and the facets of the fracture surface. Figure 112 shows the fracture surface of a sample tested in the sodium sulfate solution with the electrochemical potential held constant at -1.2 Vsce . Deposits have formed on this fracture surface also, but the outside surface has not been as aggressively attacked as the sample shown in figure 111. In figure 113, a similar sample is shown that was tested at -1.6 Vsce . This sample was more aggressively attacked by the environment at this more active

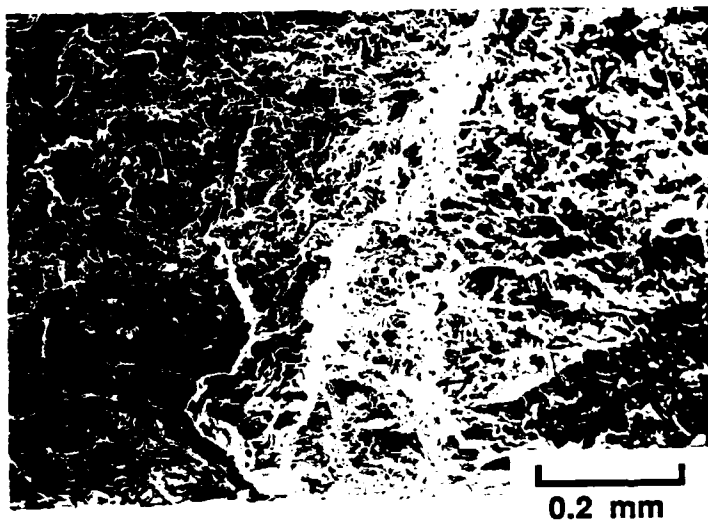


Figure 105

The fracture surface of a sample of the Al-Mg-Li alloy tested in pure water (100X).

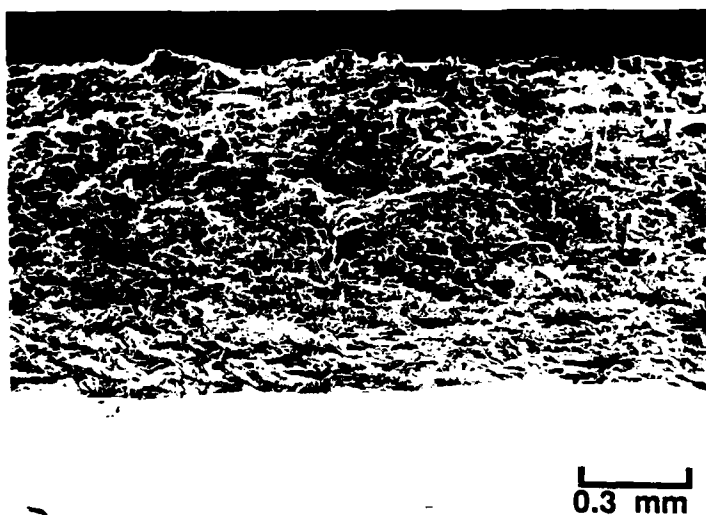


Figure 106

The fracture surface of a sample of the Al-Mg-Li alloy tested in pure water (50X).



Figure 107

Secondary transgranular cracks in the fracture surface of an Al-Mg-Li alloy sample tested in pure water (500X).

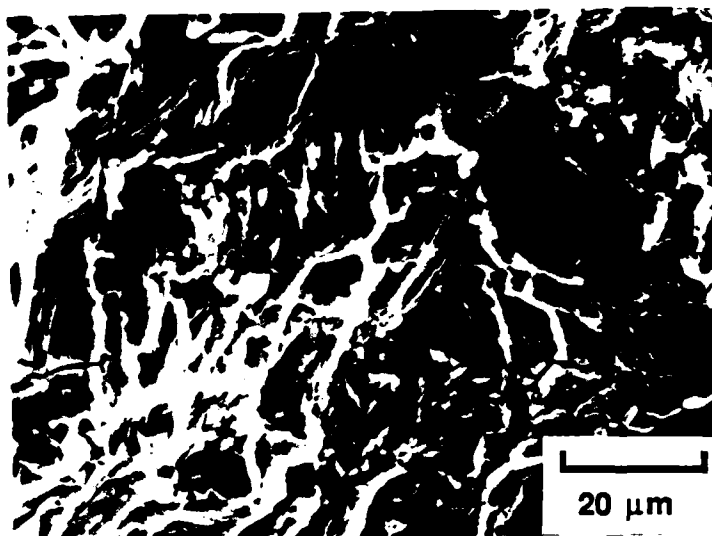
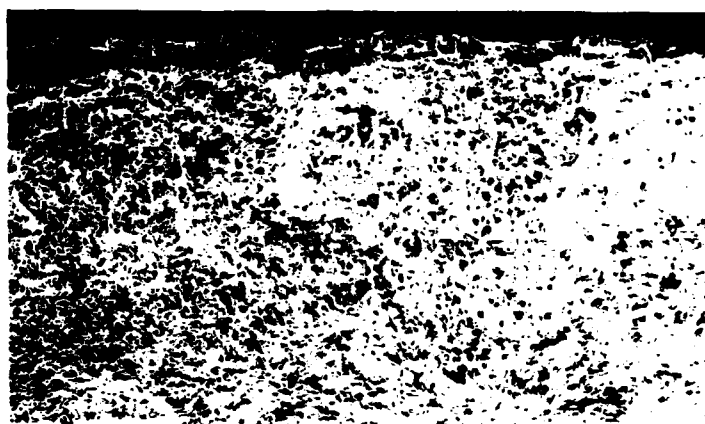


Figure 108

Secondary cracks in the fracture surface of a sample of the Al-Mg-Li alloy tested in pure water (1,000X).



0.3 mm

Figure 109

The fracture surface of a sample of the Al-Mg-Li alloy tested in 0.5 M sodium sulfate (50X).



30 μ m

Figure 110

Deposits on the fracture surface of a sample of the Al-Mg-Li alloy tested in 0.5 M sodium sulfate (500X).

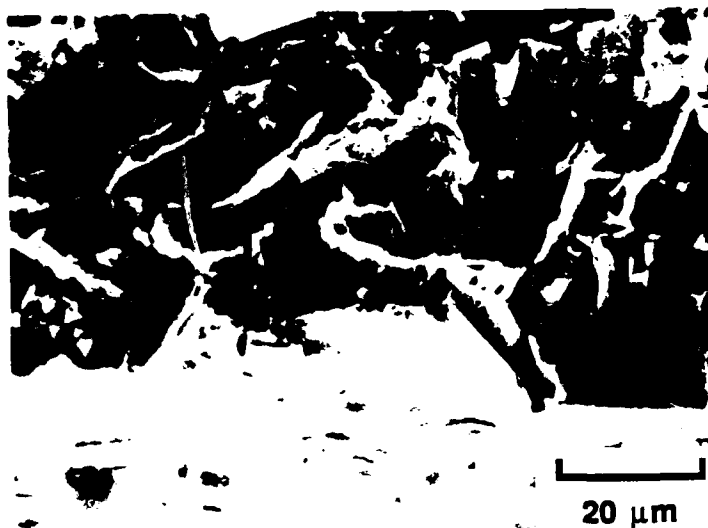


Figure 111

Deposits on the external surface of an Al-Mg-Li alloy sample tested in 0.5 M sodium sulfate (1,000X).

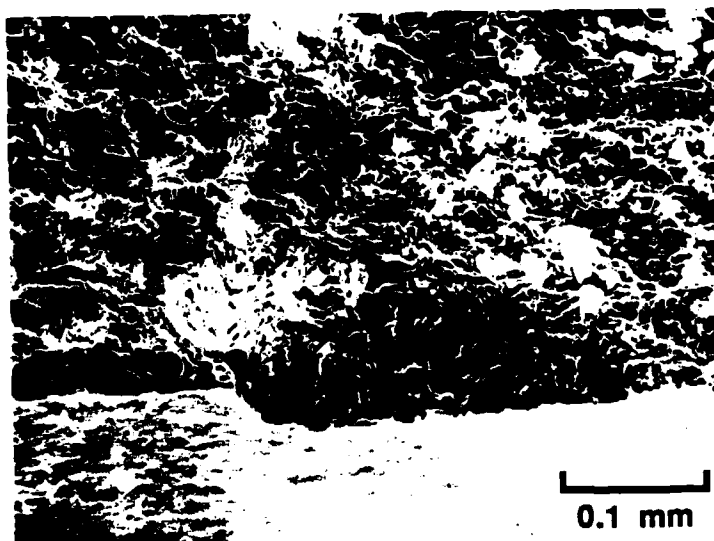


Figure 112

The fracture surface of a sample of the Al-Mg-Li alloy tested in 0.5 M sodium sulfate at a constant potential of -1.6 Vsce (200X).

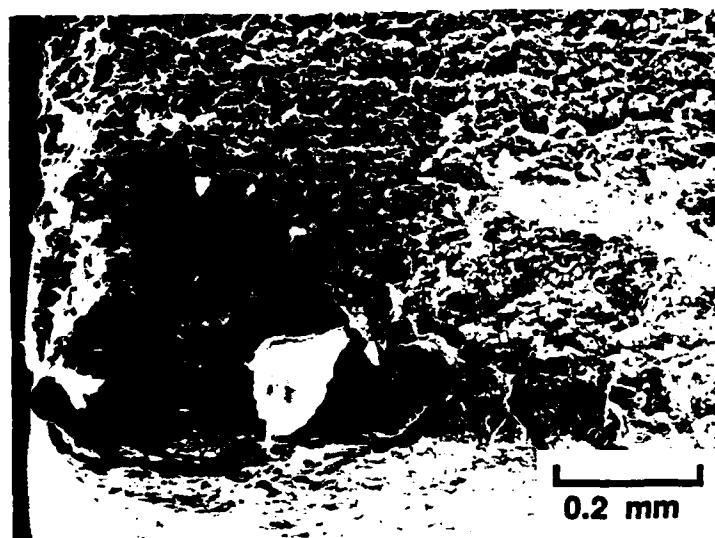


Figure 113

The fracture surface of a sample of the Al-Mg-Li alloy tested in 0.5 M sodium sulfate at a constant potential of -1.6 Vsce (100X).

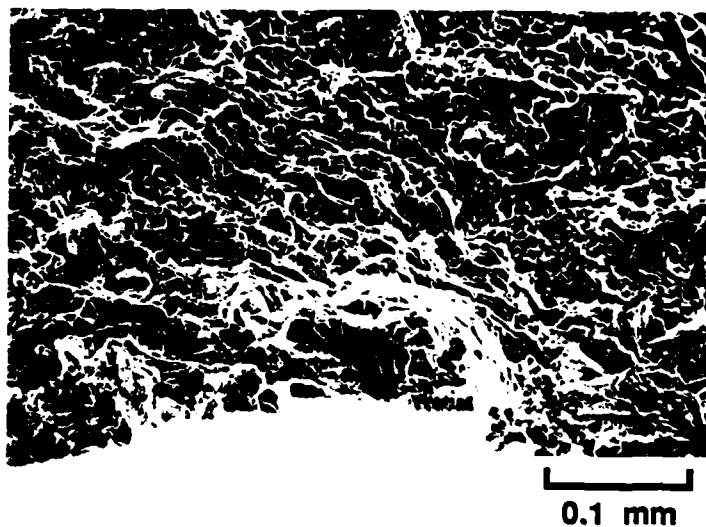


Figure 114

The fracture surface of a sample of the Al-Mg-Li alloy tested in 0.5 M sodium chloride at a constant potential of -1.2 Vsce (200X).

potential.

0.5 M Sodium Chloride: For free corrosion tests, the fatigue lives of samples of the Al-Mg-Li alloy were reduced more by the 0.5 M sodium sulfate solution than by the 0.5 M sodium chloride solution. By comparing the fracture surface of a sample tested at a constant potential of -1.2 Vsce in sodium chloride, figures 114 and 115, with the fracture surface of a sample tested at the same potential in sodium sulfate, figure 112, it can be seen that there are fewer deposits and other evidence of corrosion on the samples tested in sodium chloride. Similarly, figure 116 is compared to figure 113 for the potential of -1.6 Vsce. There are fewer deposits on the sample tested in sodium chloride at this potential also.

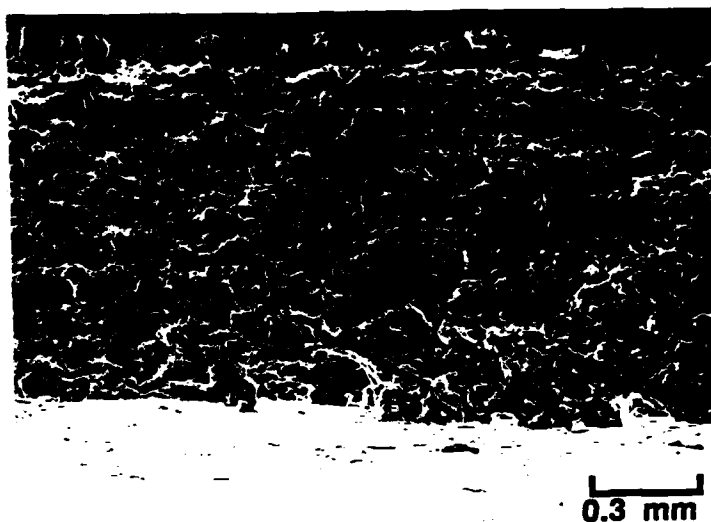


Figure 115

The fracture surface of a sample of the Al-Mg-Li alloy tested in 0.5 M sodium chloride at a constant potential of -1.2 Vsce (50X).

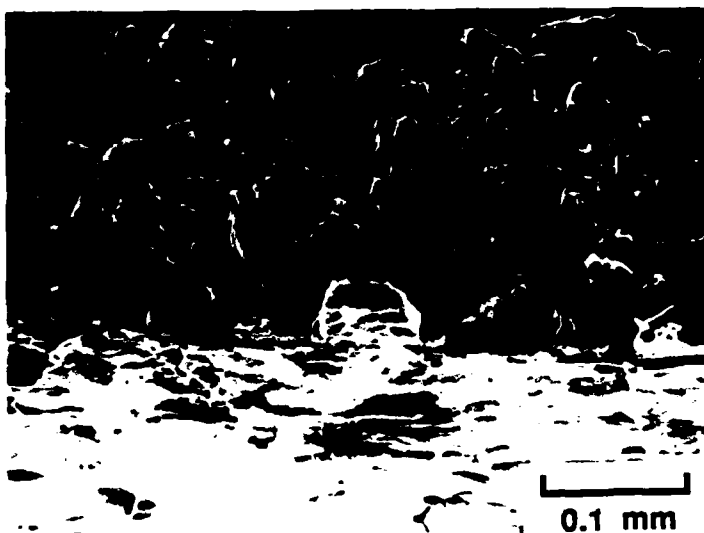


Figure 116

The fracture surface of a sample of the Al-Mg-Li alloy tested in 0.5 M sodium chloride at a constant potential of -1.6 Vsce (200X).

V. DISCUSSION

A. Material Evaluation Examinations

It is obvious from the results of these examinations that there are considerable differences between the alloys examined. The differences in composition and fabrication of the alloys result in variations in the following properties:

1. Modulus of elasticity
2. Density
3. Fracture toughness
4. Yield strength
5. Grain size
6. Precipitate morphology
7. Slip character
8. Chemical composition of matrix
9. Chemical composition of grain boundaries
10. Chemical composition of passive surface layer

The modulus of elasticity is increased approximately 8.7% for the lithium containing alloy over the Al-Zn-Mg alloy and the density is decreased approximately 7.8%. This results in a significant change in the specific modulus (modulus/density). However, neither of these factors should effect the results of the fatigue tests. Also, while the change in the fracture toughness will effect the crack length when final critical fracture occurs, this is where crack growth rates are the greatest and this difference alone will would have little effect on the total number of cycles to failure.

The grains of the lithium alloy are much smaller than

the grains in the Al-Zn-Mg alloy. It is uncertain what effect this difference has on the corrosion fatigue behavior of the alloys. However, the Al-Zn-Mg alloy had a tendency toward intergranular cracking with finer grains. This trend appears to be due to the availability of convenient intergranular crack paths and not due to the formation of a continuous layer of an anodic phase (82,83,108,112). If a continuous layer of some segregated species were required for intergranular cracking, then it would be expected that at some grain size there would no longer be enough of this species to maintain a continuous film. This would indicate that finer grains should be more resistant to cracking but this is not what is observed. Stoltz and Pelloux (108) found that grain refinement was detrimental to the resistance of alloy 7075 to corrosion fatigue crack propagation and it is generally accepted that the short transverse loading direction is more susceptible to stress corrosion cracking than the other loading directions (63,69).

This investigation has shown that an Al-Li alloy is more resistant to intergranular cracking than an Al-Zn-Mg alloy. Similarly, Christodoulou et. al. (75) found that an Al-Li binary alloy was not susceptible to intergranular stress corrosion cracking unless the AlLi phase and the accompanying strain fields were present at the grain

boundaries. They concluded that intergranular cracking was the result of the precipitate/matrix mismatch strain and not due to the dissolution of the AlLi phase (75).

Investigations have shown that the slip character of an alloy influences its fracture behavior. Slip character has been shown to influence liquid metal embrittlement (6,7,183), fatigue crack propagation (55,93,95-99,160,165), fracture toughness (55,186), and stress corrosion cracking (73,160) of aluminum alloys. It is believed that this is one of the factors reducing the fracture toughness of Al-Li alloys (48). The lithium alloy, however, demonstrated that it has a more homogenous deformation character than the Al-Zn-Mg alloy. This helps avoid the concentration of strain at the grain boundaries and will result in improved resistance to intergranular cracking.

The segregation of species, either impurities or alloy components, to the grain boundaries or the free surface has not been thoroughly studied. Investigators have studied segregation to the surface and to the grain boundaries of Al-Zn-Mg alloys and the susceptibility of these alloys to stress corrosion cracking (64,68,168,175,176). These results have indicated that the segregation of magnesium to the surface and the grain boundaries is related to increased susceptibility of these alloys to SCC.

The lithium containing alloy has considerably more

magnesium in it than the Al-Zn-Mg alloy. The Auger results presented in section IV were an attempt to determine if there was significant segregation of lithium or magnesium to the surface of the Al-Mg-Li alloy during exposure to humid air. Lithium was not detected in the surface film and the magnesium surface concentration was not significantly different for the two alloys. The atomic concentration of lithium in the alloy is less than 8%. If oxygen is added to the alloy surface in stoichiometric proportion to the elements and no segregation or dealloying occurs, then the atomic concentration of oxygen, aluminum, magnesium and lithium in the surface film would be 54.9%, 36.6%, 1.8%, and 3.3% respectively. The minimum atomic concentration of lithium which can be detected is unknown but lithium was detected in the lithium chloride standard (50 At. % lithium).

B. Corrosion Evaluation Tests

Potentiodynamic Polarization Tests

Aeration: Increasing the oxygen content of the environment increases the oxygen in the passive film and increases the nobility of the sample. This reduces the corrosion rate, as indicated by the reduction in the passive current density, but it also increases the driving force for

pitting by increasing the oxidation potential of the solution. If the free corrosion potential reaches the critical pitting potential, pitting results. The 7050 alloy frequently pitted prior to initiation of a scan in aerated sodium chloride solutions. Since the free corrosion potential is more active for the lithium containing alloy than the Al-Zn-Mg alloy, it did not pit in this situation.

pH: Aluminum oxides are soluble in both high and low pH solutions (59,142). As a result, either increasing the pH or decreasing the pH increases the corrosion rate of both alloys. Foley et. al. studied the relative behavior of several anions toward the oxides of aluminum and the passive film on aluminum surfaces (142,143). They concluded that while halides were very detrimental, the most aggressive anion was the hydroxide ion. However, pit initiation is apparently pH independent for both alloys.

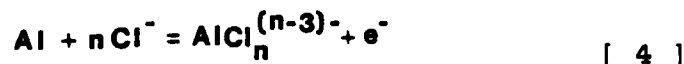
Temperature: Increasing the temperature decreased the pitting potentials. Bohni and Uhlig (144) found little temperature dependence on the pitting potentials of pure aluminum, however other investigators report a similar effect for pure aluminum to that reported here for the alloys (145,146). Bohni and Uhlig attributed the negligible temperature effect of aluminum to the absence of temperature sensitive hydration and structure of the passive film. The observed potential shift with temperature of the 7050 is

greater than for the Al-Mg-Li alloy. This suggests that either the scan rate-temperature dependence is different for the alloys or the temperature dependence of passive film hydration is different. It should be noted that the observed difference is in the range of reported differences by different investigators for pure aluminum (144-146).

Chloride Ion Concentration: The chloride ion concentration changes the pitting potential according to the relation (144):

$$E_p = E_p^0 + n \left(\frac{RT}{3F} \right) \ln [Cl^-] \quad [3]$$

Where "n" in the relationship is the stoichiometric factor or reaction order in the pitting reaction:



For the Al-Mg-Li alloy, the slope was found to be 106 mV/decade and the intercept was found to be at -0.843 Vsce. Stirrup et. al. (145) found a slope of 100 mV/decade and an intercept of -0.757 Vsce for pure aluminum. While Bohni and Uhlig (144) found a slope of 124 mV/decade and an intercept of -0.746 Vsce for pure aluminum.

The more active intercept of the chloride activity vs. pitting potential plot for the Al-Mg-Li alloy indicates that

this alloy is more susceptible to pitting at all chloride concentrations than pure aluminum. Since the slopes for the alloy and pure aluminum are the same, then the pitting reaction is the same or at least of the same order. This indicates that the protective passive film on the lithium alloy is the same or at least similar to the film on pure aluminum. The increased susceptibility to pitting may be due to either retardation of film repair kinetics or to an increase in the flaws in the film. This would also explain the shift in the free corrosion potential toward more active potentials.

Alloy Effect: For the Al-Mg-Li alloy compared to the 7050 alloy, the corrosion potential is usually more active and the pitting potential is also slightly less noble. Also, the passive current density at a given potential is higher. This indicates that the passive film on the lithium alloy is less protective.

The active shift in pitting potential indicates less resistance to pit initiation for the Al-Mg-Li alloy. The difference between the intercept of the chloride ion activity verses pitting potential line, discussed above, for the Al-Mg-Li alloy and pure aluminum is about 100 mV. Thus, for a given electrochemical potential, pits will initiate in the lithium containing alloy more readily than in pure aluminum or alloy 7050. However, the reduced free corrosion

potential reduces the probability of pitting under free corrosion conditions. If the Al-Mg-Li alloy is galvanically coupled with either pure aluminum or alloy 7050, the Al-Mg-Li alloy would be expected to preferentially pit. The lithium in the alloy is not necessarily responsible for the shift in pitting potential. Bohni and Uhlig found that additions of either Mg or Mn shifted the pitting potential in the active direction for pure aluminum (144). Since the lithium alloy also contains more magnesium than the 7050 alloy, table III, the increased pitting susceptibility cannot be attributed to lithium alone.

The shift to more active corrosion potentials of lithium containing alloys has been shown to be primarily due to the addition of lithium, and results in increased free corrosion rates (61,53). However, the polarization behavior indicates that the free corrosion potentials are still in the passive regime and that the corrosion rates estimated from the curves are not significantly different compared to the accuracy of the techniques for estimating corrosion rates.

Corrosion Rates

The rapid increase in corrosion rates under either anodic or cathodic polarization is not surprising because aluminum normally is protected from corrosion by an

amphoteric oxide surface film. That is, the passivating layer is composed of an oxide which is soluble in either acidic or basic solutions. Under either high anodic or cathodic polarization currents, the pH at the surface shifts, either acidic or basic, outside the stability range of the oxide. As a result, the dissolution rate of the metal increases dramatically when the pH at the surface, either generally or locally, deviates from the range of stability.

C. Fatigue Tests

Dry Nitrogen Gas

In dry nitrogen gas, the fatigue curves of the two alloys, figure 68, are almost identical. However, by examining the fatigue strength coefficients and exponents in table VIII a difference is discerned. The Al-Zn-Mg alloy appears to have a slightly lower strain hardening exponent indicating a more planar slip character. This is in accordance with the phase contrast microscopy observations of figure 52.

Humid Nitrogen Gas

The results of the fatigue tests conducted in humid nitrogen gas show significant differences between the

alloys. Both the 10^6 cycles fatigue limit and the fatigue lives of the Al-Zn-Mg alloy were reduced by this environment while only the fatigue lives of the Al-Mg-Li alloy were reduced. The 10^6 cycles fatigue limit of the lithium alloy appears to be unaltered by exposure to water vapor. This results in reduced fatigue strength coefficients and exponents for the Basquin or low amplitude part of the Coffin-Manson relationship for both alloys, table VIII.

The Basquin or low amplitude part of the Coffin-Manson relationships indicates that for strain controlled fatigue testing conditions there is no true fatigue limit. However, Lukas and Polak (192) studied the low amplitude strain controlled fatigue behavior of five alloys and reported evidence for the existence of what they termed a "fatigue strain limit", below which irreversible fatigue damage does not occur (192).

Pre-Exposure to Humid Air

Pre-exposure to humid air was as detrimental to the fatigue resistance of the Al-Zn-Mg alloy as water vapor in the test environment. The same fatigue lives were found for tests in either dry or humid nitrogen after a pre-exposure to humid air. Also, the same fatigue lives were determined in humid nitrogen after either a vacuum pre-exposure or pre-exposure to humid air. The pre-exposure effect was

shown to be reversible if sufficient time was allowed for hydrogen desorption. Hydrogen embrittlement mechanisms are the only proposed mechanisms of environmental cracking which can explain these results. It appears from these results that hydrogen is absorbed into the metal during exposure to water vapor and that this hydrogen is responsible for the reduction in fatigue resistance.

The Al-Mg-Li alloy was not effected by pre-exposure to humid air. Neither exposure to humid air for up to ten months nor exposure to 70°C water vapor saturated air for up to eight weeks resulted in any reduction in the fatigue resistance. The Al-Mg-Li alloy either absorbs less hydrogen during this exposure period or it is less embrittled by the same quantity of hydrogen absorbed.

Aqueous Solutions

In aqueous solutions, the Al-Zn-Mg alloy exhibited essentially the same behavior as was previously found for alloy 7075 (76). The most detrimental corrosion fatigue environment was 0.5 M sodium chloride. Both the 0.5 M sodium sulfate solution and humid nitrogen were more detrimental to the fatigue lives than pure water. The aqueous environments demonstrated reduced fatigue strength coefficients and exponents for the Basquin or low amplitude part of the Coffin-Manson relationship as shown in table

VIII. Also, table VIII lists the estimated strain range for an estimated fatigue life of 10^5 cycles for each environment and is good for evaluating the relative severity of each environment.

No different fracture features were observed in the aqueous solutions except for a fragmented surface layer on some of the intergranular fracture facets similar to that reported by Ciaraldi (80). Both transgranular and intergranular crack propagation were found on the fracture surfaces similar to that found in humid and dry nitrogen except that in aqueous solutions, the fractures were almost entirely intergranular while transgranular cracking predominated in the gaseous environments.

The corrosion fatigue behavior of the lithium alloy in the aqueous solutions was significantly different from that of the Al-Zn-Mg alloy. For free corrosion conditions, the lowest fatigue lives were observed in sodium sulfate instead of sodium chloride (see table VIII). Even humid nitrogen was more detrimental to the fatigue lives of the samples than 0.5 M sodium chloride. Also, similar to the findings in humid nitrogen, the 10^6 cycles fatigue limit of this alloy was not reduced by exposure to aqueous environments.

The features on the fracture surfaces of the Al-Mg-Li alloy were essentially the same in gaseous and aqueous environments. No intergranular cracking was found in any

environment except near the final fractures where the stress intensities were relatively large. Crack propagation in the Al-Zn-Mg alloy was predominately intergranular in the aqueous environments. Apparently, the improved corrosion fatigue performance of the Al-Mg-Li alloy can be at least partially attributed to the resistance of this alloy to intergranular corrosion fatigue crack propagation.

The constant electrochemical potential fatigue tests showed that the fatigue lives were reduced by both anodic and cathodic polarization for each of the alloys. Dissolution and hydrogen evolution can occur during anodic and cathodic polarization by local cell action (58,59). As a result, the only conclusion that can be drawn from the fatigue tests at constant potentials is that the removal or rupture of the protective oxide film is the rate controlling step for corrosion fatigue in aqueous environments.

For cathodic polarization, the same fatigue lives were observed for both 0.5 M sodium sulfate and 0.5 M sodium chloride. Therefore, it appears that corrosion fatigue during cathodic polarization of these alloys is not influenced by the anion present in the solution. For anodic polarization, 0.5 M sodium chloride was more detrimental to the fatigue lives of both alloys than 0.5 M sodium sulfate. Since passivation at the crack tip is the rate controlling step (9), then it would appear that chloride ions at the

surface of the sample retard this process for both alloys (154,157). However, for free corrosion, the Al-Mg-Li alloy exhibited longer fatigue lives in 0.5 M sodium chloride than in 0.5 M sodium sulfate. It would appear that sodium chloride either promotes passivation or lowers the free corrosion potential.

Since sodium chloride was not as detrimental to the corrosion fatigue behavior of the Al-Mg-Li alloy as other environments that did not contain halides and since environments which do not contain halides are very detrimental to the fatigue lives of the Al-Zn-Mg alloy, halides are not required for corrosion fatigue.

Rate Limiting Steps

Hydrogen which is available to diffuse to the crack tip and interact with the deforming metal will cause embrittlement. Hydrogen which is present in the alloy but is irreversibly trapped will not cause embrittlement. In this discussion, "hydrogen absorbed" refers to hydrogen available to cause embrittlement.

The lower susceptibility of the Al-Mg-Li alloy to corrosion fatigue could result from this alloy either absorbing less hydrogen from the environment or its being less embrittled by the same quantity of hydrogen absorbed. The Al-Mg-Li alloy would absorb less hydrogen if either the

absorption rate or the solubility of hydrogen were reduced.

Hydrogen Absorption Rate: The rate of hydrogen absorption into the Al-Mg-Li samples may be reduced by either the passive film acting as an absorption barrier or by a reduction in the diffusivity of hydrogen in this alloy.

The diffusivity of hydrogen could be reduced by lithium trapping the incoming hydrogen. However, no evidence was found of any pre-exposure effect for exposures up to 100 times those which caused embrittlement in the Al-Zn-Mg alloy. Also, this postulate cannot explain the difference in the behavior of the fatigue limits of the alloys with changes in the environment.

Differences in the rate of hydrogen absorption could also result from differences in the passive films on the alloys. Figure 24 shows the steps in the absorption of hydrogen from water vapor investigated by Scamans and Tuck in an Al-Zn-Mg alloy (87). The first steps in this sequence are the hydration of the passive layer and the permeation of water through the passive layer to the underlying metal. Hydrogen then forms at the interface between the passive layer and the metal, causing blistering and cracking as shown in figure 98. After this, hydrogen is absorbed into the metal and diffuses into the metal where it causes the embrittlement. If the presence of lithium prevents any of the steps of this process, then an improvement in the

fatigue behavior would be expected.

The absorption or desorption of hydrogen in aluminum alloys is very sensitive to the exact nature of the surface film. Scamans et. al. (83) found that the surface treatment given an Al-Zn-Mg alloy effected the embrittlement and the recovery of ductility on storage in vacuum. Hill and Williams (57) theorized that lithium in the alloy could react with the hydrogen evolved at a slip step forming stable lithium hydride on the surface and preventing hydrogen absorption.

If the passive layer on the lithium alloy provides better protection for the metal, then hydrogen cannot be absorbed into the metal unless mechanical loading ruptures the passive film. Once the film is ruptured, hydrogen enters and causes the reduced fatigue lives. This implies that the "fatigue limit" is determined by the stress range required to rupture the surface film. This could explain why this alloy does not have a reduced "fatigue limit" during corrosion fatigue and why pre-exposure to humid air has no effect. However, If the "fatigue limit" were determined by the mechanical properties of the oxide, then it would be expected to change with the test environment.

The mechanical properties of the passive layers on aluminum alloys have been found to change considerably on exposure to water and water vapor (113-115). Also, the

Auger results showed no evidence of a significant difference in the composition of the surface films on the alloys. The polarization results showed that the alloys demonstrated similar polarization and pitting behavior except that the lithium alloy had lower corrosion and pitting or breakdown potentials. Since the pitting potential of aluminum alloys is a measure of the chemical stability of the passive layer (144), then the lower pitting potential of the Al-Mg-Li alloy indicates that the oxide on this alloy is less protective. While these arguments do not dispell the possibility that the surface film on the lithium alloy prevents hydrogen absorption, they do cause reservations about its veracity.

Hydrogen Solubility: The Al-Mg-Li alloy could have a lower hydrogen solubility than the Al-Zn-Mg alloy and therefore absorb less hydrogen during exposures to humid and aqueous environments. This difference in solubilities could result from either the difference in the composition of the matrices or from the differences in the precipitate/matrix strain fields.

Hill and Williams (57) found that the addition of lithium to aluminum alloys increased the total hydrogen content of the alloys. However, there may be a considerable difference between the total hydrogen content of an alloy and the content of diffusable hydrogen available to cause

embrittlement. Lithium hydride forms when lithium is exposed to hydrogen gas or water vapor (57). This hydride will remain stable in molten aluminum and would be included in the alloy. As a result, the determination of hydrogen in solid solution in the alloy matrix is difficult. The determination of the effect of lithium will require the development of special techniques.

Green et. al. (70,71) demonstrated that an alloy embrittled by hydrogen during mode I loading was not embrittled during mode III loading, figure 21. This effect was attributed to the hydrostatic stresses at the crack tip during mode I loading increasing the solubility of hydrogen while no hydrostatic stresses were present during mode III loading (71,72). However, if precipitate/matrix strain fields are present, then there are hydrostatic stresses present in the matrix even without external loading. The $MgZn_2$ precipitates in the Al-Zn-Mg alloys have large precipitate/lattice mismatch strain fields which are a maximum at the peak aged condition. These strain fields in the matrix and at the grain boundaries could increase the solubility of hydrogen. This would result in more hydrogen absorbed into the alloy during pre-exposures and at lower stress intensities. This would explain why environmental assisted failure occurs for mode III loading of Al-Zn-Mg alloys and not for other hydrogen embrittled alloys and why

embrittlement is reduced for over and under aged samples (65,66,71,72,76).

The absence of precipitate/matrix strain fields in the lithium alloy could explain the differences between the corrosion fatigue behavior of the alloys. This could result in less hydrogen absorbed into the lithium alloy during pre-exposures and during cycling at low stress intensities. At higher stress intensities, the hydrostatic stresses at the crack tip are greater resulting in increased hydrogen absorption and embrittlement. This could explain why the fatigue life curves of the lithium alloy converge as the "fatigue limit" is approached and why the "fatigue limit" is unchanged by the environment.

While Al-Zn-Mg alloys are most susceptible to environmental cracking in the peak aged condition, Al-Li alloys are the most susceptible in the overaged condition (63,69,75). The strength level is the highest in the peak aged condition and the slip character is the most planar in the peak aged condition for both alloys (48,69). However, while the precipitate/matrix strain fields are the greatest for the Al-Zn-Mg alloy in the peak aged condition, precipitate/matrix strain fields are greater for the overaged condition of Al-Li alloys. Overaging Al-Li alloys results in the precipitation of the AlLi phase at the grain boundaries. This phase has large precipitate/matrix

mismatch strain fields and, as a result, is difficult to nucleate in the grains. Christodoulou et. al (75) found that overaged Al-Li binary alloys with AlLi precipitates and their large strain fields at grain boundaries failed by intergranular stress corrosion cracking while peak aged samples were almost immune to this type of failure. They concluded that this was not due to dissolution of the AlLi phase but was due to hydrogen embrittlement of the material adjacent to the AlLi precipitates (75). As a result, it appears that while strength level and slip character have a strong influence on the fracture, the most important parameter may be the hydrostatic stresses in the strain fields about the precipitates at the grain boundaries and in the matrix. This is in accordance the suggestion that the precipitate/matrix strain fields effect hydrogen absorption and that SCC and corrosion fatigue occur by similar mechanisms.

Susceptibility to Embrittlement: If the same quantity of hydrogen is present in the alloys, then the differences in the behavior of the two alloys must be due to differences in the susceptibilities of each alloy to hydrogen assisted fracture. Since intergranular fracture did not occur in the Al-Mg-Li alloy, the resistance of this alloy to this type of failure is the most significant difference in the susceptibilities of the two alloys. This difference could

be due to changes in the composition of the grain boundaries, grain boundary precipitation, precipitate morphology and/or slip character. If the diffusivity were the rate controlling step for crack propagation, then a change in the diffusivity would result in reduced crack propagation rates and increased fatigue lives. However, no evidence of hydrogen absorption at a slower rate was observed in the pre-exposure tests and this postulate cannot explain the difference in the behavior of the fatigue limits of the alloys.

The zinc in the Al-Zn-Mg alloy could be responsible for the greater susceptibility of this alloy to corrosion fatigue. Most investigators attribute the increased susceptibility of Al-Zn-Mg alloys to the segregation of magnesium to the grain boundaries and to the surface. As discussed earlier, Viswanadham et. al. (64,176) and Joshi et. al. (68,168) used Auger electron spectrometers to study the effect of heat treatment and segregation on the stress corrosion cracking of 7000 series alloys. They related the segregation of magnesium to the grain boundaries and the surface to the embrittlement of these alloys. The magnesium content of the lithium alloy is greater than the magnesium content of the Al-Zn-Mg alloy. The presence of lithium or the absence of zinc in the alloy could effect the diffusion and the segregation of the magnesium. However, no evidence

of a difference in the segregation of magnesium was found in the Auger results of this investigation. Thorough studies of the composition of the surface films and the grain boundaries with Auger and SIMS (secondary ion mass spectroscopy) will be required to evaluate this possibility.

Summary: Three different possibilities have been proposed to explain the differences between the behavior of the two alloys. Reservations have been expressed for each of the proposals. However, the proposal that the precipitate/matrix strain fields increase the susceptibility of the alloys by increasing hydrogen absorption is capable of explaining many of the observations in the literature as well as those of this investigation. First, this could explain why peak aged Al-Zn-Mg alloys are susceptible to environmentally induced cracking in mode III loading while other hydrogen embrittled alloys are immune in mode III loading (71,72). Second, this could explain the beneficial effect of overaging on stress corrosion cracking susceptibility of Al-Zn-Mg alloys (63,69) while overaging is deleterious to the stress corrosion cracking susceptibility of Al-Li alloys (75). Third, this could also explain why Al-Zn-Mg alloys are the most susceptible aluminum alloy to stress corrosion cracking. However, distinction between the different possibilities for the behavior of the alloys is not possible based solely on the results of this

investigation and each may contribute in some way to the observed differences.

Mechanisms of Failure

Usually the environmental assisted failure of aluminum alloys is attributed to either anodic dissolution or hydrogen embrittlement mechanisms. Since no bulk phase is present for the removal of ions in the humid or dry nitrogen gas environments, anodic dissolution cannot be responsible for the corrosion fatigue failure of the samples in these environments. The lithium alloy was not affected by pre-exposure but it still demonstrated reduced fatigue lives in humid nitrogen. Hydrogen embrittlement mechanisms are the only mechanisms capable of explaining these results.

In the aqueous environments, the distinction is not as clear. Since the rate limiting step for either mechanism would be the removal or rupture of the protective oxide, distinction between the proposed mechanisms is not easy (9). However, no new fracture features were found which would indicate a change in the actual mechanism(s) of fracture. As a result, it seems logical to assume that the same fracture mechanism, hydrogen embrittlement, is responsible for crack extension.

While the results of this investigation were not able to identify the mechanism of hydrogen assisted fracture, it

should be beneficial to review the mechanisms which have been proposed and how the experimental observations of this program and those in the literature fit each proposed mechanism. Several different mechanisms of hydrogen embrittlement have been proposed but these can be classified into five categories. These are:

1. High Pressure Bubble Formation.
2. Surface Adsorption.
3. Stress Induced Hydride Nucleation and Fracture.
4. Tensile Decohesion.
5. Plastic Deformation Effects.

High Pressure Bubble Formation: It has been proposed that high pressure bubbles of hydrogen gas could form in the plastic zones at crack tips and cause hydrogen embrittlement (193-195). Due to the large difference in the solubilities of hydrogen in molten aluminum and solid aluminum, hydrogen blistering during cooling from the melt or during subsequent heat treatments is common (132). Albrecht et. al. (77) studied the effect of cathodic charging of aluminum alloy 7075 in hydrochloric acid on the size of dimples found on tensile fracture surfaces. They found a statistically significant increase in the diameter of the dimples with increasing charging time. After studying the size and distribution of the dimples, they concluded that hydrogen in the alloy enhanced microvoid nucleation and growth (77). Christodoulou and Flower (86) observed the growth of

pre-exposure embrittlement cracks in a transmission electron microscope and observed the nucleation and growth of hydrogen gas bubbles at interface between the MgZn precipitates and aluminum grains along the grain boundaries. They found that the particles at the grain boundaries acted as heterogeneous nucleation sites for the hydrogen bubbles and that a critical size of about 20 nm was required for the nucleation of the bubbles. Since embrittlement was reduced by over aging to the point where the hydrogen bubbles formed, these investigators concluded that hydrogen in solution at the grain boundaries was responsible for the embrittlement and that the grain boundary particles trapped hydrogen in the bubbles reducing embrittlement (83,86).

In aluminum alloys exposed to water, the hydrogen fugacities are extremely high but the solubility and the diffusivity of hydrogen in aluminum are so low that the gas pressure required to cause embrittlement probably cannot be maintained in gas bubbles in the plastic zone during crack propagation. Ford (9) quantitatively compared this mechanism of hydrogen embrittlement to corrosion fatigue crack propagation rates of an Al-7% Mg alloy and found it to be incapable of producing the observed crack growth rates at potentials above approximately -0.9 Vsce.

No fractographic evidence, such as dimples, was found in this study to support this mechanism as a mechanism of

corrosion fatigue crack propagation of these alloys.

Surface Adsorption: It has been proposed that the adsorption of hydrogen onto the surface of a metal could reduce the fracture stress by reducing the surface energy of the new fracture surface created during fracture (199,200). Two objections have been raised to this surface adsorption embrittlement mechanism (139). First, while hydrogen adsorption can reduce the surface energy, the total fracture energy of ductile metals is almost entirely due to the energy required for the plastic deformation which accompanies crack propagation (201,202). Second, while hydrogen will adsorb onto surfaces, so will other gaseous species such as water, oxygen and nitrogen. These species can reduce the surface energies of metals by as much or even more than hydrogen and yet, for most metals, they are not as detrimental (203). However, these objections neglect the relationship between the surface energy and the strain energy derived by Gilman (208) and shown to be in agreement with experimental results (208).

Stress Induced Hydride Nucleation and Fracture: Some metals which form hydrides are severely embrittled by hydrogen (ie. Nb, Ta, V, Zr and Ti). Usually, there is a positive volume change on nucleation of a metal hydride and the hydrides are usually brittle. This mechanism assumes that hydrides will nucleate in the plastic zone at the crack

tip under the influence of hydrostatic stresses and then fracture. Several measurements and experiments have shown this to be a realistic mechanism for alloys which readily form hydrides. However, for aluminum, hydrides do not form except at very high hydrogen fugacities.

Ciaraldi et. al. (80,198) examined the intergranular facets of Al-Zn-Mg alloys tested in tension after charging with hydrogen by either exposure to water vapor or by abrasion in water. They found flakes on the intergranular fracture facets which they examined in the transmission electron microscope. They identified these flakes by electron diffraction as aluminum hydride. Koch (163) found similar flakes on the fracture surfaces of an Al-Zn-Mg alloy embrittled by exposure to ionized hydrogen gas. Ciaraldi (80) concluded that embrittlement was due to the stress assisted nucleation and fracture of aluminum hydride at the grain boundaries.

The flakes reported by these authors were rarely observed on the intergranular facets of this investigation. Also, in humid nitrogen or after precharging the predominant fracture mode of the Al-Zn-Mg alloy was transgranular and cleavage-like not intergranular. The Al-Mg-Li alloy exhibited very little intergranular cracking in any environment. The transgranular cleavage-like crack propagation has been observed by other investigators and

also attributed to hydrogen embrittlement (197). No evidence has been found of hydrides being involved in this type of fracture of these alloys.

Tensile Decohesion: It has been proposed that if brittle fracture results from the local stress at a crack tip exceeding the atomic bond strength, then hydrogen embrittlement would result if hydrogen present in solution reduces the bond strength of the host metal (202,204,205). It has been proposed that fatigue cracks, even in inert environments, propagate by a cyclic cleavage process (95,96,103-105). This could explain the similarity between the transgranular cleavage-like fracture in the inert environment and that observed in the presence of hydrogen.

Scamans and Swann (83) studied stress corrosion cracks of Al-Zn-Mg alloys in the transmission electron microscope and found that intergranular cracking of this alloy occurred at the interface between grains or at the $MgZn_2$ precipitate grain boundary interfaces and not through either phase. They did not observe any evidence of deformation or of the formation of a hydride. They concluded that this indicated decohesion of the grain boundary interface as a result of hydrogen in solution (83).

Plastic Deformation Effects: It has been proposed that hydrogen causes embrittlement by modifying the plastic deformation that accompanies the fracture process.

Originally, it was proposed that hydrogen in solution would strengthen the material at the crack tip, restricting plastic deformation and crack tip blunting (206). However, more recently Beachem (185) has proposed that the opposite effect may be occurring. He suggested that hydrogen does not strengthen the metal but causes localized softening at the crack tip. Lynch (150) has extended this concept by proposing that environmentally enhanced crack tip plasticity resulted from lowering the stress required to nucleate dislocations at the crack tip. This would lead to intense localized deformation at the crack tip resulting in the macroscopically observed embrittlement (150). Similarly Lynch (93) has proposed that fatigue cracks propagate by a cyclic deformation process rather than cyclic cleavage. Then, hydrogen would reduce the plastic zone size and increase the brittle appearance of the fracture. This is very similar to the previous models except that the fracture results from plastic processes rather than cleavage (139).

Summary: The only proposed hydrogen embrittlement mechanism which is inconsistent with the fractographic evidence of this investigation is the high pressure bubble formation mechanism. However, investigators have found that in tensile tests the fracture mode changes from microvoid coalescence (dimples) to a transgranular cleavage-like fracture and then to intergranular fracture as the

availability of hydrogen increases (77-80,197,198). Therefore, this mechanism may contribute to reduced ductility during tensile deformation with low hydrogen concentrations in the samples, but, it does not appear to play a role in the corrosion fatigue of these aluminum alloys. Similarly, while there is fractographic evidence of flakes similar to those found and identified as hydrides by Ciaraldi (80), these are rare and not found at all on most fracture surfaces. Thus, while stress induced hydride nucleation and fracture may play a role in crack propagation at high hydrogen fugacities and slow strain rates, but it does not appear to be responsible for corrosion fatigue failure under the environmental conditions that these alloys are most likely to see in service.

VI. CONCLUSIONS

The electrochemical experiments of this investigation demonstrated that the Al-Mg-Li alloy has significantly more active corrosion potentials and slightly more active pitting potentials than the Al-Zn-Mg type alloys. Therefore, the passive film on the Al-Mg-Li alloy is less protective than the film covering the Al-Zn-Mg alloy. As a result, if the Al-Mg-Li alloy and the Al-Zn-Mg alloy were placed in an environment at the same electrochemical potential, the lithium containing alloy would be expected to pit first. However, the lower free corrosion potential of the Al-Mg-Li alloy results in a lower probability of the lithium containing alloy pitting during free corrosion.

The fatigue tests of this investigation demonstrated that sample preparation procedures which minimizes the hydrogen in the samples and testing in an environment which will not supply hydrogen to the surface of the sample results in essentially the same fatigue lives for the two alloys. Three differences were found in the corrosion fatigue behavior of the two alloys. First, the Al-Zn-Mg alloy was reversibly embrittled by pre-exposure to humid air while the Al-Mg-Li alloy was not. Second, the corrosion fatigue limits (10^6 cycles) of the Al-Zn-Mg alloy were considerably reduced compared to the fatigue limits in the

inert environment, while the fatigue limits of the Al-Mg-Li alloy were essentially unchanged. And third, the Al-Zn-Mg alloy exhibited intergranular fractures in all environments with the percentage of intergranular fracture increasing with the aggressiveness of the environment while very little intergranular cracking was observed for the Al-Mg-Li alloy.

These results are consistent with the hypothesis that hydrogen accelerates fatigue failure of these alloys. The differences in the corrosion fatigue behavior of the alloys is attributed to either:

1. Reduced hydrogen absorption rates in the Al-Mg-Li alloy due to a difference in the surface film.
2. Reduced hydrogen solubility in the Al-Mg-Li alloy at the grain boundaries or in the matrix due the absence of precipitate/matrix strain fields.
3. Reduced susceptibility of the Al-Mg-Li alloy to hydrogen assisted intergranular fracture due to differences in the segregation of elements to the grain boundary and/or slip character.

Linear regression analysis of the logarithm of the total strain range versus the logarithm of the cycles to failure, in the region where the plastic strains approach zero, demonstrated that the aggressive environments simultaneously reduced both the fatigue strength coefficient and exponent for both alloys. According to the generally accepted physical interpretation of these terms, this

indicates that the environment is simultaneously reducing the ultimate tensile strength and the cyclic work hardening coefficient. This may be indicative of the actual mechanism of the process of hydrogen assisted fatigue of these alloys.

Two significant implications result from this work. First, the test results indicate that high strength aluminum alloys can be developed which, while not immune to corrosion fatigue, have essentially the same fatigue limits in inert and aggressive environments. Since the application of high strength aluminum alloys is severely restricted by low corrosion fatigue limits and stress corrosion cracking thresholds, this is an important result. Second, it has been demonstrated that in an investigation of the mechanical properties of aluminum alloys, experiments should be conducted in inert environments and the samples should be handled so as to avoid absorption of any embrittling hydrogen.

VII. SUGGESTIONS FOR FUTURE WORK

Based on the results of this investigation, there are a number of areas where it would be beneficial to conduct research. These are:

1. Environmental effects in low cycle fatigue.
2. Pre-crack nucleation fatigue damage and the effect, if any, of the environment.
3. Surface chemical reactions and repassivation rates.
4. Surface chemistry and protective film composition changes.
5. Heat treatments and the effects of grain boundary precipitate morphologies, elemental segregation, precipitate free zones and precipitate/matrix strain fields versus environmental cracking susceptibility.
6. Third element additions to the Al-Li binary coupled with heat treatments to modify precipitate structure versus environmental cracking.

Low Cycle Fatigue Behavior: This investigation has shown that both the coefficients and the exponents of the Basquin or low amplitude part of the Coffin-Manson relationship are effected by the test environment. The origin of these changes with the test environment is unknown. Accordingly, a thorough program to study the cyclic plastic deformation characteristics and the high and low amplitude strain controlled fatigue lives of these alloys under controlled

environmental conditions would be beneficial. This coupled with transmission electron microscopy studies to determine dislocation substructures and interactions in the pre-crack nucleation regime, will determine the origin of the environmental effects.

Passivation and Repassivation: It appears that the reactions at the surface of the samples and the nature of the passive layer control not only the corrosion properties of the alloys but also the corrosion fatigue and the stress corrosion cracking behavior of the alloys. However, almost no information is available on the exact composition, structure, and properties of the films on these alloys and how changes effect film permeability and protectiveness. Therefore, a program to study the composition of the surface films and the kinetics of film formation on a bare surface would be beneficial. This would involve scratching electrode experiments to determine repassivation rate variables as a function of environmental parameters such as solution chemistry and alloy composition as well as AES and SIMS studies to determine the exact nature of the surface films. Also, the surface of a lithium free sample could be doped with lithium by ion implantation or some other means to determine the effect of incorporation of lithium into the passive film on the corrosion properties.

Metallurgical Variables: Heat treatment appears to be

highly effective in controlling the susceptibility of the Al-Li alloys to environmental cracking. There is a more dramatic effect of heat treatment in these alloys than found in conventional 7XXX series alloys. The results of this work suggests that there is a relationship between the susceptibility of aluminum alloys to environmental cracking and the local strain fields about the precipitates at the grain boundaries and in the matrix. These strain fields could effect hydrogen solubility and permeability. Therefore, it would be beneficial to study the effect of heat treatment on the development of precipitate/matrix strain fields and the susceptibility of alloys to environmental cracking. This would combine SCC and CF studies with TEM studies to determine the strain field parameters to determine if there is a correlation.

REFERENCES

1. M. Gell and D. J. Duquette; "The Effects of Oxygen on Fatigue Fracture of Engineering Alloys", Corrosion Fatigue, NACE-2, (1972), p366.
2. D. J. Duquette and M. Gell; "The Effects of Environment on the Elevated Temperature Fatigue Behavior of Nickel-Base Superalloy Single Crystals", Met Trans, v3, July 1972, p1899.
3. H. N. Hahn; "Corrosion Fatigue Behavior of Copper and Copper Base Alloys", PhD Thesis, Rensselaer Polytechnic Institute, Troy NY, May 1977.
4. T. W. Crooker; "The Need for Standards Development in Corrosion Fatigue Testing with Precracked Specimens", ASTM Standardization News, May 1975, p17.
5. R. P. Wei; "Rate Controlling Processes and Crack Growth Response", Hydrogen Effects in Metals, Ed. A. W. Thompson and I. M. Bernstein, The Metall. Soc. of AIME, Warrendale, PA, p677, (1981).
6. S. P. Lynch; "Mechanisms of Fatigue and Environmentally Assisted Fatigue", Fatigue Mechanisms, J. T. Fong ed., ASTM-STP-675, Kansas City, May 1978, p174.
7. S. P. Lynch; "A Comparative Study of Stress-Corrosion Cracking, Hydrogen-Assisted Cracking and Liquid-Metal Embrittlement" Hydrogen Effects in Metals, ibid. p863.
8. F. P. Ford; "Corrosion Fatigue Crack Propagation in Al-7% Mg Alloy", Corrosion, v35, n7, p281, (1979).
9. F. P. Ford; "Quantitative Examination of Slip-Dissolution and Hydrogen-Embrittlement Theories of Cracking in Al Alloys", Met Sci, July 1978, p326.
10. J. A. Feeney, J. C. McMillan, and R. P. Wei; "Environmental Fatigue Crack Propagation of Al Alloys at Low Stress Intensity Levels", Met Trans, v1, p1741, (1970).
11. R. P. Wei; "Fatigue-Crack Propagation in a High-Strength Aluminum Alloy", Intl J of Fracture, v4, n2, p159, (1968).
12. A. S. Tetelman; "Recent Developments In Classical

- (Internal) Hydrogen Embrittlement", Hydrogen in Metals, Ed. I. M. Bernstein & A. W. Thompson, American Society for Metals, Metals Park, OH, (1974) p17.
13. R. H. Cook and R. P. Skelton, "Environment-Dependence of the Mechanical Properties of Metals at High Temperatures", Intl Metl Rev, v19, p199, (1974).
 14. R. P. Wei; "The Effect of Temperature and Environment on Subcritical-Crack Growth", Fracture Prevention and Control, Ed. D. W. Hoepfner, ASM Metals Park, Ohio (1974) p73.
 15. R. P. Wei; "On Understanding Environment Enhanced Fatigue Crack Growth A Perspective View (1963-1977)", Tech Rpt #7, ONR Cont N00014-75-C-0543, NR 036-097, May 1978.
 16. H. Eyring and E. M. Eyring, Modern Chemical Kinetics, Reinhold Publ. Corp. NY, (1963).
 17. D. P. Williams and H. G. Nelson; "Embrittlement of 4130 Steel by Low Pressure Gaseous Hydrogen", Met Trans, v1, n1, p63, (1970).
 18. G. W. Simmons, P. S. Pao, and R. P. Wei; "Fracture Mechanics and Surface Chemistry Studies of Subcritical Crack Growth in AISI 4340 Steel", Met Trans, v9A, August 1978, p1147.
 19. R. P. Gangloff and R. P. Wei; "Gaseous Hydrogen Embrittlement of High Strength Steels", Met Trans, v8A, July 1977, p1043.
 20. G. W. Simmons, P. S. Pao and R. P. Wei; "Fracture Mechanics and Surface Chemistry Studies of Subcritical Crack Growth in AISI 4340 Steel", Tech. Rpt. n4, ONR Cont N00014-15-C-0543, NR036-097, September 1977.
 21. H. G. Nelson, D. P. Williams and A. S. Tetelman; "Embrittlement of a Ferrous Alloy in a Partially Dissociated Hydrogen Environment", Met Trans, v2, April 1971, p953.
 22. W. A. Van Der Sluys; "Mechanisms of Environment Induced subcritical Flow Growth in AISI 4340 Steel", Engr. Frac. Mech., v1, p447, (1969).
 23. S. R. Bala and D. Tromans; "Effect of Temperature Upon Stress Corrosion Cracking of HY-180M Steel in 3.5 Pct

- NaCl", Met Trans, v11A, July 1980, p1161.
24. S. R. Bala and D. Tromans; "Stress Corrosion Cracking of High Strength HY-180M Steel in 3.5 Pct NaCl", Met. Trans., v9A, p1125, (1978).
 25. R. P. Wei, P. S. Pao, R. G. Hart, T. W. Weir and G. W. Simmons; "Fracture Mechanics & Surface Chemistry Studies of Fatigue Crack Growth in an Al Alloy", Met Trans A, v11A, January 1980, p151.
 26. F. J. Bradshaw and C. Wheeler; "The Influence of Gaseous Environments and Fatigue Cracks in Some Al Alloys", Intl J of Fract Mech, v5, n4, December 1969, p255.
 27. R. P. Wei and G. W. Simmons; "Recent Progress in Understanding Environment Assisted Fatigue Crack Growth", Tech. Rpt n8, ONR N00014-75-C-0543, NR 036-097, January 1979.
 28. H. H. Smith, P. Shahinian, M. R. Achter, "Fatigue Crack Growth Rates in Type 316 Stainless Steel at Elevated Temperature as a Function of Oxygen Pressure", Trans TMS-AIME, v245, May 1969, p947.
 29. D. J. Duquette and M. Gell; "The Effect of Environment on the Mechanism of Stage I Fatigue Fracture", Met Trans, v2, May 1971, p1325.
 30. T. W. Weir, R. G. Hart, G. W. Simmons, and R. P. Wei; "A Model for Surface Reaction and Transport Controlled Fatigue Crack Growth", Scripta Met., v14, p357, (1980).
 31. C. M. Austin, "Fatigue Crack Propagation in a Directionally Solidified Cobalt-Base Eutectic", PhD Thesis, Rensselaer Polytechnic Institute, Troy, NY, December 1979.
 32. J. M. Barsom; "Effect of Cyclic Stress Form on Corrosion Fatigue Crack Propagation Below K(1SCC) in a High Yield Strength Steel", Corrosion Fatigue, NACE-2, Nat. Assn of Corro. Engr., Houston TX, (1972) p424.
 33. J. M. Barsom' "Corrosion-Fatigue Crack Propagation Below K(1SCC)", Engr Fract Mech, v3, p15, (1971).
 34. P. C. Paris and F. Erdogan; "A Critical Analysis of Crack Propagation Laws", J Basic Engr, v85, p528, (1963).

35. D. B. Dawson and R. M. N. Pelloux; "Corrosion Fatigue Crack Growth of Titanium Alloys in Aqueous Environments", *Met Trans*, v5, March 1974, p723.
36. D. B. Dawson; "Fatigue Crack Growth Behavior of Ti-6Al-6V-2Sn Methanol and Methanol-Water Solutions", *Met Trans*, v12A, May 1981, p791.
37. R. P. Wei and J. D. Landes; "Correlation Between Sustained-Load and Fatigue Crack Growth in High-Strength Steels", *Mats Res and Stds*, ASTM, July 1969, p25.
38. A. S. Porter and F. C. Tompkins; "The Sorption of Hydrogen and Other Gases by Evaporated Iron Films", *Proc. Roy. Soc. London*, vA217, p544, (1953).
39. P. S. Pao, W. Wei and R. P. Wei; "Effect of Frequency on Fatigue Crack Growth Response of AISI 4340 Steel in Water Vapor", Environmental Sensitive Fracture on Engineering Materials, Z. A. Foroulis ed. The Metall. Soc. of AIME, Warrendale PA, (1979), p565.
40. R. P. Wei and G. W. Simmons; "Surface Reactions and Fatigue Crack Growth", *Proceedings, 27th Army Materials Research Conf.*, Bolton Landing, NY, July 1980.
41. R. P. Wei and G. Shim; "Fracture Mechanics and Corrosion Fatigue", Corrosion Fatigue: Mechanics, Metallurgy, Electrochemistry and Engineering, Crooker and Leis eds., ASTM-STP-801, (1982).
42. J. Gjønnes and C. J. Simensen; "An Electron Microscope Investigation of the Microstructure in an Al-Zn-Mg Alloy" *Acta Met*, v18, August 1970, p881.
43. N. Ryum; "Ageing and Plastic Deformation of an Al-Zn-Mg Alloy", *Acta Met*, v17, July 1969, p821.
44. N. Ryum; "The Influence of Dislocation Arrangement on Recrystallization in an Al-Zn-Mg Alloy", *Acta Met*, v17, July 1969, p831.
45. C. E. Lyman and J. B. Vandersande; "A TEM Study of the Early Stages of Precipitation in an Al-Zn-Mg Alloy", *Met Trans*, v7A, August 1976, p1211.
46. R. M. Allen and J. B. Vandersande; "The Oriented Growth of Precipitates on Dislocations in Al-Zn-Mg: Part 1 Experimental Observations", *Acta Met*, v28, p1185,

(1980).

47. K. K. Sankaran and N. J. Grant; "Structure and Properties of Splat Quenched 2024-Al alloy Containing Lithium Additions" Aluminum-Lithium Alloys, T. H. Sanders and E. A. Starke Jr. eds., The Met. Soc. of AIME, Warrendale PA, p205, (1981).
48. E. A. Starke and T. H. Sanders; "New Approaches to Alloy Development in the Al-Li System", J. of Metals, August 1981, p24.
49. T. H. Sanders and E. S. Balmuth; "Al-Li Alloys: Low Density and High Stiffness", Metal Prog., March 1978, p32.
50. G. E. Thompson and B. Noble; "Precipitation Characteristics of Al-Li Alloys Containing Magnesium" J. Inst. Met., v101, p111, (1973).
51. B. Noble and G. E. Thompson; "Precipitation Characteristics of Al-Li alloys", Met. Sci., v5, p114, (1971).
52. D. B. Williams and J. W. Eddington; "The Precipitation of Delta Prime (Al₃Li) in Dilute Al-Li Alloys", Met. Sci., v9, (1975), p529.
53. P. Niskanen, T.H. Sanders, Jr., J.G. Rinker and M. Marek; "Corrosion of Aluminum Alloys Containing Lithium", Corro. Sci., v22, n4, (1982), p283.
54. I. N. Fridlyander, T. I. Nilok'skaya, V. S. Sandler and B. V. Tyirin; Metallovd. Term. Obrab. Met., n8, August 1972, p7.
55. T. H. Sanders; "Factors Influencing Fracture Toughness and Other Properties of Aluminum-Lithium Alloys", Alcoa Final Report, Naval Air Development Center, Contract No. N62269-76-C-0271, June 14, 1979.
56. F. W. Gayle, R. F. Ashton, D. S. Thompson, S. A. Levy and G. E. Spangler; "The Development of Aluminum-Lithium Alloys", Reynolds Aluminum Final Report, Contract No. N00010-78-C-0485 Naval Air Systems Command (July 31, 1980)
57. D. P. Hill and D. N. Williams; "Relationship Between Hydrogen Content and Low Ductility" Final Rpt. Cont. No. N00019-81-C-0433, Naval Air Systems Command,

October 19, 1982.

58. H. P. Goddard, W. B. Jepson, M. R. Bothwell, and R. L. Kane, The Corrosion of Light Metals, John Wiley & Sons, Inc. New York, (1967)
59. M. Pourbaix; Atlas of Electrochemical Equilibrium Diagrams in Aqueous Solutions, National Association of Corrosion Engineers, Houston Texas, (1974).
60. J. W. Diggle and A. K. Vijh; Oxides and Oxide Films Vol. 4 Dekker Inc. NY, (1976), p229.
61. P. Niskanen, T. H. Sanders, Jr., M. Marek and J. G. Rinker; "The influence of Microstructure on the Corrosion of Al-Li, Al-Li-Mn, Al-Li-Mg and Al-Li-Cu Alloys in 3.5% NaCl Solutions" in Aluminum-Lithium Alloys, Edt. by T. H. Sanders Jr., and E. A. Starke Jr., The Metl Soc. of AIME, Warrendale PA, (1981), p347.
62. M. J. Feeney, "The Corrosion of Al-Li Alloys: A Study of Heat Treatment vs. Polarization Behavior", B.S. project, Rensselaer Polytechnic Institute, Troy, New York (1982)
63. J. T. Staley; "Stress-Corrosion Cracking in Aluminum Alloys", Metl. Engr. Q., November 1973, p52.
64. R. K. Viswanadham, T. S. Sun, and J. A. S. Green; "Influence of Moisture on The Composition on Al-Zn-Mg: An AES Study" Corro. v36, n6, June 1980, p275.
65. J. A. S. Green and W. G. Montague; "Observations on the Stress Corrosion Cracking of an Al-5%Zn-2.5%Mg Ternary and Various Quaternary Alloys", MML TR-74-23c, O.N.R. Contract N00014-74-C-0277, NR 031-716, October 26, 1973.
66. J. R. Pickens, D. Venable, and J. A. S. Green; "The Delayed Fracture of Aluminum Alloys", MML TR-81-6c, O.N.R. N00014-74-C-0277, P00007 January 1981.
67. W. W. Gerberich and W. E. Wood; "The Mechanical Nature of Stress-Corrosion Cracking in Al-Zn-Mg Alloys: II Electrochemical-Mechanical Model", Met Trans, v5, June 1974, p1295.
68. C. R. Shastry, M. Levy, and A. Joshi, "The Effect of Solution Treatment on Stress Corrosion Susceptibility

- of 7075 Al Alloy", Corro Sci, v21, n9, p673, (1981).
69. M. O. Speidel, "SCC of Aluminum Alloys", Met Trans, v6A, April 1975, p631.
 70. M. O. Spiedel, "Hydrogen Embrittlement of Aluminum Alloys?", in Hydrogen in Metals, eds. I. M. Bernstein and A. W. Thompson, Am. Soc. for Metals, Metals Park, Ohio (1974) p249.
 71. J. A. S. Green, and H. W. Hayden; "Influence of Two Modes of Loading on the Stress Corrosion Susceptibility of Ti-8 Al-1 Mo-1 V in Various Chloride containing Environments", in Hydrogen in Metals, ed. by I. M. Bernstein and A. W. Thompson, Am. Soc. for Metals, Metals Park Ohio, p235, (1974).
 72. J. A. S. Green, H. W. Hayden and W. G. Montague; in Effect of Hydrogen on Behavior of Materials, ed. by A. W. Thompson and I. M. Bernstein, The Met Soc. of AIME, NY, (1976), p200.
 73. J. G. Rinker; "Effect of Precipitation Heat Treatment on the Microstructure, Toughness and Stress Corrosion Crack Propagation Resistance of Al Alloy 2020", Ph.D. Thesis, Georgia Institute of Technology, September 1982.
 74. P. P. Pizzo; "The Relative Stress Corrosion Susceptibility of Candidate Al-Li Alloys for Aerospace Applications", NASA Contract Rpt. 3578, Contract No. NAS 10365, January 1982.
 75. L. Christodoulou, L. Struble and J. R. Pickens; "Stress Corrosion Cracking in Al-Li Binary Alloys" Presented at the 2'nd Intl. Conf. On Al-Li alloys at Monterey CA. April 1983 and to be published in the proceedings by The Metl. Soc. of AIME, Warrendale PA.
 76. R. J. Jacko; "Corrosion Fatigue of Aluminum Alloy 7075" Ph.D., Rennselaer Polytechnic Institute, Troy, NY (1978)
 77. J. Albrecht, A. W. Thompson and I. M. Bernstein; "The Role of Microstructure in Hydrogen Assisted Fracture of 7075 Aluminum" Met. Trans, v10A, November 1979, p1759.
 78. D. Hardie, N. J. H. Holroyd and R. N. Parkins; "Reduced Ductility of High Strength Aluminum Alloy During or After Exposure to Water" Met Sci, v13, Nov. 1979, p603.

79. N. J. H. Holroyd and D. Hardie; "Strain-Rate Effects in the Environmentally Assisted Fracture of a Commercial High-Strength Aluminum Alloy", Corro Sci, v21, (1981), p129.
80. S. W. Ciaraldi; "Internal Hydrogen Embrittlement in the Al-Zn-Mg System", Ph.D. Thesis, University of Illinois Urbana- Champaign, (1980).
81. R. Gest; "Environmentally Induced Failure of A High Strength Aluminum Alloy" PhD Thesis, Case Western Reserve University, June 1972.
82. L. Montgrain and P. R. Swann; "Electron Microscopy of Hydrogen in a High Purity Al-Zn-Mg Alloy", in Hydrogen in Metals, I. M. Bernstein and A. Thompson eds., Am. Soc. for Metals, Metals Park Ohio, (1974), p575.
83. G. M. Scamans, R. Alani, and P. R. Swann; "Pre-Exposure Embrittlement and Stress Corrosion Failure in Al-Zn-Mg Alloys", Corro. Sci., v16, p443, (1976).
84. R. M. Latanision, O. H. Gastine, and C. R. Compeau; "Stress Corrosion Cracking and Hydrogen Embrittlement: Differences and Similiarities" in Environment-Sensitive Fracture of Engineering Materials, Z. A. Foroulis edt., The Metl. Soc. of AIME, Warrendale PA, (1979), p48.
85. T. F. Klimowicz and R. M. Latanison; "On The Embrittlement of Aluminum Alloys by Cathodic Hydrogen: The Role of Surface Films", Met. Trans., v9A, April 1978, p597.
86. L. Christodoulou and H. M. Flower; "Hydrogen Embrittlement and Trapping in Al-6% Zn-3% Mg", Acta Met, v28, p481, (1980).
87. G. M. Scamans and C. D. S. Tuck; Embrittlement of Aluminum Alloys Exposed to Water Vapor" in Environment-Sensitive Fracture of Engineering Materials, Z. A. Foroulis edt., The Metl. Soc. of AIME, New York (1979). p464.
88. C. D. S. Tuck and G. M. Scamans; "Comparative Hydrogen Permeation Studies of Aluminum Alloys Exposed to Water Vapor" Second Intl. Congress on H in Metals, Paris, France, 4A11, p1
89. G. M. Scamans and C. D. S. Tuck; "The Role of H in Environment Sensitive Mechanical Behavior of Al-Zn-Mg

Alloys", Mechanisms of Environment Sensitive Cracking of Materials, P. R. Swann, F. P. Ford, and A. R. C. Westwood eds., The Metals Soc., London, p482, (1977).

90. P. J. E. Forsyth; "Fatigue Damage and Crack Growth in Al Alloys", *Acta Met*, v11, July (1963), p703.
91. C. Laird and D. J. Duquette; "Mechanisms of Fatigue Crack Nucleation", in Corrosion Fatigue, NACE-2, Nat. Assn. Corro. Engr., Houston TX, (1972), p88.
92. D. H. Avery and W. A. Backofen; "Nucleation and Growth of Fatigue Cracks", Fracture of Solids, D. C. Drucker ed., Interscience, New York, (1963), p339.
93. S. P. Lynch; "A New Model for Initiation and Growth of Fatigue Cracks", *Met Sci*, v9, p401, (1975).
94. C. A. Stubbington; "Some Observations on Air and Corrosion Fatigue of and Al-Zn-Mg Alloy", *Metallurgia*, v65, p109, (1963).
95. M. Nageswararao, and V. Gerold; "Fractography of Stage 1 Fatigue Facets of and Al-Zn-Mg Alloy", *Met Sci*, January 1977, p31.
96. M. Nageswararao and V. Gerold; "Fatigue Crack Propagation in Stage 1 in an Al-Zn-Mg Alloy: General Characteristics", *Met Trans*, v7A, December 1976, p1847.
97. W. Vogel, M. Wilhelm, and V. Gerold; "Persistent Slip Bands in Fatigued Peak Aged Single Crystals- II. Persistent Slip Bands in Front of Stage 1 Fatigue Cracks", *Acta Met*, v30, p31, (1982).
98. W. Vogel, M. Wilhelm, and V. Gerold; "Persistent Slip Bands in Fatigued Peak Aged Al-Zn-Mg Single Crystals-I. Development of Dislocation Microstructure and Change of Precipitation Distribution", *Acta Met*, v30, p21, (1982).
99. M. Nasgeswararao, M. Wilhelm and V. Gerold; "Influence of Precipitate Microstructure on the Resistance to Stage 1 Crack Propagation During Fatigue of Age Hardening Aluminum Alloys" ICSMA 4, Nancy France, August 1976, p832.
100. R. J. H. Wanhill; "Fractography of Fatigue Crack Propagation in 2024-T3 and 7075-T6 Aluminum Alloys in Air and Vacuum" *Met Trans*, v6A, August 1975, p1587.

101. D. Broek; "Some Contributions of Electron Fractography to the Theory of Fracture", Intl. Metl. Rvws., v19, p135, (1974).
102. D. J. Duquette and P. R. Swann; "An Electron Microscope Examination of Pre-Crack Fatigue Damage in Age Hardened Al-5% Zn-2.5% Mg", Acta Met, v24, p241, (1976).
103. C. A. Koss and K. S. Chan; "Fracture Along Planar Slip Bands" Acta Met, v28, p1245, (1980).
104. M. Gell and G. R. Leverant; "The Characteristics of Stage 1 Fatigue Fracture in a High Strength Nickel Alloy" Acta Met, v16, April 1968, p553.
105. D. J. Duquette, M. Gell, and J. W. Piteo; "A Fractographic Study of Stage 1 Fatigue Cracking in a Nickel-Base Superalloy Single Crystal" Met Trans, v1, November 1970, p3107.
106. P. J. E. Forsyth, C. A. Stubbington, and D. Clark; "Cleavage Facets Observed on Fatigue-Fracture Surfaces in an Aluminum Alloy", J. Inst. Metals, v90, (1961-62) p238.
107. C. A. Stubbington and P. J. E. Forsyth; "Some Corrosion Fatigue Observations on a High-Purity Al-Zn-Mg Alloy and Commercial D.T.D. 683 Alloy", J. Inst. Metals, v90, (1961-62) p347.
108. R. E. Stoltz and R. M. N. Pelloux; "Mechanisms of Corrosion Fatigue Crack Propagation in Al-Zn-Mg Alloys", Met. Trans., v3, Sept. 1972, p2433.
109. R. M. N. Pelloux; "Mechanisms of Formation of Ductile Fatigue Striations", Trans ASM, v62, p281, (1969).
110. R. M. N. Pelloux; "Corrosion Fatigue Crack Propagation", p731, Fracture 1969, P. L. Pratt ed., Chapman and Hall, London, (1969).
111. D. Broek and C. Q. Bowles; "The Microstructure of Fatigue Fracture Surfaces", Intl. J. Fract. Mech., v5, p350, (1969).
112. E. F. Smith; "The Corrosion Fatigue Behavior of a High Purity Al-Zn-Mg-Cu Alloy" Ph.D. Thesis, Rensselaer Polytechnic Institute, Troy, NY (1976).
113. G. A. Beitel and C. Q. Bowles; "Influence of Anodic

Layers on Fatigue Crack Nucleation in Aluminum", Met Sci, v5, (1971), p85.

114. J. C. Grosskreutz; "Mechanical Properties of Metal Oxide Films", J. Electrochem. Soc., v116, n9, Sept. 1969, p1232.
115. E. G. Eeles; "The Effect of Thin Anodic Oxide Films on the Fatigue Behavior of an Aluminum Alloy", J Inst. of Metals, v95, (1967) p156.
116. R. J. Gest and A. R. Troiano; "Stress Corrosion and Hydrogen Embrittlement in an Aluminum Alloy", Corro, p274, (1974).
117. T. Broom and A. Nicholson; "Atmospheric Corrosion-Fatigue of Age-Hardened Aluminum Alloys", J. Inst. Metals, v89, p183, (1960-61).
118. L. V. Corsetti and D., J. Duquette; "The Effect of Mean Stress and Environment on Corrosion Fatigue Behavior of 7075-T6 Aluminum", Met. Trans., v5, May 1974, p1087.
119. E. F. Smith, R. J. Jacko and D. J. Duquette; "The Fatigue Behavior of High Strength Aluminum Alloys under Cathodic Charging Conditions", Second Intl. Congress on Hydrogen in Metals, Paris France, 3C1, p1, (1977).
120. R. J. Jacko and D. J. Duquette; "Hydrogen Embrittlement of a Cyclically Deformed High Strength Aluminum Alloy", Met. Trans., v8A, Nov. 1977, p1821.
121. R. J. Jacko and D. J. Duquette; "The Role of Hydrogen on Environmental Fatigue of High Strength Aluminum Alloys" in Hydrogen Effects in Metals, I. M. Bernstein and A. W. Thompson eds., The Metl. Soc. of AIME, Warrendale PA, (1981).
122. S. Lebeau; "Corrosion Fatigue Crack Propagation of 7075 Aluminum", M.S. Thesis, Rensselaer Polytechnic Institute, Troy, NY (1978).
123. G. S. Owens; "Environmental Effects on the Fatigue Performance of 7050 Aluminum", M.S. Thesis, Rensselaer Polytechnic Institute Troy, NY (1980).
124. J. Lindigkeit, G. Terlinde, A. Gysler and G. Lutjering; "The Effect of Grain Size on The Fatigue Crack Propagation Behavior of Age Hardened Alloys in Inert and Corrosive Environments" Acta Met., v27, p1717,

(1979).

125. E. S. Tankins; "Evaluation of an Al-Mg-Li Alloy", Naval Air Development Center, Final Report No. NADC-79031-60, Feb. 1, 1979.
126. R. E. Bolz and G. L. Tuve; Handbook of Tables for Applied Engineering Science CRC Pres, Cleveland Ohio, (1973).
127. N. D. Green; Experimental Electrode Kinetics, Rensselaer Polytechnic Institute, Troy NY, (1972).
128. J. Crank; The Mathematics of Diffusion, Clarendon Press, Oxford England, (1975).
129. E. P. Popov; Mechanics of Materials, Prentice-Hall Inc. New York, (1952).
130. S. H. Crandahl, N. C. Dahl, T. J. Lardner; An Introduction to the Mechanics of Solids, McGraw Hill, New York, (1972).
131. M.-L. Saboungi, C. C. Hsu; "Estimate of Isothermal Sections of Ternary Phase Diagrams of Al-Li-Mg System", NBS SP-496, "Applications of Phase Diagrams in Metallurgy and Ceramics" Gaithersburg MD, (1977), p1109.
132. D. E. J. Talbot; "Effects of Hydrogen in Aluminum, Magnesium Copper and Their Alloys" Intl. Metl. Reviews, n201, v20, (1975), p166.
133. W. Eichenauer, K. Hattenbach, and A. Pebler; "Die Loslichkeit von Wasserstoff in Festem und Flussigem Aluminum" Z. Metallkunde, v52, (1961), p682.
134. C. E. Ransley and D. E. Talbot; "Wasserstoff-Porositat in Metallen unter Besonderer Berucksichtigung des Aluminiums" Z. Metallkunde, v46, (1955), p328.
135. W. Eichenauer and J. Markopolous; "Messung des Diffusionskoeffizienten von Wasserstoff in Flussigen Aluminum" Z. Metallkunde, v65, (1974), p649.
136. K. Papp and E. Kovacs-Csetenyi; "Diffusion of Hydrogen in Solid Aluminum" Scripta Met., v11, (1977), p921.
137. K. Papp and E. Kovacs-Csetenyi; "Diffusion of Hydrogen in High Purity Aluminum", Scripta Met., v15, (1981),

pl61.

138. R. A. Outlaw, D. T. Peterson and F. A. Schmidt; "Diffusion of Hydrogen in Pure Large Grain Aluminum", *Scripta Met.*, v16, p287, (1982).
139. H. K. Birnbaum; "Hydrogen Related Failure Mechanisms in Metals" in Environment-Sensitive Fracture of Engineering Materials, Z. A. Foroulis ed., The Metall. Soc. of AIME, Warrendale PA, p326, (1979)
140. C. D. S. Tuck and G. M. Scamans; "Comparative Hydrogen Permeation Studies of Aluminum Alloys Exposed to Water Vapor" Second Intl. Congress of Hydrogen in Metals, Paris France, 4A11, pl, (1977).
141. W. Latimer, Oxidation Potentials, Prentice Hall, Englewood Cliffs, New Jersey (1952).
142. T.H. Nguyen and R.T. Foley, "The Chemical Nature of The Anion dependency of the Corrosion of Aluminum Corrosion III: Dissolution Mechanisms of Aluminum Oxide and Aluminum Powder in Various Electrolytes", *J. Electrochem. Soc.*, v127, p2563, (1980).
143. R.T. Foley and P.P. Trazaskoma, "The Chemical Nature of the Anion Dependency of the Corrosion of Aluminum Alloy 7075-T6" *Corro*, v33, n12, p435, (1977).
144. H. Bohni and H.H. Uhlig, "Environmental Factors Affecting the Critical Pitting Potential of Aluminum" *J. Electrochem. Soc.*, v116, n7, p906, (1969).
145. B.N. Stirrup, N.A. Hampson, I.S. Midgley, "Pit Formation in Relation to the Etching of Aluminum in Chloride Solutions", *J. Applied Electrochemistry*, v5, p229, (1975).
146. A. Broli and H. Holtan, "Use of Potentiokinetic Methods for The Determination of the Characteristic Potential for Pitting Corrosion of Aluminum in a Deaerated Solution of 3% NaCl", *Corrosion Sci.*, v13, p237, (1973).
147. S. Dallek and R. T. Foley, "Mechanism of Pit Initiation on Aluminum Alloy 7075", *J. Electrochem. Soc.*, v123, n12, p1775, (1976).
148. T. P. Hoar "The Production and Breakdown of the Passivity of Metals", *Corrosion Sci.*, v7, p341, (1967).

149. O. H. Basquin; "The Exponential Law of Endurance Tests", Proc. Am. Soc. Testing Matls., v10, p625, (1910).
150. L. F. Coffin and T. F. Tavernelli; "The Cyclic Straining and Fatigue of Metals", Trans. TMS-AIME, v215, October 1959, p794.
151. L. F. Coffin, Jr.; "Low Cycle Fatigue: A Review", Apd. Matls. Res., v1, n3, October 1962, p129.
152. L. F. Tavernelli and L. F. Coffin: "A Compilation of Cyclic Strain Faigue Tests on Metals", Trans ASM, v51, p488, (1959).
153. T. F. Tavernelli and L. F. Coffin, Jr.; "Experimental Support for Generalized Equation Predicting Low Cycle Fatigue", Trans ASME D, J Basic Engr, v84, n4, December 1962, p533.
154. S. S. Manson; Discussion of ref no. 153
155. R. W. Smith, M. H. Hirschberg and S. S. Manson; "Fatigue Behavior of Materials Under Strain Cycling in Low and Intermediate Life Range", NASA Tech Note D-1574, April 1963.
156. S. S. Manson and M. H. Hirschberg; "Fatigue Behavior in Strain Cycling in the Low and Intermediate Cycle Range", Tenth Sagamore Army Materials Research Conf., Sagamore, New York, Aug. 13-16, 1963.
157. J. D. Morrow and F. R. Tuller; "Low Cycle Fatigue Evaluation of In 713 and Waspaloy", Trans ASME D, J Basic Engr., June 1965, p175,
158. C. E. Feltner and J., D. Morrow; "Micro-Plastic Strain Hysteresis Energy as a Criterion for Fatigue Fracture", Trans ASME D, J Basic Engr., v83, p15, (1961).
159. R. D. Stout and A. W. Pense; "Effect of Composition and Microstructure on the Low Cycle Fatigue Strength of Structural Steels", Trans ASME, J Basic Engr, June 1965, p269.
160. F. S. Lin and E. A. Starke; "The Effect of Cu Content and Degree of Recrystallization on The Fatigue Resistance of 7XXX Type Al Alloys I. Low Cycle Corrosion Fatigue", Mat Sci and Engr, v39, p27, (1979).

161. D. W. Chung and N. S. Stoloff; "Effect of Hydrogen on Fatigue Crack Propagation in Vanadium", Met Trans, v9A, January 1978, p71.
162. K. S. Lee and N. S. Stoloff; "Fatigue of Vanadium-Hydrogen Alloys", Effect of Hydrogen on Behavior of Metals, A. W. Thompson and I. M. Bernstein eds., The Metl. Soc. of AIME, New York, (1976) p404.
163. G. H. Koch; "Hydrogen Induced Fracture of a High Strength Aluminum Alloy", Corro, v35, n2, (1979), p73.
164. L. F. Coffin, Jr.; "The Multi-Stage Nature of Fatigue: A Review", Met Sci, February 1977, p68.
165. T. H. Sanders, R. R. Sawtell, and J. T. Staley; "Effect of Microstructure on Fatigue Crack Growth of 7XXX Aluminum Alloys Under Constant Amplitude And Spectrum Loading", Final Rpt., Naval Air Development Center, Cont No. N00019-76-C-0482, April 14, 1978.
166. R. W. Hertzberg; Deformation and Fracture Mechanics of Engineering Materials, John Wiley and Sons, New York, (1976).
167. K. Dinsdale, S. J. Harris, B. Noble; "Relationships Between Microstructure and Mechanical Properties of Al-Li-Mg Alloys", Aluminum-Lithium Alloys, T. H. Sanders and E. A. Starke eds., The Metl. Soc. of AIME, Warrendale PA, (1981)
168. A. Joshi, C. R. Shastri and M. Levy; "Effect of Heat Treatment on Solute Concentration at Grain Boundaries in 7075 Aluminum Alloy", Met Trans, v12A, June 1981, p1081.
169. J. R. Pickens, D. Venables, J. A. S. Green; "The Delayed Failure of Aluminum Alloys", Office of Naval Research, Cont. No. N00014-81-C-0342, March 1982.
170. J. R. Pickens, D. Venables, J. A. S. Green; "The Delayed Failure of Aluminum Alloys", Office of Naval Research, Cont. No. N00014-82-C-0378, March 1983.
171. D. J. Duquette; "Mechanisms of Corrosion Fatigue of Aluminum Alloys", AGARD Conf. Proc. No. 316 Corrosion Fatigue, North Atlantic Treaty Organization.
172. D. J. Duquette; "The Effects of Environment on Fatigue Crack Initiation and Early Propagation", Corrosion

Fatigue: Mechanics, Metallurgy, Electrochemistry and Engineering Crooker and Leis eds., ASTM-STP-801, (1982).

173. V. A. Garten and R. B. Head; "An Experimental Model of Crack Nucleation by Slip Bands", Intl. J. of Fract. Mech., v7, n3, September 1971, p343.
174. T. Ogura and S. Karashima; "Substructure Formation Around Fatigue Cracks and Its Role in The Propagation of Fatigue Cracks in Aluminum", Trans JIM, v13, (1972), p428.
175. J. M. Chen, T. S. Sun, R. K. Viswanadham and J. A. S. Green; "Grain Bouyndary Segregation of Al-Zn-Mg Ternary Alloys", Tech Rpt. No. 4, Office of Naval Research, Cont. No. N00014-74-C-0277, April 1977.
176. R. K. Viswanadham, T. S. Sun and J. A. S. Green; "Grain Boundarty Segregation in Al-Zn-Mg Alloys-Implication to Stress Corrosion Cracking", Tech. Rpt. No. 5, Office of Naval Research, Cont. No. N00014-74-C-0277, August 1978.
177. L. K. L. Tu; "A Study of Fracture Mechanics: Part II An Examination of the Corrosion Fatigue Crack Tip Zone", PhD Thesis, Cornell University, Ithica NY, August 1975.
178. D. L. Davidson and J. Lankford; "Crack Tip Plasticity Associated With Corrosion Fatigue", Interim Rpt., Office of Naval Research, Cont. No. N00014-75-C-1038, November 15, 1982.
179. D. L. Davidson and J. Lankford; "Crack Tip Plasticity Associated With Corrosion Fatigue", Interim Rpt., Office of Naval Research, Cont. No. N00014-75-C-1038, May 31, 1979.
180. J. J. DeLuccia; "Electrolytic Hydrogen in Beta Titanium", PhD Thesis, University of Pennsylvania, Phil. PA, (1976).
181. P. N. Adler; "Localized Hydrogen Analysis in Simulated Grain Boundaries of Aluminum Alloys Exposed to Stress Corrosion", Final Rpt., Naval Air Systems Command, Cont. No. N00019-75-C-0394, February 1978.
182. J. Kruger, J. J. Carroll, A. J. Melmed, J. J. Ritter, J. R. Ambrose; "Passive Films Surface Structure and Stress Corrosion and Crevice Corrosion Susceptibility",

NBSIR 79-1904(NAVY), National Bureau of Standards, Washington, D.C.

183. R. J. H. Wanhill; "Cleavage of Aluminum Alloys in Liquid Mercury", Corro, v30, n10, October, 1974.
184. S. Gahr, B. J. Makenas, H. K. Birnbaum; "Hydrogen Embrittlement-Hydride Fracture", Tech. Rpt. Office of Naval Research, Cont. No. N00014-75-C-1012.
185. C. D. Beachem; "A New Model for Hydrogen-Assisted Cracking (Hydrogen "Embrittlement")", Met Trans, v3, n2, February 1972, p437.
186. S. P. Lynch; "Tensile Deformation and Fracture in High Strength Al-Zn-Mg Alloys", Met. Sci. J., v7, (1973), p93.
187. A. J. Sedriks, J. A. S. Green, and D. L. Novak; "The Influence of Heat Treatment on The Stress-Corrosion Susceptibility of a Ternary Al-5.3%Zn-2.5% Mg Alloy", Tech. Rpt. No. 7, Office of Naval Research Cont. No. N00014-67-C-0496, May 1973.
188. D. W. Levinson and D. J. McPherson; "Phase Relations in Mg-Li-Al Alloys", Trans of ASM, v48, (1955) p689.
189. G. S. Ansel and R. Vennett; "Hydrogen Embrittlement", Final Report, Army Research Office, AT(30-1)-3479, June 1968.
190. W. J. Baxter; "Gel Electrode Imaging of Fatigue Cracks in Aluminum Aloys", Intl. J. of Fatigue, January 1983, p37.
191. A. J. Sedriks, P. W. Slattery and E. N. Pugh; "Deformation Within Precipitate Free Zones in Aged Al-Zn-Mg Alloys", Trans ASM, v62, (1969) p815.
192. P. Lukas and J. Polak; "Cyclic Stress-Strain Response in Low Amplitude Region", Work Hardening in Tension and Fatigue, A. W. Thompson ed., The Metl. Soc. of AIME, New York, NY, (1977) p177.
193. C. Zapffe and C. Sims; "Hydrogen Embrittlement, Internal Stress and Defects in Steel", Trans AIME, v145, p225, (1941).
194. A. S. Tetelman and W. D. Robertson; "Direct Observation and Analysis of Crack Propagation in Iron-3% Si Single

Crystals", Acta Met, v11, May 1963, p415.

195. J. K. Tien, A. W. Thompson, I. M. Bernstein and R. J. Richards; "Hydrogen Transport by Dislocations", Met Trans, v7A, June 1976, p821.
196. H. H. Johnson and J. P. Hirth; "Internal Hydrogen Supersaturation Produced by Dislocation Transport", Met Trans, 7A p1543, (1976).
197. J. L. Nelson and E. N. Pugh; "The Occurrence of Transgranular Cleavage-Like Fracture in an Al-Zn-Mg Alloy During Tensile Testing", Met Trans, v6, p1459, (1975).
198. S. W. Ciaraldi, J. L. Nelson, R. A. Yeske, and E. N. Pugh; "Studies of Hydrogen Embrittlement and Stress-Corrosion Cracking in and Al-Zn-Mg Alloy", Hydrogen Effects in Metals, I. M. Bernstein and A. W. Thompson eds., The Metl. Soc. of AIME, New York, N.Y. (1981) p437.
199. N. J. Petch and P. Stables; "Delayed Fracture of Metals Under Static Load", Nature, v169, n4307, May 1952, p842.
200. N. J. Petch; "The Lowering of Fracture-Stress Due to Surface Adsorption", Phil Mag, ser. 8, v1, n4, April 1956, p331.
201. E. Orowan; "Fundamentals of Brittle Behavior in Metals", Fatigue and Fracture of Metals, W. M. Murray ed. John Wiley and Sons, Inc., New York, (1952), p139.
202. R. A. Oriani and P. H. Josephic; "Equilibrium and Kinetic Studies of the Hydrogen-Assisted Cracking of Steel", Acta Met, v25, n9, Sept. 1977, p979.
203. G. G. Hancock and H. H. Johnson; "Hydrogen, Oxygen and Subcritical Crack Growth in a High Strength Steel", Trans AIME, v236, n4, April 1966, p513.
204. T. E. Scott and A. R. Troiano; "Interstitials and Fracture of Metals", Nature, v185, n4710, Feb. 6, 1960, p372.
205. E. A. Steigerwald, F. W. Schaller, and A. R. Troiano; "The Role of Stress in Hydrogen Induced Delayed Failure", Trans AIME, v218, n5, Oct. 1960, p832.

- 206. A. N. Stroh; "A Theory of the Fracture of Metals", Adv. in Physics, v6, n24, Oct. 1957, p418.
- 207. A. R. Troiano; "The Role of Hydrogen in the Mechanical Behavior of Metals", Trans ASM, v52, (1960), p54.
- 208. J. J. Gilman; "Fracture of Zinc-Monocrystals and Bicrystals", Trans AIME (met), v212, Dec. 1958, p783.
- 209. J. A. Collins; Failure of Materials in Mechanical Design, John Wiley and Sons, New York, NY (1981).

APPENDIX I:

The Derivation of Strain, Load and
Displacement Relationships

The radius of curvature (ρ) of an arc is defined as:

$$\frac{1}{\rho} = \frac{d^2y/dx^2}{\left[1 + \left(\frac{dy}{dx}\right)^2\right]^{3/2}} \quad [I-1]$$

For small curvatures this may be approximated as:

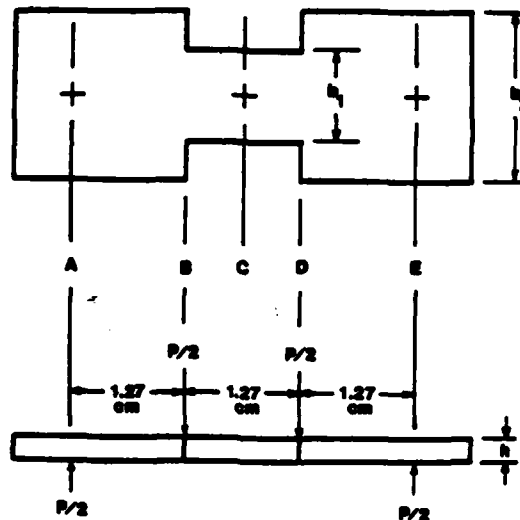
$$\frac{1}{\rho} \approx \left(\frac{d^2y}{dx^2}\right) \quad [I-2]$$

Then, by substituting the bending moment (M), the bending moment of inertia (I), and the modulus of elasticity (E) into this equation for the radius of curvature this equation becomes:

$$\frac{M}{EI} = \frac{d^2y}{dx^2} \quad [I-3]$$

This differential equation is an approximation of the exact differential equation which would be obtained if the approximation above is not made. However, this equation can be solved directly by integrating twice over the proper boundary conditions to obtain a relationship for the displacement.

For the bending tests employed the specimen geometry can be approximated as:



For this geometry the boundary conditions are:

1. $Y_A = Y_E = 0$ (Points A and E are fixed at zero.)
2. $\theta_A = \theta_E$ (Slope at points A and E are the same.)
3. $\theta_B = \theta_D$ (Slope at points B and D are the same.)
4. $\theta_C = 0$ (Slope at middle point.)

Between points A and B the bending moment of inertia is:

$$I = \frac{bh^3}{12} \quad [I-4]$$

and the bending moment is:

$$M = \frac{1}{2} Px \quad [I-5]$$

The differential equation is:

$$\frac{d^2y}{dx^2} = \frac{6Px}{Eb_1h^3} \quad [I-6]$$

Which when it is integrated it becomes:

$$\theta = \frac{dy}{dx} = \frac{3Px^2}{Eb_1h^3} + C_1 \quad [I-7]$$

Where the constant of integration is the slope at point A (θ_A). Integrating this a second time yields:

$$Y = \frac{Px^3}{Eb_1h^3} + \theta_A x + Y_A \quad [I-8]$$

The displacement at point A was defined as zero and the displacement at point B is the experimentally measured stroke which is:

$$y_B = \frac{P}{8Eb_1h^3} + \frac{\theta_A}{2} \quad [I-9]$$

Between points B and C, the bending moment is constant and the differential equation becomes:

$$\frac{d^2y}{dx^2} = \frac{3P}{Eb_2h^3} \quad [I-10]$$

When this is integrated it becomes:

$$\frac{dy}{dx} = \frac{3Px}{Eb_2h^3} + \theta_B \quad [I-11]$$

Where the slope at point B (θ_B) can be determined from equation [I-3] as:

$$\theta_B = \left(\frac{dy}{dx} \right)_B = \frac{3P}{4Eb_1h^3} + \theta_A \quad [I-12]$$

Now by substituting this into equation [I-11] and solving for the slope at point C gives:

$$\theta_C = \frac{3P}{4Eb_2h^3} + \frac{3P}{4Eb_1h^3} + \theta_A = 0 \quad [I-13]$$

Which since the slope at point C is set at zero (boundary condition 4) this yields:

$$\theta_A = \frac{-3P}{4Eh^3} \left[\frac{b_1 + b_2}{b_1 b_2} \right] \quad [I-14]$$

Since the displacement (δ) is measured at point B then equation [I-14] is used to solve equation [I-9] as:

$$\delta = \frac{-P}{8Eh^3} \left[\frac{3b_1 + 2b_2}{b_1 b_2} \right] \quad [I-15]$$

This equation relates the measured displacement (δ) and the measured load (P). To get the strain at the surface (the maximum strain), from this equation the relationship:

$$\epsilon_{\max} = \frac{3P}{2Ebh^3} \quad [I-16]$$

is substituted in for the strain to give:

$$\delta = \frac{\epsilon_{\max} b_2}{12h} \left[\frac{3b_1 + 2b_2}{b_1 b_2} \right] \quad [I-17]$$

Which if a constant (k) is defined as (b_1/b_2) then:

$$\epsilon/\delta = \left[\frac{12hk}{3k+2} \right] \quad [I-18]$$

APPENDIX II:

Absorption or Desorption from a Plane Sheet

For the absorption of the desorption of a species from the surface of a plane sheet, the surface boundary condition is:

$$-D\left(\frac{\partial C}{\partial x}\right) = \alpha(C_0 - C_s) \quad [\text{II-1}]$$

Where (C_0) is the surface concentration of the species in equilibrium with the atmosphere, (C_s) is the actual surface concentration as a function of time and (α) is a proportionality constant.

For a sheet initially at a uniform concentration (C_2) and the exchange defined by equation [II-1] for both surfaces, the solution is (128):

$$\frac{C_1 - C_2}{C_0 - C_2} = 1 - \sum_{n=1}^{\infty} \frac{2L \cos\left(\frac{\beta_n x}{l}\right) \exp\left(-\frac{\beta_n^2 Dt}{l^2}\right)}{(\beta_n^2 + L^2 + L) \cos \beta_n} \quad [\text{II-2}]$$

Where the β_n 's are the positive roots of the equation:

$$\beta \tan \beta = L \quad [\text{II-3}]$$

and for the thickness of the sheet equal to $(2l)$ L is:

$$L = \frac{l\alpha}{D}$$

[II-4]

To determine the percent absorbed or desorbed this equation becomes:

$$\frac{M_t}{M_\infty} = 1 - \sum_{n=1}^{\infty} \frac{2L^2 \exp\left(-\frac{\beta_n^2 Dt}{l^2}\right)}{\beta_n^2 (\beta_n^2 + L^2 + L)} \quad [\text{II-5}]$$

For large L 's the β_n terms can be approximated by the terms for the argument approaching infinity which for the first two terms gives (128):

$$\beta_1 = 1.5708$$

$$\beta_2 = 4.7124$$

This is a good approximation for L 's greater than one hundred.

From this, it can be seen that the second term of the series is small compared to the first term and that a first term approximation to the infinite series will be good for all but short times. This equation is:

$$\frac{M_t}{M_\infty} = 1 - (0.81057) \left[\frac{L^2}{(1.5708^2 + L^2 + L)} \right] \exp \left[-2.467 \left(\frac{Dt}{l^2} \right) \right] \quad [\text{II-6}]$$

Since L^2 is very large compared to $(1.5708)^2$, this relationship can be approximated further as:

$$\frac{M_t}{M_\infty} = 1 - (0.81057) \exp \left[2.4674 \left(\frac{D_t}{\ell^2} \right) \right] \quad [\text{II-7}]$$

However, determining diffusivities from this relationship usually requires curve fitting and estimating. For data which does not fit smoothly this technique may lead to interpretation errors. As a result, a statistical technique was employed. This technique uses a standard linear regression program and the relationship:

$$\left(\frac{M_\infty - M_t}{M_\infty} \right) = (0.81057) \exp -2.4674 \left(\frac{D_t}{\ell^2} \right) \quad [\text{II-8}]$$

Which by taking the logarithms becomes:

$$\log \left[\frac{M_\infty - M_t}{M_\infty} \right] = \log(0.81057) - 2.4674 \left(\frac{D_t}{\ell^2} \right) \quad [\text{II-9}]$$

It can be seen that this relationship is a linear function in terms of the log of the measures percent absorbed or desorbed versus the time of exposure. The diffusivity can be estimated from the slope of the line of best fit through the data.

APPENDIX III:

Linear Regression Analysis of Low Amplitude
Strain Controlled Fatigue Data

The fatigue life in terms of strain is frequently represented as a summation of elastic and plastic contributions as:

$$\Delta\epsilon_{\text{total}} = \Delta\epsilon_{\text{plastic}} + \Delta\epsilon_{\text{elastic}} \quad [\text{III-1}]$$

This is frequently called the "Coffin-Manson" equation. The relationship originally proposed by Tavernelli and Coffin (150,153) was for plastic strains and is:

$$\Delta\epsilon_{\text{pl}} = \epsilon_f' N_f^c \quad [\text{III-2}]$$

When inelastic strains are immeasurably small in strain controlled fatigue tests, the results may be represented by the Basquin equation which is (164,149)

$$\Delta\epsilon_{\text{el}} = \left(\frac{\sigma_f'}{E} \right) N_f^{-b} \quad [\text{III-3}]$$

This is the elastic part of the "Coffin-Manson" relation but was originally proposed by Basquin in 1910 (149). If the logarithms are taken of equation [III-3], this yields:

$$\log (\Delta \epsilon) = \log \left(\frac{\sigma_f'}{E} \right) - b \log (N_f) \quad [\text{III-4}]$$

This is a linear relationship and can be analyzed with a standard linear regression program to determine the parameters. However, in the experiment, the strain is held constant and the cycles to failure are measured. As a result, the correct linear regression analysis of the results should be with the log of the strain range as the independent variable and with the log of the cycles to failure as the dependent variable. This is:

$$\log N_f = \frac{-1}{b} \log (\Delta \epsilon) + \frac{1}{b} \log \left(\frac{\sigma_f'}{E} \right) \quad [\text{III-5}]$$

If the correlation coefficient of the linear regression analysis is unity, then either variable can be chosen and used as the independent variable in the calculation with the same results. However, this only occurs for a perfectly straight line and is not very likely for real experimental results. As a result, linear regression analysis was performed with the cyclic strain as the independent variable and the cycles to failure as the dependent variable as described by equation [III-5].

END

FILMED

2-86

DTIC